DYNAMICS OF EQUATORIAL SPREAD *F* USING GROUND-BASED

OPTICAL AND RADAR MEASUREMENTS

by

Narayan P. Chapagain

A dissertation submitted in partial fulfillment
of the requirements for the degree

of

DOCTOR OF PHILOSOPHY

in

Physics

UTAH STATE UNIVERSITY
Logan, Utah

2011

DYNAMICS OF EQUATORIAL SPREAD *F* USING GROUND-BASED

OPTICAL AND RADAR MEASUREMENTS

by

Narayan P. Chapagain

A dissertation submitted in partial fulfillment
of the requirements for the degree

of

DOCTOR OF PHILOSOPHY

in

Physics

Approved:
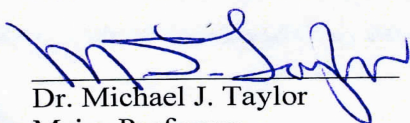
_____
Dr. Michael J. Taylor
Major Professor

_____
Dr. Bela G. Fejer
Committee Member
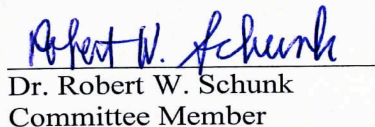
_____
Dr. Robert W. Schunk
Committee Member
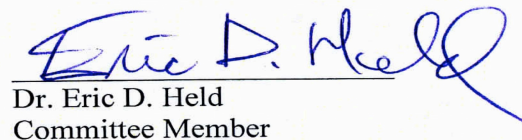
_____
Dr. Eric D. Held
Committee Member

_____
Dr. Randy Jost
Committee Member
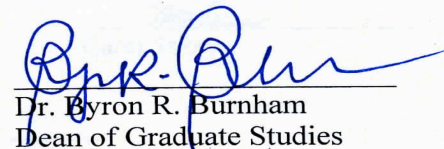
_____
Dr. Byron R. Burnham
Dean of Graduate Studies

UTAH STATE UNIVERSITY
Logan, Utah

2011

ABSTRACT

Dynamics of Equatorial Spread *F* Using Ground-Based Optical and

Radar Measurements

by

Narayan P. Chapagain, Doctor of Philosophy

Utah State University, 2011

Major Professor: Dr. Michael J. Taylor
Department: Physics

The Earth's equatorial ionosphere most often shows the occurrence of large plasma density and velocity fluctuations with a broad range of scale sizes and amplitudes. These night time ionospheric irregularities in the F-region are commonly referred to as equatorial spread *F* (ESF) or plasma bubbles (EPBs). This dissertation focuses on analysis of ground-based optical and radar measurements to investigate the development and dynamics of ESF, which can significantly disrupt radio communication and GPS navigation systems. OI (630.0 nm) airglow image data were obtained by the Utah State University all-sky CCD camera, primarily during the equinox period, from three different longitudinal sectors under similar solar flux conditions: Christmas Island in the Central Pacific Ocean, Ascension Island in South Atlantic, and Brasilia and Cariri in Brazil. Well-defined magnetic field-aligned depletions were observed from each of these sites enabling detailed measurements of their morphology

and dynamics. These data have also been used to investigate day-to-day and longitudinal variations in the evolution and distribution of the plasma bubbles, and their nocturnal zonal drift velocities. In particular, comparative optical measurements at different longitudinal sectors illustrated interesting findings. During the post midnight period, the data from Christmas Island consistently showed nearly constant eastward bubble velocity at a much higher value (~80 m/s) than expected, while data from Ascension Island exhibited a most unusual shear motion of the bubble structure, up to 55 m/s, on one occasion with westward drift at low latitude and eastward at higher latitudes, evident within the field of view of the camera.

In addition, long-term radar observations during 1996-2006 from Jicamarca, Peru have been used to study the climatology of post-sunset ESF irregularities. Results showed that the spread F onset times did not change much with solar flux and that their onset heights increased linearly from solar minimum to solar maximum. On average, radar plume onset occurred earlier with increasing solar flux, and plume onset and peak altitudes increased with solar activity. The F-region upward drift velocities that precede spread F onset increased from solar minimum to solar maximum, and were approximately proportional to the maximum prereversal drift peak velocities.

(218 pages)

DEDICATION

In memory of my parents

ACKNOWLEDGMENTS

CONTENTS

LIST OF TABLES

LIST OF FIGURES

CHAPTER 1

INTRODUCTION

1.1. Introduction

The Earth's ionosphere often shows the occurrence of highly irregular plasma density and velocity fluctuations with a large range of scale sizes and amplitudes at almost all altitudes throughout the latitude and longitude sectors. The plasma irregularities at F-region ionosphere are predominantly a nighttime phenomenon and this is a region of greatest interest to space scientists because of the complex dynamical phenomena and instability occurrence in this region. The horizontal geomagnetic field lines at the magnetic equator perpendicular to gravity, and also prevailing natural wind and background electric field, compose unique phenomena to develop the plasma irregularities in the equatorial region. This post-sunset phenomenon is commonly referred to as equatorial spread *F* (ESF) or simply plasma irregularity or depletion. These plasma irregularities are generally magnetic field aligned. They have zonal widths of typically a few tens of km and extend along the magnetic field lines for hundreds to thousands of km depending on the peak altitude of the irregularity (bubble) development (e.g., *Sobral et al.,* 2002), while their vertical heights range from a few tens of km to several hundred km [e.g., *Labelle et al.,* 1997].

When radio signals propagate through these disturbed regions, they cause scintillation. This results in a fade in received signal power, meaning a loss of signal. Scintillations are known to occur on frequencies below 3 GHz and are a concern to many sectors, both civilian and military. The generation of these irregularities is one of the

most spectacular manifestations of space weather in the Earth's ionosphere. Understanding the day-to-day variability of these irregularities has become a highly active area of research in the aeronomy community and much work remains to be done before we have a complete understanding of this phenomenon.

Ionospheric irregularities were first reported by scientists using HF (High-Frequency) radio ionospheric sounding experiments that took place about seven decades ago. *Berkner and Wells* [1934] described well known accounts of ionosonde reflections above the nighttime F peaks. *Booker and Wells* [1938] published nighttime ionograms with virtual height traces that were mysteriously spread in altitude. The bottomside profiles of the plasma were also found to be disturbed after sunset, which affected radio wave propagation near the critical frequency. This disturbance, called equatorial spread *F,* is now known as the process that causes large-scale plasma depletions (termed bubbles, wedges, or plumes). As the plasma depletions advect upwards from the bottomside to the topside ionosphere, they generate a broad spectrum of disturbances that can be detected by digital ionosondes and ionospheric radars and result in spectacular airglow images. *Haerendel* [1973] published a theory for bubbles where he applied the concept of flux tube integrated variables. In 1973, *Hanson and Sanatoni* used the satellite observations and reported density bite-outs of over three orders of magnitude deep in the bottomside F-region. *Woodman and LaHoz* [1976] used radar observations from Jicamarca, Peru, and reported plume-like structures extending to high altitudes. In addition to the ionosonde and radar observations [e.g., *Fejer and Kelley,* 1980], the plasma irregularities (or bubbles) have been detected by satellite [e.g., *McClure et al.,*

1977], rockets [e.g., *Kelley et al.,* 1982], as well as other ground-based optical instruments [e.g*., Weber et al.,* 1978; *Mendillo and Baumgardner*, 1982; *Taylor et al.,* 1997].

The instability mechanism responsible for the development of ESF (discussed in Chapter 2) is most effective at the magnetic equator in the post-sunset time period, although occasionally post-midnight and pre-sunrise events have been observed. Much progress in studying ESF has been made, but several important questions remain unclear including an understanding of the seeding mechanisms favorable to instability growth. The several-generation mechanisms of the ESF have been reported, which often include a complex interplay of plasma, electrostatic turbulence, convection, chemical and neutral atmospheric effects, and particle precipitation. The Rayleigh-Taylor instability (RTI) process was first suggested as the physical mechanism for the generation of ESF by *Dungey* [1956]. RTI can develop when heavier plasma is supported by the lighter plasma, which is exactly the case in the post-sunset F-region ionosphere. The conditions required for the RTI are generally met around post-sunset at the magnetic equator where the bottomside of the F-layer has recombined and the entire F-layer itself has been raised considerably by the pre-reversal enhancement in the eastward electric field. This creates a very sharp vertical density gradient that is unstable to vertical perturbations in the ionosphere. The exact source of the perturbation is still the cause of much debate, and several mechanisms, including gravity waves [*McClure et al.,* 1998] have been suggested. The resultant release of gravitational energy stored in the height of the ionosphere leads to the growth of an equatorial plasma bubble (EPB). Internal to this

depleted region are intense, small-scale perturbations in the electric field and electron density. These perturbations cause the widespread effects of ESF, which sometimes reach more than 20º latitude from the generation region at the magnetic equator [e.g., *Kelley et al.,* 2002; *Makela and Kelley,* 2003]. This is due to the large conductivity along the magnetic field lines, allowing the perturbed electric fields to efficiently map poleward where they can affect the local ionosphere.

These electric fields perturb the local ionosphere poleward of the equator and allow for ground-based imaging techniques to capture two-dimensional spatial information on the depletions. Several previous studies have employed all-sky imagers pointed to the zenith to make observations of the kilometer-and-greater scale-size depleted regions associated with ESF [e.g., *Mendillo and Baumgardner*, 1982; *Taylor et al.,* 1997; *Makela*, 2006]. The advantage of imaging over other techniques of studying these irregularities (e.g., coherent radar observations and VHF scintillation measurements) is that imaging reveals the two-dimensional structure of these depleted regions rather than their properties along a single viewing direction.

The occurrence and severity of an ESF event depends on the condition of the local equatorial ionosphere, as well as that of the plasma in electrical contact with it (namely, the off-equatorial E-region) through coupling within the appropriate magnetic flux tube. Convective plumes of turbulent plasma that develop during strong ESF events rising to higher altitudes can degrade communications system and can last for several hours as the plumes (bubbles) drift as fossilized bubbles with the background plasma. Consequently, further study of development and propagation of the plasma bubbles during the night-

time period has become very important for space weather prediction. Additionally, the knowledge of space and time variations of the ionospheric zonal and vertical drifts in the equatorial region is of fundamental importance to the understanding of the low-latitude ionospheric climatology [*Fejer et al.,* 1991]. The study of these drifts also helps us to better understand the local mechanisms of coupling processes of the ionosphere-thermosphere (I-T) system under magnetically quiet conditions, as well as global mechanisms of the equatorial ionosphere coupling with magnetosphere, interplanetary medium and high-latitude I-T system under magnetic storm conditions. On the other hand, ESF has been convincingly linked to variations in the strength of the prereversal enhancement (PRE), which is an increase in the vertical drift velocity during the post-sunset period that drives equatorial plasma to higher altitudes where conditions are more conducive to instability. Therefore, the studies of several ionospheric parameters including the onset heights and times of the ESF and plumes that are associated with the variations of PRE with solar activities are significant for the characterizations of ESF.

1.2.   Overview of This Work

In this dissertation, we present detailed investigations of the generation, structures, and development of equatorial plasma bubbles as measured by airglow imaging systems in the equatorial F-region. We focus on the study of the zonal drift velocities of EPB from several sites near the magnetic equator on different longitude sectors. Furthermore, the ESF have also been characterized using long-term coherent and incoherent scatter radar observations from Jicamarca Radio Observatory, Jicamarca, Peru.

The content of this dissertation generally progresses from the general introduction to the specific research work. Chapter 2 gives an overview of the upper atmosphere. The review begins with neutral atmosphere, ionosphere, airglow layers, equatorial F-region ionosphere with introduction of equatorial fountain effect and equatorial anomaly. We briefly discuss equatorial spread F or plasma bubbles, and Rayleigh-Taylor instability. In addition, the day and nighttime zonal and vertical plasma drift velocities derived from Jicamarca radar measurements have been introduced.

In Chapter 3, we review the experimental techniques from which data have been used in this research work. We will briefly discuss airglow measurement techniques, the Utah State University (USU) all-sky (180° field of view) charge couple device (CCD) camera, and airglow measurement campaigns carried out to study the ionospheric plasma irregularities. There is also brief discussion of coherent and incoherent scatter radar techniques used from Jicamarca Radio Observatory.

In Chapter 4-6, we deal with results of optical measurements of airglow depletions obtained from ionospheric campaigns from different sites near equatorial regions using the USU all-sky CCD camera. Chapter 4 presents detailed investigations of the airglow depletions using the first time optical image measurements from Christmas Island in the central Pacific Ocean. We present the equatorial plasma bubble generation, their spatial characteristics and propagation. We also compare observational zonal drift results with model drift velocity obtained from simple electric field model. Chapter 5 reports the airglow depletion results from Ascension Island in the South Atlantic Ocean, which is close to the equator region, but at different longitude sectors from Christmas

Island. This Chapter also highlights the latitudinal shear velocities of the plasma bubble. In Chapter 6, we turn our attention to evidence of the longitudinal variability of equatorial ionospheric evolution, spatial structures and development of the plasma bubbles using the image data obtained simultaneously from two closely spaced sites at Brasilia and Cariri in Brazil. The airglow depletion velocity is also compared with coincidence measurements of the GPS scintillation drift.

Chapter 7 presents climatological results of post-sunset equatorial spread F using long-term coherent and incoherent scatter radar observations during 1996-2006 from Jicamarca, Peru. We investigated the seasonal, solar cycle variations of the equatorial spread F parameters including onset times and heights of initial equatorial spread F and that of radar plumes.

Finally, in Chapter 8, we review some of the most important results presented in this dissertation. We conclude with suggestions for future research work on equatorial spread F.

CHAPTER 2

LOW-LATITUDE IONOSPHERE

This Chapter presents the background physics of the Earth's atmosphere including the structure of the neutral atmosphere and ionosphere, airglow layers, and the low-latitude ionospheric electrodynamics with introduction of fountain effects and the equatorial anomaly. We also present the equatorial Spread *F* and plasma bubbles with a brief explanation of the Rayleigh-Taylor instability that is considered to be the primary mechanism responsible for the generation of equatorial spread *F*. Finally, we will review the vertical and zonal plasma drift velocities from the equatorial F-region ionosphere, derived from ground-based radar measurements.

2.1. Atmospheric Structure

The regions of the neutral atmosphere are classified on the basis of variation of height with the temperature, the composition, and the state of mixing. The primary classification is according to temperature gradient that includes the troposphere, stratosphere, mesosphere, thermosphere, and exosphere [*Schunk and Nagy, 2000*; *Kelley*, 1989] as shown in Figure 2.1. The data are derived from the MSIS (Mass Spectrometer-Incoherent Scatter) model over Jicamarca, Peru (12˚S, 76.9˚W, dip latitude 1˚N) on solar minimum and maximum conditions on September 22, 2006 and 2001, respectively. The temperature structure is governed by the absorption of solar radiation, and different wavelength bands are absorbed by various constituents in the region. The troposphere, the region associated with atmospheric weather phenomena, is defined by a well-mixed
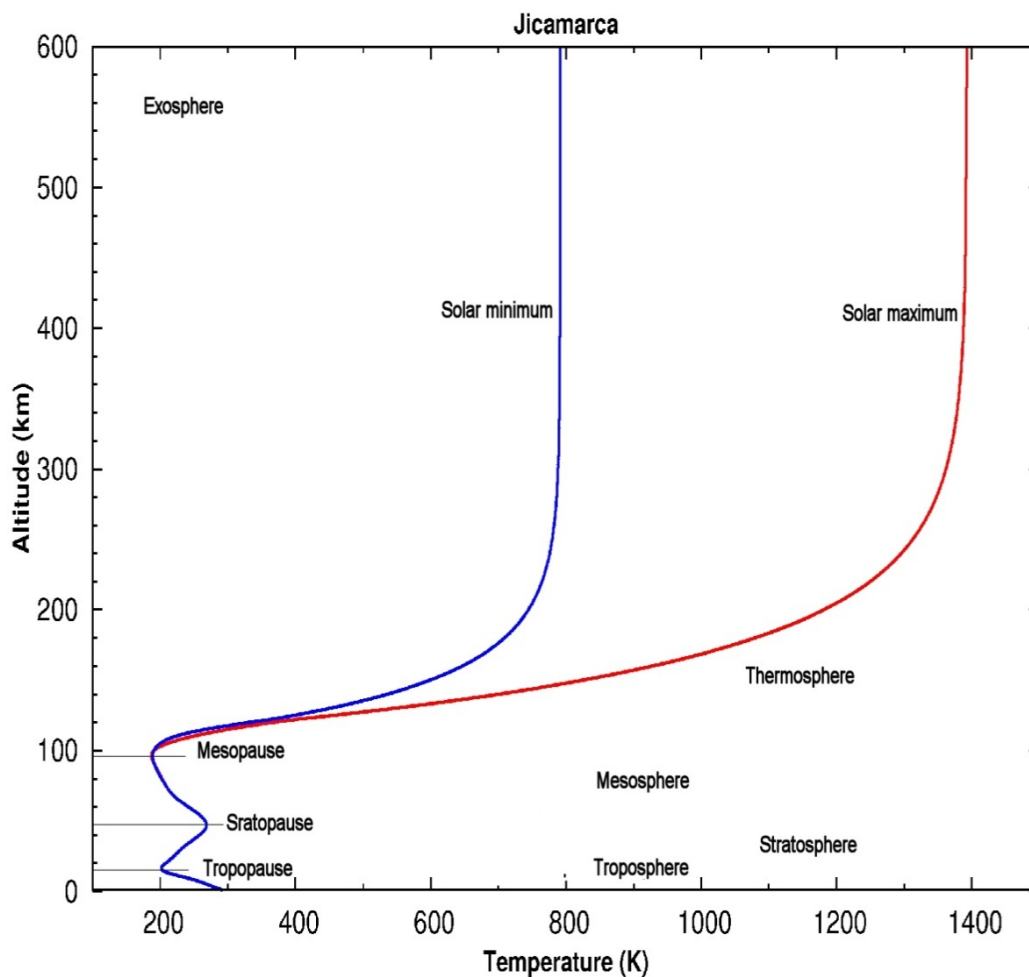
Figure 2.1. Structure of the Earth's neutral atmosphere on the basis of temperature gradient from MSIS model for solar minimum and maximum conditions.

composition of primarily molecular nitrogen and oxygen, with decreasing temperatures with height, and ranges from the surface to tropopause at around 10-12 km. The stratosphere is the region where the ozone layer exists, and extends from the tropopause to a height of around 45-50 km. Its temperature increases with height due to the absorption of solar ultraviolet radiation and this region is thermodynamically stable. The mesosphere is a middle atmosphere, which extends from the stratopause (45-50 km)

altitude up to the mesopause around 90-95 km. In this region, the temperature decreases with increasing height to a minimum at the mesopause with a temperature around 180 K, which is the coldest part of the atmosphere. This region experiences very little solar absorption and consists of primarily molecular nitrogen and oxygen, but, in addition, there are many minor species. Some metals, such as iron and sodium, are suspended in the mesosphere from meteor debris.

The thermosphere is the region that extends from about 90 km to 500 km. In this region, the temperature initially increases with altitudes to a maximum value of ~1000 K (during the solar maximum condition) and eventually becomes almost constant with altitude. This is the hottest part of the atmosphere. This is the region where most of the radiation from the atmospheric atoms and molecules in the visible spectrum originate, i.e., the night glow, day glow, and aurora. The transition to the thermosphere is due to the dissociation of diatomic oxygen and ionization through solar radiation absorption. The exosphere is the uppermost layer of the atmosphere near Earth space where the atmosphere gets very tenuous. Particles of light species, like hydrogen, moving fast enough are able to escape the Earth's gravity. Gas molecules in this region are unlikely to collide with other molecules due to the low-density atmosphere. The outermost region where the geomagnetic field controls particle motion is termed the magnetosphere. The thermosphere is coupled energetically, dynamically, and chemically to the mesosphere at its lower bound, and to the exosphere and magnetosphere at its upper bound.

2.2. Ionosphere

The ionosphere is the ionized region of the upper atmosphere extending from ~60

km to beyond 1000 km. This region contains significant numbers of free electrons and positive ions and also some negative ions in lower altitudes. The electron concentration may amount to only about one percent of the neutral concentration. However, the presence of these electrons has a profound effect on the properties and behavior of the medium.

The vertical structure of the ionosphere has been divided into four layers according to ion constituent and associated chemistry. These distinct layers develop because (a) the solar spectrum deposits its energy at various heights depending on the absorption characteristics of the atmosphere, (b) the physics or recombination depends on the atmospheric density, and (c) the composition of the atmosphere changes with height. The vertical structure of the electron density of the ionosphere at the local noon (solid lines) and local midnight (dashed lines) for solar minimum (blue lines) and solar maximum (red lines) conditions are shown in Figure 2.2. The data were obtained by running the International Reference Ionosphere (IRI) model [*Bilitza,* 1990] for solar minimum (September 22, 2006) and maximum conditions (on September 22, 2001) at Jicamarca, Peru, which lies close to the dip latitude. The dip latitude is the imaginary horizontal line running east-west normal to the magnetic field lines and is an angular measurement in degrees ranging from 0° at the magnetic equator to 90° at the magnetic poles.

During the day, the ionosphere separates into several layers depending upon the local time of day. The main layers are D-region, E-region, F1-region, and F2-region. The layers are generally characterized by a density maximum at a certain altitude and a density
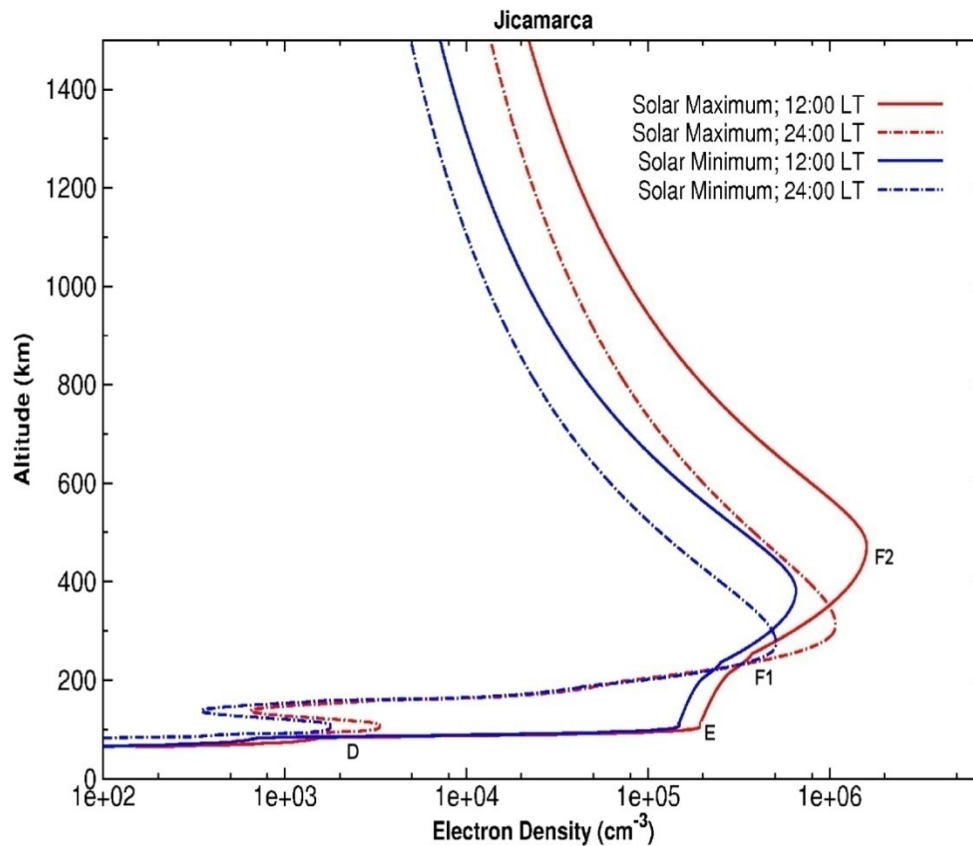
Figure 2.2. IRI model of electron density profile of the equatorial ionosphere at noon (solid lines) and midnight (dashed lines) for solar minimum (blue lines) and solar maximum conditions (red lines) [Courtesy of *David Hansen*, CASS, Utah State University, 2010].

decrease with altitude on both sides of the maximum. The D-region ranges from about 60 km to 90 km and is controlled by ionization of neutrals by solar X-Rays and Lyman alpha radiation, which cause two- and three-body recombination and electron attachment. The dynamics of the D-region are mostly dominated by the neutral atmosphere. In this region, the plasma density range is 10^2-10^4 cm^{-3}. The E-region extends from ~90 km to 150 km altitude with an electron density ~10^5 cm^{-3}. This region is chemically dominated and contains molecular ions such as N_2^+, O_2^+, NO^+ as primary constituents. The F_1-region

ranges from ~150 km to 200 km altitude with electron density range of ~10^5-10^6 cm^{-3}. The F$_2$-region extends from an altitude of ~200 km to 500 km and the electron density maximum varies around 300 km up to 10^6 cm^{-3}. This is the region of peak electron density of the ionosphere, which is usually over an order of magnitude greater than the E-region peak density. These F$_1$- and F$_2$-regions are dominated by monoatomic oxygen and the ions transported through diffusion.

The D- and F$_1$-regions vanish during the night and the E-region become much weaker. The daytime electron densities are greater than that of the nighttime and also larger during the solar maximum than in solar minimum. At solar maximum, the electron densities are greater by a factor of two to four than at solar minimum, especially in the F-region. The E-region and lower part of the F-region undergo relatively greater variations in electron density between day and nighttime than does the upper F-region. The F$_2$- layer is the principle reflecting layer for HF communications and is responsible for most sky wave propagation of radio waves. Thus, this region is of the greatest interest for radio wave propagation. Unfortunately, this layer is also the most anomalous, the most variable and the most difficult to predict.

Furthermore, the dynamics of the upper atmosphere are primarily driven by solar heating tidal forces. On the dayside, solar radiation sets up a global system of neutral winds that tend to flow toward the colder regions on the nightside. When these neutral winds push the ionospheric plasma across magnetic field lines, electric fields and currents are generated, which play an important role in the distribution of ionization. On the other hand, collisions between the neutral atmosphere and the ions, the ions and electrons, and

the neutrals and electrons are the cause of the conductivity in the ionosphere.

The ionospheric conductivity plays a major role in the electrodynamics of the F-region. These conductivities are: Pedersen, Hall, and parallel conductivity. The conductivity parallel to the electric field, but perpendicular to the magnetic field, is called Pederson conductivity. The conductivity perpendicular to both the electric and magnetic fields is called Hall conductivity, while the conductivity parallel to the magnetic field alone is defined as the parallel conductivity. The magnitudes of these conductivities as a function of altitudes are shown in Figure 2.3. The Pedersen and Hall conductivity decrease with increasing altitudes, whereas the parallel conductivity increases
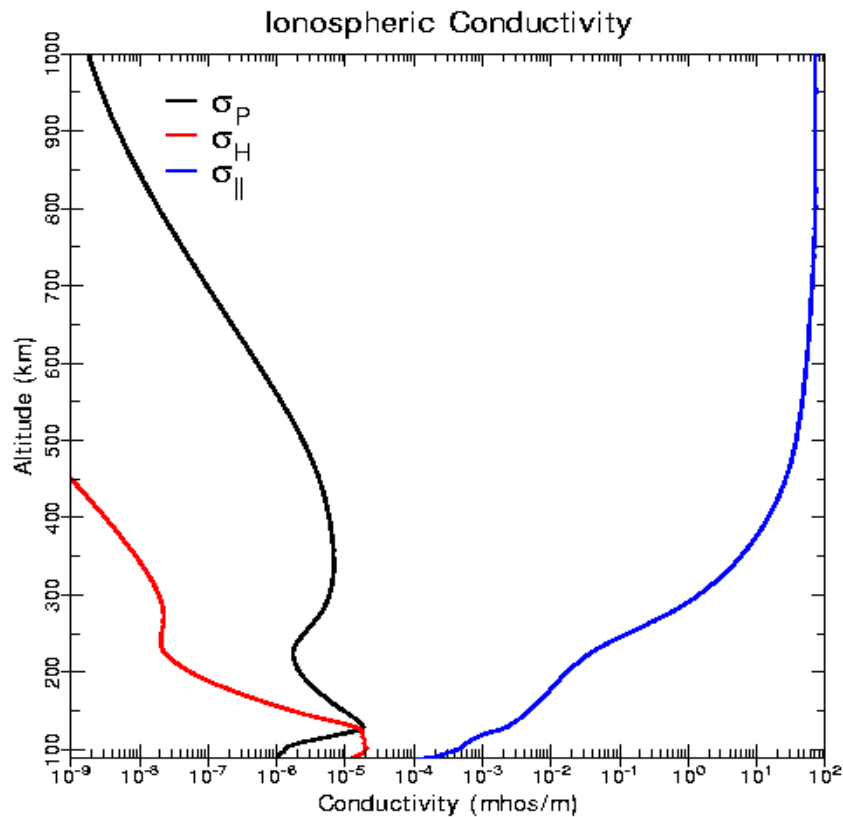
Figure 2.3. Pedersen (σ_p), Hall (σ_H), and parallel (σ_l) conductivity at 10˚N, 105˚E [Courtesy of Christian Wohlwend, CASS, Utah State University, 2008].

continuously with altitude. The parallel conductivity is several orders of magnitude larger than both the Pedersen and Hall conductivities everywhere above 100 km altitudes. Therefore, ionospheric electric fields can be transferred along these lines virtually uninhibited.

2.3.   Airglow Layers

In the Earth's atmosphere, there are additional sources of light during the nighttime period in addition to the moon and stars. From the ground we can observe the continuum of frequencies of light, as well as a series of lines emissions that have sharp peaks in intensity, referred to as airglow. The airglow energy source is primarily stored chemical energy provided by sunlight, and it therefore occurs at all latitudes. A detailed description of the mechanisms involved in the production of airglow emission and in its reactance to dynamic disturbances is beyond the scope of this dissertation; however, a brief overview is important and is presented in this section.

The atmospheric airglow layers have been observed from rocket experiments. The layers have an abundance of a number of chemical constituents that undergo chemical processes producing light (airglow) at certain wavelengths. The brightest of the airglow emissions are the NIR (near infrared) hydroxyl (OH), 557.7 nm (O^1S), the 630.0 nm (O^1D), and the emissions from metallic atoms such as sodium, calcium, potassium, and magnesium. The OH NIR and 557.7 nm emissions are due to reactions between neutral species. They originate in the MLT (Mesosphere-Lower-Thermosphere) region where the chemistry is dominated by the neutrals, but where the density is not so great as to quench the emissions. In comparison, the 630.0 nm reaction involves ion chemistry and so occurs

at much higher altitudes, where the atmosphere has plasma embedded in it. Figure 2.4

shows the heights of the different airglow layers viewed with the digital Charge Coupled

Device (CCD) cameras. The full width at half maximum (FWHM) of the mesospheric

layers is generally on the order of ~10 km for OH (NIR) and green line emissions at

altitudes of 87 km and 96 km, respectively [*Baker and Stair*, 1988]. On the other hand,

the width of the FWHM for the OI 630.0 nm emissions in the thermosphere is about 100

km between 200 and 300 km altitudes [*Mendillo and Baumgardner,* 1982]. We cannot

independently determine the height from our integrated measurements, but several rocket

experiments have verified the illustration in Figure 2.4 [e.g., *Tsunoda et al.,* 1982].
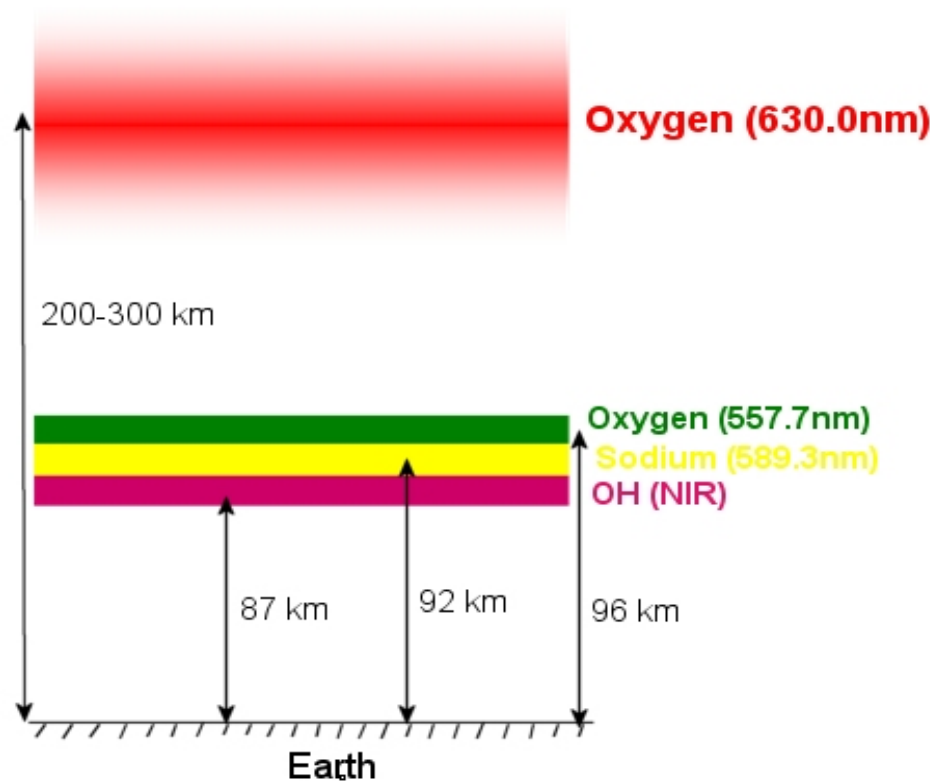
Figure 2.4. Illustration of heights of the different airglow layers viewed with the CCD imagers along with the wavelengths of the emissions (not to scale).

2.4.   The OI (630.0 nm) Airglow Emission

Atomic oxygen emits at a wavelength of 630.0 nm in the visual spectrum at altitude range of 200-300 km to form red airglow, when it decays from the excited state to the ground state. The excited atomic oxygen is available from ionized atomic oxygen as shown in the following reaction [*Mendillo and Baumgardner,* 1982]:

$$O^+ + O_2 \longrightarrow O_2^+ + O,$$

$$O^{2+} + e \longrightarrow O(^1D) + O(^3P),$$

$$O(^1D) \longrightarrow O(^3P) + h\nu \ (\lambda=630.0 \ nm).$$
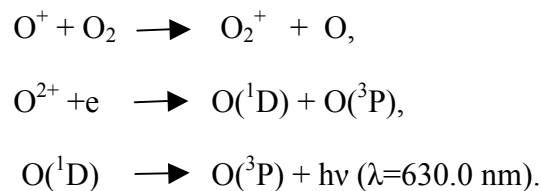
That is, the (O^1D) state is populated by the dissociative recombination of O^{2+}, which itself arises from a collision charge transfer between neutral molecular oxygen and ionized atomic oxygen. This emission is from a forbidden transition with a lifetime of 110 sec in the thermosphere [*Mendillo and Baumgardner,* 1982]. Hence by observing the depleted airglow intensity using OI (630.0 nm) all-sky images, equatorial F-region ionospheric irregularities (or plasma depletions) can be studied.

However, the OI (630.0 nm) emissions, which are emitted during the process of recombination of ionized molecular oxygen, come from the thermosphere. The emission layer is highly dependent upon the F-layer, and so its peak height and width is also significantly variable. The height of the F-peak, which can be measured using an ionosonde or incoherent scatter radar, may vary for about 250 km to 400 km or more and its width at half maximum is several tens of kilometers. The assumed emission heights used in these studies employing the OI (630.0 nm) emission range from 250 to 300 km.

The model results show this assumed height varies approximately 10 km over the course of the evening.

The 630.0 nm emission is effective at tracing out the dynamics of the ionosphere near the F-region peak (250-300 km). Its volume emission rate is dependent on both the electron density and the neutral O_2 density. So its peak emission altitude follows the rise and fall of the F-layer with the peak emission altitude in general lying below the F-peak. Furthermore, the emission intensity drops off dramatically with altitude if the F-layer rises. This effect is easily confused with decreasing intensity due to a drop in electron content. The total airglow intensity viewed from the ground is given by the height integral of the volume emission rate. It is clear that if the electron density profile were to rise, the airglow intensity would fall because of the exponential drop-off of the O_2 concentration. For the same reason the airglow intensity would increase if the electron density profile fell.

2.5.   Low-Latitude Ionosphere

Low-latitude ionospheric electrodynamics strongly affect various ionospheric and thermospheric phenomena such as the equatorial anomaly, the global distribution of low-latitude ionization, the generation of equatorial spread *F*, and radio wave scintillations. Overviews of these phenomena have been presented by several authors [e.g., *Kelley,* 1989; *Schunk and Nagy,* 2000].

The dynamo electric fields generated in the equatorial E-region by thermospheric winds are transmitted along the dipole magnetic field lines to F-region altitudes because of the high parallel conductivity [*Schunk and Nagy*, 2000]. The daytime dynamo electric

fields are directed eastward, which causes an upward $\mathbf{E}\times\mathbf{B}$ plasma drift as shown in Figure 2.5, while the reverse occurs at night. The upward drift in the daytime raises freshly ionized plasma near the equator to great heights, where recombination is slow. Subsequently, the plasma diffuses down along the magnetic field lines and away from the equator under the action of gravity that adds extra plasma to that produced locally at higher altitudes. These combined phenomena of electromagnetic drift and diffusion produce a fountain-like pattern of plasma motions. This phenomenon is referred to as the fountain effect or the equatorial fountain. Because of this fountain motion, the ionization peaks are formed in the subtropics on each side of the magnetic equator to form two crests with maximum ionization density near ±15° magnetic latitude (as denoted by crests in Figure 2.5) and minimum ionization at the magnetic equator. This feature is termed the equatorial anomaly or Appleton anomaly. The equatorial anomaly varies during the day, with a maximum about 14:00 local time (LT), and a second often larger peak, occurring in the late evening.

The latitude of the peak electron density formations is often not symmetrical about the magnetic equator because of plasma transport along the magnetic field lines produced by an interaction with the neutral winds. The neutral winds usually cause plasma to be pushed from the summer hemisphere to winter hemisphere. Such a wind acts to transport plasma up the field lines in the southern hemisphere and down along the field line to the northern hemisphere. This causes an unsymmetrical form of equatorial anomaly peaks between the two hemispheres as shown in Figure 2.5, with a larger crest on winter hemisphere than that in summer hemisphere. An example of this equatorial
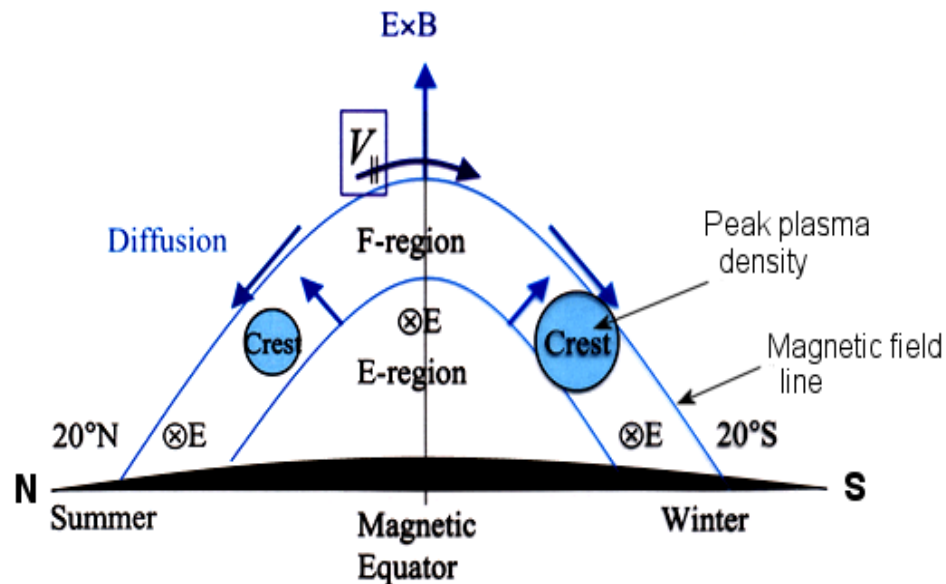
Figure 2.5. Schematic of the formation of the latitudinal variation of ionization density in the equatorial F-region, known as the equatorial anomaly. **E×B** upward plasma drift and following the downward diffusion along the field lines are shown by the arrows, producing the fountain effect. The two equatorial anomaly peaks (crests) are shown on both hemispheres [Courtesy of David Anderson, University of Colorado, Boulder, 2004].

anomaly is also shown in Figure 2.6, which was calculated with a numerical model for December solstice conditions on day 363, 1998 [Courtesy of David Anderson, University of Colorado, Boulder, 2004]. The figure represents contour plot of electron density with altitudes as a function of magnetic latitudes at 14:00 LT. The upward E×B drift raises the F-layer at the magnetic equator to ~800 km. This leads to ionization peaks on both sides of the magnetic equator due to the fountain effect, as explained above. The figure also indicates larger electron density profiles in winter hemisphere than in summer hemisphere.

1998, Day 363, 1400 LT
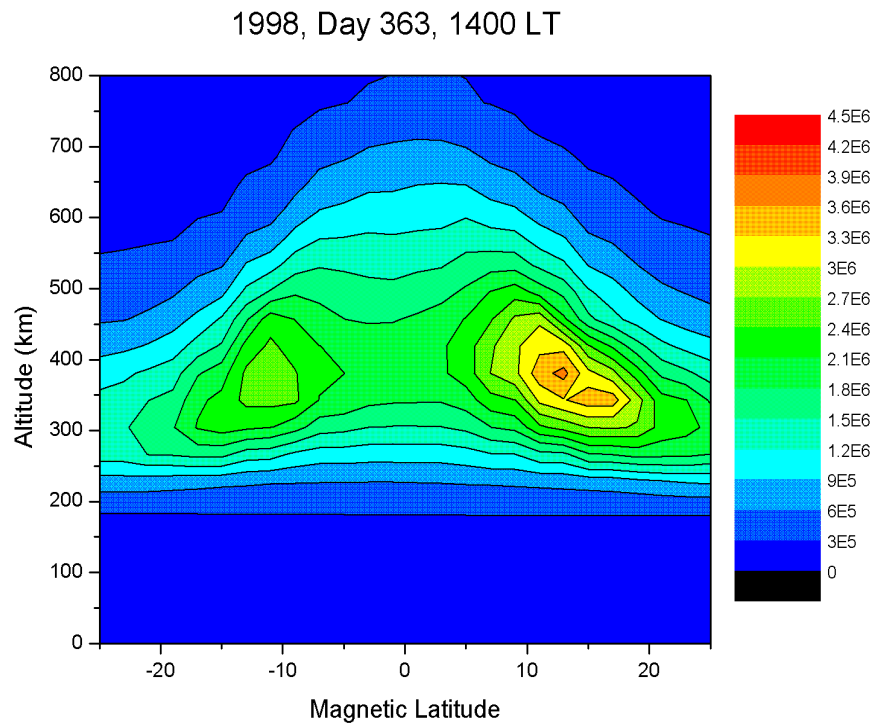
Figure 2.6. Electron density contour plot as a function of altitude and magnetic latitude for December solstice conditions [Courtesy of David Anderson, University of Colorado, Boulder, 2004]

2.6. Equatorial Spread *F* and Plasma Bubbles or Plumes

The occurrence of the nighttime plasma irregularities in the equatorial F-region ionosphere is commonly referred to as equatorial spread *F* (ESF). The term spread *F* was introduced first by *Berkner and Wells* [1934] from the spreading of the ionogram traces. Since then, numerous studies have been carried out on the observational and physical theories of ESF. Several reviews of ESF have been published [e.g., *Fejer and Kelley*, 1980; *Ossakow*, 1981]. The ESF echoes are caused by scattering from kilometer scale irregularities when HF radio waves are vertically reflected by the disturbed nighttime F-region ionosphere. The wide spectral distribution of plasma bubble irregularities are

known to cause interference with satellite-to-ground-based telecommunication channels, and the degradation of navigation and GPS systems due to the random fluctuations of the amplitude and phase of the radio waves as they pass thorough these irregularity regions [e.g., *Basu et al.,* 1999].

The ionospheric irregularities have broad range scale sizes over several orders of magnitude from tens of centimeters to hundreds of kilometers. They extend from the F-region up to ~1700 km altitudes within the dip latitudes of about ±20° and are driven by a number of wave generation processes. Due to the high parallel conductivity and mobility in the ionosphere, the signature of ESF can be observed in all latitudes between the Appleton anomalies. The spread *F* occurrences in the equatorial F-region can be particularly severe, although they can appear at all latitudes. However, their occurrences depend on the season, solar cycle, latitude, and longitude.

At night, a fully developed ESF is characterized by plasma bubbles (the region of the deep plasma depletion). The plasma density inside the bubbles can be up to three orders of magnitude lower than that of its surroundings. Figure 2.7 shows an example of an OI (630.0 nm) airglow image measured by the USU all-sky CCD camera on September 28, 1995 from Christmas Island. The dark bands on the image are plasma depletion structures or plasma bubbles. During the development phase of the plasma bubbles, they are known to drift upward and eastward. When the ESF onset ends, generally during the post-midnight period, the upward drifts ceases and the bubble becomes a fossilized one. The fossil bubbles then drift eastward with the ambient plasma, while the bubbles at higher-latitudes generally tend to lag behind.
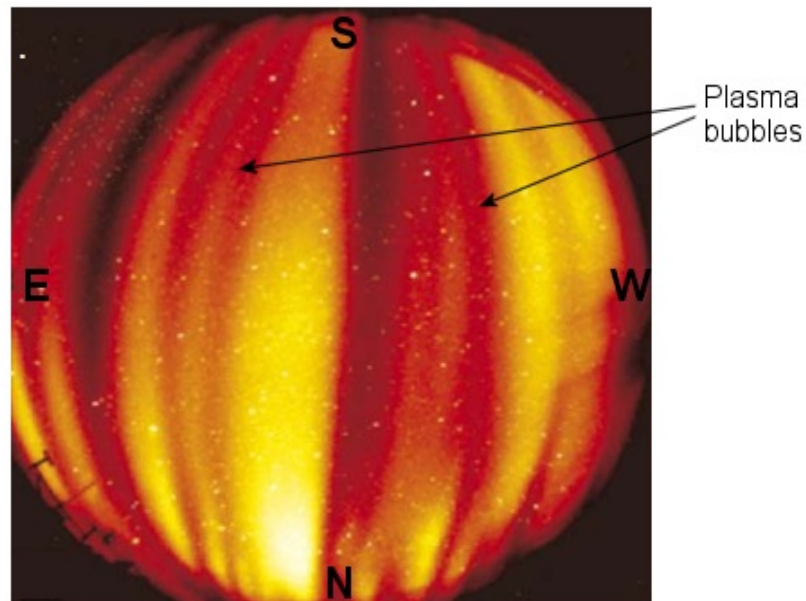
Figure 2.7. An example of OI (630.0 nm) airglow depletion image measured by the USU all-sky CCD camera from Christmas Island on September 28, 1995. White dots in the image are stars and dark bands denote the plasma bubbles.

Figure 2.8 presents an example of a very large quasi-periodic structure of plasma depletions with a sequence of radar plumes observed using the 50 MHz Jicamarca radar on September 18, 1996. The radar plumes are vertically elongated wedges of the depleted plasma convected upward from beneath the bottomside F-layer to the top side of the ionosphere. These echoes were strong and tilted westward.

Figure 2.9 shows a schematic diagram to explain the phenomena of the generation of the ESF (or EPB) [*Schunk and Nagy*, 2000]. An eastward dynamo electric field **(E)** is generated in the lower ionosphere during the daytime by the thermospheric wind. This electric field is mapped to the F-region altitude along the magnetic field **(B)** lines. The upward **E**×**B** plasma drift is produced in the F-region due to this combination of eastward
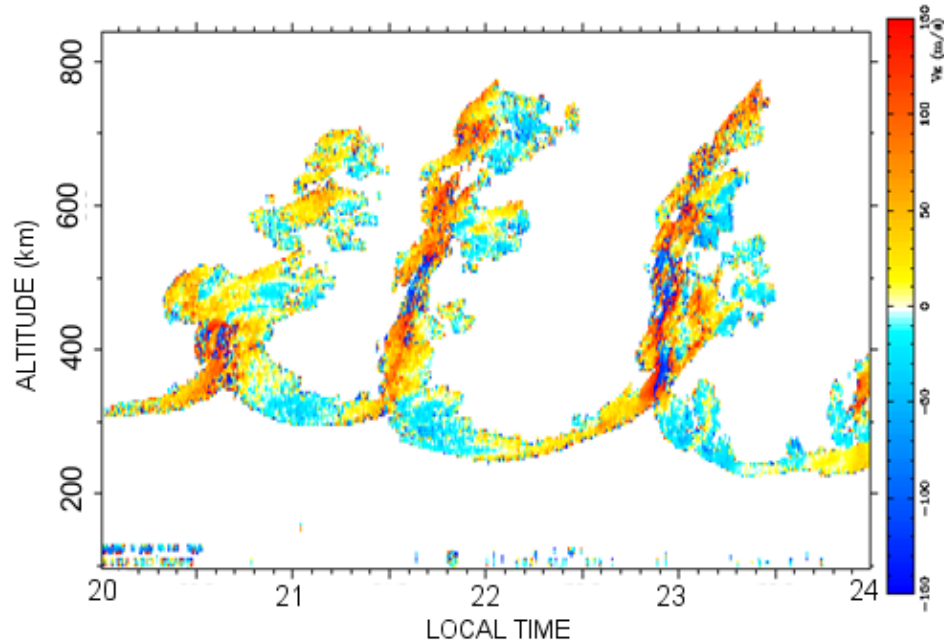
Figure 2.8. Backscatter power of 3-m irregularities (i.e. the radar plume) observed by the Jicamarca radar, Peru.

electric field and the northward magnetic field as explained above. When the ionosphere co-rotates with the Earth toward the dusk terminator, the eastward component of the neutral wind increases with the wind blowing predominantly across the terminator from the dayside to the nightside. The combination of the increased eastward wind component with the sharp day-night conductivity gradient across the terminator leads to the prereversal enhancement (PRE) in the eastward electric field [*Schunk and Nagy,* 2000]. As a result, the F-layer rises when the ionosphere co-rotates into darkness. On the other hand, the lower ionosphere rapidly decays in the absence of sunlight and a steep vertical density gradient develops on the bottomside of the raised F-layer, as shown in the vertical electron density profile (NE) in Figure 2.9. In this condition, a heavier fluid (plasma in this case) is situated above the lighter one (magnetic field lines), which is the necessary
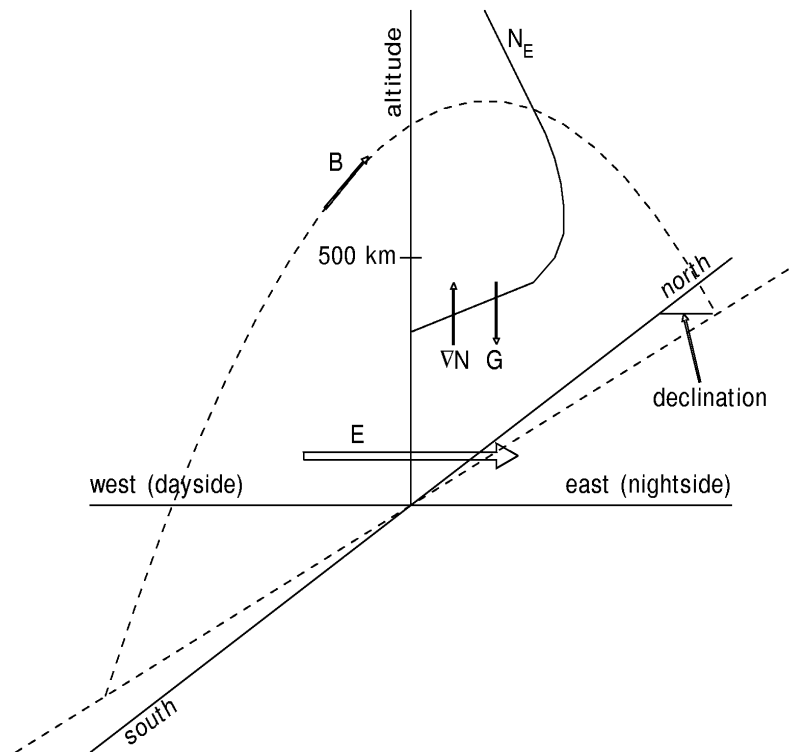
Figure 2.9. A schematic diagram to show the classical configuration for the Rayleigh-Taylor instability [*Schunk and Nagy,* 2000, Figure 11.29].

configuration for the Rayleigh-Taylor instability (RTI).

2.7.   **Rayleigh-Taylor Instability**

The theory of the cause of the Rayleigh-Taylor instability in the ionosphere was first presented by *Johnson and Hulburt* [1950], with the work of *Dungey* [1956] making a connection between the Rayleigh-Taylor instability and ESF. The simplest form of the RTI (also known as the interchange instability) occurs when a high-density fluid is situated on top of a low-density fluid in a gravitational field. Any fluctuation at the fluid interface allows gravity to pull the high-density fluid downwards so that the low-density fluid ends up on top and an interchange of the two fluids takes place. More generally,

interchange instability occurs when two types of fluid are situated with an external force such that the heavy fluid pushes against the light fluid, and the potential energy of the system is not a minimum. In plasmas with a magnetic field, both the plasma and the field have an associated pressure; therefore the plasma may interchange position with the magnetic field.

The RTI theory involves a vertical plasma density gradient with dense F-region plasma over less dense E-region plasma, enhanced by the steeping of the bottomside at night. This gradient, when perturbed, will generate polarization electric fields that grow the perturbation through $\mathbf{E} \times \mathbf{B}$ plasma drift. The situation shown in Figure 2.10 is post-sunset equatorial ionosphere just below the F-region. The D- and E-regions disappear due to recombination after sunset steepens the bottomside and prevents the shorting of the F-region currents. We can approximate the layer below the F-region as a vacuum in terms of plasma density with heavy fluid supported by the lighter one, as shown in Figure 2.10 (upper panel). The electrons and ions drift in opposite directions. As a result of random thermal motion of electrons and ions, a ripple develops along the interface. The further drift velocity will cause the ripple to grow as shown in bottom panel of Figure 2.10, and they cause a charge build up on the side of the ripple. Additionally, an electric field E develops, which changes the sign from crest to trough in the perturbation wave. The $\mathbf{E} \times \mathbf{B}$ drift is always upward in the upper surface of the ripple and is downward in the lower region of the ripple. As a result, the ripple becomes unstable producing the small-scale irregularities. As they rise, these irregularities spread out along the magnetic field lines in north and south higher latitudes.
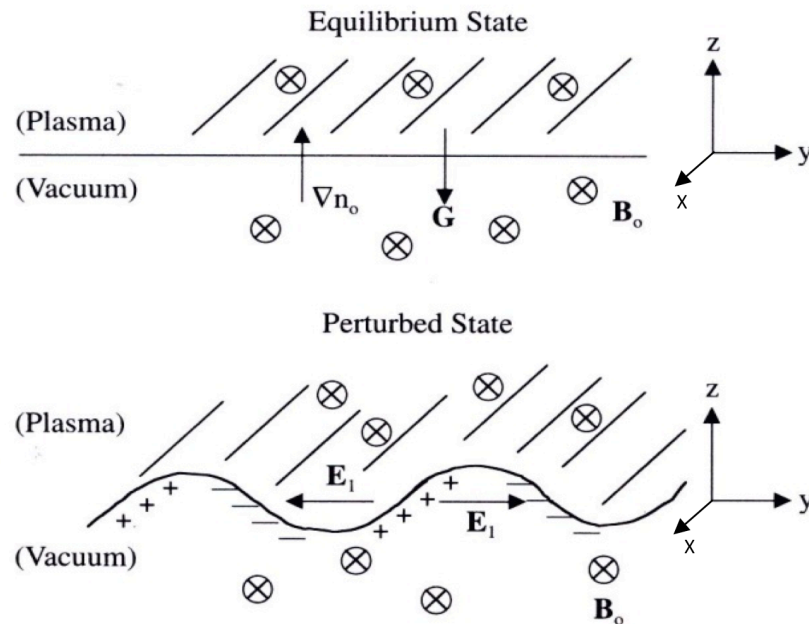
Figure 2.10. Characterization of Rayleigh-Taylor instability in equatorial ionosphere at dusk. Axes x, y, and z point to the south, east and upward directions, respectively. Here, ∇n_0 is the electron density gradient, G is the gravitational field, and B_0 is the Earth's magnetic field [*Schunk and Nagy*, 2000, Figure 11.30].

The F-region fields cause the F-layer to rise at higher altitude, which reduces the collisions between the charged particles and the neutral species, and hence, the E-region conductivity, which then enhances the R-T growth rate [e.g., *Balsley et al.,* 1972; *Haerendel*, 1973; *Sultan,* 1996]. Seeds are necessary to set the linear instabilities in motion, and the fact nonlocal linear growth for interchange instabilities decreases with increasing wavelength suggests that strong seeds are necessary to incite large-scale (very-long wavelength) F-region irregularities. Numerous theoretical and experimental studies have suggested the importance of gravity wave effects on the seeding and evolution of ESF [e.g., *Klostermeyer,* 1978; *Kelley et al.,* 1981; *Hysell et al.,* 1990; *Vadas and Fritts,* 2009; *Takahashi et al.,* 2009]. Recently, much attention has gone toward identifying

seeds for waves that will grow and produce radar plumes in their mature stage. Additionally, the onset of ESF may also be affected by breaking of gravity waves propagating upward from the lower altitude and by electric field perturbations of high-latitude origin during the magnetic disturbed conditions. On the other hand, there are several processes, such as meridional neutral winds, electric field shear effects, diffusion, and E-region conductivity, which inhibit the growth of the irregularities. The large number of potentially important factors effecting ESF evolution make it difficult to model and predict the day-to-day and short-term variability of ESF, which is one of the outstanding problems in the study of ESF.

2.8.   Equatorial F-Region Plasma Drifts

The climatology and characteristics of low-latitude F-region plasma drift have been extensively studied over the past few decades using ground-based radar observations, optical measurements, ionosonde, and satellite observations [e.g., *Woodman,* 1972; *Mendillo and Baumgardner,* 1982; *Sobral et al.,* 1985; *Fejer et al.,* 1991, 2005; *Taylor et al.,* 1997; *Martinis et al.,* 2003; *Makela et al.,* 2004; *Jensen and Fejer,* 2007; *Pautet et al.,* 2009]. The majority of the information about plasma drifts at equatorial latitudes has come from observations at the Jicamarca Radio Observatory near Lima, Peru using incoherent scatter radar (ISR) at 50 MHz [e.g., *Woodman,* 1972; *Fejer et al.,* 1991, 2005].

Figure 2.11 shows the seasonal and solar flux (*F10.7* cm) dependence of the average vertical plasma drift velocities in the height range of about 200-600 km over Jicamarca [*Fejer et al.,* 1991]. Upward drifts correspond to positive values in the plots.

The plasma drifts are upward during the day and downward during the night. The daytime drifts are typically solar flux independent and peak at about 11:00 LT with magnitudes around 20 m/s during the equinox (March-April, September-October) and winter (May-August) seasons, with quiet smaller magnitudes during summer (November-February). The large evening upward drift velocities commonly known as prereversal velocity enhancement were observed during the equinox and summer (December solstice), while a much smaller enhancements were seen during winter (June solstice).
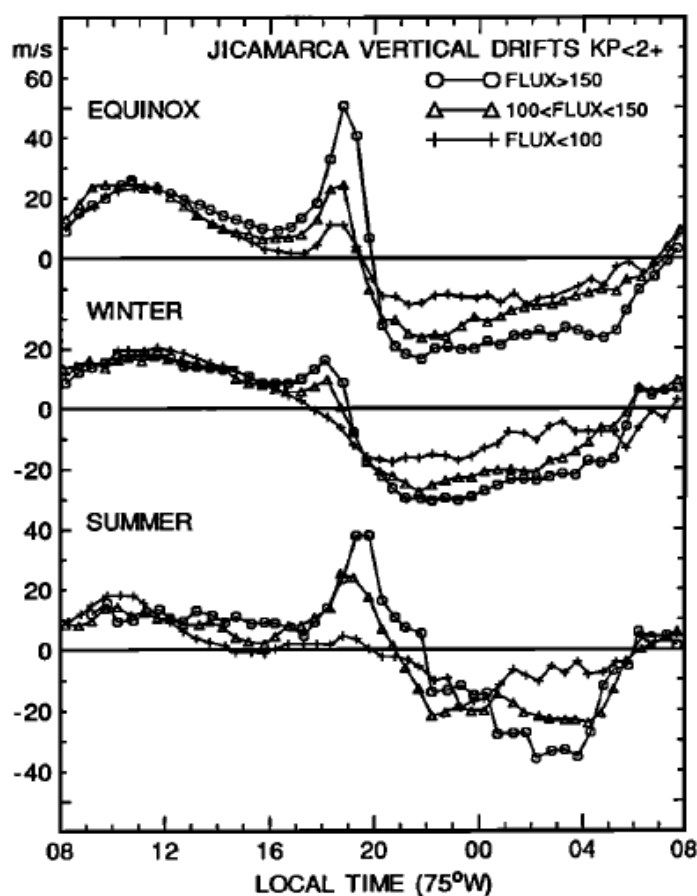
Figure 2.11. Average vertical plasma drift velocities over Jicamarca for equinox (March-April, September-October), southern hemisphere winter (May-August), and summer (November-February) at low, moderate, and high solar flux conditions [*Fejer et al.*, 1991].

The prereversal enhancement has clear solar flux dependence during all seasons with greater upward drifts at higher fluxes. The nighttime downward drifts have typical values of 10-30 m/s, and their magnitudes increase with solar flux. The evening reversal times show significant solar flux variation, while the morning reversal times are almost independent of solar flux during all seasons.

Figure 2.12 shows the F-region model zonal plasma drift velocities above Jicamarca during all seasons for low and moderately high solar flux conditions as reported by *Fejer et al.* [2005]. The eastward drifts correspond to positive values in the plots. Open circles represent solar minimum conditions, whereas filled symbols are for solar maximum conditions. During the day, these zonal drifts are westward and reach values up to 40 m/s, and at nighttime they become eastward and have large variations in magnitudes from ~40 m/s to 160 m/s. The zonal drifts have a large eastward peak near 21:00 LT, shortly after the evening reversal, and then they slowly decrease throughout the night. The daytime westward drifts and evening reversal times are almost solar flux independent while the nighttime eastward drift increase with solar flux, which is more pronounced during the December solstice and the equinox. It is also noted that the zonal drifts are much larger than the vertical drifts, and the peak eastward drift is about twice as large as the peak westward drift. The detailed description of equatorial vertical and zonal plasma drifts velocities has been reported by *Fejer et al.* [1991, 2005].

The daytime westward and nighttime eastward zonal drift velocities are due to the upward vertical electric field during the day and the downward field during the night, respectively. Similarly, the upward and downward drifts during the day and night are
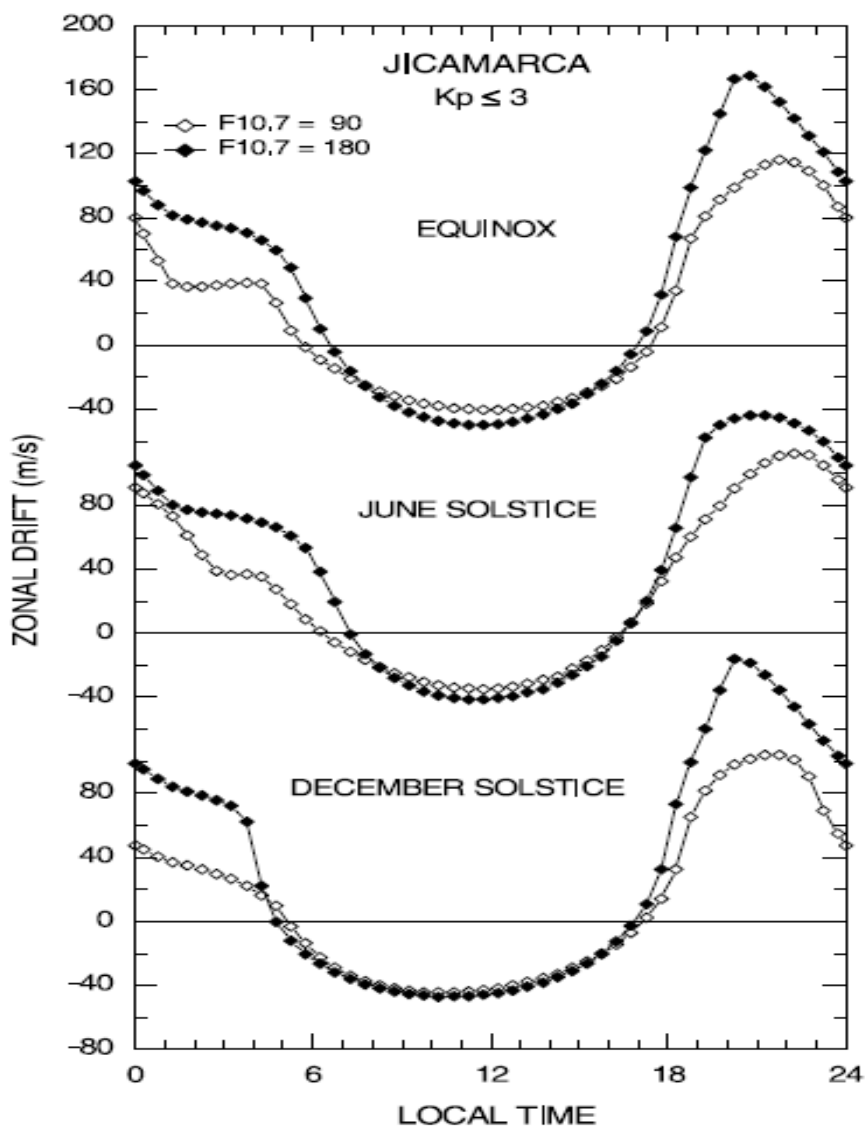
Figure 2.12. Jicamarca model zonal drift velocities at low and moderately high solar flux conditions during the equinox, June, and December solstice [*Fejer et al.*, 2005].

caused by the eastward and westward electric fields developed on the day and nighttime period, respectively [e.g., *Woodman,* 1970; *Fejer et al.,* 1981, 1991, 1995; *Coley and Heelis,* 1989; *Maynard et al.,* 1995]. The zonal electric fields are developed due to separation of positive and negative charges caused by their differential motions. The magnitude of these electric field changes with solar local time and hence the plasma drift. The zonal velocity of equatorial plasma bubbles in the premidnight sector corresponds to the velocity of the ambient plasma during the quiet magnetic day.

Furthermore, a prereversal enhancement (PRE) of the vertical plasma drift has been seen shortly after sunset (see in Figure 2.11) as the drift reverses from upward to downward from the day to night transition. The important feature of PRE is that it drives the F-layer to higher altitudes (at about 400 km) after the sunset, where the growth rate of Rayleigh-Taylor instability is larger, which leads to the equatorial spread *F* occurrence. To explain this PRE phenomenon, several theories have been developed [e.g., *Risbeth,* 1971; *Farley et al.,* 1986; *Haerendel et al.,* 1992; *Eccles* 1998], however, more research work needs to be done to investigate the actual physical process involved on this phenomenon.

CHAPTER 3

MEASUREMENT TECHNIQUES

Ionospheric irregularities can be detected by using several techniques including radar measurements [e.g., *Farley et al.,* 1970], in situ space probe [e.g., *Tinsley et al.,* 1997; *Tsunoda et al.,* 1982], radio wave propagation and scintillation experiments [e.g., *Valladares et al.,* 1996], airglow-measurements [e.g., *Mendillo and Baumgardner,* 1982; *Taylor et al.,* 1997], and ionosonde [e.g., *Hammer and Bourne,* 1976]. In this dissertation work, we use airglow measurements from the USU all-sky CCD camera and radar observations from Jicamarca, Peru. In this section, we briefly review these techniques.

3.1. Airglow Measurements

The atmospheric nightglow emissions provide an excellent medium for the remote sensing of short-period gravity waves in the upper mesosphere and lower thermosphere, and plasma depletion in the thermosphere. Gravity waves are generated in the troposphere by frontal systems by airflow over mountains. These waves are important for transferring momentum from the troposphere to the stratosphere/thermosphere and play a key role in controlling the dynamics of the middle atmosphere.

As the airglow is faint, we cannot see it readily because the strongest airglow emission lies outside the range of the human eye's sensitivity, in the near infrared region [e.g., *Wayne,* 1991]. However, we can use sensitive optical equipment, such as photometers and CCD cameras, to observe airglow emissions during the nighttime period. As atmospheric disturbances, such as internal gravity waves, pass through the

airglow layers, they cause perturbations in the temperature and density of the relevant constituents, which in turn, produce intensity fluctuations of the airglow. These intensity variations are used to study the disturbances in the upper atmosphere, including the ionospheric plasma irregularities.

As discussed in the previous chapter, the ionospheric plasma depletion is measured by observing the OI (630.0 nm) airglow intensity depletion. However, the volume emission rate of 630.0 nm $O(^1D)$ decreases at higher altitudes as molecular oxygen density exponentially decays with height. As a result, the higher minimum F-layer height required for plume formation leads to low airglow intensities. Thus, it is unlikely that the development of plumes after sunset will be observed through 630.0 nm airglow photometry near the magnetic equator. When the post-sunset ionosphere decreased in virtual height to less than ~275 km, airglow intensities increased and fully developed depletions became visible as dark bands in the ambient airglow. On the other hand, when the virtual height at the magnetic equator is above ~275 km for the entire night, the airglow depletion will not be visible, even though plumes and scintillations will have occurred [*Mendillo and Baumgardner,* 1982].

The development of highly sensitive CCD cameras has proven to be an ideal instrument for the imaging of nighttime airglow in the sky and the study the upper atmospheric phenomenon. *Taylor and Hill* [1991] were able to obtain high-quality images of wave structure using a CCD camera. These cameras were first used for narrow field of view (FOV) measurements. They further developed a fish-eye (180˚ FOV) lens to image airglow emissions. *Taylor and Garcia* [1995] have published the first results using

this method for the airglow measurements. Since then, numerous studies have been carried out using this technique [e.g., *Taylor et al.,* 1997; *Santana et al.,* 2001; *Makela and Kelley,* 2003; *Mukherjee,* 2003; *Martinis et al.,* 2003; *Arruda et al.,* 2006].

3.1.1. USU All-Sky CCD Camera

The development of the USU all-sky CCD camera (optical imager) has proven to be a powerful additional instrument in nighttime airglow measurements. The principle components of the USU CCD imager are shown in Figure 3.1. The imaging system consists of an all-sky or fish-eye (180˚FOV) telecentric lens system, a computer-controlled filter wheel, and a CCD camera head fitted with a 1024×1024 pixel back-illuminated bare CCD (quantum efficiency ~80% at visible and 50% at NIR wavelengths). The incoming light passes through the fish-eye lens and it further passes through one of the filters in the filter wheel and is reimaged onto the CCD chip in the camera head with dimensions of 25mm×25mm in the cooled CCD camera. The chip itself is thermoelectrically cooled to a temperature of about -50˚C and the heat is removed using a liquid circulation heat exchange. By cooling the chip to a very low temperature, the power of the thermal noise has been reduced so the data recorded will be of good quality. The data are transferred to a PC and stored on a hard disk. Control software on the PC automatically operates the imager system, and the detailed parameters of observation, such as the start and end times, can be changed remotely by editing the parameter file on the network.

Table 3.1 lists the details of filter characteristics with wavelengths, bandwidth, transmission efficiency and exposure times of the CCD camera that can be used for
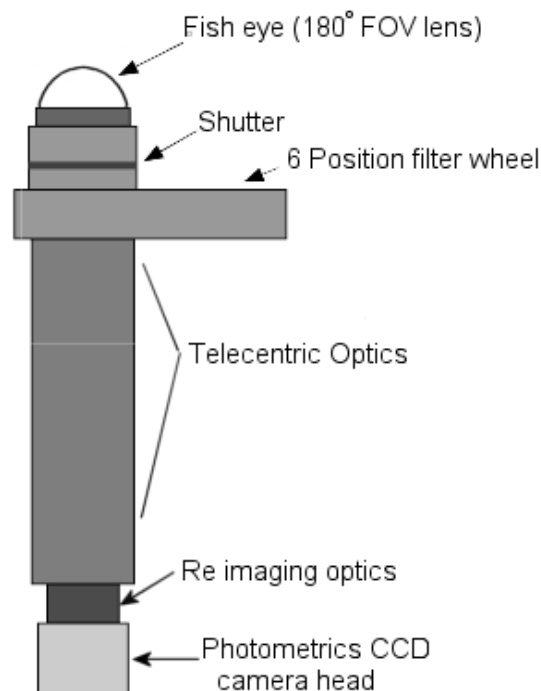
Figure 3.1. The principal components of the USU all-sky CCD camera.

different types of airglow emissions measurements for different purposes. Six emissions

were measured as: the OI (557.7 nm) green line emission, the OI (630.0 nm) red line

emission, Na (589.2 nm) line emission, the near infrared (NIR) hydroxyl (OH) Meinel

broadband emission (710-930 nm), and the O_2 (0,1) band at 865.5 nm. In addition,

background sky measurements (Bg) were also made at 572.5 nm to aid the analysis of the

visible wavelength data, which is used to monitor cloud coverage and to provide a

background measure for the narrow band filters. The NIR OH filter incorporated a notch

at 865.5 nm to limit contributions from the O_2 (0,1) band. The exceptional sensitivity of

the imager enabled sequential measurements at a high repetition rate of 3-12 min. Further

details of this imaging system and the filter specifications are given in *Taylor et al.*

[1995]. As explained earlier, the OI (630.0 nm) airglow red line emissions were used to

Table 3.1. Filter details and exposure times for the USU CCD camera.

Filter	Wavelength (nm)	Bandwidth (nm)	Transmission (%)	Integration Time (sec)
OI	557.7	2.65	~83	90
Bg	572.5	2.67	~83	90
Na	589.1	2.50	~80	120
OI	630.0	2.40	~80	90-180
$O_2(0,1)$	865.5	12.0	~85	90
OH	715-930	215	~80	15

study the thermospheric plasma depletion, and our dissertation work will be focused on the data obtained from these measurements.

3.1.2. USU Campaigns

The USU cameras were deployed at several sites to measure the OI (630.0 nm) thermospheric airglow emission. Table 3.2 summarizes the sites of the campaigns, geographic locations, dip latitudes, average solar flux index during the campaign, average range of geomagnetic index (Kp), and date of the campaign using the USU all-sky CCD cameras. Figure 3.2 shows the map of the locations of sites and the solid lines represent the plots for dip latitudes. White disks represent the airglow images with the field of view covered by the camera at 250 km altitude in respective locations. The dark bands aligned approximately in the north-south direction in the images are the plasma depletions (bubbles). These optical images have been used during minimum solar flux and magnetic quiet conditions from Christmas Island, Alcantara and Brasilia in Brazil, and Ascension Island for detail analysis of the equatorial plasma bubbles in this dissertation work.

Table 3.2. USU campaigns for OI (630.0 nm) airglow emission measurements.

Sites	Geographic location	Dip latitude	Solar flux index (F10.7 cm)	Avg. Kp value	Campaign period
Alcantara, Brazil	2.4°S 44.4°W	6°S	79	<3.5	October 1994
Christmas Island	2.1°N 157.4°W	2.8°N	73	<4	Sep-Oct 1995
Ascension Island	7.6°S 14.4°W	16°S	74	<3	Mar-Apr 1997
Brasilia, Brazil	14.8°S 47.6°W	10.6°S	75	<4	Sep-Nov 2005
Cachoeira, Paulista, Brazil	22.7°S 45°W	17.5°S	95-200		1998-2000
Petrolina, Brazil	9.7°S 40.7°W	10°S	72		2009-2010
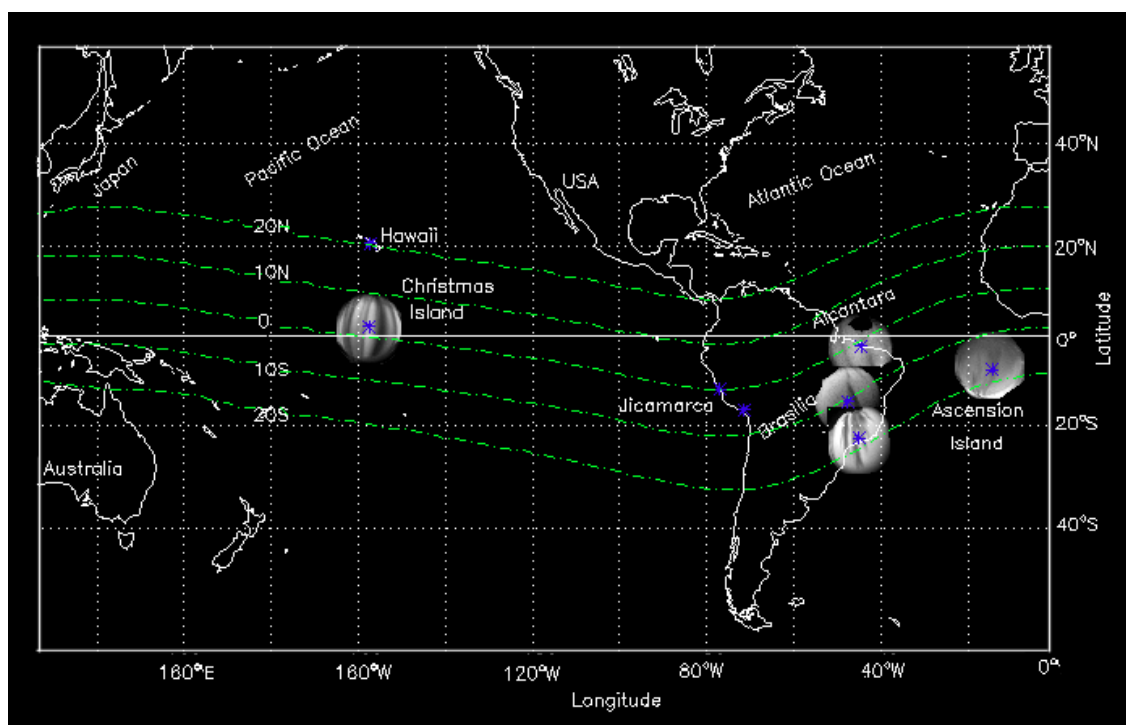
Figure 3.2. Map showing the locations of USU OI (630.0 nm) airglow emissions campaigns. White disks represent the airglow images with the field of view covered by the camera at 250 km altitude in respective locations. The dark bands in the images are the plasma bubbles.

3.1.3. Processing of Optical Image Data

The fish-eye lens has the advantage of imaging the entire sky, but at the expense of adding geometric distortion. The image must be carefully calibrated in order to map pixel locations to physical positions in the sky, enabling sequential observations of several different airglow emissions with an interval of several minutes. The imager has a sensitive back-thinned solid state 1024×1024 pixels CCD array and data were 2×2 binned on a chip providing a spatial zenith resolution of approximately 0.5 km. Since the CCD camera is a linear device, it is easy to convert from pixel counts to intensity once a calibration has been done. It is also important to perform accurate spatial calibrations for mapping between pixel locations and positions along the airglow layer. Pixels away from zenith correspond to much larger geographic areas than the pixels near zenith do. Therefore, it should be noted that even small errors in the spatial calibration will contribute significant error in the final analysis, and so we should be careful to account for this.

The stars in the images are very useful for calibration and are also good indicators of the quality of the images. In general, the more stars that are visible, the higher the image quality. However, the stars become a problem as they cause streaking when averaging images together or when projecting them onto a geographic grid. Figure 3.3 (left image) is an example of a raw image with stars measured from Christmas Island on September 28, 1995. The raw image is calibrated with help of the star references and this calibrated image has been unwarped with the geographic projection onto 1500×1500 km grid as shown in right image in Figure 3.3. In this case, the stars are removed. These
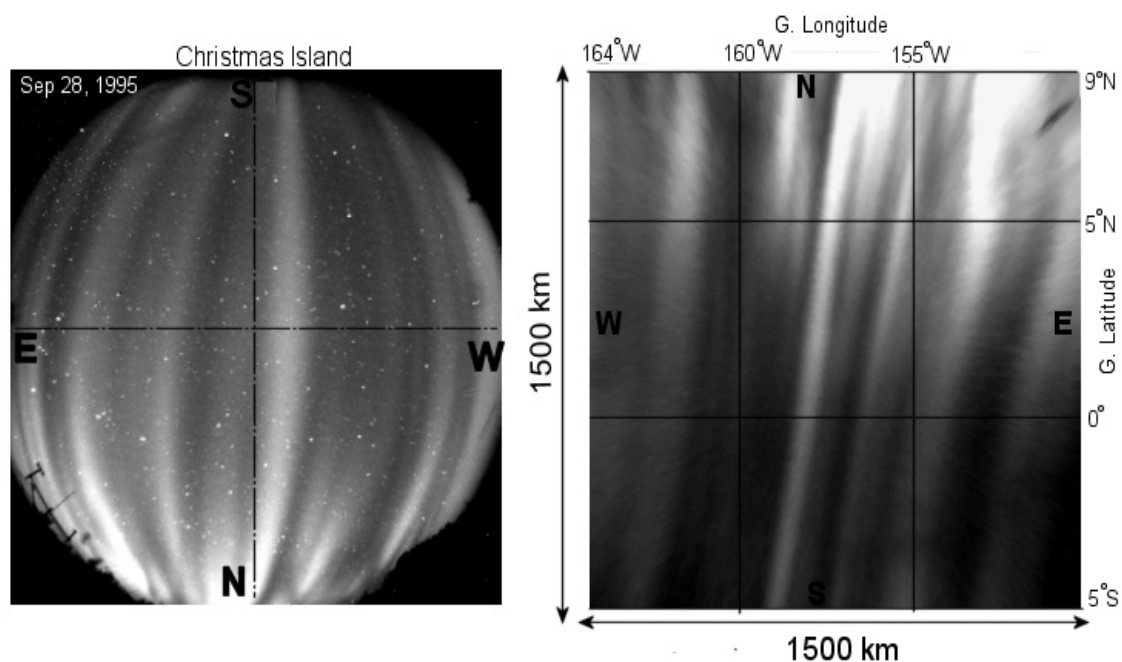
Figure 3.3. Examples of OI (630.0 nm) airglow raw image (left side) and unwarped image onto 1500×1500 km geographic grid (right side).

processed images were then used for further detail analysis. Here, the dark bands in the image are plasma bubbles that are aligned along the magnetic field lines due to high parallel conductivity. Similarly, most bubble structures from all observation sites have been seen to be aligned along the magnetic north-south direction. These dark bands, the region of the airglow emission minima (i.e. the center of the plasma depletion), can be assumed to represent in time and space a value corresponding to a minimum in the plasma density. These dark bands are used as a reference from successive images for calculating the zonal drift velocities of depletion structures and their scale sizes or distance between adjacent structures.

3.2. Radar Techniques

Radar techniques have been used since the dawn of the space age in the 1950s to study the ionosphere [*Gordon*, 1958]. In this study, long-term Jicamarca incoherent and coherent scatter radar observations from 1996 to 2008 have been used. Here, we briefly discuss these two radar techniques.

3.2.1. Incoherent Scatter Radar

Incoherent scatter radar (ISR) is a very powerful ground-based remote sensing technique that can be used to measure many ionospheric quantities including electron density, electron temperature, ion temperature, and line-of-sight ion flow velocity, as well as some of the properties and behavior of the neutral atmosphere. It can also observe both sides of the peak electron density region simultaneously. It has a larger antenna relative to the radio wavelength and hence, it produces a narrow beam and achieves far better resolution. As incoherent radar scatter has to work with very weak signals, it requires a high power transmitter, a large antenna and the most sensitive receiver and sophisticated data processing available. This can be observed in very powerful radars like Jicamarca and Arecibo.

The physical basis of the incoherent radar technique is Thomson scattering in which the echo is the result of the scattering of electromagnetic energy radiated by the radar and reflected by electrons in the ionospheric plasma. Incoherent radars transmit a radar signal and receive a reflected echo from the ionosphere. ISRs' usually emit at a frequency of a few hundred MHz up to ~1200 MHz [*Kelley,* 1989], which is much higher than the peak plasma frequency. Since the frequencies used by ISR are much higher than

the plasma frequency, almost the entire transmitted signal passes through the ionosphere and out into space. Therefore, ISR can probe the ionosphere above the F-region peak. The transmitted signals are emitted in pulses so the distance of the echoing region (altitude) can be calculated from the delay time and the speed of light. However, there is a very small amount of the transmitted signal that gets reflected by the ionosphere and is received back to the radar. It is the spectrum of this received signal that contains the information about the ionospheric region being investigated. Overviews of this technique have been presented by several authors [e.g., *Kelley,* 1989; *Hargreaves,* 1995].

Thermal backscatter level is the source of the ISR echoes often used to determine ionospheric parameters. This method requires a minimum plasma density in the scattering volume determined by the system noise, antenna size, transmitter power, integration time etc. For the Jicamarca radio observatory, this minimum is $\sim 10^4$ cm^{-3}. This limitation usually prohibits measurements at night in the altitude range below the F peak.

The Jicamarca Radio Observatory (JRO) is in the equatorial region of the western hemisphere and was established in 1961 at Lima, Peru (12˚S, 76.9˚W, dip latitude ~1˚N). The 50 MHz incoherent scatter radar has a beam width of 7˚ with a bandwidth of ~1 MHz. Figure 3.4 shows an example of radar echo measured by ISR from Jicamarca on September 14, 2005. The figure indicates three nicely developed plumes with quasi-periodic ESF structure on its bottom. The altitudinal resolution was 25-40 km with an integration time of 5 min. In this dissertation work, we use extensive F-region ISR data from Jicamarca to investigate the relationships between spread *F* onset velocities and the prereversal drift peak velocities with variations of solar flux on different seasons. These
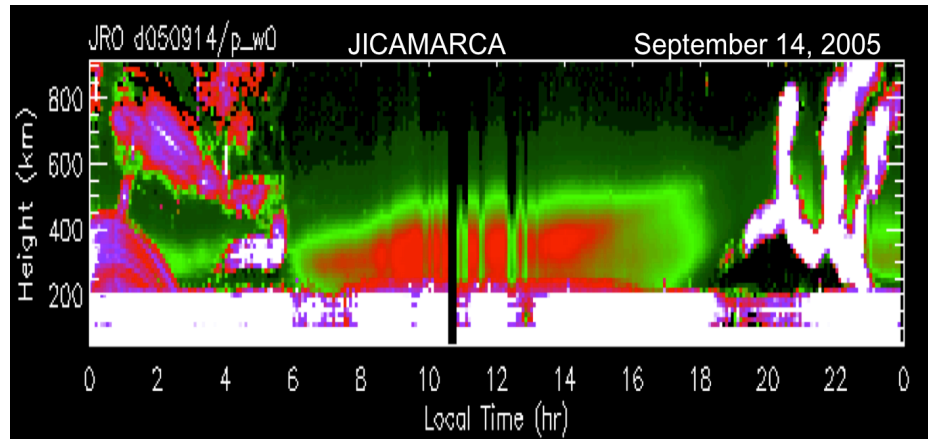
Figure 3.4. An example of radar echo obtained from Jicamarca incoherent scatter radar observation on September 14, 2005.

velocities were calculated at altitude range of ~300-400 km, where signal-to-noise ratio is large.

3.2.2. Coherent Scatter Radar

The radar scatters from irregularities in the medium, $\mathbf{k}_m$, according to the relationship [e.g., *Kelley,* 1989]

$$\mathbf{k}_T = \mathbf{k}_s + \mathbf{k}_m, \tag{3.1}$$

where, $\mathbf{k}_T$ and $\mathbf{k}_s$ are transmitted and scattered wave, respectively. Since $\mathbf{k}_s = -\mathbf{k}_T$ for backscatter, $\mathbf{k}_m = 2\mathbf{k}_T.$ Thus, the scattering wavelength is one-half the transmitted wavelength.

When plasma instabilities are present in the ionosphere, the amplitude of fluctuations in the medium can grow to values much greater than the thermal level. If the wave number of these fluctuations matches the requirement in equation (3.1), then smaller radar systems can be used to detect these fluctuations. The Doppler spectrum in

such a case is then representative of the phase velocity of the nonthermal waves rather than of the bulk motion and temperature of the plasma.

Most of the plasma instabilities detected by coherent scatter radars (CSRs) produce waves with **k** vectors nearly perpendicular to the magnetic field. At the magnetic equator, the plane perpendicular to **B** includes the vertical direction. Thus, coherent scattering can occur at all elevations in that plane. The large antenna at Jicamarca can be oriented only a few degrees off vertical, but smaller steerable antennas are used to look obliquely east or west to study electrojet and spread *F* instabilities. It is easier to keep the beam perpendicular to **B** in the case of the equator.

The CSR echoes can be observed even with relatively modest radar systems. It operates in the frequency range 20-50 MHz. The strong abnormal signals can appear in a time of less than 8 msec over regions of kilometers across. Sometimes these echoes persist for hours and during this time, the altitude of a particular irregularity patch will often increase by hundreds of kilometers. In addition, Jicamarca Unattended Long-term investigations of the Ionosphere and Atmosphere (JULIA) have been used for studying the equatorial ionosphere. JULIA is a MST/Coherent scatter radar used for studying the day-to-day and long-term variability of ESF, 150-km drift echoes, and neutral atmospheric waves.

Figure 3.5 shows an example of radar echo (plume) measured by coherent scatter radar observations from Jicamarca, Peru on September 14, 2002. Initially, the echo was observed at early evening (~19:15 LT) and then a very tall plume was developed after ~2 hours (at ~21:00 LT) that extended to altitudes beyond 1600 km. Such types of very tall
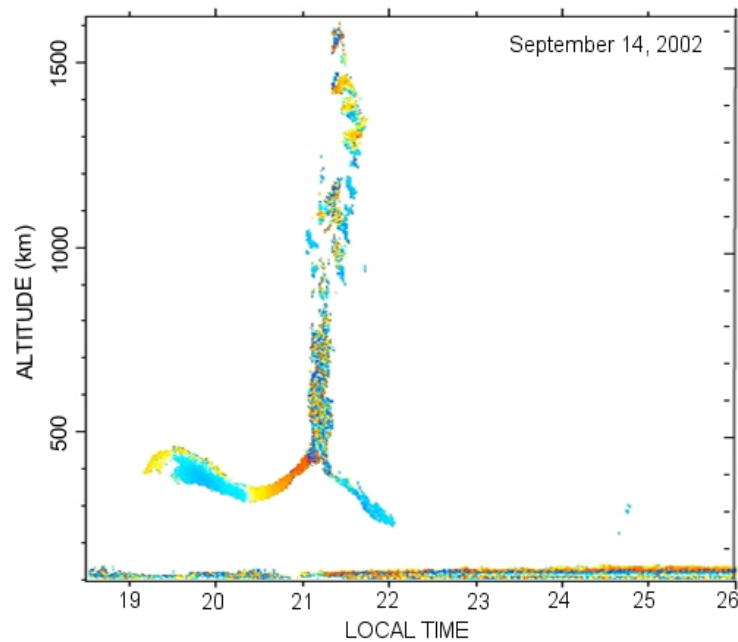
Figure 3.5. An example of coherent scatter radar echo (plume) observed from Jicamarca Radio Observatory.

plumes were observed on solar maximum conditions, while at solar minimum condition, relatively short plumes occurred from Jicamarca, Peru. In our dissertation work, we have focused on detail analysis of coherent and incoherent radar echoes to investigate the solar flux and seasonal dependence of onset time and height of initial spread *F* and also that of radar plumes.

3.3.   Other Techniques

Ionosondes techniques work by transmitting radar signals, usually in the 1-20 MHz range, and receiving a returned echo at a later time. The transmitted signal reflects from the ionosphere at the altitude where its frequency equals the local plasma frequency. The ionospheric plasma density is measured as a function of altitude by varying the transmitted frequency, which measures densities at different altitudes. These altitudes are

estimated by using the time taken to travel by the signals. However, this technique can only measure plasma density at altitudes below the plasma peak density, which is usually the F-region peak at around 400 km altitude. This is because transmitted frequencies above the peak plasma frequency will pass right through the ionosphere.

The other devices used to study the ionospheric irregularities are in situ measurements, such as diagnostic probes flown aboard sounding rockets and satellites. Common spacecraft instruments include Langmuir probes or plasma frequency probes for measuring the electron density. Satellite scintillation techniques are used to study irregularities at any given latitude and longitude sectors. Spaced-receiver techniques can be used to estimate remotely the drift velocity and the velocity variance of ionospheric motions along the ray path. Global Positioning System (GPS) techniques for studying the ionosphere have come to the fore within the past two decades. Traditionally, GPS studies of the ionosphere have focused on total electron content (TEC) measurements and the undisturbed ionosphere. Two GPS techniques are used to study the ionospheric irregularities by measuring the change in Total Electron Content (TEC) and scintillation.

3.4.   Comparison with Other Techniques

The ionosondes technique can only measure plasma density at altitudes below the F-region peak electron density. Occasionally, the measurements are restricted in the E-region (~100 km) because of the enhancement of electron precipitation exceeding the electron density of the F-region. Whereas the coherent scatter radars can measure the irregularities echoes up to 2000 km altitudes. Similarly, the plasma depletion can be

measured up to 3000 km using the OI (630.0 nm) airglow image measurements through the apex mapping.

Spacecraft have the advantage over remote sensing equipment of being able to provide very high resolution analysis precisely in the regions of greatest interest. Their disadvantage is that they require a tremendous amount of support and, in the case of rockets, only fly for short intervals (~10 min) every few years. Low-latitude atmospheric satellite programs are rare by comparison, but the durations of satellite missions are much longer. The common spacecraft instruments, such as Langmuir probes or plasma frequency probes, measure the same kind of physical properties as in incoherent scatter radar, but ground-based and in situ data are quite different in nature. Whereas the radar acts like a pass band filter in wave number space and makes statistical, time-averaged observations, spacecraft probes make instantaneous, broadband observations along their trajectory. Rocket and satellite data are physically local, but spectrally non-local. Both spacecraft and ground-based data additionally suffer from varying degrees of ambiguity as to what degree where variations are spatial or temporal. For example, ground-based GPS diagnostics will never match radar installations for wealth of ionospheric data.

All-sky airglow optical images taken of the OI (630 nm) ionospheric emissions provide a powerful technique to obtain two dimensional images of the depleted regions of the ionosphere associated with the radar plumes and ESF. Depletions show up as dark bands or regions in the all-sky images. By assuming the emissions come from a relatively narrow layer around 250-300 km and the depletions are elongated along the magnetic fields line, it is possible to map the horizontal images to an image of the depletions in the

(magnetic) equatorial East-West-vertical plane. The technique complements the radar images nicely, not only showing the large-scale morphology of the depletions, but also the assumed correspondence between these depletions and the small scale irregularities are responsible for the radar echoes [e.g., *Mendillo et al., 2005*; *Makela, 2006*, and references therein]. The characteristics of radar echoes can be changed drastically if the plasma bubble arises just passing the field of view of the radar antenna or it passes away from some sideway or just after the radar field of view. Since the optical imaging can be taken wherever and whenever one wishes, such limitations can be overcome by the simultaneous measurements from these techniques.

CHAPTER 4

AIRGLOW OBSERVATIONS AND MODELING OF F-REGION

DEPLETION ZONAL VELOCITIES OVER

CHRISTMAS ISLAND[1]

Abstract

We report image measurements of plasma depletions (bubbles) in the equatorial F-region ionosphere over Christmas Island (2.1°N, 157.4°W, dip latitude 2.8°N) in the central Pacific Ocean. The observations were made during the equinox period, September-October 1995 using a Utah State University CCD imaging system filtered to observe thermospheric OI (630.0 nm) airglow emissions centered at ~280 km altitude. Well-defined magnetic field-aligned depletions were observed on 18 nights during the campaign, including strong post-midnight fossilized structures, enabling detailed measurements of their morphology and dynamics. The number of bubbles during each night was influenced by their initial onset times and their persistence. The separations between adjacent bubbles ranged from ~150-250 km in good agreement with results from Alcantara, Brazil and also with prior observations from other sites. However, measurements of their eastward zonal drift speeds indicated normal behavior peaking around 90-100 m/s prior to local midnight, with exceptionally high velocities, ~80 m/s during the post-midnight period that persisted until dawn. These results differ markedly from optical measurements at similar equatorial latitudes, but at different longitude

---

sectors suggesting the zonal drift velocities can have a significant longitudinal dependence. Model drift velocities calculated using a simple electric field model with winds defined by the Horizontal Wind Model (HWM-07) produced an eastward drift throughout the night, but their post-midnight magnitudes were much smaller than observed. Using a modified HWM-07 wind field, a basic nighttime trend similar to the Christmas Island trend was successfully obtained.

4.1. Introduction

Optical observations of the nighttime F-region equatorial ionosphere have been conducted from various low-latitude sites over the past three decades to study plasma irregularities associated with equatorial spread *F* (ESF) [e.g., *Weber et al.,* 1978; *Sahai et al.,* 1981; *Mendillio and Baumgardner,* 1982; *Meriwether et al.,* 1985; *Taylor et al.,* 1997; *Santana et al.,* 2001; *Kelley et al.,* 2002; *Mukherjee,* 2003; *Makela et al.,* 2004]. These irregularities originate at or near the magnetic equator in the post-sunset ionosphere. As they rise up with time through the F-region ionosphere, they map along the magnetic field lines, thereby extending over a large region of the low-latitude ionosphere, greater than ±15° dip latitude [e.g., *Mendillo and Tyler*, 1983; *Rohrbargh et al.,* 1989; *Sahai et al.,* 1994]. These regions of deep plasma depletions are also referred to as equatorial plasma bubbles (EPBs). They have zonal widths of typically a few tens of km and extend along the magnetic field lines for hundreds to thousands of km depending on the peak altitude of the irregularity (bubble) development (e.g., *Sobral et al.,* 2002), while their vertical heights range from a few tens of km to several hundred km [e.g., *Labelle et al.,* 1997; *Muralikrishna and Abdu,* 2006]. When radio waves propagate

through such plasma-depleted regions, they suffer significant amplitude and phase distortions producing disruptions in communications and degrading the capability of GPS navigation systems [e.g., *Basu et al.,* 1999].

Studies of the structure and time evolution of large-scale airglow depletions measured in the thermospheric OI (630.0 nm) airglow emissions have proven to be very useful for investigating the onset, spatial development and dynamics of F-region plasma irregularities [e.g., *Mendillo and Baumgardner,* 1982; *de Paula et al.,* 2002; *Makela et al.,* 2004; this study]. The OI (630.0 nm) airglow emission is a well-known nighttime phenomenon that results when excited atomic oxygen $O(^1D)$ decays into its ground state as explained in section 2.4. The excited atomic oxygen is produced by charge exchange between O^+ and O_2 followed by dissociative recombination of O_2^+ in the ionospheric F-region [e.g., *Tinsley et al.,* 1973; *Mendillo and Baumgardner*, 1982]. The emission intensity depends on the O^+ and O_2 altitude profiles and peaks at about 250-300 km altitude (depending on the solar activity) in the bottomside of the F–region layer. The localized regions of reduced airglow emission intensity represent in time and space minima in the O^+ ions (i.e. regions of low plasma density) and have been used successively for measuring the zonal motions of the depletions [e.g., *Mendillo and Baumgardner,* 1982; *Taylor et al.,* 1997; *de Paula et al.,* 2002; *Martinis et al.,* 2003; *Makela et al.,* 2004; *Arruda et al.,* 2006].

The equatorial F-region plasma depletion zonal velocity has proven to be an important parameter for modeling the electrodynamics of the equatorial ionosphere used for the prediction of ionospheric scintillations [e.g., *Valladares et al.,* 2002]. The plasma

drift velocity was first described by *Woodman* [1972] using radar measurements at Jicamarca, Peru (12°S, 76.9°W). Since then, extensive studies of plasma depletion zonal velocities have been carried out using a variety of techniques including ground-based radar, thermospheric airglow, and satellite measurements [e.g., *Fejer et al.,* 1991; *Sobral et al.,* 1985, 1999; *de Paula et al.,* 2002; *Pimenta et al.,* 2003a; *Sagawa et al.,* 2003; *Terra et al.,* 2004; *Abalde et al.,* 2004; *Arruda et al.,* 2006]. All of above cited studies show that plasma bubbles propagate eastward during the nighttime, and rarely westward, under quiet magnetic conditions [e.g., *Taylor et al.,* 1997; *Abdu et al.,* 2003].

At equatorial latitudes, ionospheric plasma zonal drifts are driven by the F-region vertical electric fields, which in turn, are generated by the E- and F-region neutral wind dynamos [e.g., *Haerendel et al.,* 1992]. The background plasma zonal drift reaction to the neutral winds is not a local effect, but a result of the interaction of the zonal winds with the plasma along the flux tube. The plasma depletions embedded in the background ionosphere mostly develop in the nighttime ionosphere and are also due to a field-line-integrated electrodynamics with the field-line-integrated Rayleigh-Taylor instability (RTI) driving the bubble development [e.g., *Haerendel,* 1973; *Sultan,* 1996]. During its growth, the plasma velocity within a bubble is different from the ambient background plasma drift velocity. However, for fully-grown, mature bubbles, the depletions move together with the background plasma drift as fossilized structures until the morning sunlight refills the depleted flux tubes due to enhanced ionization [*Makela et al.,* 2004].

Several studies obtained by different techniques have reported longitudinal variations of EPB development and their nocturnal zonal drift velocities [e.g., *Maruyama*

and Matuura, 1984; *Tsunoda,* 1985; *Immel et al.,* 2004; *Makela et al.,* 2004; *Henderson et al.,* 2005; *Jensen and Fejer,* 2007; *Pautet et al.,* 2009]. Of importance for this paper are studies of plasma irregularities in the Pacific sector mainly using airglow measurements with the earliest observations in the mid -1980s [*Rohrbaugh et al.,* 1989; *Tinsley et al.,* 1997]. Subsequently, *Kelley et al.* [2002] deployed two airglow imagers on the summit of Haleakala Volcano, Maui, Hawaii [20.7°N, 156.2°W] for long-term measurements of the low-altitude thermosphere. Simultaneous observations of equatorial depletions were made using an all-sky (180˚) CCD imager and a co-located narrow field [47°] imager pointing southward along the magnetic meridian [e.g., *Kelley et al.,* 2003; *Makela et al.,* 2004]. In particular, they mapped depletions to apex heights of ~1500 km extending close to Christmas Island, which is at the same geographic longitude, but about 2000 km due south of Hawaii. Using these instruments, *Yao and Makela* [2007] presented further equatorial plasma bubble zonal drift velocity measurements during 2002-2005 from Hawaii, while *Makela et al.* [2009] recently reported on low-latitude ionospheric events observed from Hawaii in coordination with the 50 MHz coherent scatter radar measurements from Christmas Island.

In this study, we report on detailed observations of airglow depletions in the equatorial F-region ionosphere from Christmas Island in the central Pacific Ocean. The measurements were made during the autumnal equinox period (September 1995) using an all-sky CCD imager filtered to observe the thermospheric OI (630.0 nm) airglow emission, as well as several mesospheric emissions. In Section 4.2, we present the basic observations and analysis of the bubble developments and their nighttime propagation.

Section 4.3 presents the derived zonal velocity from Christmas Island, which was found to be unusually high during the post-midnight period (~80 m/s) as compared with previous results from established sites, mainly at different geographic longitudes. The results are discussed in section 4.4 and the effects of background thermospheric winds on zonal drift velocities are also examined using the simple electric field model of *Eccles* [1998] in this section. Summary of the results are presented in Section 4.5.

4.2.   Observations and Data Analysis

As part of a collaborative program with the Naval Postgraduate School, Monterey, CA, a Utah State University (USU) all-sky CCD airglow imager was set up and operated at Christmas Island, Republic of Kiritimati (2.1°N, 157.4°W, dip latitude 2.8°N) for exploratory optical measurements of plasma bubbles in the central Pacific sector. The measurements were made during a limited one-month period in September-October 1995. The imager is a well-proven field instrument fitted with a sensitive back-thinned solid state 1024×1024 pixels CCD array and data were 2×2 binned on chip resulting in a zenith spatial resolution of 0.5 km. During the campaign, sequential observations of the thermospheric OI (630.0 nm) airglow emission, as well as the mesospheric near infrared (NIR) hydroxyl (OH) Meinel broadband emissions (710-930 nm) and the OI (557.7 nm) green line emission were made using exposure times of 120 sec, 15 sec and 90 sec, respectively. A background sky measurement was also recorded to discriminate between mesospheric and thermospheric structures and meteorological clouds. Further details of the all-sky instrument and its operational system are given in *Taylor et al.* [1995]. The main purpose of this campaign was to study the occurrence,

spatial characteristics, and dynamics of the ionospheric plasma bubbles and mesospheric gravity waves at equatorial latitudes.

Figure 4.1 is a map of the Pacific region showing the central location of Christmas Island, about 2000 km due south of Hawaii. The open circle centered on Christmas Island represents the geographic field of view (FOV) of the all-sky imager (~1500 km diameter) for F-region measurements assuming a reference altitude of airglow emissions at 280 km appropriate for this latitude and solar minimum conditions (at average solar flux index *F10.7* ~73). The enlarged airglow image below illustrates the orientation and typical structure in the F-region data recorded during this campaign. The dashed lines show the dip latitudes at the magnetic equator, 10°S, and 10°N. The dark
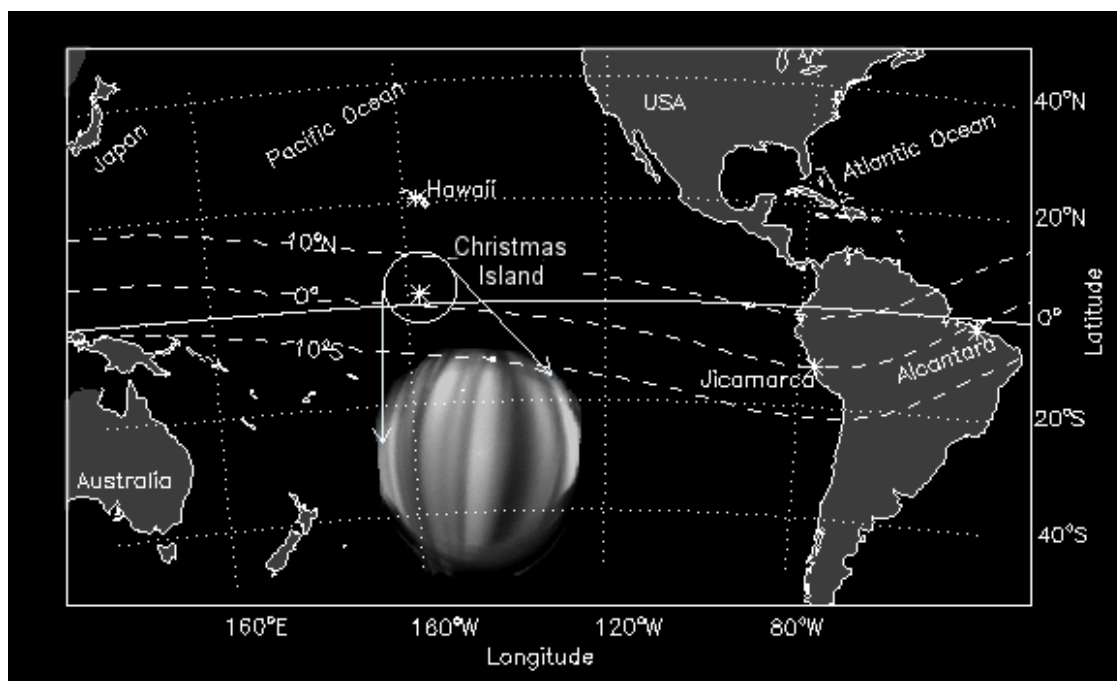
Figure 4.1. Map showing the central Pacific location of Christmas Island (2.1°N, 157°W), the field of view covered by the all-sky imager (circle), and an example of OI (630.0 nm) airglow image. The dashed lines represent the dip latitudes at the magnetic equator, 10°S, and 10°N.

bands in the image depict magnetic north-south aligned plasma bubbles appearing as a series of depletions in the 630.0 nm airglow emission. These data have been used to study morphology and dynamics of equatorial plasma depletions over Christmas Island.

During the campaign (September 15-October 3, 1995) image measurements were made from dusk to dawn throughout the moon down period. OI (630.0 nm) image data were obtained using alternating time intervals of ~5 and ~11 minutes resulting in typically 34–76 images per night. The observing conditions were generally good during this period and plasma depletions were observed on all 18 nights, with high contrast EPB displays imaged on 15 of these nights. Although localized, intermittent clouds occasionally interfered with the time series measurements, but they did not limit our ability to measure the motion of the bubbles and their horizontal scale-sizes during the course of each night

This data analysis method is well developed and is similar to that used by *Pimenta et al.* [2001] and is described further by *Pautet et al.* [2009]. This technique has been used on several prior occasions to investigate plasma depletions properties [e.g*., Pautet, et al.*, 2009]. The images were first calibrated using the known star field to determine the parameters of the imager, such as its orientation and pixel scale-size. The stars were removed from the image sequences, which were then unwarped (to correct for the all-sky lens format) [e.g., *Garcia et al.,* 1997; *Pautet and Moreels,* 2002], and projected onto a 1500×1500 km uniformly spaced geographic grid, as shown in Figure 4.2 (assuming an emission altitude of 280 km). The field of view of the unwarped image extends from about 5˚S to 9˚N latitude and 150˚-164˚W longitude. The zenith spatial resolution was ~
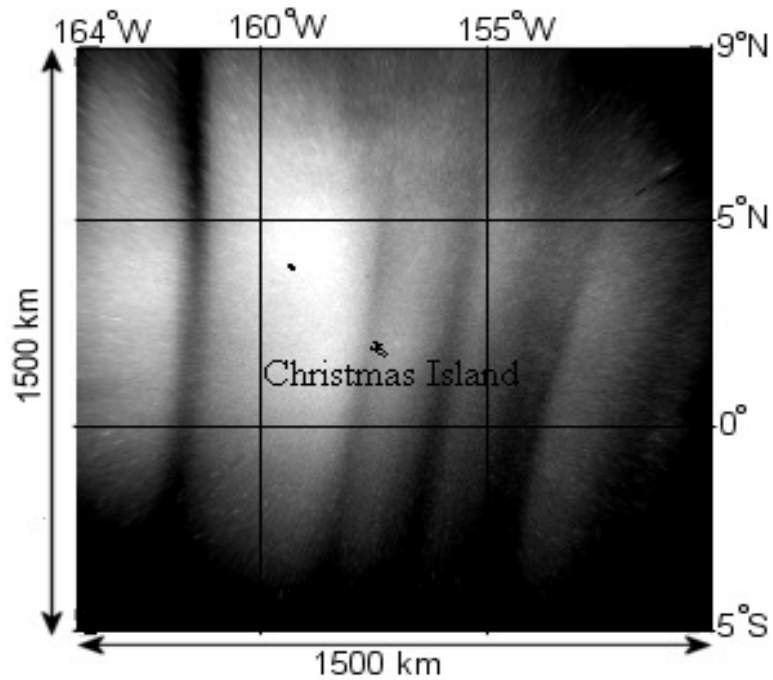
Figure 4.2. An example of an unwarped OI(630.0 nm) image from Christmas Island projected onto a 1500×1500 km uniform geographic grid assuming altitude of airglow emissions at 280 km.

3 km per pixel. The horizontal scale-sizes of the structures were computed using a standard 2-D Fourier spectral analysis [e.g., *Taylor and Garcia,* 1995; *Garcia et al.,* 1997]. Drift speeds of individual bubbles were then determined by selecting two sequential images with time steps of ~16 min. Motion was measured at various positions along a given bubble to determine its average velocity. This procedure was repeated for subsequent image pairs during the course of the night to determine the mean zonal drift speed of the depletions as a function of local solar time. (Note, the time difference between Local Solar Time (LST) at Christmas Island and Universal Time (UT) is 10.5 hours).

Figure 4.3 shows a time series of unwarped images of prominent F-region structures recorded during the night of September 28-29. The left side axis plots the magnetic latitude (0° and 10°N) indicated by dash-dotted lines, while the right side indicates geographic latitude. On this occasion, a faint broad depletion was first detected at 19:57 LST and over the next hour the display evolved into several magnetic north-south aligned dark bands extending across the camera's FOV. Multiple bubbles were observed for the next ~4 hours moving eastward, as indicated by the white arrows. On this occasion, the early evening structures comprised new bubbles evolving in the vicinity of Christmas Island, as well as fully developed airglow depletions moving into the camera's FOV from the west. By 02:00 LST most of the bubbles had exited the field of view to the east. Thereafter, a single fossilized bubble was observed (as seen in figure at 03:01 LST) drifting steadily eastward. Moreover, multi bubbles again enter into the field of view of the camera near the dawn, as shown in the last image of Figure 4.3 (at 04:41 LST). After local midnight, the F-region structures were dominated by fossilized bubbles progressing steadily eastward across the camera's FOV.

Figure 4.4 contains data from several nights (in all-sky format) measured during the campaign at the premidnight period. Nine nights of data are shown in Figure. Each image was taken at approximately the same time at ~23:30 LST (~10:00 UT) to compare bubble activity and their spatial characteristics. Although some night-to-night variability is evident in the number of depletions and their spatial separations, all of the images contain well-developed, extensive plasma bubbles aligned along the magnetic field lines by this time. This situation prevailed for 15 nights. The bubbles were numerous and
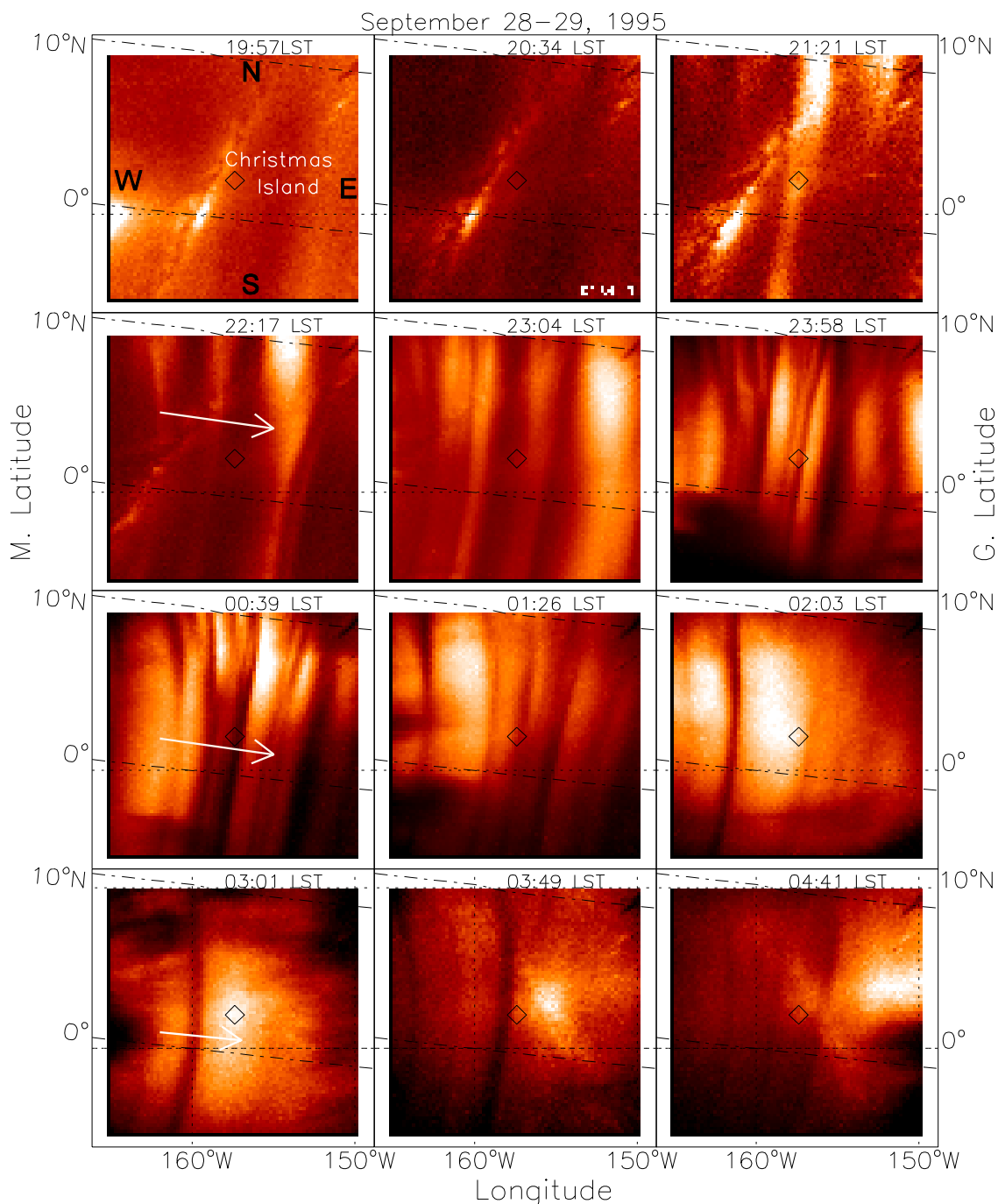
Figure 4.3. Sequence of unwarped all-sky OI (630.0 nm) airglow images showing the spatial characteristics and time evolution of ionospheric airglow structures associated with plasma depletion (dark bands) imaged from Christmas Island during the night of September 28-29, 1995, from 19:57 to 04:41 LST (07:30-15:11 UT). The dashed lines are magnetic latitudes at 0° and 10°N.
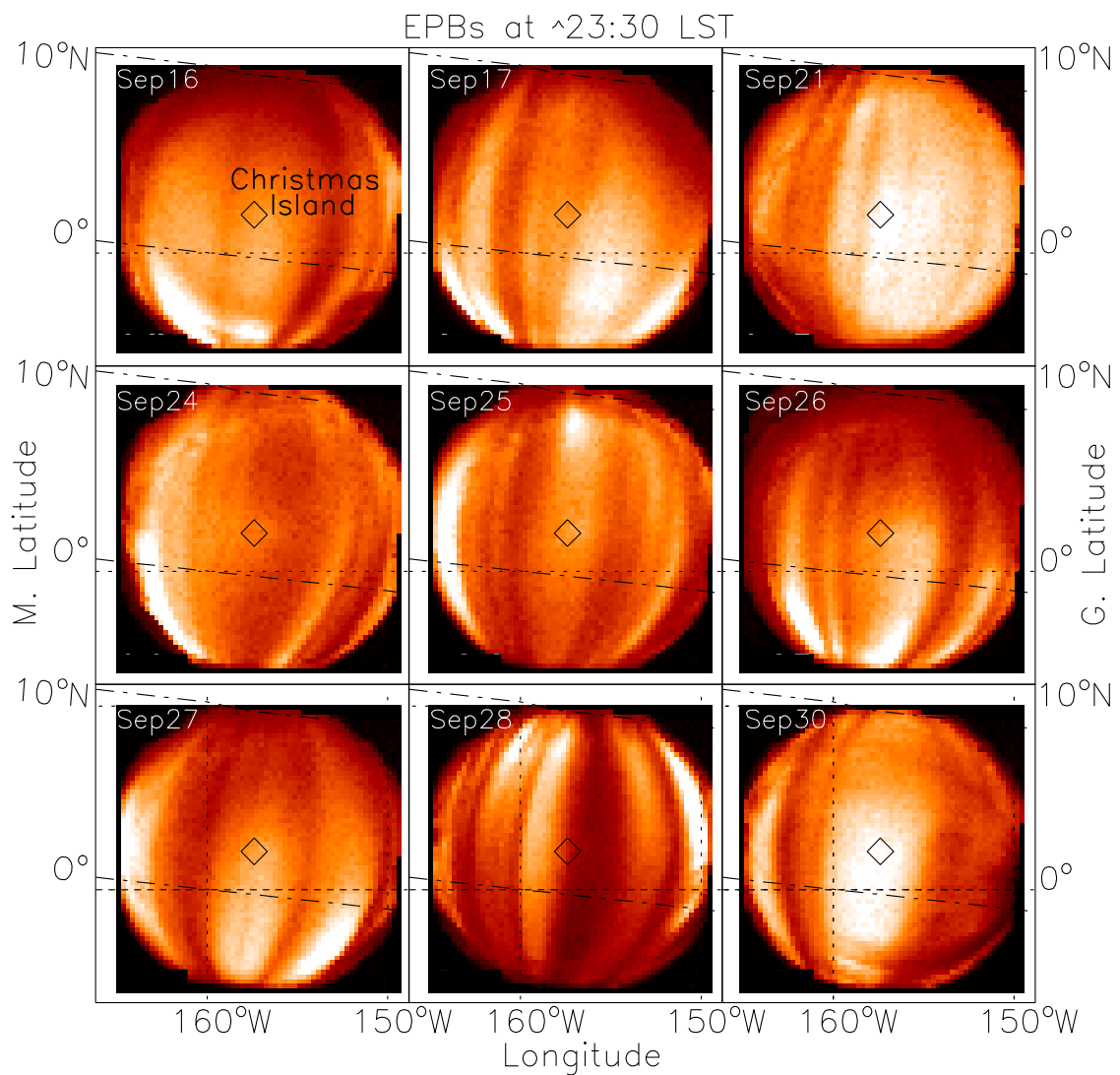
Figure 4.4. EPBs imaged over Christmas Island at the pre-midnight around 23:30 LST (10:00 UT). Strong EPBs structures were observed on all clear sky nights prior to midnight.

exhibited the highest eastward drift speed during this period (discussed further in section 4.3.3).

In comparison, Figure 4.5 shows nine examples of the post-midnight EPBs activities imaged between 01:00 and 04:44 LST. These data contained mainly fossilized EPBs that appeared fully developed when they entered into the camera's FOV. They exhibited little change in their east-west dimensions as they drifted eastward and often persisted until dawn, which were aligned along the magnetic field lines. Together, these data illustrate the strong and persistent F-region activity recorded during this equinox period.

4.3.   Results

These high-quality image data have been used to investigate several key characteristics of the plasma depletions observed from Christmas Island.

4.3.1. Depletion Occurrence, Onset, and Duration

Figure 4.6 top panel plots the number of plasma bubbles observed on each night during the campaign. A large day-to-day variation in their total number was observed which ranged from 1 to 14 per night. As mentioned earlier, some of the nights were intermittently cloudy, but this did not restrict our ability to determine the number, and duration of the depletions. For example, their low occurrence on UT days 262-263 and 266 (indicated by the dashed-dotted lines) was not due to limited sky conditions.

The middle panel presents the initial onset times of EPBs that were observed to grow inside the FOV of the camera (mainly to the west of Christmas Island). During most
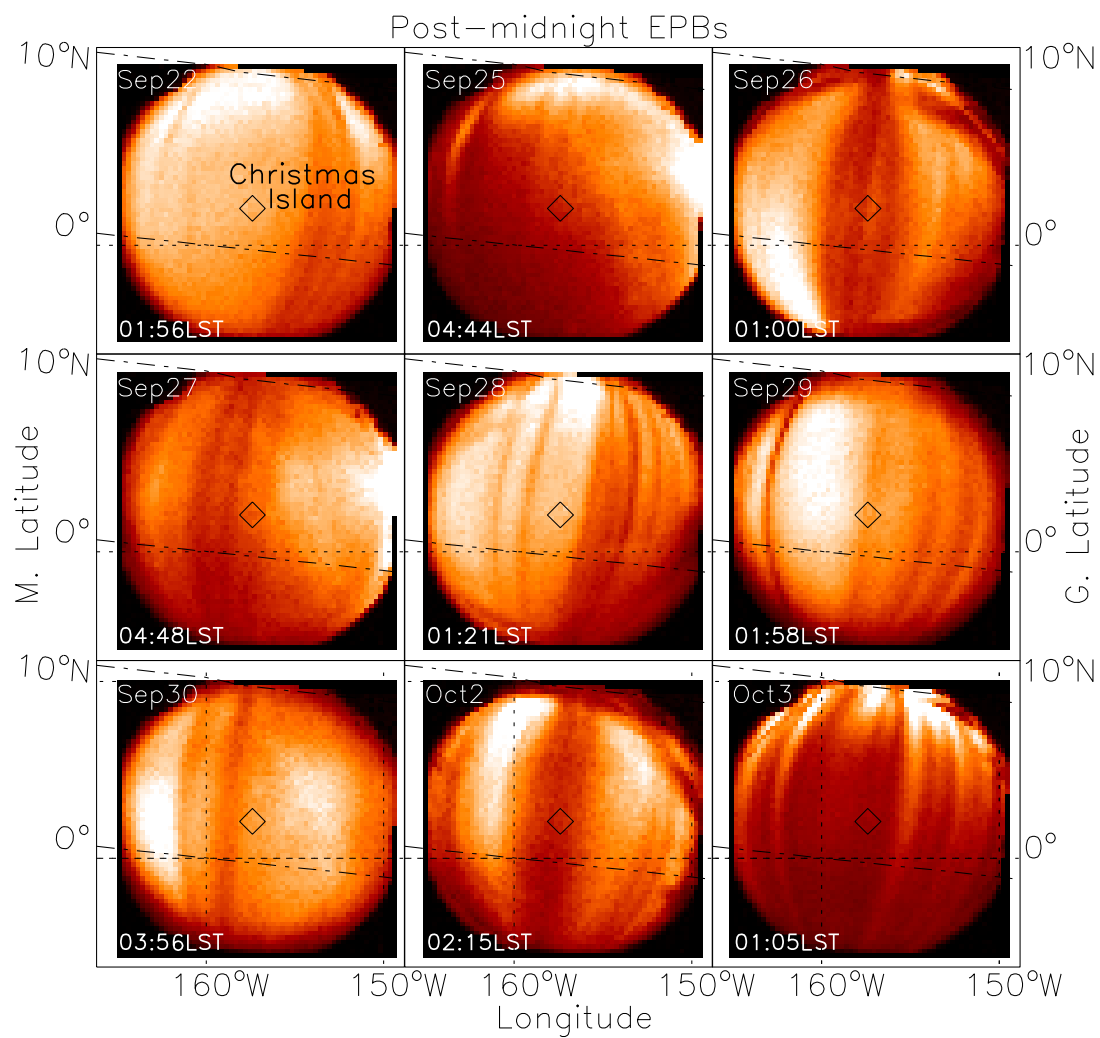
Figure 4.5. EPBs imaged over Christmas Island for the post-midnight periods during the nine nights of the campaign. The fossilized bubble structures were occasionally observed until the dawn.
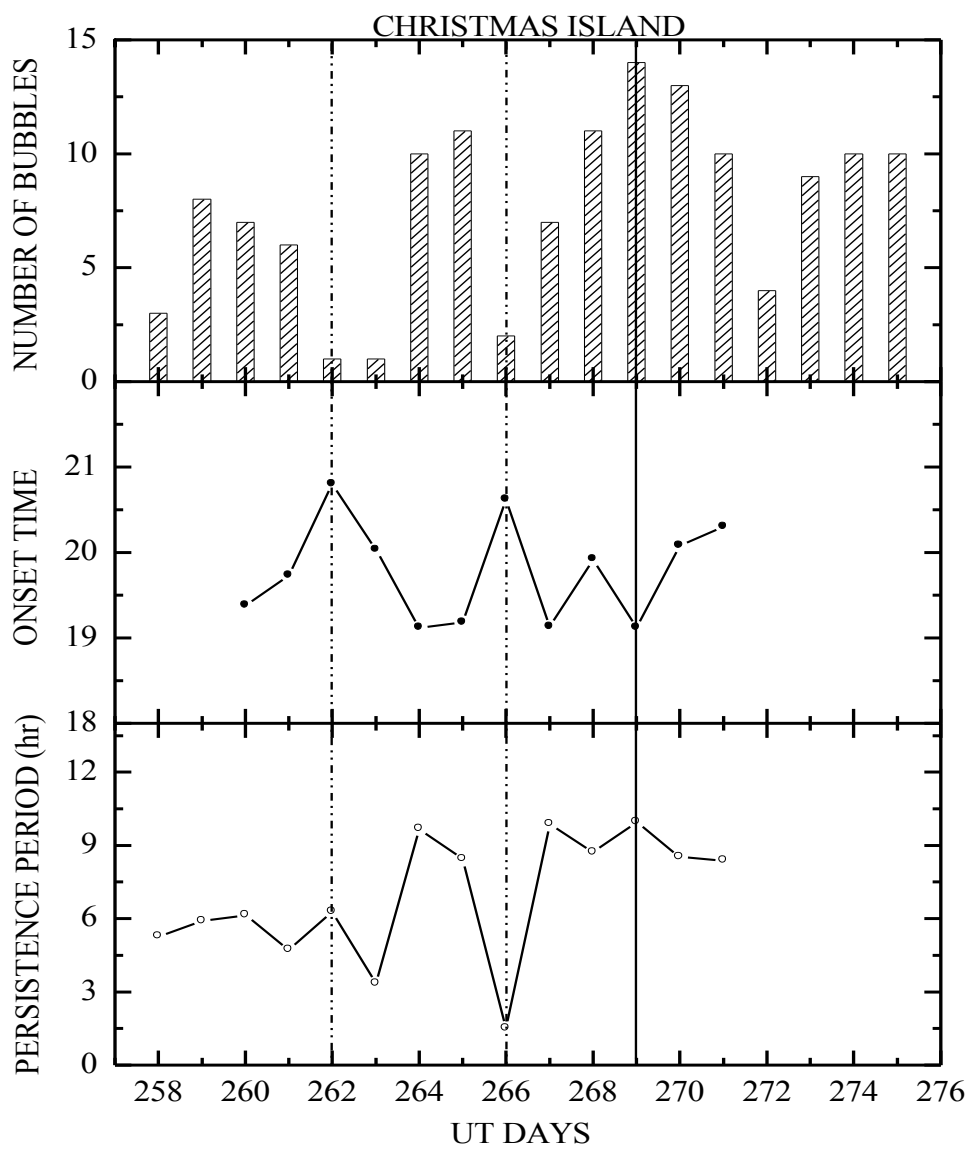
Figure 4.6. Top panel shows the total number of EPBs observed each night, the middle panel plots the onset time of the bubbles over Christmas Island, while the lower panel indicates their nocturnal duration.

of the nights, the onset time of these EPBs occurred in the early evening hour around 19:30 to 20:30 LST, which is consistent with previous climatological results obtained from radar observations of ESF from Jicamarca, Peru recently reported by *Chapagain et al*. [see Chapter 7]. Note, for the first two nights and towards the end of the campaign, it was not possible to estimate the onset time of bubble growth due to the presence of pre-existing bubbles drifting in from the west. For comparison, the lower panel plots the estimated duration of the EPB display for each night. Taken together these three plots show the number of bubbles observed was strongly influenced by their initial onset time and their persistence. The figure clearly illustrates the number of plasma bubbles was maximum when the EPB onset was early and their persistence period was long (~9-10 hours). For example, on UT day 269 (September 26-27) the onset time was ~19:30 LST and 14 bubbles were observed during the course of the night (indicated by the solid vertical line). In contrast, on UT days 262-263 and 266 (indicated by the dashed-dotted lines), a few bubbles were observed, their onset time was ~1 hour later, and the bubbles persisted for a relatively short period of time, ~2-5 hours.

4.3.2. Horizontal Scale-Size of the EPBs

The magnetic field aligned bubble structures observed over Christmas Island (e.g., Figure 4.3) exhibited a range of zonal separations that differed during the course of a night, and from night-to-night. Similar morphology structures were observed by the USU camera a year earlier from Alcantara, Brazil (2.3°S, 44.4°W, and dip latitude 6.7°S) during the NASA-INPE Guara Campaign [*Taylor et al.,* 1997]. Figure 4.7 plots the distribution of the zonal distance between adjacent EPBs observed during the campaign.

The separations ranged from as little as several km up to 550 km, but were most frequently spaced 100-250 km apart. (Note, the minimum separation between the bubble structures reported in this plot was 25 km.) For comparison, the results from Alcantara, Brazil (October 1994) under similar solar minimum conditions were also plotted. The Brazilian observations were more limited by clouds, but both data sets revealed similar dominant scale-sizes for their zonal separations, ranging from ~150-250 km over Christmas Island (42% of events), and ~100-200 km over Alcantara (~52% of events). The Christmas Island results are closely consistent with the distances between two consecutive bubble structures observed under similar solar flux conditions from Brazil. The detail observations from the Brazilian site will be discussed in Chapter 6. This
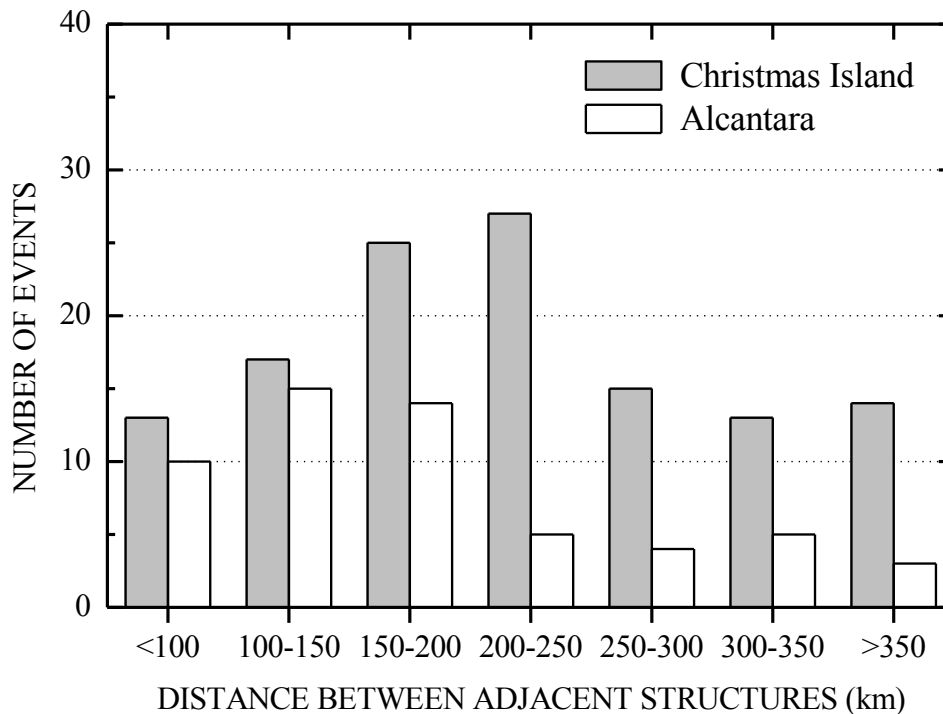
Figure 4.7. Histogram plots of the distance between two consecutive plasma bubbles observed over Christmas Island and Alcantara, Brazil.

spacing between the consecutive bubbles is a long observed feature of large plasma bubble development [*Whitehead,* 1971; *Kelley et al.,* 1981] and is evidence of the suggested required structuring of the sunset F-region for Rayleigh-Taylor instability for plasma bubble to develop [*Tsunoda,* 2008].

4.3.3. Overview of Bubble Evolution and Propagation

Figure 4.8 shows two keogram plots summarizing the evolution, development, and propagation of EPBs observed on two nights (18-19 and 28-29 September) during the campaign. In each plot, the curved band in the bottom left is due to the passage of Milky Way (which was not fully removed during the image processing), while the horizontal dashed line indicates the zenith. The plots were made by taking a horizontal (west-east) slice passing through the zenith of each unwarped image. The data were then spliced together to create a time series showing the zonal development of the depletions observed on both of these nights. Although keogram plots lose much of the two-dimensional spatial information present in the original images, they provide an important overview of depletion activity during the night. The dark bands progressing in time from the bottom left to the top right (i.e. from west to east) show the onset and subsequent motion of several depletions, as indicated by the arrows. The near-linear slopes of these bands, which give the depletion zonal drift velocity in the geographic frame, indicate that they were moving with almost constant, but different magnitude of velocities, on these two occasions.
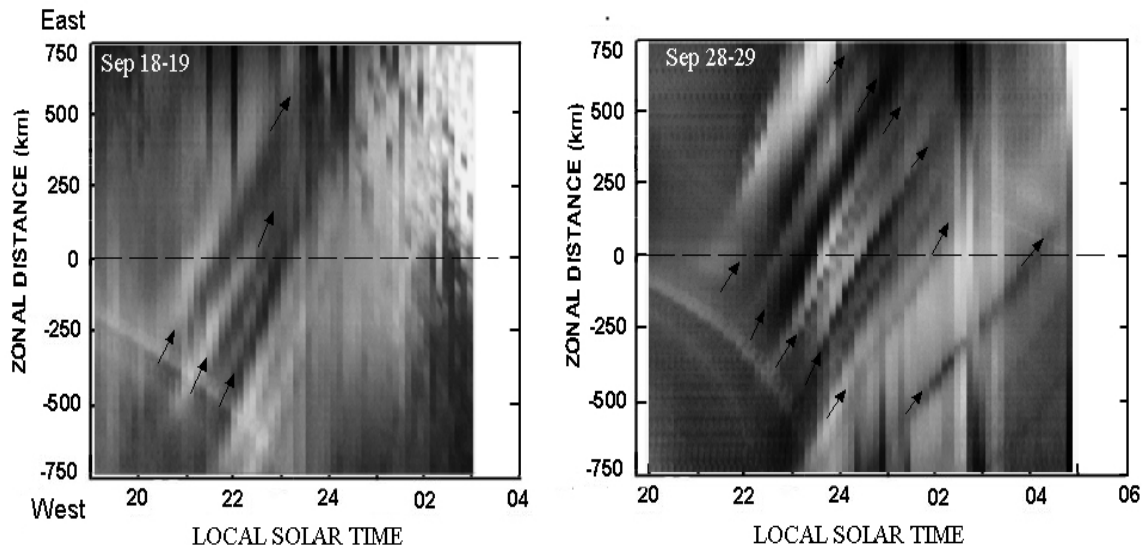
Figure 4.8. Example of keogram plots summarizing the west-east (zonal) evolution of depletions observed on two occasions from Christmas Island. The arrows show the direction of motion of the plasma bubbles (dark bands), while their slopes indicate almost constant zonal velocities during the nights.

On September 18-19, the first two bubbles appeared to develop within the camera's FOV prior to ~20:30 LST; subsequently, other already well-developed bubbles entered into the FOV. The slopes of all of the bubble paths are linear indicating almost constant zonal velocity of ~70-80 m/s throughout the night. Around local solar midnight, the leading bubble exited the camera's FOV, while subsequent bubbles began to fade. On September 28-29, a similar situation occurred, and multiple structures were observed to evolve inside the FOV, but somewhat later, around 22:00 LST. These depletions then moved steadily eastward with a higher constant velocity (~90-110 m/s), and persisted longer, at least until ~02:00 LST when they exited the camera's FOV to the east. A single isolated bubble was also observed during the post-midnight period until dawn, again moving steadily eastward but with a slightly lower velocity (~60 m/s). Similar trends for

the bubble motions were observed during most of the nights from Christmas Island, as described below.

4.3.4. EPB Zonal Velocity

The zonal velocities of the individual plasma bubble as a function of LST were measured on 17 near-consecutive nights. As described in Section 4.2, the unwarped images were used to determine an average drift velocity for each depletion structure. To calculate the bubble velocity, the displacement of an individual structure was measured from two consecutive images. The speeds were then estimated by dividing the average distance between the structures by the corresponding time interval. The drift velocities were usually calculated from bubbles as they moved through the zenith sky. However, these data were often supplemented by measurements of bubbles closer to the edges of the camera's FOV and were adjusted to the same LST.

Figure 4.9 plots the derived zonal velocity of several consecutive EPBs as a function of local solar time for the night of September 28-29. The OI image at 23:51 LST shows example of bubble structures (numbered 1-7), but several other bubbles were also measured during the night to determine the EPB motion. The drift velocity of each bubble overlaps very well. The average velocity indicated by the bold line peaked at ~115 m/s around 23:00 LST and then decreases over the next ~2 hours down to ~60 m/s, and thereafter remained approximately constant until at dawn ~04:45 LST.

Using the above procedure, Figure 4.10 shows the average EPB zonal velocities as a function of LST for 16 nights during the campaign. Due to limitations in the camera operation caused by moonlight, the measurements were restricted to evening time during

the first part of the campaign and the post-midnight during the latter part on the campaign. However, it is clear from this figure that good measurements were obtained during most of the campaign period. The gaps in the drift velocity data on September 15-16, 18-19, 20-21 and 24-25 were due to clouds, while on September 21-22, 29-30 and September 30-October 1, they were caused by strong fading of the bubbles. The vertical bars on each plot represent one standard deviation in the measurement uncertainty at that time.

To examine the influence of the magnetic activity on zonal drift velocity during the campaign, we checked the average values of three hourly geomagnetic indexes <Kp>
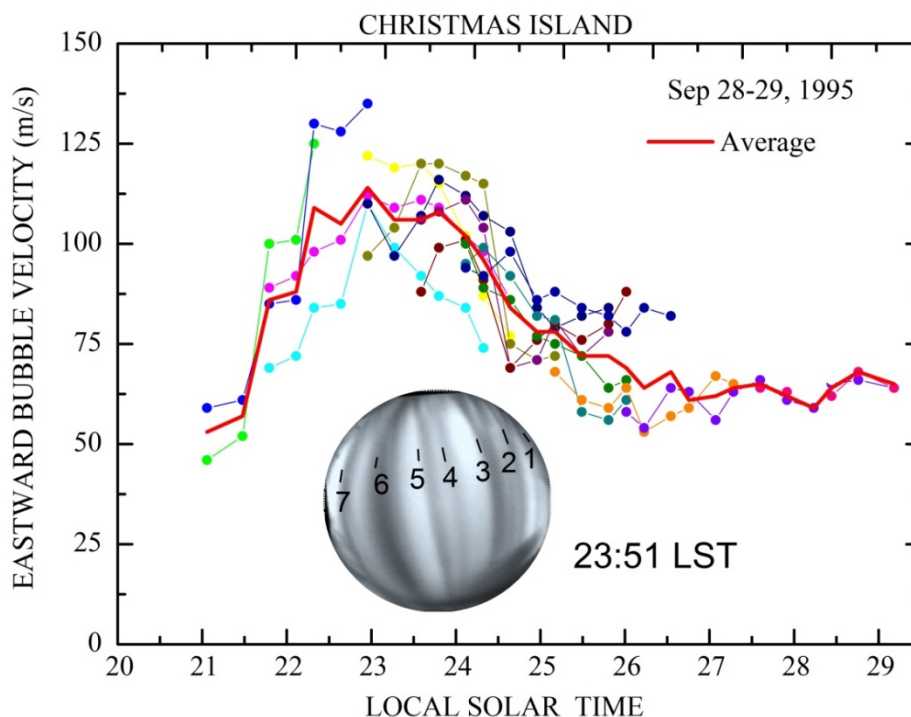
Figure 4.9. EPBs drift velocities for several consecutive bubbles during the night of September 28-29. Examples of bubble numbers (1, 2, 3, 4, 5…. etc.) are also shown in the OI image at 23:51 LST. The bold line represents the averaged velocity of all bubbles.

over a nine-hour period (13:30-22:30 LST) and are given in each plot. This interval includes six hours prior to local sunset during which ESF onset may be influenced by geomagnetic storms. However, the geomagnetic activity was quiet with minor activity (< 3) except September 15 and 28 when $<K_p>$ was slightly larger than 3 and no significant difference in EPB activity was evident. This result was to be expected as geomagnetic storms during solar minimum condition, are known not to significantly affect zonal drift velocities; however, the storms prior to sunset may still inhibit the onset of ESF [e.g. *Fejer et al.,* 2005].

Figure 4.10 reveals a significant night-to-night variability in the derived EPB drift velocities. On several nights, they generally increase in early evening hours, peaking around 22:00-23:00 LST (velocities >100 m/s). The velocities then decrease to a minimum around local solar midnight and then increase slightly in magnitude in the early morning hours. On the other hand, some nights (e.g., September 22-23) exhibit very little change in the magnitude of the velocity, which remains relatively high throughout the night. Figure 4.10 also shows low eastward velocity of ~7 m/s, and westward motion of ~20 m/s in the early evening hours on September 26-27, and September 24-25, respectively.

Figure 4.11 summarizes the average bubble zonal velocities (during 17 nights) as a function of LST. While the individual plots show significant night-to-night variability in the derived depletion drift velocities, the data ensemble show good temporal coverage (from ~19:00 to 05:00 LST) during the campaign, with a clear nocturnal signature. This is indicated by the bold curve, which plots the average velocity of all measurements,
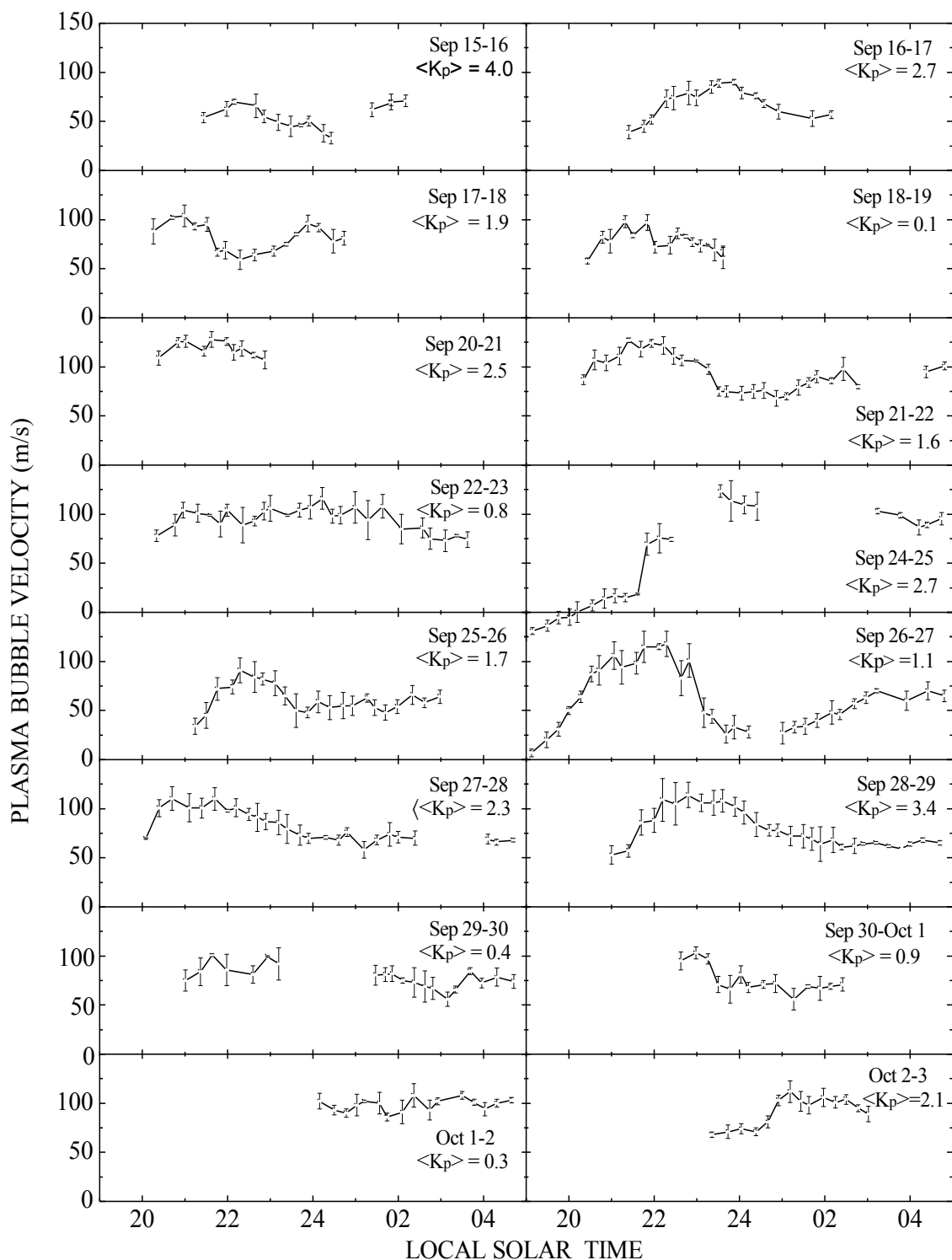
Figure 4.10. The average EPBs velocities calculated from two successive images for time binned at ~16 minutes during 16 nights, assuming a reference altitude of airglow emissions at 280 km. K_p index represents average geomagnetic activity during nine-hour period.
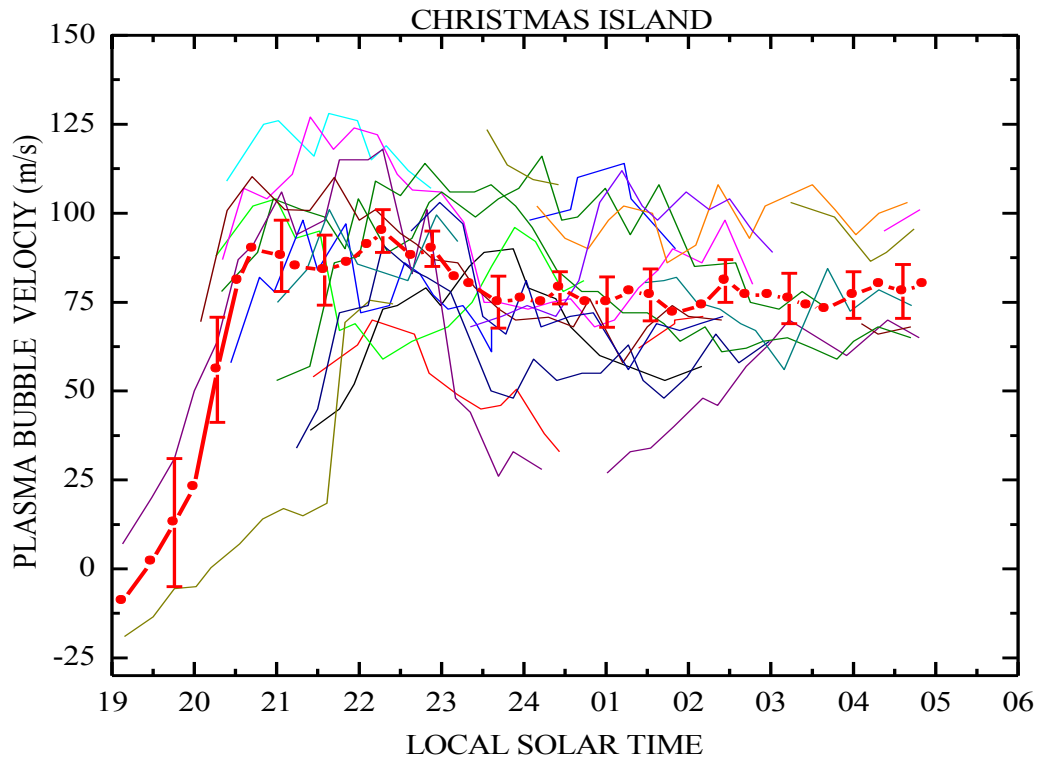
Figure 4.11. Superposition of EPB velocities for all 17 nights of campaign. Bold data points represent averaged velocity, and the vertical bars are the standard deviations from the mean.

while the vertical bars indicate their standard deviations from this mean. Limited observations (only for two nights) shortly after dusk (~19:00 LST) revealed very low drifts reversing from west to eastward. By 20:30 LST, multiple observations show that the average zonal velocity then increased rapidly during the early evening hours and peaked around 21:30-23:00 LST with a mean value ~90 m/s (with individual velocities up to 125 m/s). The average drift velocity then decreased slightly to ~80 m/s by midnight LST and thereafter remained approximately constant over the next ~5 hours until dawn. In general, the average premidnight velocity results agree well with previous ground-based measurements in equatorial regions under similar solar minimum conditions [e.g.,

Fejer et al., 1991; *Taylor et al.,* 1997; *Valladares et al.,* 2002; *de Paula et al.,* 2002; *Martinis et al.,* 2003]; however, the post-midnight velocities were significantly higher.

Figure 4.12 divides the data of Figure 4.11 into two different groups based on the nocturnal evolution of the bubble velocities. The top panel (a) comprises nine nights of data sets that exhibited a premidnight peak in velocity, while the bottom panel (b)
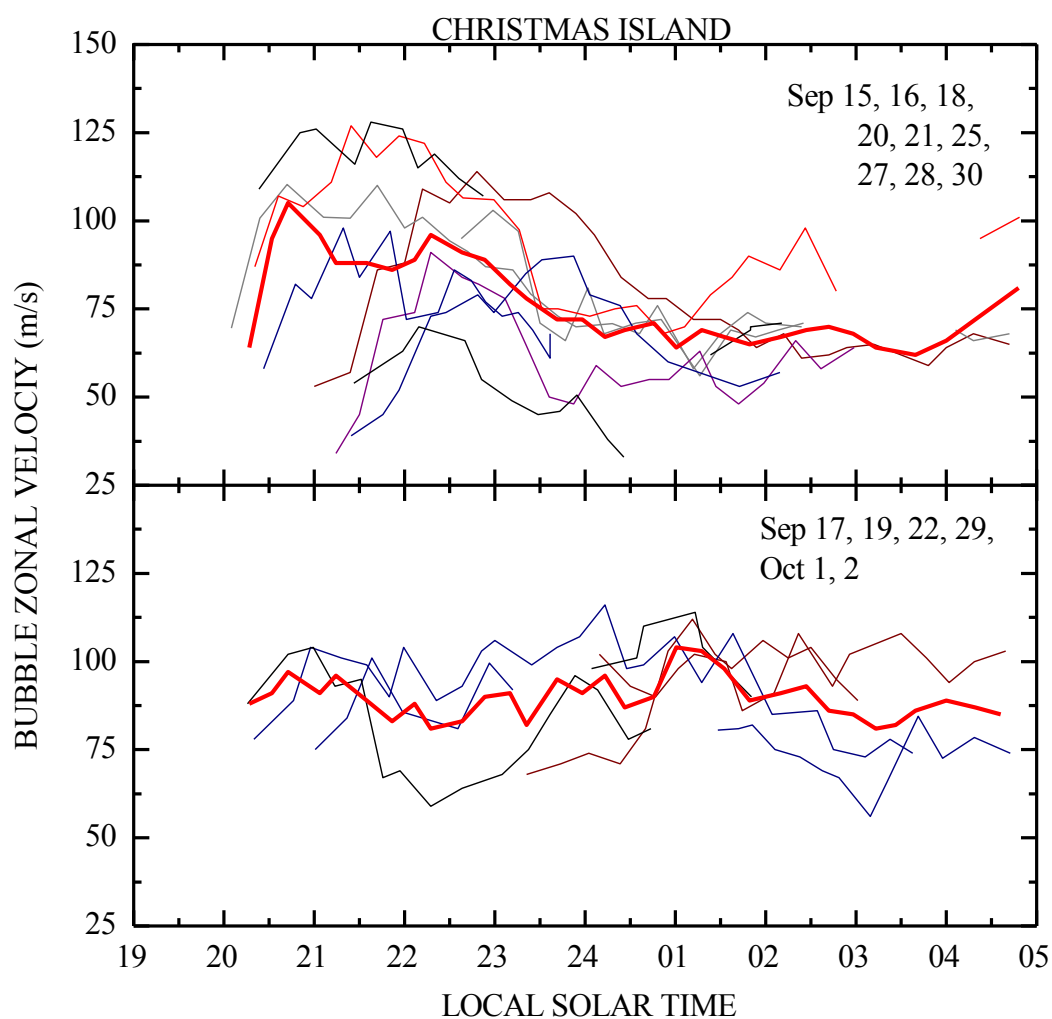
Figure 4.12. (a) Combined EPB velocity plots exhibiting a premidnight peak, and (b) superposition of velocity plots that remained nearly constant throughout the night. The bold lines represent the average velocity.

contains six nights of data where no peak was detected and instead the drift velocity remained almost constant throughout the night (from 20:30 to 04:30 LST) with a high mean value of ~90 m/s indicated by the bold line that illustrate the unusual nature of the post-midnight drift velocity. (Note, the two nights of anomalously low and westward motion in early evening are not included in these plots.) In Figure 4.12a the velocity variations were large, ranging from ~40 to 125 m/s, while in Figure 4.12b there were more restricted to ~75-110 m/s.

4.4. Discussion

4.4.1. Characteristics in the Christmas Island Airglow Structures

The depletions observed from Christmas Island are clearly similar to OI (630.0 nm) thermospheric observations from other sites at equatorial and low latitudes. Their magnetic meridian alignment, sharp east-west gradients in the airglow structure and spacing of the dark bands strongly suggest they are the airglow signature of the medium-scale field-aligned plasma bubbles generated by the R-T instability. Studies of ESF irregularities using Atmospheric Explorer E (AE-E) plasma density measurements reported the irregularities have the form of sharp quasi-periodic depletions [e.g., *Tsunoda et al.,* 1982; *Hysell and Kelley,* 1997]. *Abalde et al.* [2001] presented the fine structure of the quasi field aligned ionospheric plasma bubbles using the OI 777.4 nm emission image measurements. Since the Christmas Island observations were from close to the dip equator, the results only show the airglow structure of the bottomside F-region modulations in the plasma depletions. Therefore, these data cannot demonstrate these F-

region plasma bubble structures penetrated to the topside ionosphere, though they likely did. Particularly in the early evening, some structures may only have been bottomside modulations, yet to grow into topside bubbles.

Most of the nights, the depletions were developed inside the FOV of the camera during early evening and then drifted eastward. They were seen close to 19:30 LST (one hour after ground level local sunset) to 04:00 LST (9:30 hours after local sunset). Thus, these early evening plasma depletions and possible plasma bubbles have their initial development near Christmas Island longitude. Later in the evening airglow signatures of depletions forming at other longitudes drifted into the FOV as fossil depletions just as observed by *Makela et al.* [2004]. The airglow signatures of the fossil structures sometimes will remain until local sunrise when the sun reionizes the ionosphere.

4.4.2. Longitudinal and Latitudinal Characteristics of the Zonal Drifts

In Figure 4.13 we compared the average depletion zonal velocities from Christmas Island with previous optical observations from Haleakala, Hawaii (20.7°N, 157.2°W, dip latitude 21°N) [*Yao and Makela,* 2007], and Alcantara, Brazil (2.3°S, 44.5°W, dip latitude 6.7°S) [*Taylor et al.,* 1997], all of which were obtained under similar low solar flux conditions. The smooth curve plots the empirical model results derived from radar measurements during 1970-2003 from Jicamarca, Peru (12°S, 76.9°W, dip latitude 1°N), for low solar flux conditions (average F10.7 = 90) [*Fejer et al.,* 2005]. Figure 4.13 shows the local time dependence of the depletion zonal velocities prior to midnight LST were quite similar from Christmas Island and Haleakala, which are almost

at the same longitude, but separated in latitude by ~20°. Furthermore, the premidnight Christmas Island drift velocities are consistent with the measurements from Alcantara, Brazil (obtained a year earlier), and the Jicamarca climatological model results with drift velocities peaked at ~110 m/s within the observed range of measurements reported herein (see Figure 4.11). However, it is clear the Christmas Island post-midnight velocities remained elevated in magnitude over the post-midnight drifts of the previous studies.

The depletion zonal drift observations at Christmas Island and Alcantara, Brazil
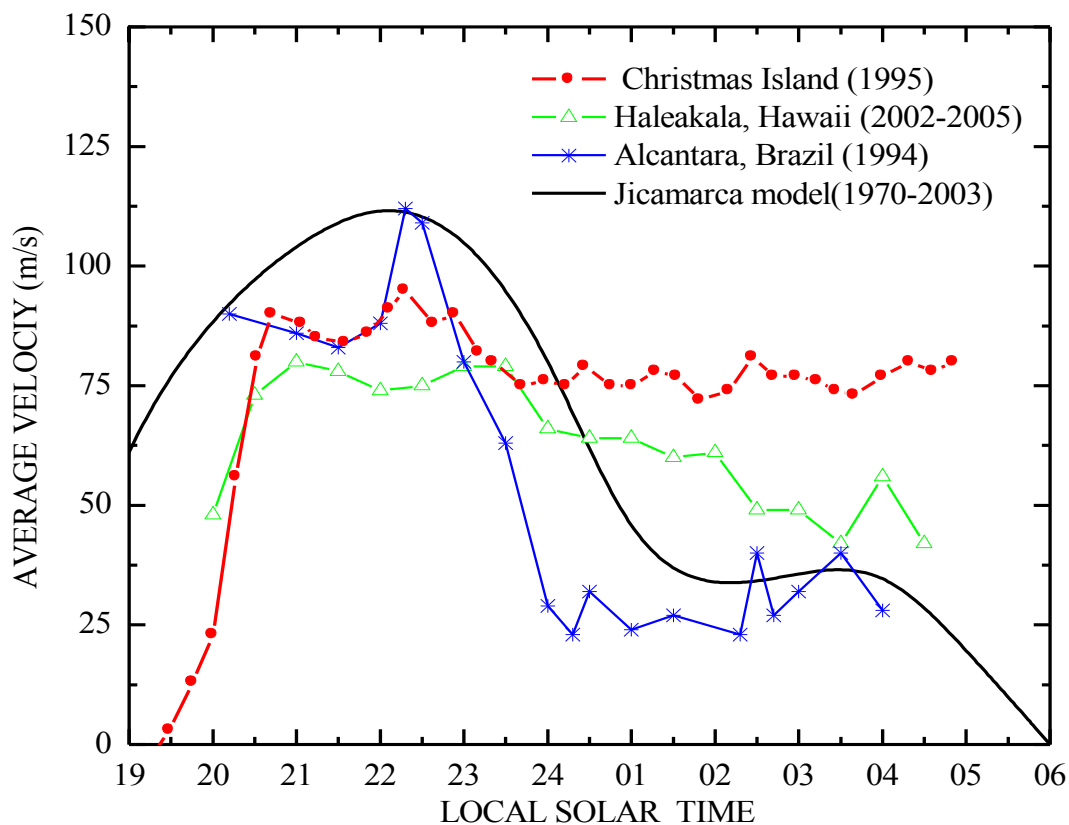
Figure 4.13. Comparison of the average airglow depletion zonal velocities from Christmas Island with previous observations (replotted) from Haleakala-Hawaii [*Yao and Makela,* 2007], Alcantara in Brazil [*Taylor et al.,* 1997], and empirical model of the plasma drift velocities derived from the radar measurement (replotted) from Jicamarca, Peru [*Fejer et al.,* 2005].

(Figure 4.13) are both near the dip equator, but exhibited very different zonal drifts throughout the night. Similarly, the plasma zonal drift model from Jicamarca Radar observations are also at the dip equator in the American longitude sector. Alcantara and Jicamarca lines in Figure 4.13 show strong deceleration of the zonal drifts around local midnight. The differences in average zonal plasma drift of Christmas Island and the results from the South American sector suggest significant differences between their longitude sectors such as dip equator offset, declination, and neutral winds. Satellite studies have also reported a longitudinal dependence of zonal drifts velocities [e.g., *Immel et al.,* 2004; *Jensen and Fejer,* 2007]. *Fejer et al.* [2005] also argued that longitudinal variations of the zonal drifts also point to a strong dependence of the evening vertical drift velocities with longitudes.

Figure 4.13 also shows the airglow depletion zonal drift velocities from Christmas Island were larger throughout the night than drift observed from Haleakala in the same longitude sector. The apex altitudes corresponding to the FOV of the imager at Christmas Island cover approximately from 280 to 450 km, whereas at Haleakala corresponds to at higher altitudes (up to ~950 km) [*Yao and Makela,* 2007]. The zonal plasma drift does vary with altitude in the early evening hours in particular, and also throughout the night [*Eccles,* 1998; *Fejer et al.,* 2005]. Christmas Island and Haleakala observations may also demonstrate this latitudinal (or altitudinal) variation of the zonal drift velocity. *Martinis et al.* [2003] and *Pimenta et al.* [2003a] use airglow observations to show ion drag from equatorial ionosphere anomaly cause thermospheric neutral wind and therefore plasma drift velocities to have latitudinal dependence in which velocities

decrease with increasing latitude. This is supported by the average zonal drifts of Christmas Island and Haleakala, Hawaii plotted in Figure 4.13.

However, there are several possible reasons for the differing magnitudes of the bubble drifts between our results and those presented in the airglow studies at other longitudes. For example, we have calculated the velocities at an assumed emission altitude of 280 km for the OI (630.0 nm) airglow images. It has been shown the velocities calculated at an assumed emission height of 300 km are up to 20% higher than that of 250 km [*Pimenta et al.,* 2003b]. This also will cause the differences in the magnitude of the drift velocities from other locations, but does not alter the time history during the course of the night. The Christmas Island result of a nearly constant elevated zonal drift history is strong evidence of longitudinal differences in the winds or electrodynamics resulting in different nighttime zonal drifts.

4.4.3. Early Evening Drifts

In the early evening, the average zonal drifts prior to 20:30 LST were substantially lower in magnitude from the average plasma drifts of those seen by *Fejer et al.* [2005]. These early evening drifts are from the two nights of observations (on September 24 and 26 in Figure 4.10). The Haleakala observations similarly show a late acceleration after sunset (in Figure 4.13). The zonal drift model of *Fejer et al.* [2005] is based on Jicamarca Radar drift observations of the F peak plasma. Airglow depletion zonal drifts are indicators of F- region bottomside drifts. The observed airglow depletion drifts prior to 20:30 LST might be associated with the post-sunset plasma flow vortex below the F-layer peak [*Haerendel et al.,* 1992; *Eccles et al.,* 1999; *Kudeki and*

Bhattacharyya, 1999]. The vertical rise and fall of the ionosphere near local sunset is accompanied by westward flow in the lower altitudes and eastward flow above. The null velocity of the zonal flow shear rises with the F-region [*Haerendel et al.,* 1992]. The vortex flow has been reported in satellite observations [*Eccles et al.,* 1999] and in radar backscatter observations [*Kudeki and Bhattacharyya,* 1999]. The backscatter figures in *Kudeki and Bhattacharyya* [1999] indicate the bottomside irregularities after sunset are embedded in the bottom of the F-region where the flow is westward (altitude <300 km). The early evening plasma plume signatures in the OI (630.0 nm) airglow from these two days of observations may have been embedded in the F-region, near the null of the shear in the zonal plasma flow. The altitude of the drift shear began to descend with the ionosphere around 19:30 LST. This descent of the F-region, the shear, and the embedded plasma structures is seen in Plate 2 of *Kudeki and Bhattacharyya* [1999]. The descent of the shear should eventually embed the airglow structures in the eastward drifting plasma.

Martinis et al. [2003] investigated the dependence of the zonal airglow depletion drifts with latitude and found the early post-sunset zonal drifts near the magnetic equator are influenced by the E-layer dynamo, while the equatorial anomaly region zonal drifts are dominated by the F-layer dynamo. These results agree with our interpretation of the early evening drift discrepancy of the Christmas Island observations and the *Fejer et al.* [1991] F-region zonal drifts.

4.4.4. Plasma Drift Modeling

These results are now compared with a physics-based model of low-latitude drifts using field-line-integrated electrodynamics. The zonal drift of F-region plasma during

magnetically quiet periods is nearly equal to the conductivity-weighted neutral wind integrated along the magnetic field line

$$V_\varphi = U_\varphi^P = \frac{\int \sigma_P u_s A dl}{\int \sigma_P B dl} \; , \tag{4.1}$$

where V_φ is the zonal plasma drift, U_φ^P is the field-line-integrated conductivity-weighted neutral wind, σ_P is the local Pedersen conductivity, u_s is the local zonal neutral wind, A and B are geometry factors, and dl is the differential along the field line [*Haerendel et al.,* 1992; *Eccles,* 1998].

The Eccles Simple Electric Field model [*Eccles,* 1998] (hereafter referred to as ESEF) is a simplified electric field model that combines a specification of the ionosphere, thermosphere density, and thermospheric winds in a single magnetic meridian to produce the low-latitude F-region electric fields using field-line-integrated quantities [*Haerendel et al.,* 1992; *Eccles*, 1998]. The ESEF model provides field-line-integrated conductivities and plasma drifts for apex altitudes from 200 to ~1000 km, based on underlying empirical models. The ESEF results have been tested against the fully global electric field model with nearly identical results for F-region plasma drifts. This simple model can be run in minutes on a single CPU computer by focusing on a single sector rather than solving the entire globe. This allows us to investigate the effects of F-region winds on the observed electric fields.

For this study we have used the International Reference Ionosphere (IRI) [*Bilitza and Reinisch*, 2008], the MSIS-90 model atmosphere [*Hedin,* 1991], and several Horizontal Wind Model (HWM) versions. The neutral wind model is of key importance

to the electric field calculation. The HWM90 [*Hedin et al.,* 1991] and HWM93 [*Hedin et al.,* 1996] versions were both used for the zonal drift calculations, but they proved to give nearly identical results. Only the HWM93 results are presented here. The new HWM 2007 version [*Drob et al.,* 2008] was also used in this study. Figure 4.14 presents the model results for the prevailing conditions of the Christmas Island observations (solid line with symbols). The two dashed lines show the computed zonal plasma drifts from the ESEF model using the HWM models without modification. The HWM93 data (long dash) provides neutral winds that drive strong eastward (positive) plasma drift early in the evening, but the rapid drop to very low drift values around midnight LST is not representative of our measurements. In contrast, the HWM07 data (short dash) maintains an eastward drift throughout the night, but the magnitude of the drift velocities is much smaller than observed.

The HWM07 winds should be appropriate for the solar minimum conditions of observations, but this study suggests that the magnitude of the zonal neutral winds are too small by half when the ESEF model drifts are compared to the Christmas Island plasma drift observations. As a simple experiment we have modified the HWM07 winds using a least-square minimization between the model and the averaged drift velocity data. It was assumed the form of the HWM07 winds in local, altitude, and latitude remained the same. The zonal winds (u_s) and northward wind (u_n) were multiplied by a factor and a constant offset was added to the scaled zonal component so

$$u_s^* = au_s + b,$$

(4.2)

$$u_n^* = au_n,$$

(4.3)

where u_s and u_n are the winds provided directly from the HWM07 model and u_s^* and u_n^* are the modified winds. The coefficients, a and b, are constants. Only the eastward wind was given an offset as an average super rotation adjustment to the zonal wind. The solid line in Figure 4.14 plots the results of the zonal plasma drifts derived from the ESEF using the optimally modified HWM07. A reasonable choice for the values of the coefficients were a = 1.5 and b = 10 m/s so the model results derived with change in magnitude of the zonal wind of the HWM07 now show good overall agreement with the Christmas Island observations except on the evening and morning reversal drifts. The values were determined by running various values for a and b, then calculating the
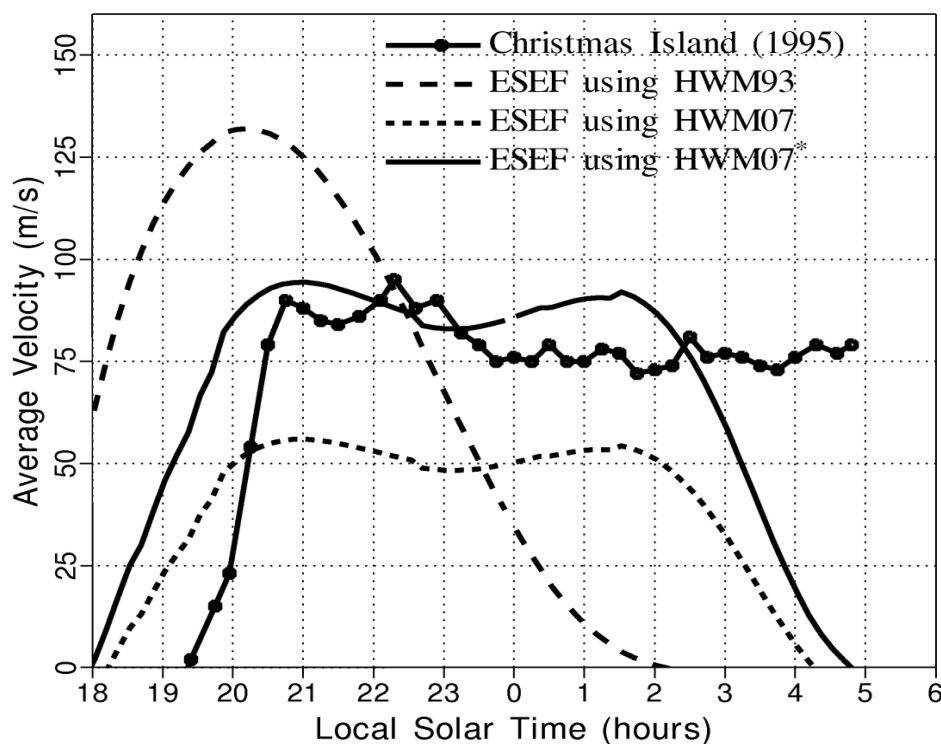
Figure 4.14. Average zonal drifts at 280 km above Christmas Island for equinox of 1995 comparing average observations with the ESEF model results using various wind models.

electric fields. The values above provided the smallest RMS error for modeled values of the zonal drifts compared to the Christmas Island nighttime drifts and the Fejer zonal drifts in the daytime. Wind motion from HWM07 does not give the accurate value on the time of the evening and morning reversal times. The magnitude of the wind motion is typically small and so we amplify its magnitude to match the drift model drift velocity.

Figure 4.15 investigates the effects of longitudinal variations in the HWM07 equatorial winds and the IGRF magnetic field on the resulting zonal plasma drifts. We model three longitude sectors: Christmas Island (200˚E), Peru (285˚E), and Brazil (320˚E). The resulting zonal drifts demonstrate that the HWM07 winds provide a basic nighttime trend similar to Christmas Island, but other longitude results do not differ significantly from the Christmas Island results even though the magnetic field declination
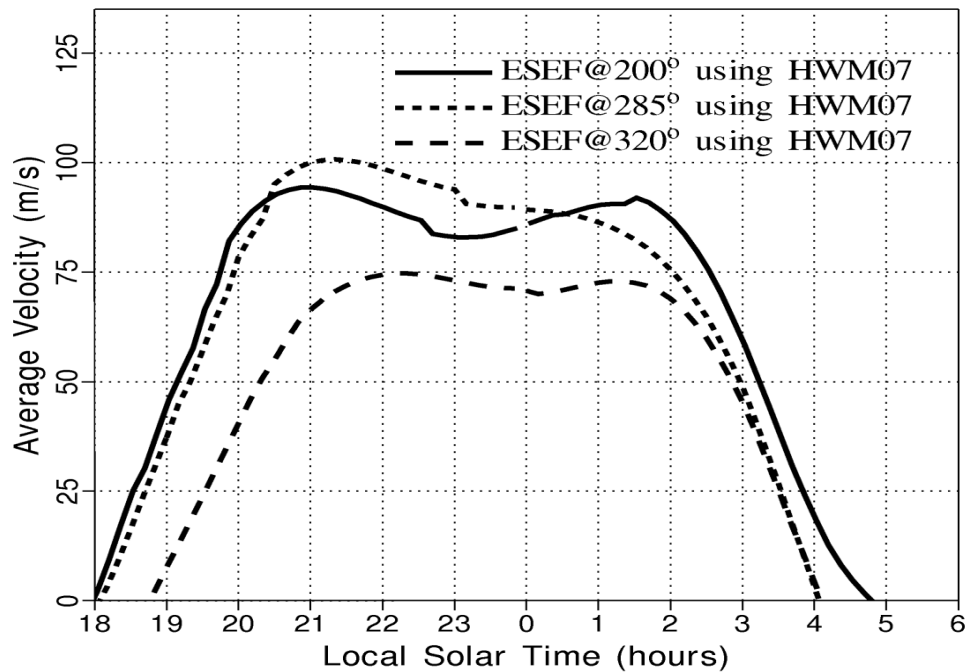
Figure 4.15. Plot of the ESEF results for three longitude sectors at Christmas Island (200˚E), Peru (285˚E), and Brazil (320˚E).

and dip equator latitude have large differences between these longitude sectors. At all longitudes the HWM07 does provide for an eastward plasma drift throughout most of the night; however, all ESEF model results indicated an earlier evening reversal in the zonal drift from westward to eastward than observed in the data from Christmas Island in the early evening. This early evening reversal is also true of the zonal drift averages of *Fejer et al.* [2005] (see Figure 4.13). The late evening reversal at Christmas Island is a puzzle, though there are only two night observations data of zonal drift velocities in the early evening local time averages. The discrepancy is most likely caused by the plasma vortex motion of the bottomside F-region plasma just after sunset [*Haerendel et al.,* 1992; *Eccles et al.,* 1999; *Kudeki and Bhattacharyya,* 1999] as discussed in section 4.4.3.

4.5.   Summary

We have presented the observations of airglow depletions from Christmas Island using all-sky images of the thermospheric OI (630.0 nm) airglow emissions. The magnetic field-aligned depletions were most likely associated with the development of EPBs and were observed on every night of the campaign. The depletions mostly developed during ~19:30-20:00 LST over Christmas Island closely consistent with previous climatological results from Jicamarca radar observations of ESF recently reported by *Chapagain et al.* [see Chapter 7]. It illustrates the active growth region of depletion was close to the west edge of the camera's FOV suggesting they were seeded to the west of Christmas Island. On several occasions, magnetic field aligned post-midnight fossilized bubble structures were seen. The number of depletions was well correlated with their initial onset times and their persistence. The spacing between structures ranged

mostly from ~150 to 250 km, which is similar to the equatorial observation from other longitudes.

Measurements of EPBs drift velocities from Christmas Island were eastward and exhibited significant day-to-day variations in their magnitudes. The average velocity peaked around 90-100 m/s approximately two hours after local sunset and remained at a nearly constant high value ~80 m/s during the post-midnight period until dawn. This post-midnight elevated eastward drift differs significantly from prior observations at other longitudes.

The ESEF drift model was used to investigate the zonal plasma drifts over Christmas Island using wind fields from existing empirical models (HWM-93 and HWM-07). The model results from the HWM07 wind model produced an eastward drift throughout the night, but their post-midnight magnitudes were much smaller than observed from Christmas Island. Using a modified HWM-07 wind field, a basic night-time trend similar to the Christmas Island was successfully obtained.

The apparent longitudinal dependence of equatorial depletions drift velocities is clearly of interest. Future studies using multiple stations at closely spaced longitudes (as recently conducted from equatorial Brazil) together with satellite observations such as those of currently being made by the US Air Force Communication/Navigation Outage Forecasting System (C/NOFS) satellite will provide crucial data for understanding the longitudinal variability.

CHAPTER 5

EQUATORIAL PLASMA BUBBLE ZONAL VELOCITY

FROM ASCENSION ISLAND

Abstract

We use OI (630.0 nm) airglow images data from Ascension Island (7.9°S, 14.4°W, dip latitude 16°S) in the South Atlantic Ocean measured by the USU all-sky CCD camera during March 20-April 7, 1997. Airglow depletions are observed only 7 out of 17 nights of measurements due to the intermittently cloudy sky during the campaign. The bubbles onsets occur in early evening hours and propagate eastward as night progresses. We examine the EPB zonal drift velocity characteristics. They exhibit noticeable day-to-day variations with the average of ~90-120 m/s eastward prior to local midnight and then they decrease around midnight and post-midnight period in good accord with previous observations from other near-equatorial sites. However, around local midnight on April 4-5, an unusual shear motion (up to 55 m/s) of the plasma bubble is seen with a reversal to westward at low latitude and eastward at higher ones. Consequently, the bubble rotates counterclockwise and tilts eastward significantly out of the magnetic field lines. The westward reversal of the drift motion probably results from a reversal in the F-region dynamo or from a large increase in the altitude of the shear in the nighttime F-region plasma drift.

5.1. Introduction

The basic characteristics of zonal plasma drift at the equatorial F-region have been presented by *Woodman* [1972] and *Fejer et al*. [1985, 1991] using Jicamarca radar

observations. They reported a typical diurnal cycle of zonal drifts of plasma that consists of westward drifts of as much as 50 m/s during the day and eastward drifts up to 120 m/s at night near solar minimum conditions resulting in a net super rotation. *Coley and Heelis* [1989] noted the average ion super-rotation velocity is greater than that for the neutral wind due to the difference between the ion and neutral wind velocities during the daytime. They further showed the local time variation of the altitude profile of the zonal drift indicates the E-region dynamo dominates the topside ion drift during the daytime, while the F-region dynamo dominates during the nighttime ion drifts and acts as the source of the electric fields driving the ion drift at low latitudes.

The post-sunset bottomside equatorial ionosphere is known to exhibit strong vertical shear in the horizontal flow at all longitudes, with plasma near the F-peak drifting rapidly eastward, while plasma at lower altitudes drifts slowly westward [e.g*., Kudeki et al.,* 1981; *Eccles et al.,* 1999]. Shear flow precedes sunset and can persist for hours afterwards [e.g., *Kudeki and Bhattacharyya*, 1999; *Hysell et al.,* 2005]. Electric field studies show the drift is usually eastward throughout the night at 200-600 km, reversing to westward near 06:00 LT [e.g., *Fejer et al.,* 1991], although reversing time depend on seasons, geomagnetic activity, and solar flux conditions. However, we observe latitudinal (or apex altitudinal) shear velocity of the bubble structures around midnight and post-midnight period from Ascension Island in the South Atlantic Ocean measured by the USU all-sky CCD camera during geomagnetic quiet and solar minimum conditions.

Mendillo and Baumgardner [1982] presented the optical image results of zonal drift velocities from Ascension Island during January-February 1981 at high solar flux

conditions. They reported airglow depletions occurred most often during 20:30-23:30 LT and drifted to the east with speeds that decreased from about 190 m/s at 21:00 LT to 80 m/s at 01:00 LT. They further noted several cases of apparently twisting, overlapping, and bifurcating depletions structures. *Basu et al.* [1999] studied a comparison of total electron content (TEC) fluctuations and scintillations at Ascension Island using GPS satellites during February-April, 1998. However, ground-based measurement of plasma depletions has not been reported in the Atlantic region during solar minimum condition.

In this Chapter, we present the plasma bubble optical signatures and the nocturnal zonal drift velocity from Ascension Island (7.9°S, 14.4°W, dip latitude 16°S) using USU OI (630.0 nm) airglow emissions measurements near solar minimum conditions. The Ascension results are compared with similar observations from Christmas Island at a longitudinal separation of ~143° to illustrate the longitudinal variations of the bubble development and propagation. In addition, we report unusual shear motion of the bubble structure observed during night of April 4-5, 1997. The bubble velocities are also compared with neutral wind velocities computed from the Horizontal Wind Model 1993 (HWM93).

5.2.   Observations

The USU all-sky CCD camera was operated at Ascension Island during 17 nights from March 20 to April 7, 1997 for the optical measurements of the ionospheric plasma depletions in the South Atlantic region. The measurement periods were often restricted during the nighttime due to the variable weather conditions and also the moon rising in the early morning hours. Therefore, the camera was often operated from early evening to

~02:00 LST. The time intervals between consecutive images were ~4-7 minutes typically resulting in 14-73 images per night. The measurements showed the plasma depletion structures were observed only on 7 out of 17 nights of the campaign due to interference of the intermittent cloud with the time series of the measurements. In several cases, the bubble structures were observed to be overlapped and bifurcated similar to the previous study reported by *Mendillo and Baumgardner* [1982] from Ascension Island.

Figure 5.1 shows a map of the location of Ascension Island in the South Atlantic Ocean, between South America and Africa. The dashed lines represent the dip latitudes at 10°S, 20°S, and 30°S. The open circle around Ascension Island represents the geographic FOV covered by the all-sky imager at assumed emission altitude of 250 km that covers the region around 10°S-24°S magnetic latitudes. An example of enlarged all-sky airglow image recorded from Ascension Island on March 27, 1997 shows the orientation of the plasma bubbles and typical structures observed in the airglow measurements. The wide dark band in the image depict the magnetic north-south aligned plasma bubble seen as the plasma depletion in the OI (630.0 nm) airglow emissions.

The all-sky images were preprocessed as explained in a previous section before they were analyzed. Each image was unwarped onto a 1500x1500 km uniform spaced geographic grid assuming an airglow emission altitude at 250 km. Depletion velocity was estimated by employing 2-D Fourier transform techniques [*Taylor and Garcia*, 1995; *Garcia et al.,* 1997] selecting pairs of consecutive images for the time binned of ~12 minutes. The motion of each bubble was measured along the various positions of its
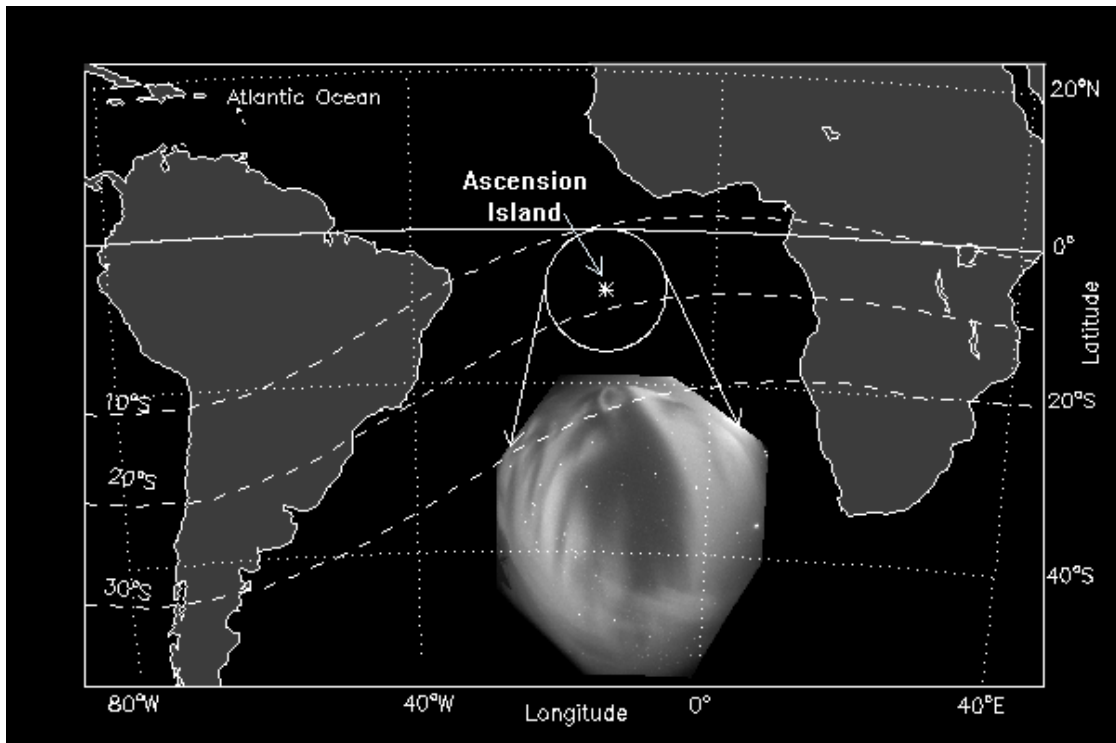
Figure 5.1. Map showing the location of Ascension Island, the field of view covered by the imager represented by the open circle assuming an emission height at 250 km, and an example of an enlarged OI (630.0 nm) airglow image.

structure. This procedure was repeated for subsequent image pairs to determine the average drift velocity of the bubble during the course of each night as a function of local solar time (LST). The difference between LST at Ascension Island and Universal Time (UT) is 56 minutes.

5.3. Results

The image data from the selective days of the campaign from Ascension Island have been used to investigate the key characteristics of the ionospheric plasma depletions.

5.3.1. Onset, Evolution, and Propagation of Plasma Bubbles

Figure 5.2 shows the initial onset times of EPBs observed inside the FOV of the camera measured by the airglow depletion signatures from Ascension Island. Since most of the nights were cloudy, we were able to calculate the onset times only 7 nights of the campaign. During most of the nights the depletions onset occurred in the early evening hour at ~19:15-20:00 LST to the west region of FOV of the camera. This result is nearly consistent with the observations from Christmas Island (as discussed in Chapter 4) and onset times of initial ESF obtained from climatological study of Jicamarca radar observations reported and discussed by *Chapagain et al.* [see Chapter 7].

Figure 5.3 shows the sequence of unwarped OI (630.0 nm) airglow images measured from Ascension Island during the night of April 4-5 from 20:00 to 02:00 LST. The figure clearly illustrates the spatial characteristics and the time evolution of the bubble structures. The left side y-axis plots the magnetic latitudes at 10°S and 20°S while
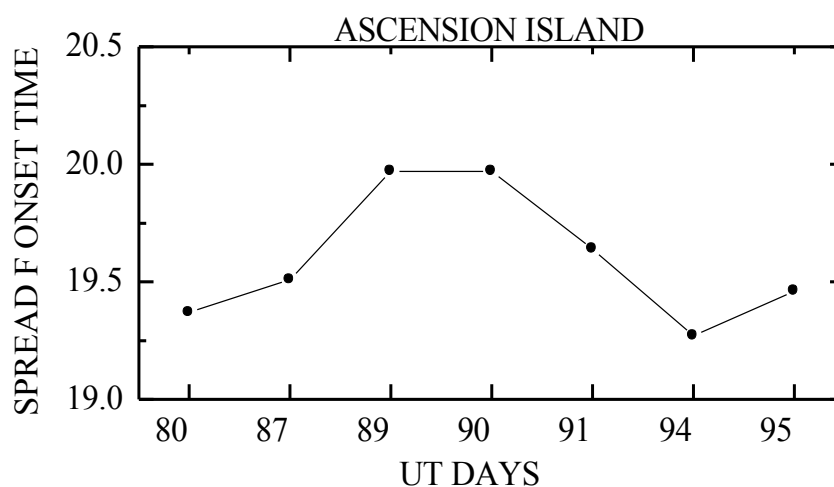
Figure 5.2. Onset times of ESF (plasma bubbles) above Ascension Island obtained from optical images from different days during the campaign.

the right side represents geographic latitude. The depletion structure initially appeared at the north-west region of the image at ~20:00 LST and then developed into a strong and matured structure over the next hour (after ~21:26 LST). They were aligned along the magnetic field lines (almost perpendicular to the magnetic latitude) and propagated eastward, as shown by the white arrows. During the post-midnight period, the bubble extended to the higher latitude beyond 20˚S dip latitude. However, the motion of the top part of the bubble structures reversed in a westward direction while the middle and bottom parts were continuously moving eastward after ~00:17 LST. Consequently, the bubbles rotated counterclockwise exhibiting the eastward tilt contrary to the westward tilt as is well-known in the literature. Regrettably, no observations data were available after 02:00 LST.

Figure 5.4 shows the keogram plot of the OI (630.0 nm) airglow emissions in west-east direction (positive eastward) from Ascension Island (top) on April 4-5, 1997, and compared with Christmas Island result (bottom) on September 28-29, 1995. Both measurements were carried out under similar low solar flux conditions using the same USU CCD camera. These plots compare the equatorial spread F activity observed in the OI (630.0 nm) airglow emissions from Ascension Island and Christmas Island. The dashed lines in the plots demarcate the central rows and columns used for creating the keogram. The figures illustrate that several bubbles (represented by dark bands) were evolved inside the FOV of the camera and propagated eastward as indicated by arrows with different magnitudes of the velocities as shown by the slopes. The slopes of the bubble paths from Ascension Island around midnight and the post midnight period show
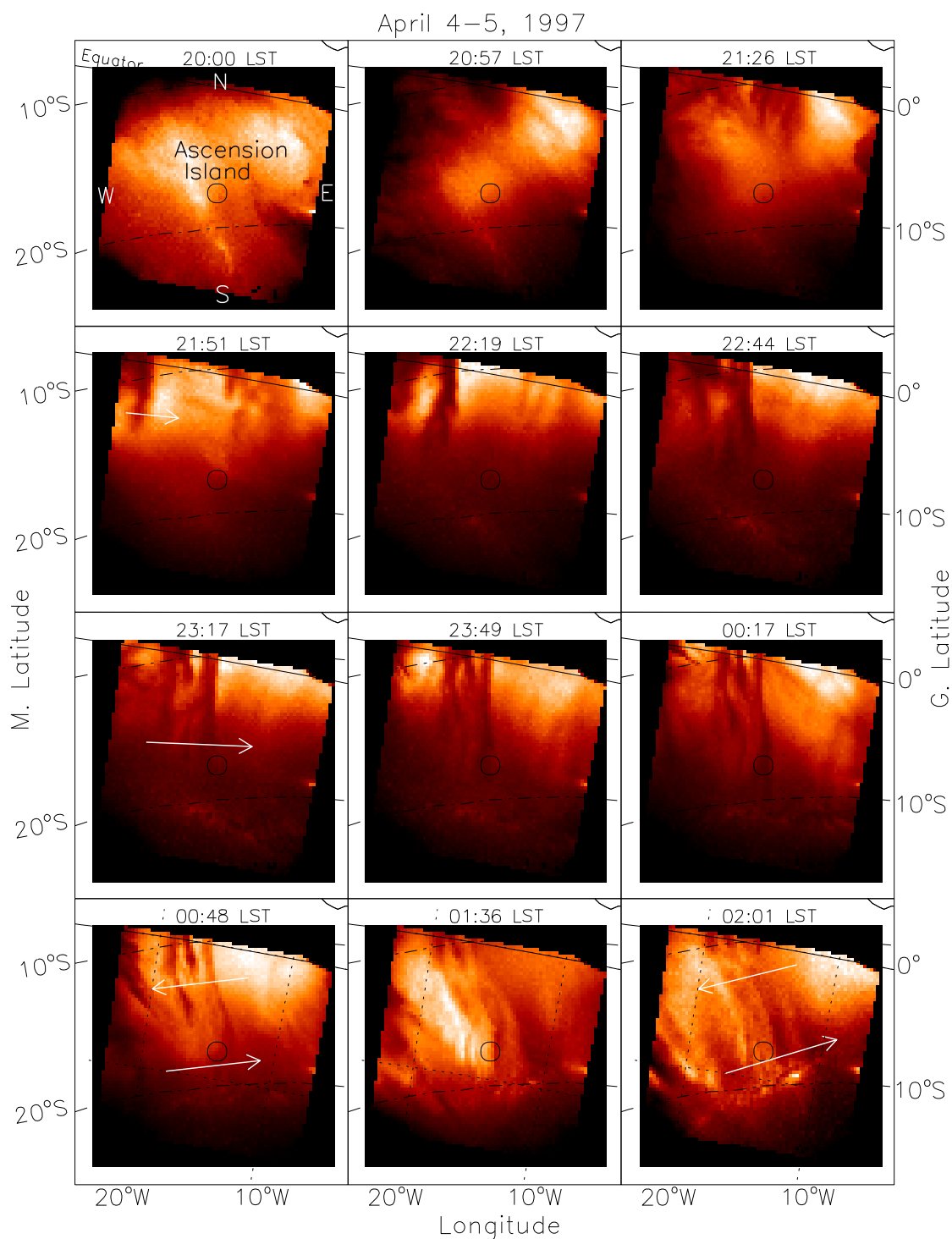
Figure 5.3. Sequences of all-sky unwarped OI (630.0 nm) airglow images showing spatial characteristics and the time evolution of ionospheric plasma bubbles over Ascension Island during 20:00- 02:00 LST on April 4-5, 1997. The images have been projected onto 1500×1500 km geographic grid at an assumed altitude of 250 km.
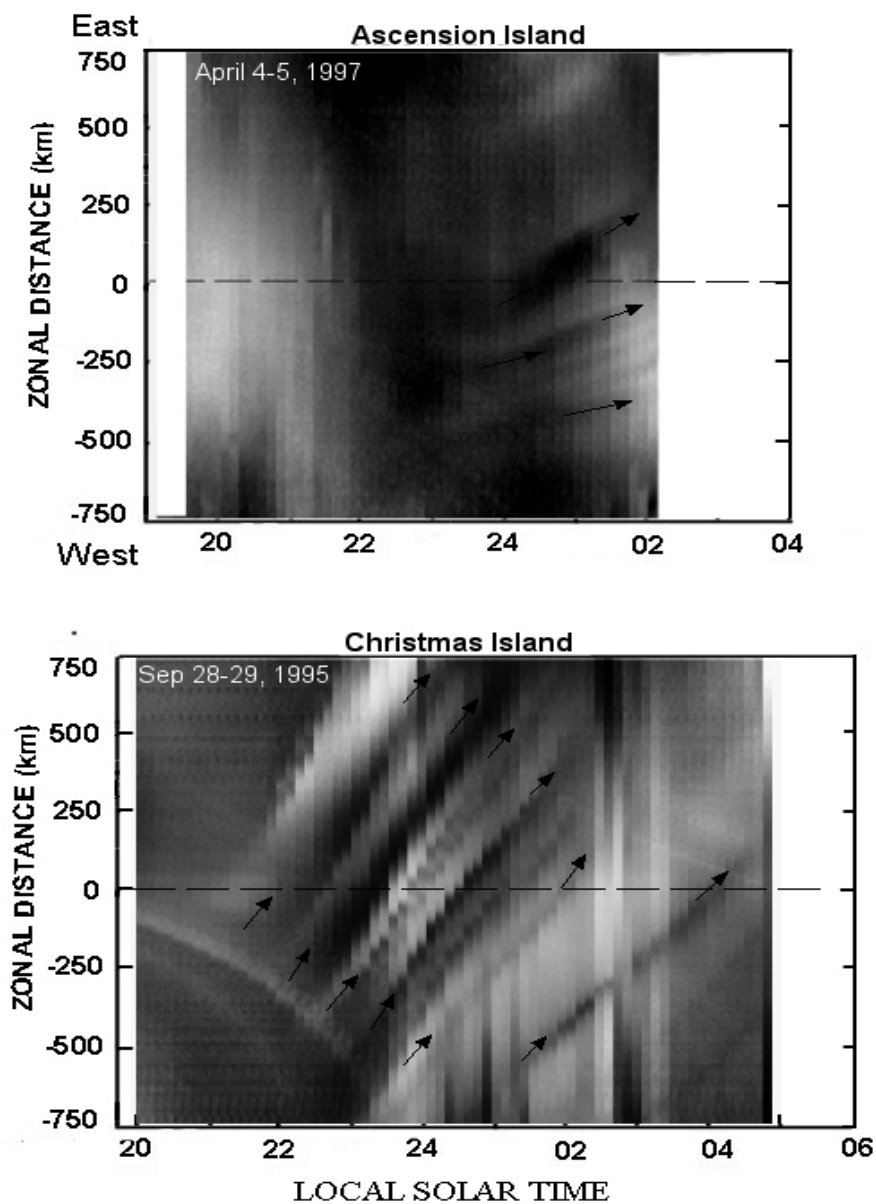
Figure 5.4. Keogram plots of the nighttime OI (630.0 nm) airglow emissions in west-east (positive eastward) direction from Ascension Island (top) and Christmas Island (bottom). The dark bands represent plasma bubbles and arrows indicate their direction of motions.

they were moving with smaller drift velocities, while the bubble paths from Christmas Island were nearly linear with large slope values, which illustrates they were moving with high and steady velocities during the course of the night.

5.3.2. Plasma Bubble Zonal Velocity

The nocturnal plasma bubble zonal velocities were calculated using the embedded depletion structures (bubbles) visible in OI (630.0 nm) airglow images. The method used to estimate the velocity was discussed in detail in Chapter 4. Figure 5.5 displays the average plasma bubble velocities as a function of local solar time during six nights of campaign, considering a reference altitude of airglow emissions at 250 km. The measurements were restricted from early evening to prior to 02:00 LST due to the limitation in the camera operations caused by moonlight in the early morning hours (after ~02:00 LST). In Figure 5.5, the vertical bars on each plot are the standard deviation in the measurement uncertainty from the mean. The missing data points in the figure are mainly due to the interference from clouds. The average solar flux index (F10.7 cm) during the measurements periods was 75. The average value of $<K_p>$ in each plot represents the three hourly geomagnetic activity index averaged over 9-hour period (13:30-22:30 LST) prior to about six hours of the local sunset during which ESF onset may be affected by the geomagnetic activity. However, all days were magnetically quiet with minor activity (Kp < 3 except on March 29-30).

Figure 5.5 illustrates the significant day-to-day variability in the bubble zonal drift velocities. The velocities generally increased during the early evening periods, peaked at ~21:00-22:00 LST, and decreased around and after the local midnight (except on March

27-28, where, the velocity decreased steadily). However, on March 20-21, 29-30, and March 30-April 1, the data were limited due to a cloudy sky during the campaigns. On April 4-5, the average velocity decreased to a very small value (~8 m/s) during post-midnight with large variations in the bubble velocities, as shown by the plots of the standard deviations. On April 5-6, the bubble velocity rapidly decreased to ~10 m/s prior to 22:45 LST and then the bubble faded out.

Figure 5.6 summarizes the plasma bubble zonal velocities during seven nights of the campaign. The line plots the average velocity of all data sets as a function of local solar time and the vertical bars are the standard deviation from the mean. The scattered data (also from large values of standard deviations) particularly during the pre-midnight period indicate large day-to-day variations in the magnitude of the bubble velocities in the range of ~10-125 m/s. The average velocity peaked to ~100 m/s at around 22:15 LST, decreased as the night progressed, and became minimum to ~10 m/s at ~02:00 LST.

To put our results into context with other measurements under similar low solar flux conditions, Figure 5.7 compares the average EPBs zonal velocities from Ascension Island with other results from Christmas Island, previous optical observations from Alcantara, Brazil (2.3°S, 44.5°W, dip latitude 1.3°S) [*Taylor et al.,* 1997], and average zonal wind velocity obtained from Horizontal Wind Model-93 (HWM-93) at 250 km altitude over Ascension Island. The wind model velocities were calculated during the same time periods and days as those of the plasma bubble velocities measurements from Ascension Island. The Ascension result is nearly consistent with the result from Christmas Island during early evening hours (prior to ~22:15 LST), but largely deviated
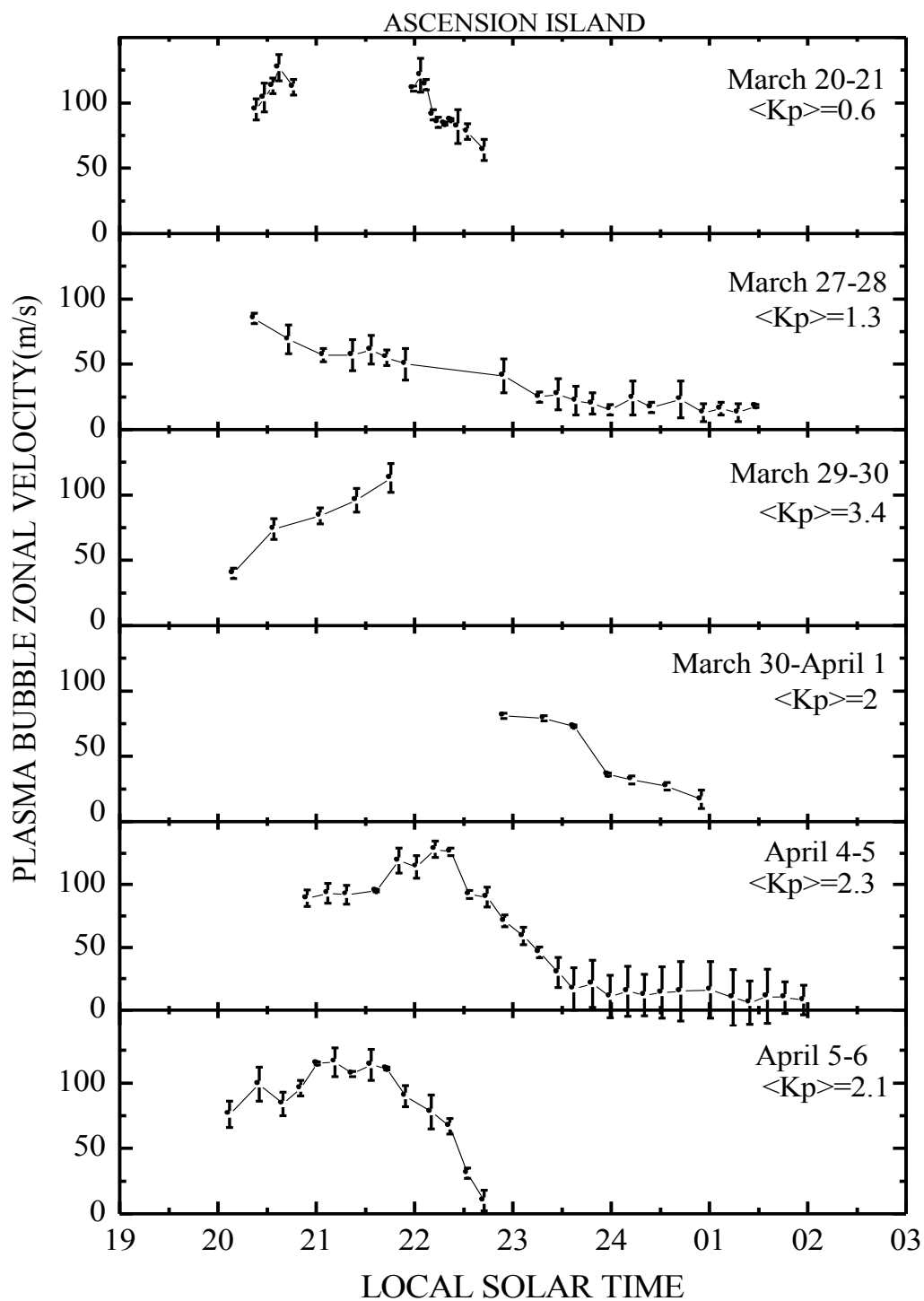
Figure 5.5. The average plasma bubble zonal velocities calculated from two successive images during six nights of the campaign considering a reference altitude of airglow emissions at 250 km.
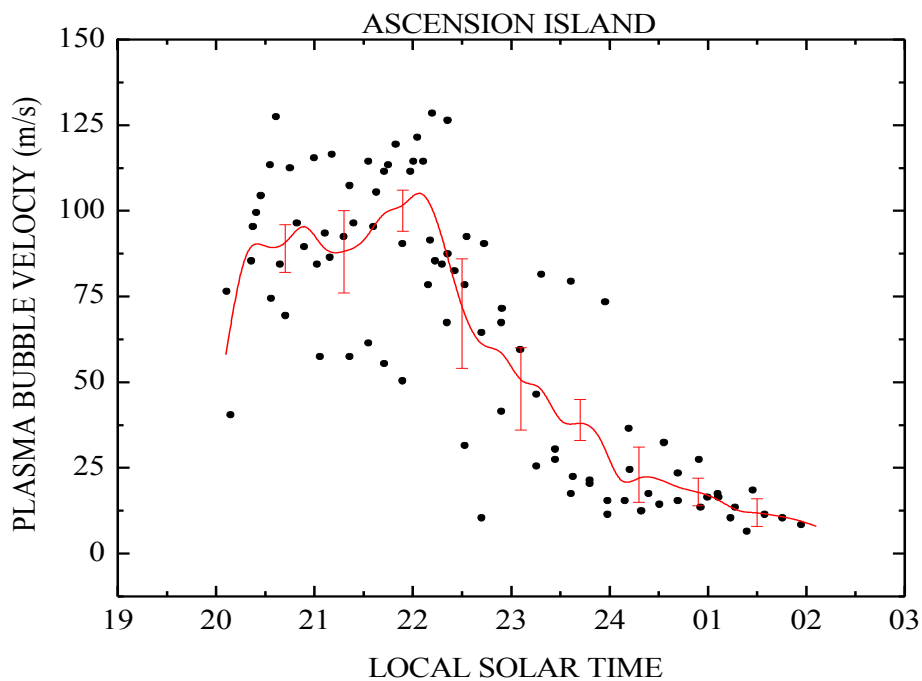
Figure 5.6. Scatter plot of the plasma bubble zonal velocities over Ascension Island during seven nights of campaign. The solid line represents the average velocity and vertical bars are the standard deviation from the mean.
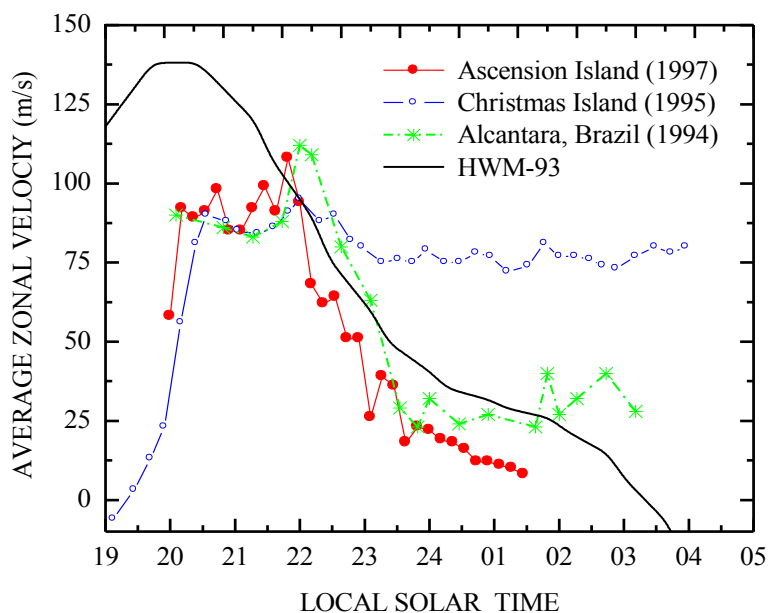
Figure 5.7. Comparison of the average airglow depletion zonal velocities from Ascension Island with Christmas Island, previous results from Alcantara, Brazil (re-plotted) [*Taylor et al.,* 1997], and zonal wind velocity from HWM-93 over Ascension Island.

during the post midnight period. Moreover, the Ascension result is closely consistent with the Alcantara result while the data during post-midnight period from Ascension Island were insufficient for the comparison. The observed bubble motion and wind motion from HWM93 have similar trends of the local time variations but the magnitude of the bubble drift is smaller than that of the wind velocity.

5.3.3. Shear Velocity of Plasma Bubble

The apex altitude (H_{apex}) of the dipole field line that passes through the airglow emission layer is calculated by using the following equation [*Sobral et al.,* 2009]:

$$H_{apex} = \frac{R_E + H_E}{\cos^2 \lambda} - R_E \, , \tag{5.1}$$

where R_E (= 6370 km) is the radius of the Earth, H_E is the airglow emissions altitude (~250 km), and λ is the dip latitude of the place.

The range of apex altitudes mapped above the magnetic equator estimated using the above equation varies from ~500 to 1600 km within the geographic latitude (~0°S-15°S) and longitudes (7°W-22°W) around Ascension Island. Figure 5.8 shows the apex altitude mapping over Ascension Island for corresponding geographic latitudes and longitudes covered by the FOV of the camera at 250 km altitude.

Figure 5.9 presents the plasma bubble zonal velocity as a function of local solar time during the night of April 4-5, 1997. The velocities v_1, v_2, and v_3 were estimated from top (~0˚S-5˚S), middle (~5˚S-10˚S), and the bottom (~10˚S-14˚S) parts of the bubble structure from unwarped images that correspond to the apex altitudes ~500-800 km, ~800
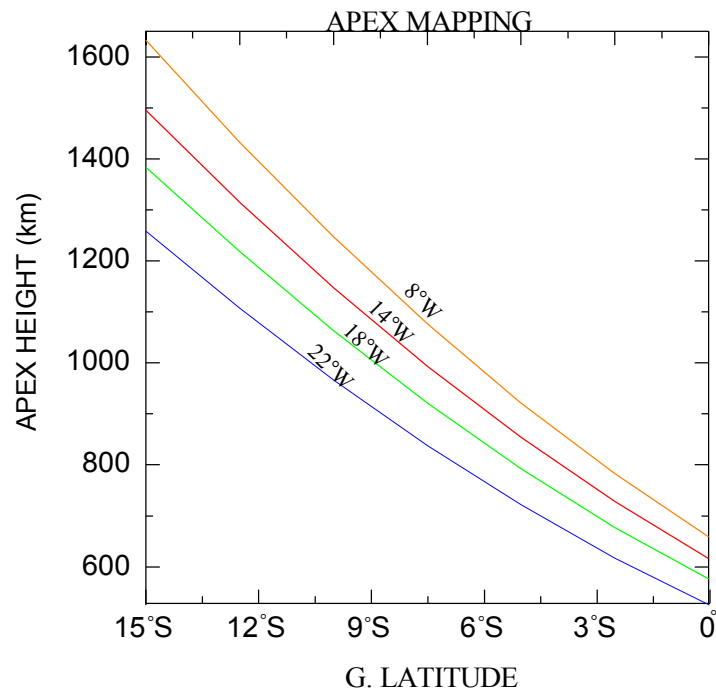
Figure 5.8. Apex mapping over Ascension Island for corresponding latitudes and longitudes covered by the FOV of the all-sky imager.

-1100 km, and ~1100-1400 km, respectively. Prior to ~23:30 LST, the bubble propagated almost with the same velocities across its latitudes, while around and after local midnight (~23:30-02:00 LST) they exhibited significant shear motions with velocities v_1, v_2, and v_3 with latitude variations (or apex altitudes) as shown in Figure 5.9. Here velocities, v_1 corresponds to westward motion with magnitude up to 20 m/s, v_2 and v_3 indicate eastward motion of magnitudes ~10-20 m/s and ~40-50 m/s, respectively. Due to this shear motion, the bubble titled eastward contrary to the previous result of westward tilt commonly reported in the literatures [e.g., *Zalesak et al.,* 1982; *Makela,* 2006]. On the other hand, the wind motion during the same night derived from HWM93 is eastward throughout the night.
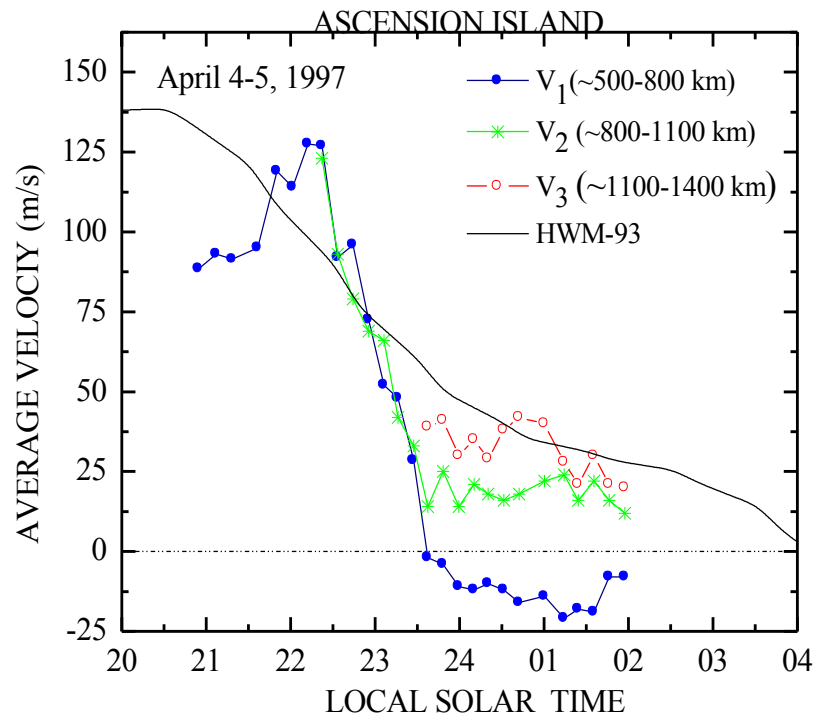
Figure 5.9. Plasma bubble shear velocity over Ascension Island on April 4-5 illustrating latitudinal shear velocity.

In order to understand the difference in the behavior of bubble propagation with wind motion, we present a contour plot of the zonal neutral wind motion as a function of local solar time and latitudes within the region covered by the FOV of the camera over Ascension Island at 250 km altitude (see in Figure 5.10). The data were computed from the HWM93 on April 4-5, 1997. Figure 5.10 shows the velocity is larger during pre-midnight, peaks at ~22:00 LST, and then decreases during the post-midnight period. The latitudinal gradient in the neutral winds is clearly seen, but reverses during premidnight and post-midnight periods. The wind exhibits eastward motion in the range of ~60-160 m/s with a decrease from low to higher latitude, while the post-midnight wind motion have smaller values of about 10-60 m/s with increasing from low to higher latitude. Our
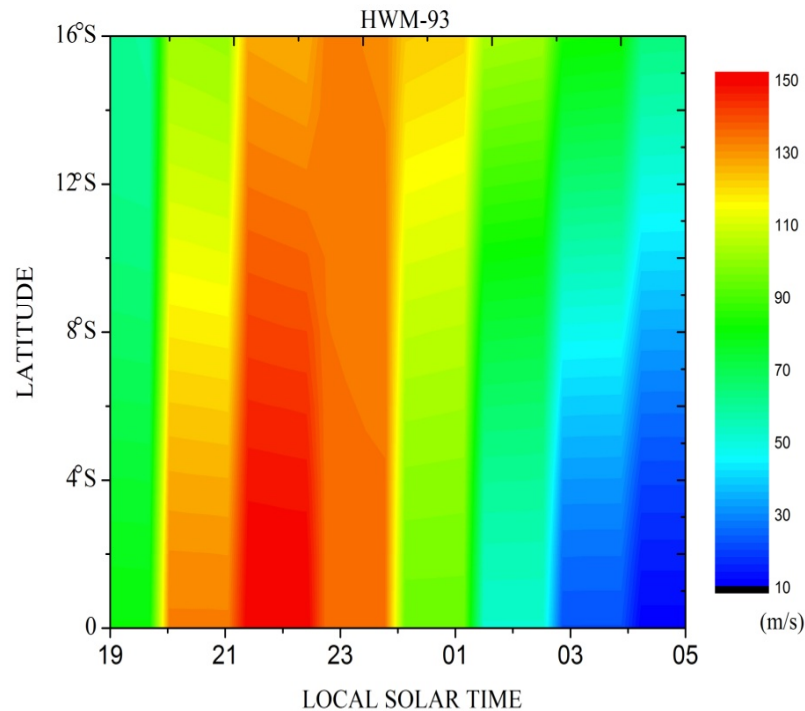
Figure 5.10. Contour plot of eastward wind velocity as a function of local solar time and latitudes covered by the FOV of camera over Ascension Island at 250 km altitude. The data were derived from Horizontal Wind Model (HWM-93).

observations during the post-midnight period also show the bubble drifts eastward at higher latitudes while it reverses westward at lower latitude.

5.4. Discussion

The plasma bubble zonal drift velocities from Ascension Island increase during early evening and peak to ~90-110 m/s at around 21:00-22:00 LST. The velocity then decreases around the local midnight and post midnight period in a similar trend to previous studies reported from a number of sites near the equatorial regions [e.g*., Fejer et al.,* 1991; *Taylor et al.,* 1997; *de Paula et al.,* 2002; *Martinis et al.,* 2003; *Pautet et al.,* 2009]. The local time dependence of the average velocities from Ascension Island and

Alcantara, Brazil, are similar and follow the same trend of average wind velocity as shown in Figure 5.7. However, the differences in post-midnight results between Ascension Island and Christmas Island (see Figure 5.7) are possibly due to the latitudinal and longitudinal variations of the zonal drift velocities as reported by previous studies [e.g., *Martinis et al.,* 2003; *Immel et al.,* 2004; *Jensen and Fejer,* 2007; *Pautet et al.,* 2009; see also Chapter 4]. The velocity measurements from these two stations correspond to the different latitudes (or apex altitudes). *Martinis et al.* [2003] and *Pimenta et al.* [2003b] also showed ion drag from equatorial ionosphere anomaly cause thermospheric neutral wind and therefore, plasma drift velocities decrease with latitudes. This may be one of the possible reasons that cause smaller post-midnight zonal drift velocities over Ascension Island than from Christmas Island.

The unusual shear motion of the plasma bubble, westward at low latitudes and eastward at higher latitudes, exhibits the eastward tilt of the structure as shown in Figure 5.3, contrary to the trend of westward tilts commonly referred to the literature (e.g., *Woodman and LaHoz*, 1976; *Zalesak et al.,* 1982; *Makela,* 2006). The westward reversal of the plasma bubble velocity at low latitude (i.e., low apex altitude) during quiet geomagnetic conditions probably resulted from a reversal in the F-region dynamo or from a large increase in the altitude of the shear in the nighttime F-region plasma drift, which would be caused by varying factors coupled into the equatorial F-region from the low-latitude ionosphere. *Taylor et al.* [1997] have also reported the westward motion of the plasma bubbles from Alcantara Brazil, during the magnetically moderate condition. They argued the drift reversal at the lower altitude is possibly due to the altitude profile of the

zonal drift with a strong eastward flow at F-region altitudes and weaker westward flow below the F-ledge. The competing E- and F- region dynamo create the shear winds, which are directed oppositely near sunset [*Haerendel et al.,* 1992]. At altitudes above F-peak, the field-line-integrated Pedersen conductivity is dominated by F-region, so the F-region dynamo controls the drifts. On the other hand, E-region dynamo dominates below the F-peak. The altitude of shear rises and falls with F-region ionosphere.

The OI (630.0 nm) airglow layer of 250-300 km might generally lie above the shear so the depletions drift eastward. One might suggest the shear may have moved above the airglow region causing depletion to move westward during the anomalous westward drifts near midnight. The Ascension Island lies on the region of equatorial anomaly and airglow layer located in the altitude region of the west-east shear drifts, which probably would be the reason for the westward bubble motion. *Valladares et al.* [2002] have also reported latitudinal gradients in neutral winds could be responsible for the effects observed in their comparisons of equatorial zonal winds and scintillations drifts. Winds do indeed have latitude dependence due to ion drag forces imposed by the latitude structure of the equatorial ionospheric anomaly.

Heelis et al. [1974] also modeled the height variation of the east-west drifts. Their results show large shears in the zonal drifts at 23:00 and 24:00 LT, with the eastward drifts decreasing slowly with altitude above the F-region peak, and westward drifts at the lower altitudes. *Fejer et al.* [1985] reported the average drifts decrease slightly with altitude above 600 km, and there is a noticeable decrease of the eastward drifts at lower altitudes. *Huba et al.* [2009] examined the effect of zonal neutral winds on the dynamics

and morphology of ESF using HWM93 and HWM07. They reported the dynamics and morphology of ESF bubbles depend strongly on the zonal neutral wind. From the simulation result, they showed the plasma bubble is distorted in the west-east direction because of the neutral wind and Pedersen conductance. For the constant neutral wind case, the bubble is vertical up to 600 km and then has a westward tilt. For the HWM07 case, the bubble has an eastward tilt at low altitude (below ~500 km) and then displays a weak tilt to the west.

5.5. Summary

Airglow depletions from Ascension Island were observed only 7 out of 17 nights of the campaign due to interference of the intermittently cloudy sky during the measurement periods. Initially the plasma bubble onsets occurred inside the FOV of camera at ~19:15-20:00 LST over Ascension Island, which is close consistent with results from Christmas Island and Jicamarca radar observations of ESF.

The average eastward plasma bubble velocities from Ascension Island were typically 90-110 m/s during premidnight and they decreased in the post-midnight period to ~10 m/s in good accord with observations from other near equatorial sites. However, on April 4-5, the latitudinal shear drift velocity was observed up to ~55 m/s after local midnight while exhibiting westward motion at lower latitudes (i.e., at apex altitudes ~500-800 km) and eastward at higher latitudes (i.e. at apex altitudes ~800-1400 km). Consequently, the bubble rotated counterclockwise and aligned significantly off the magnetic meridian and tilted to the east. On the other hand, the neutral wind motion computed from HWM-93 were eastward throughout the night.

Optical data from multi-stations with overlapping FOV are needed to corroborate the latitudinal dependence of the plasma depletions. Simultaneous measurements of plasma bubble drifts and wind motions under magnetically quiet and disturbed conditions will lead to a better understanding of the shear velocity. As explained by *Huba et al.* [2009], the correlative study between observational data, numerical simulation and effects of the zonal wind would provide a more comprehensive picture of the morphology and dynamics of the EPBs.

CHAPTER 6

SIMULTANEOUS OBSERVATIONS OF IONOSPHERIC PLASMA

DEPLETION OVER BRAZIL DURING THE

SPREAD *F* EXPERIMENT[2]

Abstract

The Spread *F* Experiment (SpreadFEx) campaign was conducted at several sites in Brazil using a variety of instruments during the moon down period from September to November, 2005 in support of the NASA Living with a Star program. The campaign was divided into two phases for two consecutive moon down periods from September 22-October 9 (17 nights), and October 28-November 9, 2005 (18 nights). During the campaign, a USU all-sky CCD camera deployed at São João d'Aliança (14.8˚S, 47.6˚W, dip latitude ~10.5˚S), near Brasilia, and the Brazilian all-sky CCD camera at Cariri (7.4˚S, 36˚W, dip latitude ~9.6˚S) simultaneously observed the evolution of the ionospheric plasma bubbles in the OI (630.0 nm) airglow emission and the mesospheric gravity wave field. The two sites were approximately the same magnetic latitude, but were separated in longitude by ~1500 km. Plasma bubbles were observed on almost every clear sky night during the campaign. The combined datasets from two sites provided important information for characterizing the ionospheric depletions during the campaign. Measurements of the drift velocities at both sites are in good agreement with

---

previous studies; however, the overlapping fields of view revealed significant differences in the occurrence and structure of the plasma bubbles, providing new evidence for localized generation. Moreover, the airglow depletion velocity is compared with coincidence measurements of the GPS scintillation drift on a typical day from Brasilia. Both airglow images and GPS scintillation measurements give consistent estimates of the eastward drift over the same time period.

6.1. Introduction

ESF irregularities are generated at the bottomside of the F-layer by the post-sunset enhancement of the electric field (PRE) caused by the influence from the F-region dynamo in conjunction with the conductivity gradient across the solar terminator [*Rishbeth,* 1971; *Heelis et al.,* 1974; *Batista et al.,* 1986; *Fejer et al.,* 1999; *Abdu,* 2001]. It is believed ESF development depends mainly on the linear growth rate for generalized Rayleigh-Taylor instability process [*Dungey,* 1956], the flux tube integrated Pedersen conductivity that controls the nonlinear development, and density perturbations that are needed to act as a seed to trigger the instability growth. These density perturbations may be produced by different seeding sources such a local variations in the vertical winds, electric fields, and gravity waves propagating upward from the troposphere [*Singh et al.,* 1997; *Abdu,* 2001]. *Kudeki et al.* [2008] have also suggested the F-region zonal wind just after sunset plays a crucial role in controlling the structuring of bottomside F-region plasma and subsequent EPB development. However, the seeding sources of ESF are the least understood and observational evidence is limited yet.

The main goal of the SpreadFEx campaign was to investigate the properties of gravity waves at ionospheric heights and their potential role in seeding Rayleigh-Taylor instabilities, strong equatorial spread *F,* and plasma bubble development. The campaign was conducted in Brazil during the equinox period (September–November 2005). Several Brazilian and US institutes utilized a broad range of instruments, including all-sky imagers, digisondes, photometers, meteor/VHF radars, and GPS receivers to cover a large area of eastern Brazil where ESF is a common occurrence. A detailed overview of the SpreadFEx campaign goals and measurements is given by *Fritts et al.* [2009].

This Chapter summarizes the optical image measurements of EPBs from SpreadFEx campaign from two neighboring sites at Brasilia and Cariri with overlapping field of view. We present the plasma bubble drift velocities from Brasilia and the coincidence measurements from Cariri. The drift velocities of the bubble structures corresponding to different apex altitudes are calculated for a typical day to ensure the shear drift velocity with altitudes. The campaign also provided co-located GPS observations from Brasilia deployed by Purdue University, Indiana, to study the onset of plasma depletions and their evolution as they traversed the sky during the night. Comparisons between the OI (630.0 nm) airglow data and GPS data demonstrated the ability of the compact dual frequency GPS array to detect the plasma bubbles and retrieve reliable propagation characteristics of the depletions [*Haase et al.,* 2011].

6.2. Data Analysis

In this study, all-sky images of the OI (630.0 nm) airglow from a CCD camera were obtained at Brasilia and Cariri, Brazil, from September 22 to November 7, 2005 for

24 nights. Out of 24 nights, the depletions were observed during 17 nights from Brasilia and 19 nights from Cariri whereas other nights were cloudy and rainy. Due to local weather conditions, only eight of these nights were common to both sites' observations and occurred on September 24-25, 28-29, 29-30, September 30-October 1, October 1-2, 26-27, 27-28, and November 6-7. However, good quality data sets of the depletions were observed only during five common nights from both stations. These data sets were used for comparative study between the two stations and provided important information for characterizing the depletions and provided the opportunity to study a unique longitudinal variation [*Pautet et al.,* 2009]. For a detailed comparison of depletions visible from two stations, two common night observations during September 30-October 1 and October 1-2 were analyzed.

Figure 6.1 shows a map of Brazil with the locations of the two observation sites at Brasilia and Cariri in Brazil. The OI (630.0 nm) airglow unwarped images from two sites show the field of view covered by the two airglow imagers (1500×1500 km) assuming an emission height of 250 km. The dark bands on the images are the bubble structures aligned along the magnetic field lines. The two sites are ~1500 km apart in approximately the same magnetic latitude. The dashed lines in the map represent dip equator, dip latitudes at 10°S, and 20°S. The field of view covered by the two imagers overlapped each other so the plasma bubbles generated over one site can be tracked on the other site by the next imager continuously. This configuration was helpful for novel comparison of the longitudinal difference in generation, characteristics, and the evolution of the plasma bubbles during the nighttime.

The OI (630.0 nm) images have been analyzed to determine the evolution, structure, and propagation of the plasma bubbles and their variability during the course of the night. Before measuring the characteristics of plasma bubbles, the raw images were first preprocessed. The method of the image processing similar to the methods employed from other measurements as discussed in a previous chapter. The drift motions of the depletions were measured by selecting four consecutive images for individual bubbles around the zenith center of the images and then estimated the averaged velocity for the
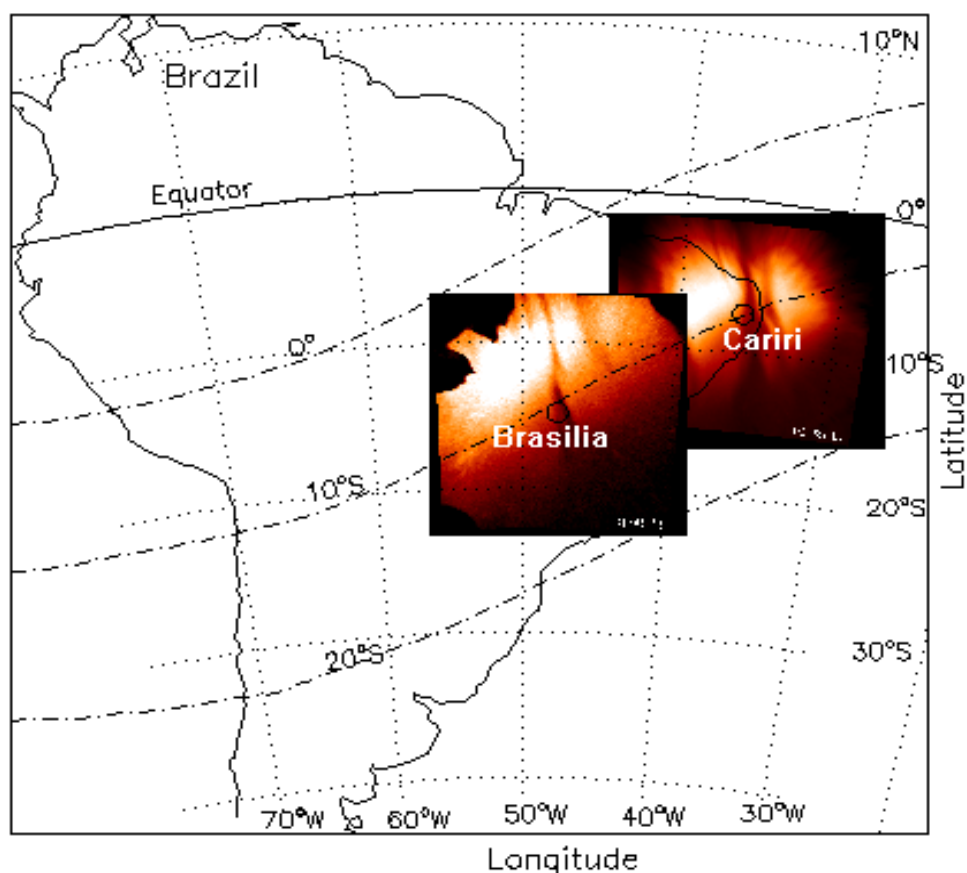
Figure 6.1. Map of Brazil and the all-sky imagers locations during the SpreadFEx campaign. The OI (630.0 nm) airglow unwarped images from Brasilia and Cariri represent the field of view covered by the imagers of area 1500×1500 km assuming an airglow emissions altitude of 250 km.

corresponding times. The time difference between Local Solar Time (LST) and Universal Time (UT) from Brasilia is 03:10 hours and from Cariri is 02:26 hours.

6.3.   Results and Discussion

The images data obtained from simultaneous measurements from two neighboring stations have been used to investigate the longitudinal variations of the evolution, development and propagation of equatorial plasma bubbles, and their zonal drift velocities.

6.3.1. Overview of EPB Evolution, Development, and Propagation

The configuration of two cameras along the same magnetic latitudes with overlapped field of view allowed the comparison of the longitudinal variability of the plasma bubble generation, characteristics and evolution. For detail analysis, two common night (September 30-October 1 and October 1-2) observations from two stations were considered. On these nights, the all-sky image camera from Brasilia was operated in a higher temporal mode where sequential images of the OI (630.0 nm) structure were obtained every 2-4 minutes, while from Cariri, measurements were made every 4-7 minutes. The sequential images during these common night observations from two sites show the following different characteristics of the plasma bubble evolution and development.

Figure 6.2 shows the sequence of the OI (630.0 nm) airglow image data collected half an hour from Brasilia and Cariri during the nights of September 30-October 1, 2005. This night was typical of the several nights of coincident image measurements. The

figure presents the depletion structures from two sites corresponding to the same local solar time. The dashed lines in the figure represent the magnetic latitudes drawn at 0˚, and 10˚S, as shown in the left side of the y-axis. (Note, the right y-axis represent geographic latitudes.) In the images, the dark bands are the plasma bubbles. The white arrows represent the direction of the propagation of the plasma bubbles. The measurements were made from early evening to early morning up to ~10 hours during 18:52-04:36 LST (22:02-07:46 UT) from Brasilia and during 18:45-04:37 LST (21:11-07:03 UT) from Cariri. However, the plasma depletions were observed during a couple of hours in the post-sunset period. A weak depletion structure first appeared at ~20:00 LST from Brasilia, as shown in the figure near the top region of the image and then started to develop the strong multi-bubble structures after ~21:00 LST. On the other hand, the depletion from Cariri was initially observed at ~21:00 LST, about an hour later than from Brasilia, and then developed into multi-structured bubbles as time progresses. The bubbles grew in size and numbers over the next couple of hours from initial depletion occurrence, which displays a broad set of bubble structures across both images.

The depletion structures were exhibiting extensive magnetic north-south alignment with similar structure pattern from both stations. They were seen to move from the Brasilian field of view into the Cariri one in a coherent manner. This reveals the bubbles generated in Brasilia, or from its west side, can propagate eastward and cross into the Cariri region. The direction of the propagation of the bubbles is shown by the white arrows in the figure. Some of the bubbles were decayed between the region of Brasilia and Cariri. From both sites, the depletion structures started to fade out after local mid-
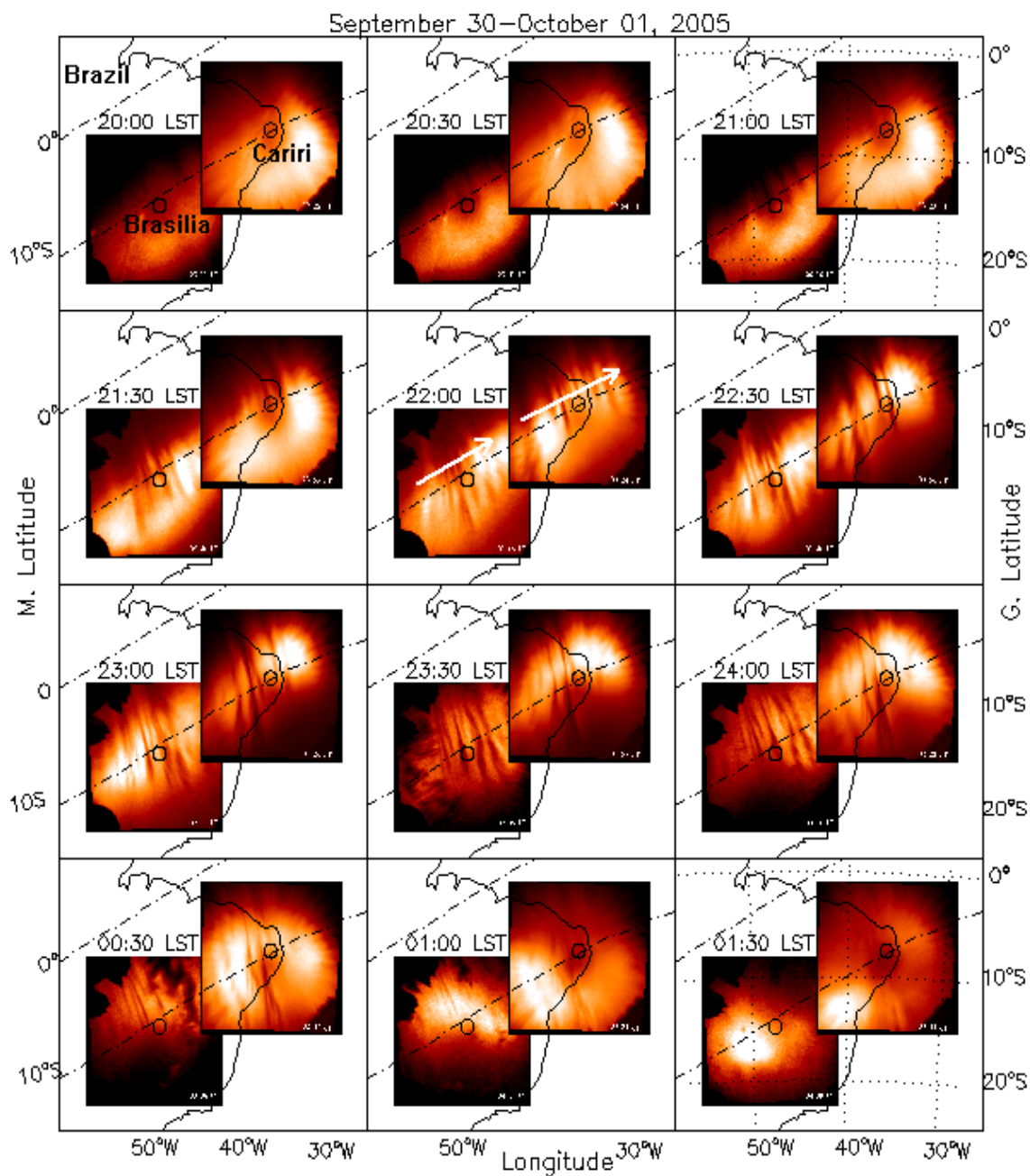
Figure 6.2. The sequences OI (630.0 nm) airglow images from simultaneous measurements from Brasilia and Cariri on intervals of every half hour during September 30-October 1, 2005. The dashed lines represent magnetic latitudes at 0˚ and 10˚S (left axis) and the geographic latitudes are denoted on the right axes.

night and then disappeared after ~01:30 LST.

Figure 6.3 shows the bubble displays for the sequences of OI (630.0 nm) airglow images on the following night (October 1-2) at an interval of every half hour from Brasilia and Cariri. The image data were obtained during 19:02-05:00 LST from Brasilia and 19:04-04:44 LST from Cariri. The figure presents the depletion structures from two sites corresponding to the same local solar time. During this night, the bubbles evolutions were quite different from one site to the other.

The depletion structure was first detected from Cariri at ~19:30 LST and from Brasilia at ~21:00 LST, one and one-half hour later than from Cariri. When the bubbles were in a mature phase from Cariri (20:30 LST), no evidence of depletion was observed from Brasilia. At ~21:30 LST, the sky was dominated by a single bubble that appeared over Brasilia and evolved into the double structures that passed over the observation site and eventually exited the camera's field of view, approximately two hours later. The main depletion grew significantly as it moved into the field of view from west to east. At about 23:00 LST, the depletion was visible from both sites, and had started to slow down. Shortly thereafter (after about midnight), the depletion over Brasilia was fading out while the depletion to the east over Cariri remained evident until dawn (~04:00 LST). However, later at ~01:00 LST, a pair of fossilized bubbles entered the Brasílian field of view from the west and remained till the dawn (~05:00 LST) showing the evidence of the post-midnight depletion structures. During this night, the initial depletion onset occurred at different times from these two stations. In addition, the depletion from Cariri were multi-
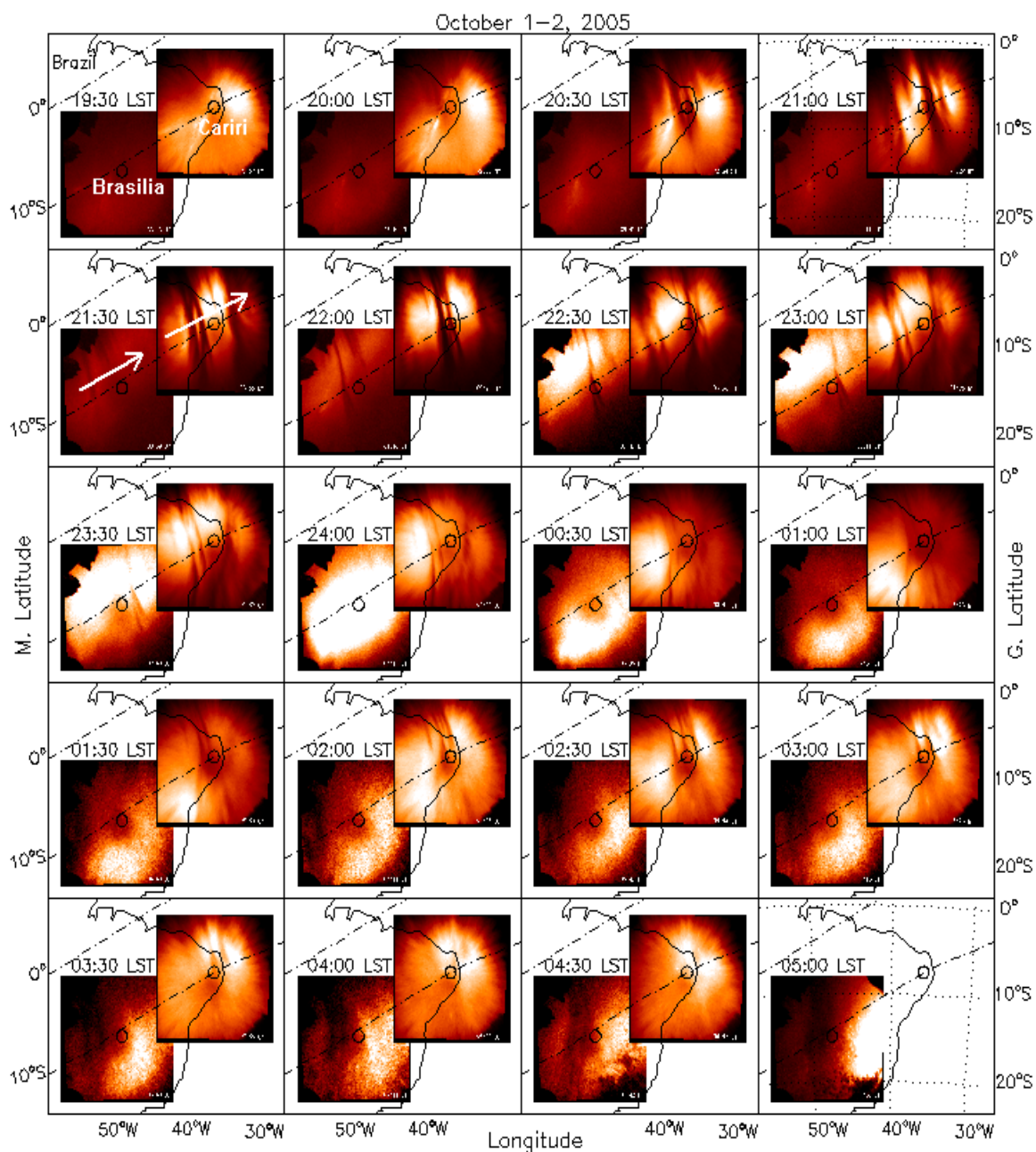
Figure 6.3. The sequences OI (630.0 nm) airglow images from simultaneous measurements from Brasilia and Cariri on intervals of every half hour during October 1-2, 2005. The dashed lines represent magnetic latitudes at 0˚ and 10˚S (left axis) and the geographic latitudes are denoted on the right axes.

structures that were stronger than those from Brasilia, which illustrate the variability of the EPBs onset and their morphology from these neighboring stations.

Figure 6.4 shows the keogram plot in the west–east direction representing an overview of the spread *F* activity observed during the nighttime OI (630.0 nm) emission from Brasilia (top) and Cariri (bottom) during the two consecutive nights of September 30-October 1 (left) and October 1-2 (right), respectively. Here, the intensity from an east-west cross-section through the airglow images is plotted as a function of local solar time.
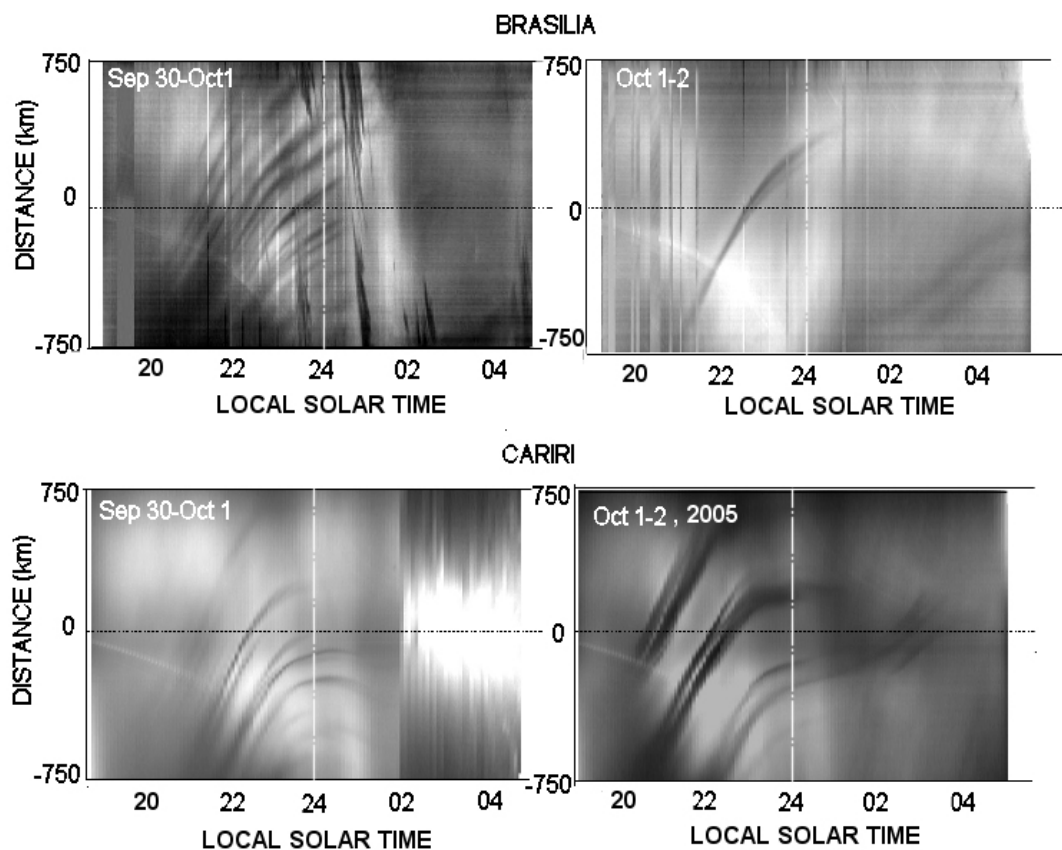
Figure 6.4. Keogram plots of the nighttime OI (630.0 nm) airglow emissions in west-east (positive eastward) direction from Brasilia (top) and Cariri (bottom) during the nights of September 30-October 1 (left) and October 1-2 (right), respectively. The dark bands are the plasma bubbles and their slopes give the depletion velocities [*Pautet et al.,* 2009, Figure 8].

In this plot, a coherent structure with dark linear features in the keogram representing plasma bubbles travels nearly from west to east. Their slopes correspond to the bubble velocities. The curved bands after about local midnight indicate a decrease in the velocity as the depletion moves to the east.

Figure 6.4 also illustrates the difference in depletion features from two consecutive nights from Brasilia and Cariri. The depletions were initially seen at ~20:00 LST and 21:00 LST on September 30-October 1, and at ~21:00 LST and ~19:30 LST on October 1-2 from Brasilia and Cariri, respectively. Over Brasilia, several bubbles were observed during the night of September 30–October 1, while just a single bubble occurred during the following night (October 1-2). The keogram summarizing the Cariri data shows the multi-bubble structures on two consecutive nights, but with different patterns. The plots illustrate similar patterns of the bubble structures on September 30-October 1 from two sites, while on the following night (October 1-2), the different pattern of the structures was seen from these stations. On September 30-October 1, their speed decreased as they propagated towards the post-midnight period and then disappeared after ~02:00 LST from both stations. From Cariri, the band structures have the negative slopes shortly after the local midnight illustrating the westward motion of the bubbles. On October 1-2, the post-midnight depletions were seen as a pair of dark bands in the bottom right corner of the keogram from Brasilia till the dawn, end of the measurement period (at ~05:00 LST), while from Cariri, depletion was observed continuously from premidnight to the dawn (~04:00 LST).

To further investigate the influence of gravity waves on the EPB generation, we have also determined the horizontal scale sizes of the structures observed in the ionospheric irregularities during this campaign. These bubble irregularities growing under Rayleigh-Taylor instability mechanism spread into a wide spectrum of scale sizes [*Haerendel,* 1973] from a few tens of meters to hundreds of kilometers. Figure 6.5 is a histogram plot showing the distribution of the separations between adjacent depletion structures observed from Brasilia and Cariri. Although significant fine scale structures are evident in the image data due to often rapid evolution of the smaller features, they were not always easy to track, and we have limited the horizontal scale sizes in the histogram
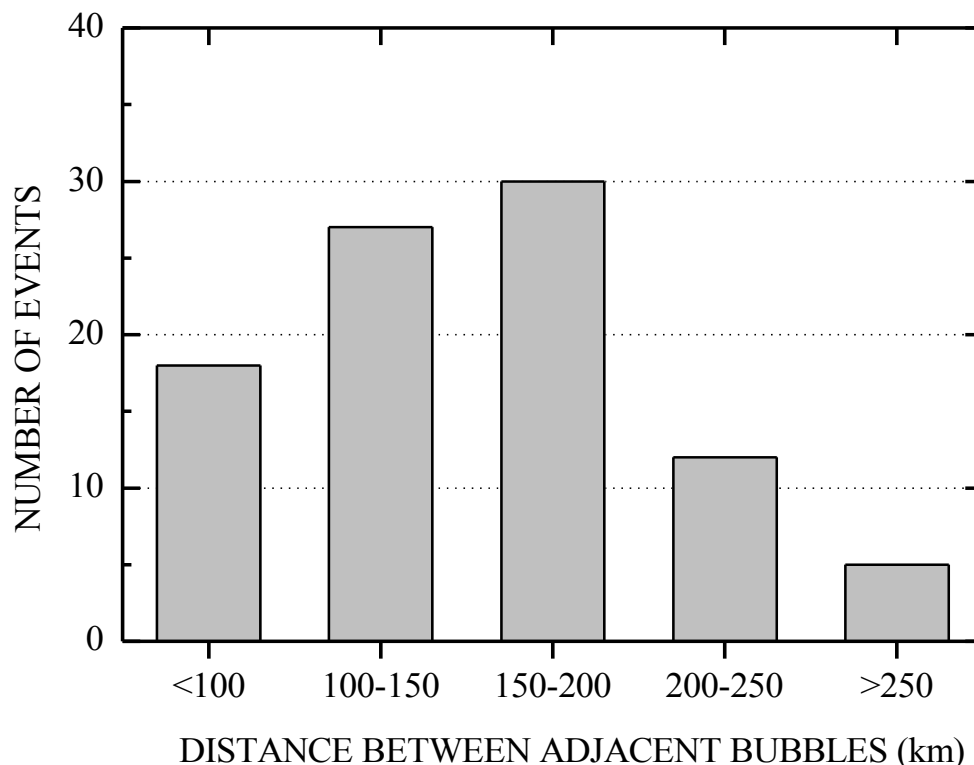
Figure 6.5. The distribution of the average separations between two consecutive plasma bubble structures observed from Brasilia and Cariri [*Pautet et al.*, 2009 Figure 10].

plot to greater than 50 km in this measurement. The majority of the bubbles exhibited separation of 100 to 200 km. *Takahashi et al.* [2009] studied the possible correlation between horizontal wavelength of the gravity waves observed while they were propagating through the MLT layer and the size of the structures of the plasma irregularities. Their results suggest a significant correlation between the observed ionospheric bubble scales and the mesospheric gravity wave horizontal wavelengths.

6.3.2. Plasma Bubble Zonal Velocity

The plasma bubble zonal velocity as a function of local solar time was measured using the embedded depletion structure visible in OI (630.0 nm) airglow images. Figure 6.6 shows the plasma bubble zonal velocities for several consecutive bubble structures during the night of September 30-October 1 over Brasilia (top panel) and Cariri (bottom panel). The bold lines represent the averaged velocity of the bubbles in the corresponding times. The example of airglow image is also shown in the upper panel from Brasilia where B_1, B_2, B_3, B_4, etc., are bubble numbers. The bubble velocity overlaps well, which gives the trend of change in velocity with local solar time. The bubble velocities increase during the pre-midnight period from ~21:00 to 22:00 LST up to 150 m/s from both sites and then decreases around midnight and the post-midnight period as the time progresses. The velocity decreases to ~10 m/s from Brasilia while from Cariri it decreases to a relatively lower value with a reversing to the westward direction to ~9 m/s at ~24:30 LST.

The same procedure was used to determine the average bubble velocities during all other nights of the campaign. Figure 6.7 shows the local time dependence of the

average plasma bubble zonal velocities calculated from four successive images for time binned to ~16 minutes during 12 nights of campaign from Brasilia considering a reference altitude of airglow emissions at 250 km. The vertical bars are the standard deviations from the mean. Bubble velocities from Cariri are also plotted (as represented by the lines without symbols) during the five common night observations on September 29-30, September 30-October 1, October 1-2, October 26-27, and October 27-28. The missing data points in the plots are either due to interference from clouds or due to the
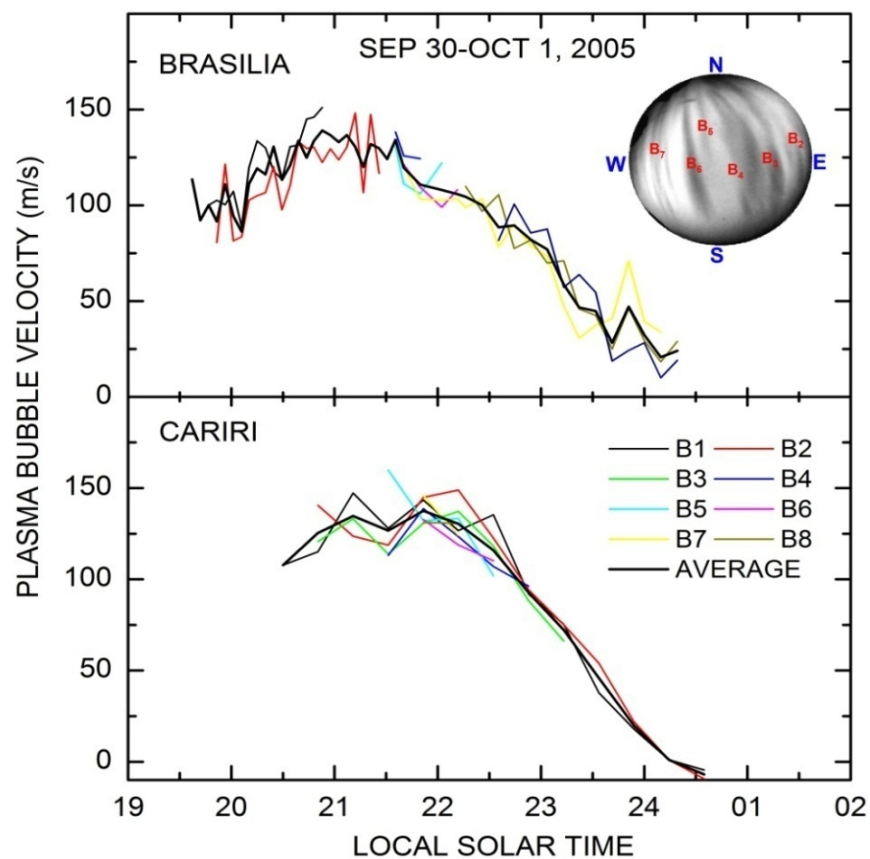
Figure 6.6. The zonal velocities of individual bubbles during the night of September 30-October 1 from Brasilia (top) and Cariri (bottom). The bold lines represent the average velocity of the bubbles. B_1, B_2, B_3, … etc. are bubble numbers on the airglow image.

fading out of the depletions. K_p represents the average of the three hourly geomagnetic index over a nine-hour period (13:30-22:30 LST) prior to six hours to local sunset as explained in the previous chapter. All days are geomagnetically quiet in the period prior to midnight with minor activity ($K_p < 3$). The average solar flux value (*F10.7* cm) during the campaign days is 75.

Figure 6.7 also illustrates the day-to-day variations of plasma bubble zonal velocities. The velocities generally increased in early evening from ~19:00 to 22:00 LST, and peaked around 21:00 LST during most of the nights. The velocities decreased as the time progresses toward the post-midnight period. The velocities obtained during the common nights of observations from the two sites are in good agreement except on October 27-28. The data during this night from Cariri were for a short period of time, which is insufficient to generate conclusive results. Moreover, the post-midnight enhancements of the zonal velocities of EPB were observed on October 1-2 from both sites, while on September 30-October 1, the enhancement was seen only from Cariri.

In general, the results from the two sites are in good agreement with zonal plasma drifts from previous ground-based measurements in equatorial regions during solar minimum conditions [e.g., *Fejer et al.,* 1991; *Taylor et al.,* 1997; *Valladares et al.,* 1996, 2002]. In most cases, the post-midnight depletions were probably due to the fossilized bubbles that exhibited no growth, moving through the FOV (e.g., *Basu et al.,* 1978). The post-midnight enhancement events are more frequent during solar minimum condition [*Fejer et al.,* 1991]. However, we do not have sufficient data during the post-midnight time to analyze in detail and make conclusive results.
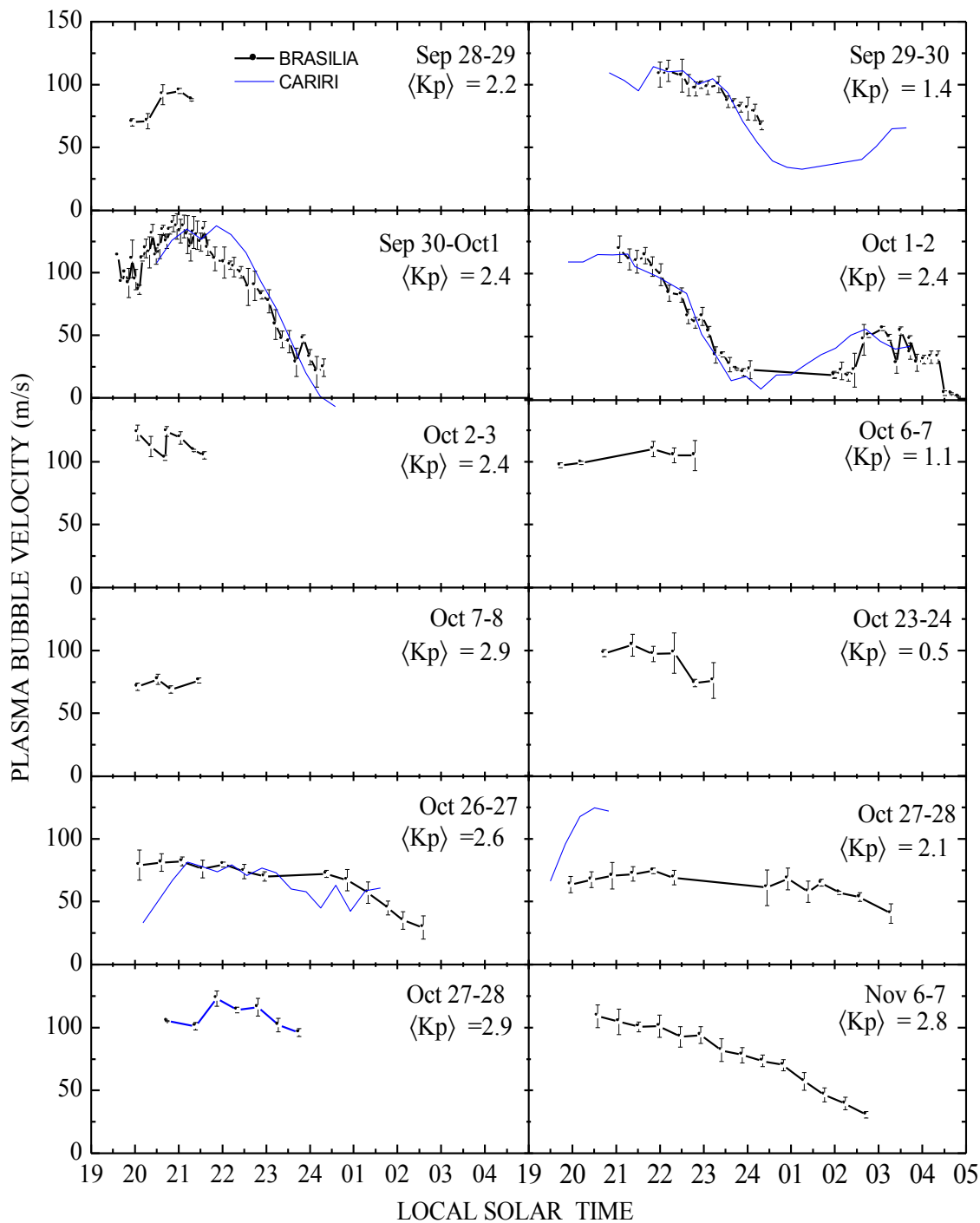
Figure 6.7. Average plasma bubble zonal velocities calculated from four successive images for time binned ~16 minutes during 12 nights of campaign from Brasilia and simultaneous measurements of five nights from Cariri. $\langle K_p \rangle$ index represents geomagnetic activity averaged over nine-hour period.

Figure 6.8 shows the superposition of average bubble zonal velocities over Brasilia (top-panel) and Cariri (lower-panel) during five common nights of simultaneous depletion observations. Most of the nights, the velocities at both sites were similar with a maximum of ~75-130 m/s around 21:00 LST, followed by a steady decrease over the next 2-3 hours. The post-midnight bubbles were weak, drifting to the east with a maximum up to 50-60 m/s around 03:00-04:00 LST, and slowed down and faded out just before sunrise. Moreover, the zonal velocities during the later phase of the campaign (October 26-27 and October 27-28) were initially significantly lower than in the first phase with a maximum of ~75 m/s and they also moved eastward and faded out later in the time period between about 02:00-03:00 LST. It is interesting to notice that the zonal velocity from Cariri on September 30-October 1 was westward (~9 m/s) shortly after local midnight and then it immediately disappeared. A similar westward motion of the plasma depletion has been reported by *Taylor et al.* [1997] using data from Alcantara, Brazil. They argued this westward motion possibly may be due to a temporary reversal of the nocturnal F-layer dynamo electric field.

Figure 6.9 shows the correlation between the airglow depletion zonal velocities observed over Brasilia and Cariri at the same local time during the nights of September 30-October 1 (top panel) and October 1-2 (lower panel). The results show very good agreement between these two measurements on each night with correlation coefficient of 0.95 and 0.90, respectively. The velocities during the night of September 30-October 1 are very similar with more consistency at higher values (greater than ~100 m/s). During the following night (October 1-2), pre-midnight bubble velocities are slightly larger from
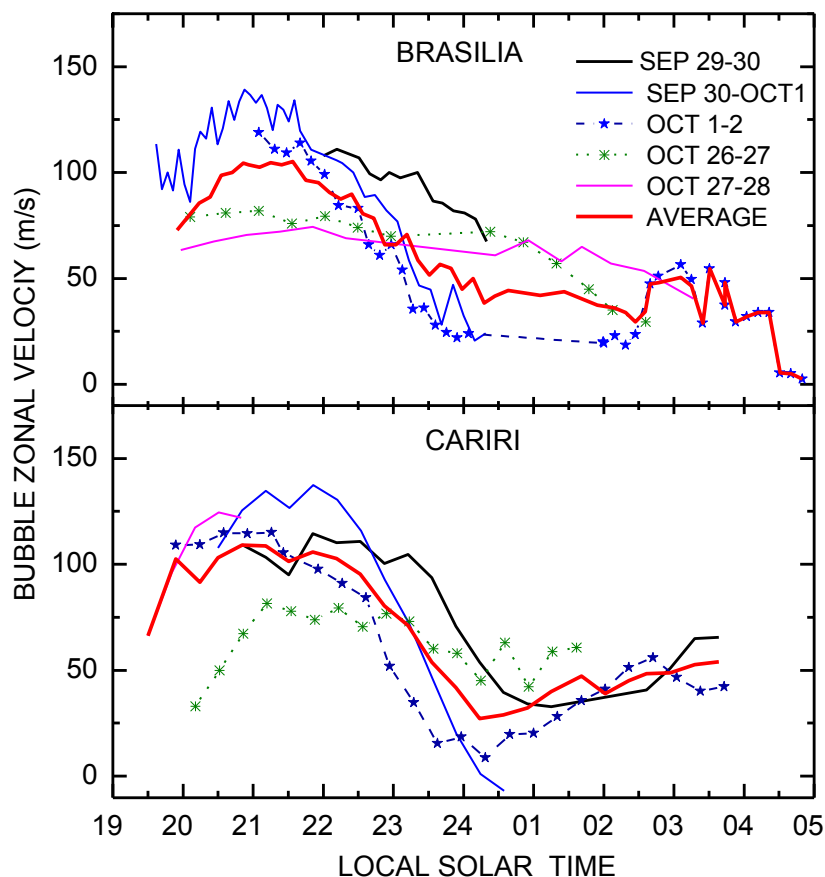
Figure 6.8. The plasma bubble zonal velocities during the common nights from Brasilia (top) and Cariri (bottom). The bold lines represent the average velocity of the bubbles.

Brasilia (~125-150 m/s) than from Cariri (~100-125 m/s), while the post-midnight velocities from Brasilia are much smaller than from Cariri.

Figure 6.10 shows the scatter plot of the plasma bubble zonal velocities during 12 nights of campaign from Brasilia. This plot illustrates large day-to-day variability in the bubble velocities ranging from ~65 to 140 m/s, (as indicated by standard deviation with vertical bars) during the pre-midnight period whereas the post-midnight velocities were much more consistent. The trends of velocity changes with local solar time were similar
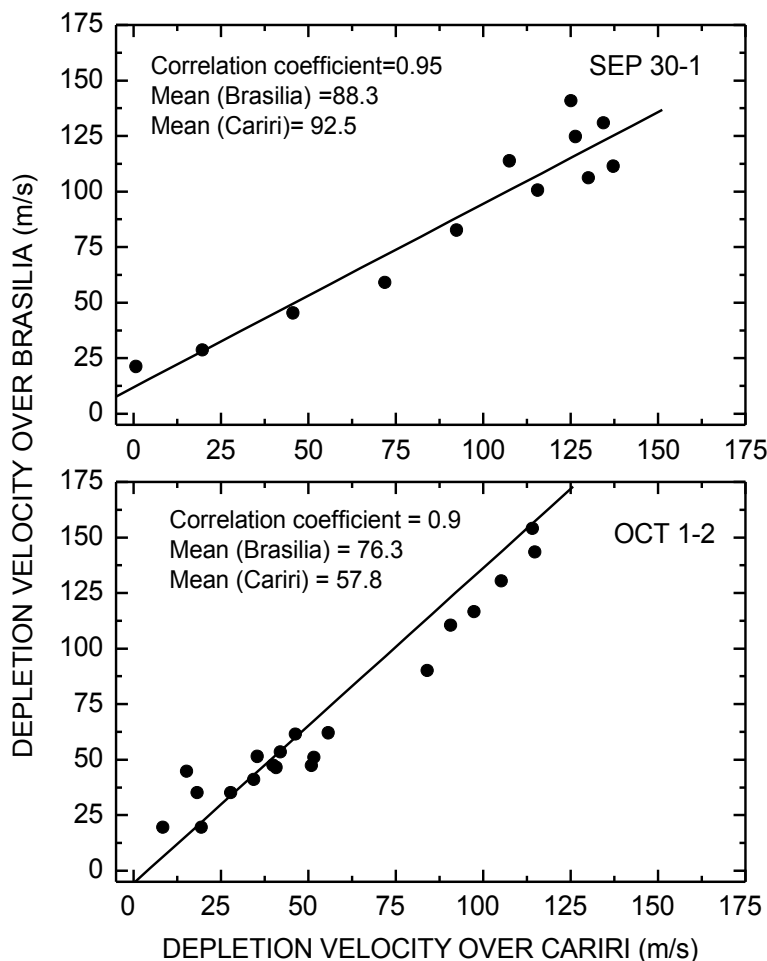
Figure 6.9. The correlation between the plasma bubble velocities from Brasilia and Cariri during the nights of September 30-October 1(top panel) and October 1-2 (lower panel) [*Pautet et al.,* 2009, Figure 9].

during all nights. They decreased as local solar time progressed toward the midnight and post-midnight periods. The curve plot is the average velocity of all data sets on the corresponding times.

For comparison, the averaged plasma bubble zonal velocities from Brasilia and Cariri are plotted in Figure 6.11 with the previous observations from the NASA, Guara campaign at Alcantara, Brazil (2.3˚S, 44.5˚W) [*Taylor et al.,* 1997] and an empirical model
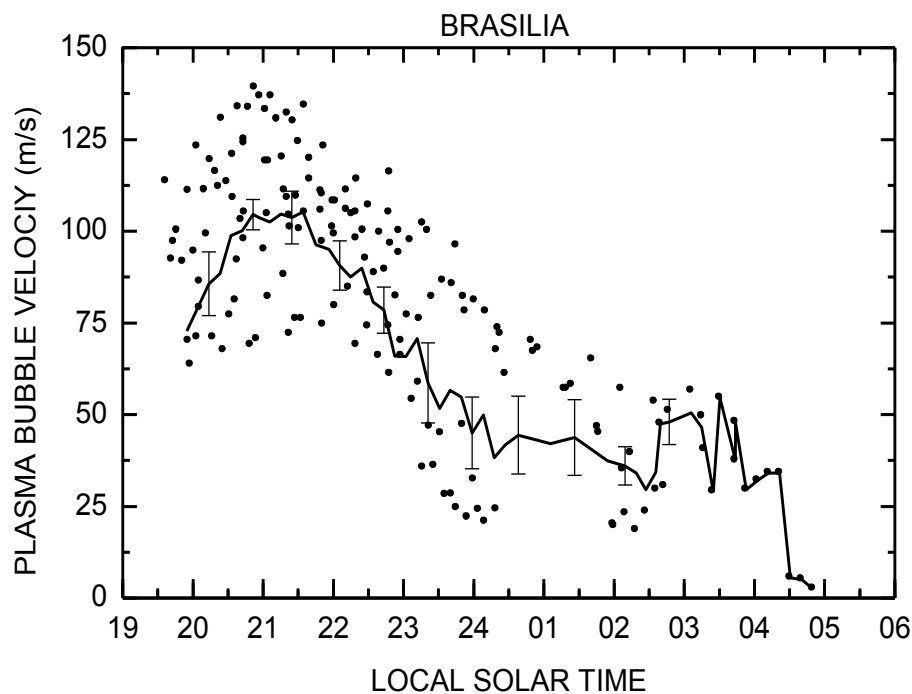
Figure 6.10. The superposition of plasma bubble zonal velocities from Brasilia during all nights of the campaign. Curve plot represents the averaged velocity derived from all nights, and vertical bars are the standard deviation from the mean.

derived from incoherent scatter radar measurements from 1968 to 2003 during solar minimum condition from Jicamarca (12˚S, 76.9˚W), Peru [*Fejer et al.,* 2005]. The local time dependence of the zonal velocities from Brasilia and Cariri are similar with a previous campaign from Alcantara, Brazil, and also with Jicamarca model results. The results are very consistent, particularly, during the pre-midnight period, and show similar magnitude and temporal variation. The average peak velocity during pre-midnight period from Brasilia and Cariri is about 110 m/s, and which is consistent with other previous results [e.g., *de Paula et al.,* 2002; *Pimenta et al.,* 2003a]. However, the occasional post midnight fossilized plasma bubbles observed causes our results to deviate (by about 10-
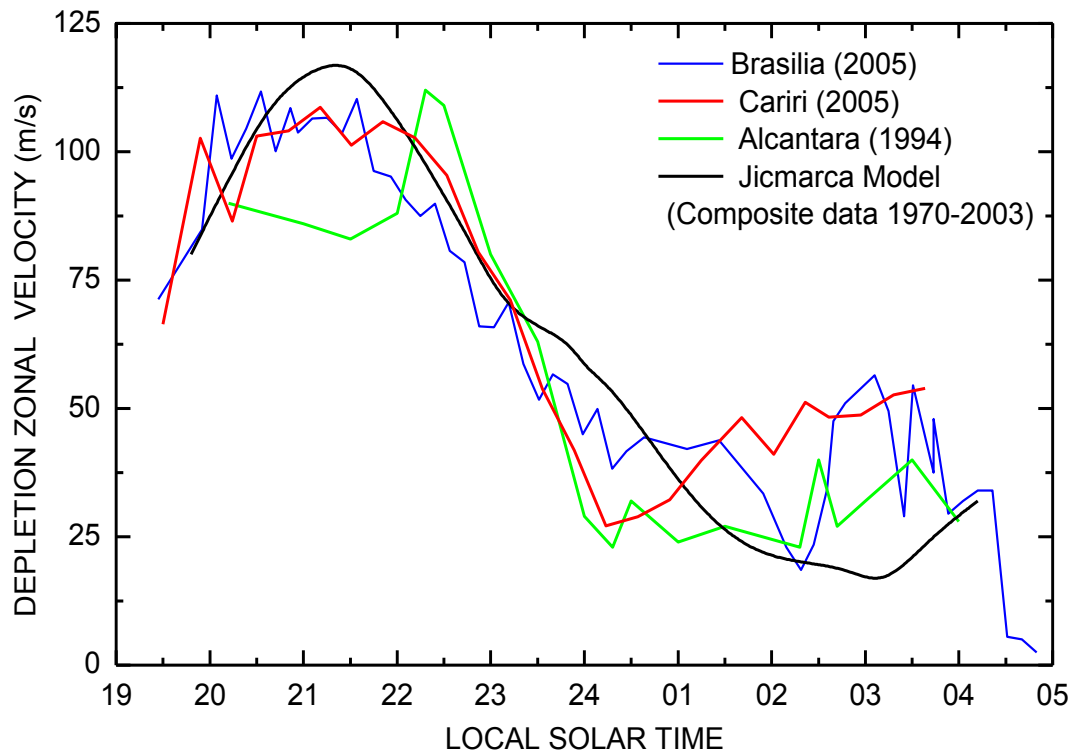
Figure 6.11. Comparison of the average plasma bubble zonal velocities from Brasilia and Cariri obtained from the SpreadFEx campaign with previous observations from Alcantara, Brazil by *Taylor et al.* [1997] and an empirical model derived from the Jicamarca radar observations by *Fejer et al.* [2005].

20 m/s) as compared with the Alcantara observations and Jicamarca model result. This small difference may be due to the latitudinal and longitudinal variations on the nocturnal zonal plasma drift as discussed in the previous chapter.

6.3.3. EPB Velocity Corresponding to Different Apex Altitudes

The field of view covered by the airglow images (geographical width) is ~1500 km×1500 km at 250 km altitude with latitude ranges of ~8˚S to 22˚S from Brasilia and ~0˚ to 14˚S from Cariiri. The bubble velocities were estimated within three geographical

latitude ranges of about 8°-13°S, 13°-17°S, and 17°-22°S from Brasilia, and about 1°-5°S, 5°-10°S, and 10°-14°S from Cariri during the night of October 1-2, 2005. We estimated the apex altitudes (using equation 5.1 from section 5.3.3), which ranged about 400-700 km, 700-1000 km, and 1000-1300 km, respectively.

Figure 6.12 shows the local time variations of the ionospheric plasma bubble zonal velocities at apex altitudes of ranges ~400-700 km (asterisk symbols), ~700-1000 km (solid circles), and ~1000-1300 km (triangles) over Brasilia and Cariri during the night of October 1-2, 2005. The velocities corresponding to lower apex altitudes (400-700 km) were slightly greater than those from higher altitudes during the pre-midnight period from both stations, while during the post-midnight period, bubble structures were
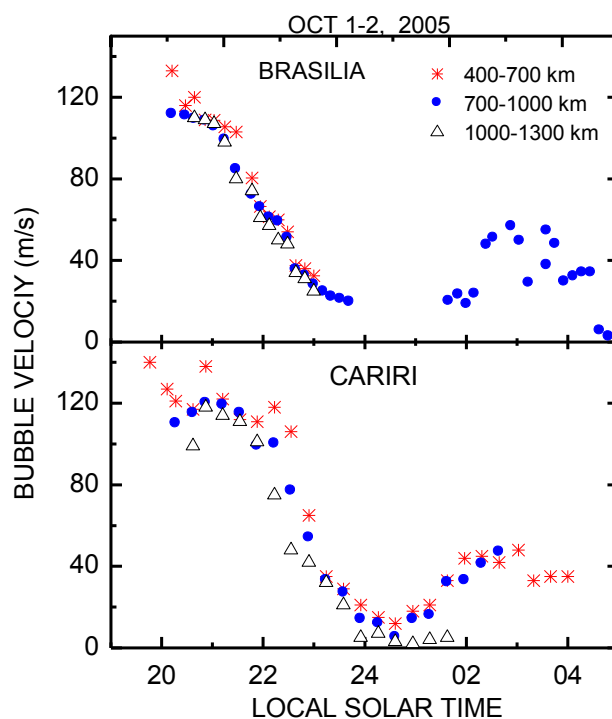
Figure 6.12. Plasma bubble velocities as a function of local solar time corresponding to different apex altitudes from Brasilia and Cariri during the night of October 1-2.

not extended to higher latitudes from Brasilia, and no significant differences were observed from Cariri. Moreover, the changes in velocities with local solar time are similar corresponding to all apex altitudes.

6.3.4. Airglow and GPS Velocity Comparison[3]

The airglow depletion velocities were compared with GPS estimated velocity from TEC data from Brasilia during the night of October 1-2, 2005. These GPS data were obtained from the Department of Earth and Atmospheric Science, Purdue University, Indiana. The temporary GPS stations were set up in a small network surrounding the all-sky imager with an approximate spacing of 100 km between sites. The data were obtained from three temporary sites at Fazenda Isabel near Brasilia, Saõ Juaõ de Alianca (FAZ1), Parco Nacional, Alto Paraiso (ALPA), and Teresina de Goias (TERE). The dual frequency GPS receivers recorded phase and signal-to-noise ratio at a 30 sec sampling interval.

The GPS receiver locations superimposed on airglow images where velocities were estimated is shown in Figure 6.13. The GPS satellite tracks are represented by PRN4, PRN8, and PRN28 on different sites ALPA, FAZI, and TERE [*Haase et al.,* 2011]. The airglow depletion signals have been observed in the past with GPS. In this case, the plasma depletion was developed early in the evening of October 1-2. The drift

---

[3]This section is coauthored by Chapagain, N. P. on paper, Haase J. S., T. Dautermann, M. J. Taylor, N. P. Chapagain, E. Calais, and P.-D. Pautet (2011), Propagation of Plasma Bubbles Observed in Brazil from GPS and Airglow Data, Adv. Space Res., doi:10.1016/j.asr.2010.09.025. Copyright 2011 ELSEVIER. Reproduced with the permission from ELSEVIER (see Appendix B).

velocity was estimated from PRN4 at the bottom part of the field of view, while the airglow depletion was in its development stage and confined spatially to the northwestern part of the image. After about an hour, the depletion was mature and the southernmost extent of the depletion in the airglow image increased in agreement with the general understanding of the increase in latitudinal extent along the magnetic field lines with time as the depletion increases in height at the magnetic equator. Similarly, the drift velocities were estimated from PRN8 and PRN28 at the middle and top region of the field of view of the camera, respectively.
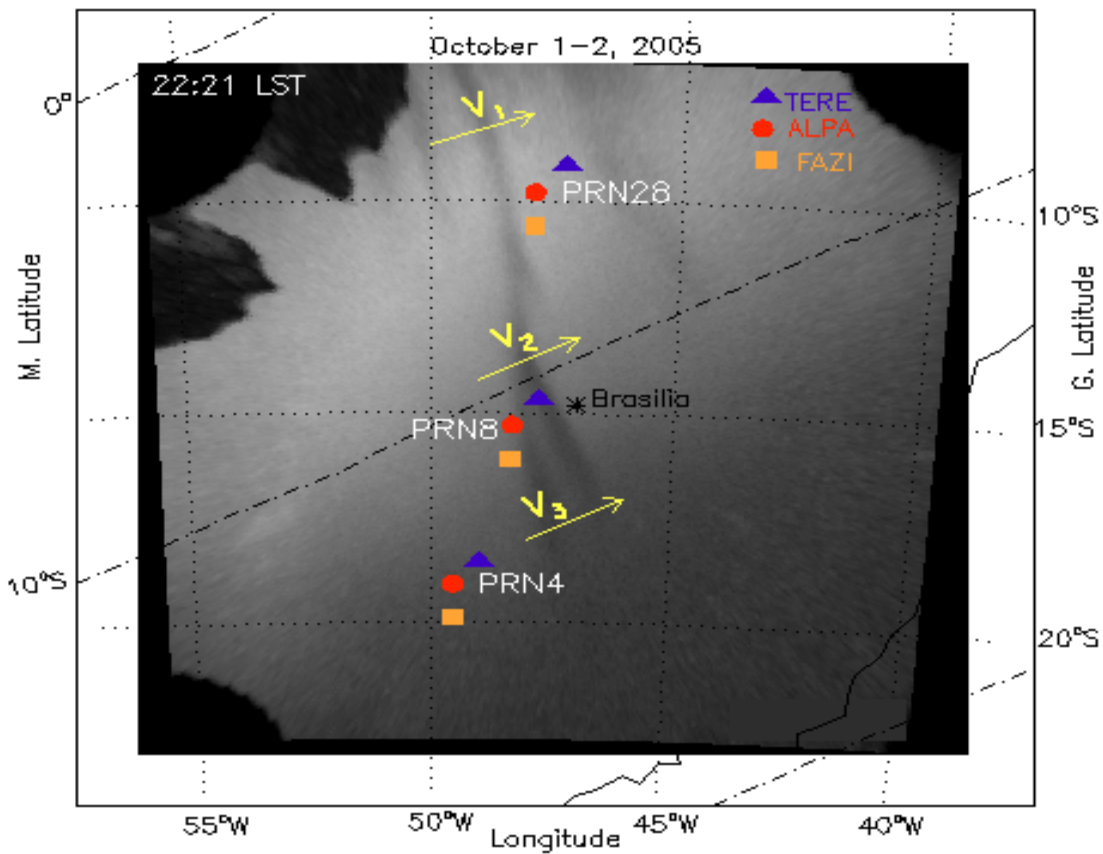
Figure 6.13. GPS receiver locations superimposed on airglow images from coincidence measurements using all-sky imager and GPS systems.

Table 6.1 summarizes the satellite tracks, sites of the GPS receivers, and the velocity comparisons around the same time (Universal Time) from airglow depletions and TEC measurements. Using PRN4, the depletion velocity estimated is 119 ± 7 m/s at an azimuth of 161.7°, which is the farthest west trace as shown in Figure 6.13. The other velocities calculated are 101±3 m/s at azimuth 161.1° using PRN8 at the center traces, and 0 ± 3 m/s at 163.6° using PRN28 in the far eastern traces. The propagation speed decreased as the disturbance propagates to the east. West of the observation site, the velocity of the plasma bubble retrieved from the airglow imager was estimated 112 ± 6 m/s, which was consistent with the value of 119 ± 7 m/s based on the GPS IEC array data. The velocity decreased as the depletion moved to the east, to 72-85 ± 5 m/s based on the airglow data and of 80 ± 3 m/s estimated from GPS. Both the airglow and GPS were able to discern the slowing of the depletion as it crossed the observation site.

Table 6.1. Velocity of depletions measured with airglow and GPS.

Satellite	Site	Airglow		TEC	
		Velocity (m/s)	Depletion Time	Velocity (m/s)	Depletion Time
PRN 4	ALPA FAZ1	112±6	0:14:57	119±7	0:15:00
	TERE	111±5	0:29:06		0:19:48
PRN8	ALPA FAZ1	105±6	0:57:26	101±3	0:57:00
	TERE	99±5	01:11:35		1:06:18
PRN28	ALPA FAZ1	85±5	01:23:27	80±3	1:23:24
	TERE	72±4	01:40:01		1:35:24

Figure 6.14 displays the comparison of airglow depletion velocities with calculated velocities from GPS IEC measurements from Brasilia during the night of October 1-2. The airglow measurement data were available throughout the night, while the IEC velocities were estimated for limited range of times at 21:11, 21:54, and 22:21 LST. Airglow depletion velocities are very consistent with the GPS IEC velocity despite the fact they are made at different latitudes where the magnetic field lines may be at higher altitudes. The plot shows airglow depletion velocity decreased from ~120 m/s at 21:15 LST to ~20 m/s at around midnight and the post-midnight period (during ~24:00-02:30 LST). Further, the post-midnight velocity enhancement was observed up to ~50 m/s at ~03:00 LST and then decreased to ~2 m/s at dawn (at ~05:00 LST).
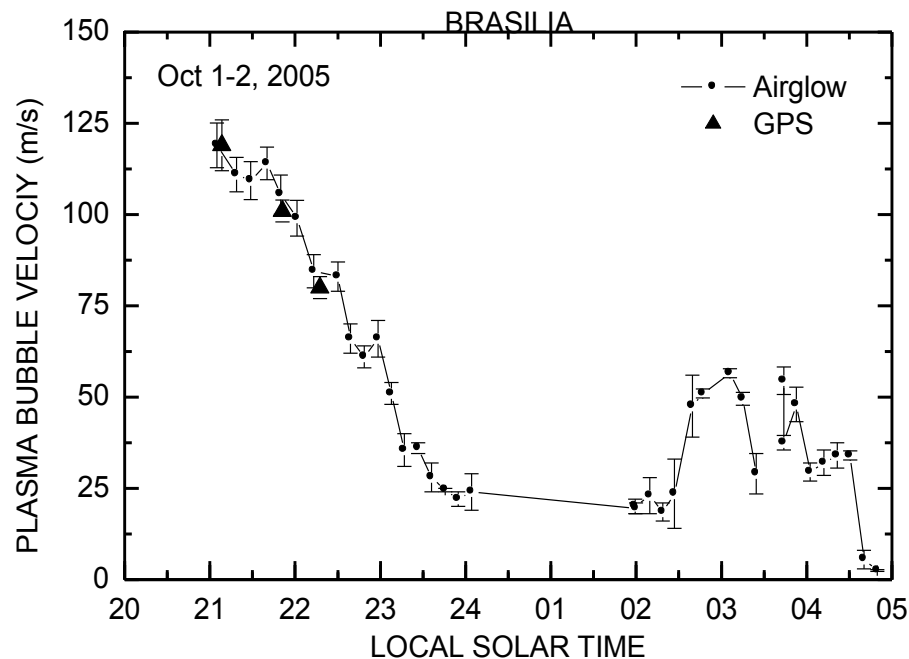
Figure 6.14. Comparison of plasma bubble zonal velocities from airglow observations and estimated GPS measurements.

6.3.5. EPB Longitudinal Comparison

We analyzed observation images from two closely spaced stations during two consecutive nights on September 30-October1 and October 1-2 as explained above (Figure 6.2-6.4). These nights were typical of the several nights of coincident image measurements. The measurements with this configuration have revealed interesting results, different in both morphology and the dynamics, of the bubble structures imaged at the same time from two adjacent sites. The comparative studies between two consecutive nights from two close sites, as presented above, further illustrates the potential for different bubble development on a night-to-night and site-to-site basis. There are several factors that may account for such longitudinal differences. First, there may be differences in the density gradient and the thermospheric zonal wind, which control the intensity of the PRE through the E-regions electrodynamical coupling process. Subsequently, the intensity of the PRE may have been different from one longitude to the other, including a modification in the plasma bubble generation. The second possibility is that the vertical drift and the post-sunset F-layer height control the growth rate of Rayleigh-Taylor instability. Since these two stations are located close to each other, it is unlikely that these factors are significantly different so that they can influence the longitudinal variations. Finally, there are the regional variation in the local density perturbation acting as a seeding source due to upward propagations of the tides and other waves from lower atmosphere [e.g., *Walker et al.,* 1981; *Immel et al.,* 2006]. In particular, the differences in the gravity waves propagating upward from the troposphere act as perturbation sources triggering the RTI process [e.g*., Vadas et al.,* 2009].

Longitudinal variability of the equatorial bubbles has been studied in the past using several techniques. *Maruyama and Matuura* [1984] used the topside soundings by the Ionospheric Sounding Satellite b (ISS-b) to determine a global distribution map of the ESF activity, while *Tsunoda* [1985] compared the seasonal scintillation activity using previously obtained datasets from several sites spread around the globe. Furthermore, *Immel et al.* [2004] utilized the FUV image data from the NASA IMAGE satellite to study the longitudinal variability of the zonal plasma drift speeds and their relation with the Dst index, during a limited three-month period (March-May 2002). *Makela et al.* [2004] compared the ionospheric airglow and GPS scintillation data acquired from Haleakala, Hawaii, with several previous studies carried out from the Pacific sector. They also investigated the occurrence of the plasma bubbles and the possible location of their source region as a function of the time of the year. Moreover, *Henderson et al.* [2005] used the GUVI imager data on board the NASA TIMED satellite to study the characteristics of the equatorial anomaly (EA) and the detection of the EPBs as a function of the longitudinal sector and season.

6.4.   Summary

All-sky images of the OI (630.0 nm) airglow emissions show that EPB structure occurred on every clear sky night during the campaign from both stations, Brasilia and Cariri. The measurements from these two neighboring stations (at ~1500 km apart) have revealed surprising day-to-day and regional variations in the generation and spatial characteristics of the plasma bubbles. They also exhibited the same general evolution phenomena as previously reported, that is generation after sunset followed by poleward

expansion, corresponding to the upward instability growth over the magnetic equator. The different evolution in the observed plasma bubbles from two stations possibly may be due to the differences in the (a) height of the F-layer, (b) zonal thermospheric wind, (c) longitudinal gradient in the flux tube integrated conductivity, and (d) seeding sources. The growth of the bubbles occurred almost simultaneously on several nights of the common observations from two stations. However, on the night of September 30-October 1, depletion onset from Brasilia was observed one hour earlier than from Cariri, while during the night of October 1-2, depletion occurred from Brasilia about one and one half hour later than from Cariri. The exact cause of the longitudinal difference in the evolution and development of plasma bubbles is difficult to explain. Nevertheless, the data are consistent with a more localized origin for the seeding/growth of the plasma bubbles observed in the night, possibly associated with tropospheric convection [e.g*., McClure et al.,* 1998; *Fritts et al.,* 2008]. Furthermore, a correlation between tropospheric convective activities, gravity waves propagating through the MLT layer, and the generation of plasma bubbles in the ionosphere has been shown in associated studies using these data from the SpreadFEx campaign [*Fritts et al.,* 2008; *Pautet et al.,* 2009; *Takahashi et al.,* 2009].

The depletion zonal velocities obtained from both Brasilia and Cariri agreed well and were eastward, changing systematically with local solar time. The averaged velocities peaked around 125 m/s, a couple of hours after sunset (at ~21:00 LST), and decreased until local midnight, thereafter the depletions faded out with time. This downward trend of velocity with local time is mainly due to the decreasing vertical

component of the ambient electric field. The post-midnight fossilized bubbles were also observed on several nights until dawn with smaller eastward drift velocities (maximum up to ~50 m/s). These results are in good quantitative agreement with previous measurements from the same longitudinal sector under similar geomagnetic and solar conditions [e.g., *Taylor et al.,* 1997; *Sobral et al.,* 2002; *Martinis et al.,* 2003]. Occasionally, a short-time westward motion of the depletion was also observed, which may be due to a reversal of the nocturnal F-layer dynamo electric field as discussed in the previous chapter.

The estimated drift velocity corresponding to different apex altitudes illustrates small shear velocities during the pre-midnight, but no distinct shear velocity was observed around midnight and in the post-midnight period. The case study of coincidence GPS and airglow depletion measurements indicates the plasma bubble velocities were very consistent with the GPS IEC velocity despite the fact they are made at different latitudes where the magnetic field lines may be at higher altitudes.

CHAPTER 7

CLIMATOLOGY OF POST-SUNSET EQUATORIAL SPREAD *F*

OVER JICAMARCA[4]

Abstract

We use radar observations from 1996 to 2006 to study the climatology of post-sunset equatorial 3-m spread *F* irregularities over Jicamarca during all seasons. We show the spread *F* onset times do not change with solar flux, and their onset heights, which occur near the altitude of the evening F region velocity vortex, increase linearly from about 260 to 400 km from solar minimum to solar maximum. Higher onset heights generally lead to stronger radar echoes. During the equinox, spread *F* onset occurs near vertical drift evening reversal times, while during the December solstice, they occur near the drift reversal times close to solar minimum, and near the time of the prereversal velocity peak for high solar flux conditions. On average, radar plume onset occurs earlier with increasing solar flux in all seasons. Plume onset and peak altitudes increase with solar activity, and the peak heights are generally highest during the equinox. The F region upward drift velocities that precede spread *F* onset increase from solar minimum to solar maximum, and are approximately proportional to the maximum prereversal drift peak velocities.

7.1.   Introduction

F-region plasma irregularities in the nighttime equatorial ionosphere are commonly referred to as equatorial spread *F* (ESF). The occurrence of these irregularities, which have scale sizes from a few centimeters to hundreds of kilometers, varies with longitude, local time, season, and solar and geomagnetic activity. Extensive studies over the last several decades have determined the main characteristics of equatorial spread *F* [e.g., *Farley et al.,* 1970; *Woodman and LaHoz,* 1976; *Fejer and Kelley*, 1980; *Hysell,* 2000].

It has been established that the height of the postsunset F layer is the most important parameter controlling the generation of equatorial spread *F* [e.g.*, Farley et al.,* 1970; *Abdu et al.,* 1983; *Jayachandran et al.,* 1993; *Fejer et al.,* 1999]. This height is determined mainly by the equatorial vertical plasma drift velocity, which is driven by evening prereversal enhancement (PRE) of the eastward electric field. The characteristics and generation mechanisms of equatorial vertical plasma drifts have been reviewed in numerous publications [e.g., *Kelley,* 1989, *Fejer,* 1991, 1997]. The generalized Rayleigh-Taylor instability (RTI) is believed to be the mechanism responsible for the initiation of an instability at the bottomside F layer that develops into flux-tube-aligned plasma depletions rising to the topside [e.g., *Kudeki and Bhattacharya*, 1999; *Huba and Joyce,* 2007; *Kudeki et al.,* 2008].

Extensive studies of 3-m spread *F* irregularities have been carried out since 1970 using radar observations at the Jicamarca Radio Observatory, Peru (12°S, 76.9°W, and dip latitude 1°N). *Woodman and LaHoz* [1976] presented the first detailed description of

the characteristics of spread *F* scattering layers observed with the Jicamarca radar. *Hysell and Burcham* [1998] and *Hysell* [2000] studied in detail the properties of bottom-type, bottomside, and topside spread *F* observed with the 50 MHz Jicamarca JULIA (Jicamarca Unattended Long-term investigations of the Ionosphere and Atmosphere) system. Bottom-type spread *F* events occur in relatively weak and narrow scattering layers (less than about 50 km thick) in the lower F region. Bottomside spread *F* events correspond to broad (about 50-100 km wide), more structured, and stronger scattering layers at relatively higher altitudes that last for a few hours. Topside layers or radar plumes represent larger-scale elongated structures originating from bottomside layers and extending to the topside ionosphere.

Kudeki and Bhattacharyya [1999] have shown that post-sunset bottomside spread *F* events commence in the interior of the F region evening plasma drift vortex. *Hysell and Burcham* [2002] presented a statistical study of the 3-m plasma irregularities measured by JULIA between August 1996 and April 2000 and discussed the relationship of these irregularities to the equatorial ionospheric electric fields during quiet and disturbed times. More recently, coherent scatter radar measurement over Brazil, Asia, and Micronesia have also been used to study the variability of spread *F* and its relationship to the post sunset rise of the equatorial F layer [e.g., *de Paula and Hysell,* 2004; *Yokoyama et al.,* 2004; *Patra et al.,* 2005; *Tsunoda,* 2005; *Tsunoda and Ecklund,* 2007].

In this study, we use detailed coherent and incoherent radar observations to examine the climatological behavior of post-sunset spread *F* over Jicamarca. This work follows up the statistical study of *Hysell and Burcham* [2002]. In the following sections,

we first briefly describe our measurements and data analysis; then we will discuss the onset heights, times of initial spread *F* radar echoes and plumes, and the peak altitudes of radar plumes, as well. Finally, we will highlight the relationships of spread *F* and radar plume onset times with the characteristics of the evening equatorial vertical drifts.

7.2.   Measurements and Data Analysis

We have used F region JULIA and incoherent scatter radar measurements over Jicamarca during 1371 evening and early night periods primarily from August 1996 to December 2006. For the June solstice, when spread *F* is less common over Jicamarca, we have also included data from 2007 and 2008. We have binned these measurements in three seasons representing equinox (March-April and September-October), December solstice (November-February), and June solstice (May-August). For each season, we classified the spread *F* structures on the basis of their thickness and range of altitudes as weak spread *F* (WSpF), plumes, and broad spread *F* (BSpF). These radar signatures are illustrated in Figure 7.1. WSpF is characterized by weak and narrow irregularity structures (smaller than about 150 km) with a typical value of 60 km, which corresponds mostly to the bottom-type and bottomside layers of *Hysell and Burcham* [1998]. We define radar plumes as large-scale plasma structures that break through to the topside and rapidly ascend to higher altitudes (an altitude range greater than about 200 km), and broad spread *F* as wide, structured layers (thickness greater than about 200 km) with temporal scales longer than about two hours. These broad structures sometimes extend to higher altitudes and occasionally produce radar plumes. The average thickness of the
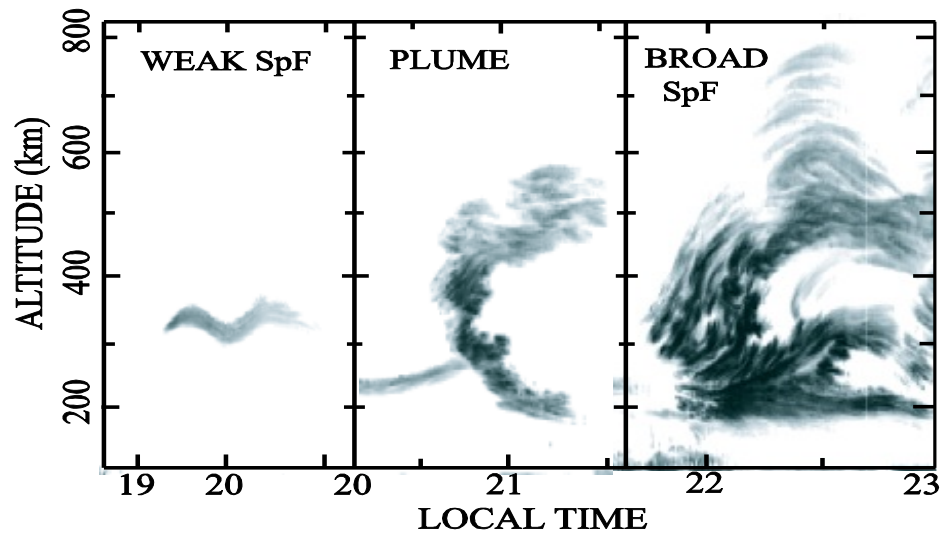
Figure 7.1. Range-time-intensity (RTI) plots of weak spread *F* (left panel) on November 3, 1999, plume (middle panel) on September 9, 1996, and broad spread *F* (right panel) on September 12, 1996, measured by the JULIA.

broad spread *F* structure is about 350 km. We define both radar plumes and broad spread *F* as strong spread *F* (SSpF).

Over Jicamarca, post-sunset spread *F* is most common during the equinox and December solstice, but only occasional during the June solstice, as illustrated in Table 7.1 (see Appendix A, Figure A.1). During the equinox and December solstice most strong spread *F* events occurred during geomagnetic quiet times; during the June solstice strong spread *F* events were observed during 33 and 18 quiet and disturbed nights, respectively. *Hysell and Burcham* [2002] pointed out the statistics of spread *F* occurrence over Jicamarca do not have significant solar cycle dependence except for a small increase in the frequency of radar plumes near solar minimum.

Figure 7.2 highlights the main spread *F* parameters we used in the present study. These are the onset time (T_I) and height (H_I) of the initial spread *F,* and the onset time

Table 7.1. Spread *F* occurrence over Jicamarca.

Radar Signature	Mar-Apr Sep-Oct		Nov-Feb		May-Aug	
	Number	%	Number	%	Number	%
No SpF	107	20	53	12	264	68
Weak SpF	166	31	194	43	73	19
Plumes	232	44	145	32	44	11
Broad SpF	25	5	61	13	7	2

(T_P), height (H_P) and peak height (H_{PK}) of radar plumes. The plume peak heights could only be determined when the measurements covered their full altitude profiles in the RTI (Range-Time-Intensity) plots. For solar flux indices generally higher than 160 units, radar plumes often extended above the standard highest height sampled (900 km), which resulted in a smaller database. In the present study, we will consider the characteristics of the initial radar plumes only. When multiplumes are present, their average periods are on the order of 1-1.5 h. *Woodman and LaHoz* [1976] pointed out the narrow beam (about 1°) of the Jicamarca radar gives only a slit camera view of the irregularities. Therefore, the observed times and heights to be discussed below correspond to the values inside the radar beam only.

7.3.   Results

In this section, we will describe the season- and solar flux dependent onset times and heights of early night spread *F* and radar plumes over Jicamarca, along with their relationships to the evening F region vertical drifts.
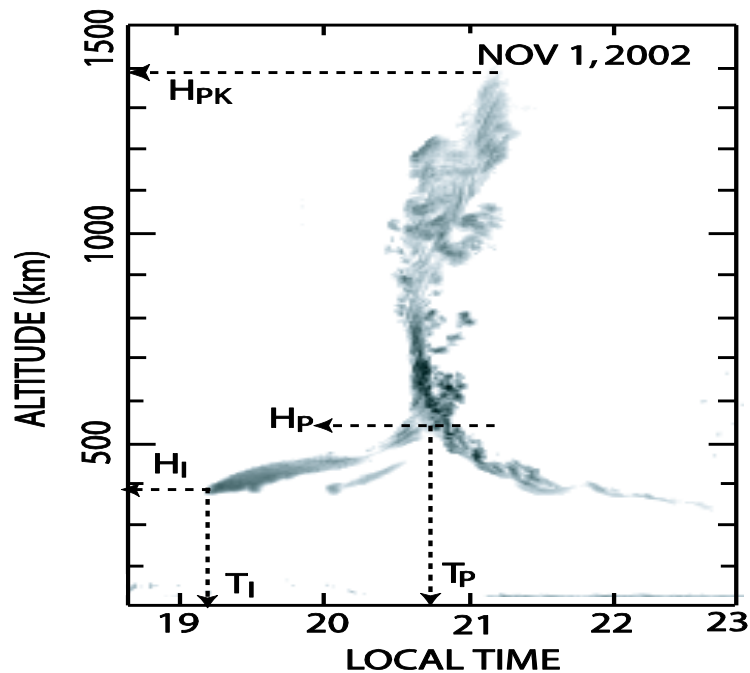
Figure 7.2. Typical JULIA radar plume over Jicamarca on November 1, 2002, illustrating the spread *F* parameters considered in this study. T_I and H_I correspond to spread *F* onset time and height, and T_P, H_P, and H_{PK}, the plume onset time and height and peak height, respectively.

7.3.1. Spread *F* Onset Times and Heights

We have initially binned the data on the basis of geomagnetic activity, as indicated by the Kp indices, following the criteria of *Fejer et al.* [1999]. Although spread *F* occurrence is clearly affected by geomagnetic activity, our results indicate the average characteristic times and heights of spread *F* events are essentially magnetic activity independent. Therefore, the results below were obtained by including all available observations, since those improve their statistical significance.

Figure 7.3 shows the seasonal and solar cycle dependence of the onset heights of weak and strong spread *F* (i.e., broad structures and plumes) obtained by binning the data

in groups of 20 solar flux (*F10.7* cm) units. The linear fits for the average onset heights (H_I) are H_I (km) = 239 + 0.7Φ for the equinox, H_I (km) = 226 + 0.7Φ for the December solstice, and H_I (km) = 203 + 0.8Φ for the June solstice, where Φ is the decimetric solar flux index. These results illustrate the strong increase of the onset heights with solar flux. The average heights vary from about 280 to 420 km in equinox, 270 to 410 km during the December solstice, and 250 to 400 km during the June solstice, as the solar flux index increases from 60 to 250. Near solar minimum, the average onset heights of both weak and strong spread *F* are nearly the same, but for higher solar conditions, the onset heights of strong spread *F* events are generally higher by about 20 km.

Jicamarca ionosonde data (see Appendix, Figure A.2) show that during spread *F* events, the base of the F-layer (h'F) increases from about 290 to 410 km in the equinox, and from 290 to 430 km during the December solstice. These results indicate, as expected [e.g., *Hysell and Burcham*, 1998; *Kudeki and Bhattacharyya,* 1999], spread *F* occurs initially in the bottomside of the F-layer.

Figures 7.4 and 7.5 present the solar flux variations of spread *F* onset times and heights and resulting radar plumes during the equinox and December solstice. The scatter bars illustrate the large variability of the data. The onset times do not change much with solar flux and have values of about 19:20 LT and 19:45 LT during the equinox and December solstice, respectively. For moderate and higher solar flux conditions, these onset altitudes are higher than shown in Figure 7.3, which also include results from weak spread *F*. We do not show the data for the June solstice, when, except for solar minimum, spread *F* events are much less frequent over Jicamarca. During the June solstice, spread *F*
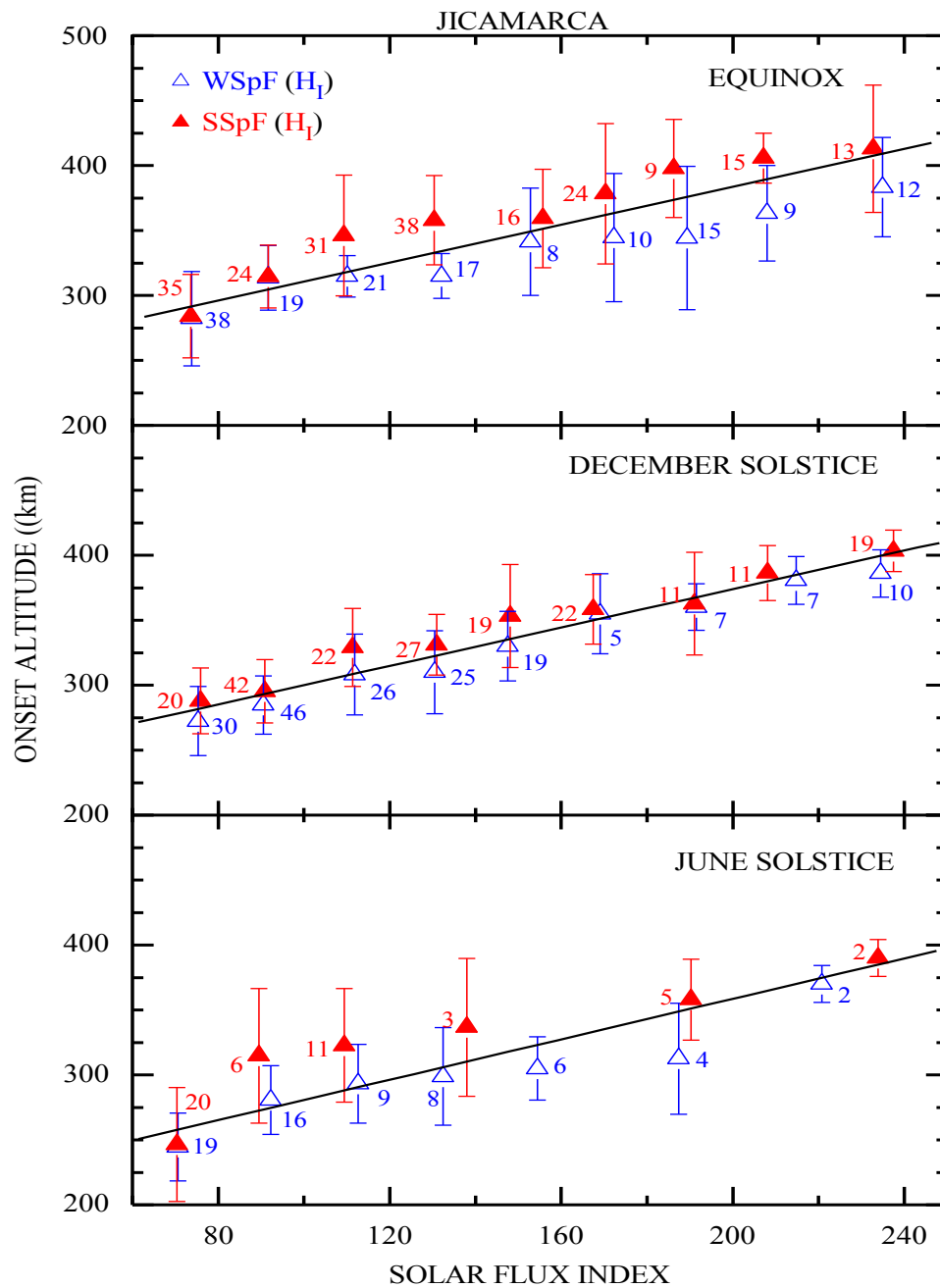
Figure 7.3. Onset altitudes of weak and strong spread *F* as a function of solar flux index. The number of samples and the standard deviations are also shown. The straight lines denote the least squares fit to the combined weak and strong spread *F* data.

onset occurs at about 19:30 LT, and plume onset times shift from about 22:00 to 20:30 LT from solar minimum to solar maximum.

Figures 7.4 and 7.5 show plume onset heights over Jicamarca increase from about 330 to 500 km during the equinox and 360 to 500 km during the December solstice from low to moderate solar flux conditions (solar flux index smaller than 180), and then remain nearly unchanged at about 500 km for higher levels of solar activity. Near solar maximum, spread F onset times remain nearly unchanged at about 20:30 LT in the equinox and 21:00 LT during the December solstice. As solar flux increases from low to moderate values, plume onset times shift from about 21:15 to 20:25 LT in the equinox and from 21:20 to 20:30 LT during the December solstice. They occur later during January and December than during February and November. This behavior is consistent with the solar cycle dependence of the evening vertical drift velocities [e.g., *Fejer et al.,* 1991].

The average plume onset heights are higher than the corresponding spread F onset heights by about 50 to 100 km during the equinox, about 80 to 150 km during the December solstice, and about 30 to 90 km during the June solstice. Near solar minimum, the average time periods from spread F onset to plume onset are about 1 h and 45 min in the equinox and about 2 h during the December solstice. For moderate and maximum solar conditions, these periods decrease to about 1 h during the equinox and 1 h and 30 min during the December solstice. Very small numbers of plumes were observed during the June solstice for moderate and high solar flux conditions.
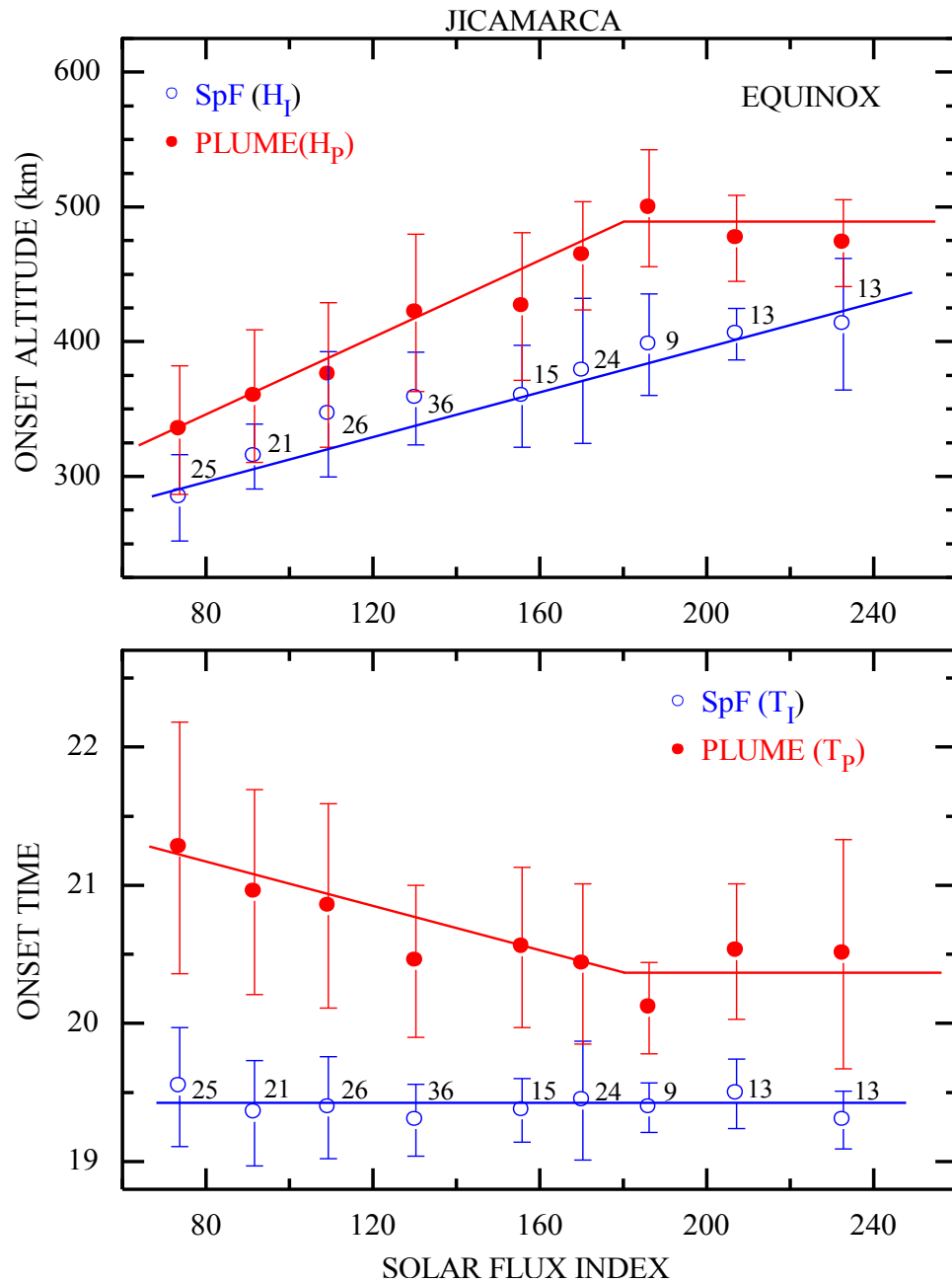
Figure 7.4. The variations of onset altitudes and times of equatorial spread *F* and resulting radar plumes with solar flux during the equinox. The solid lines denote fits to the data.
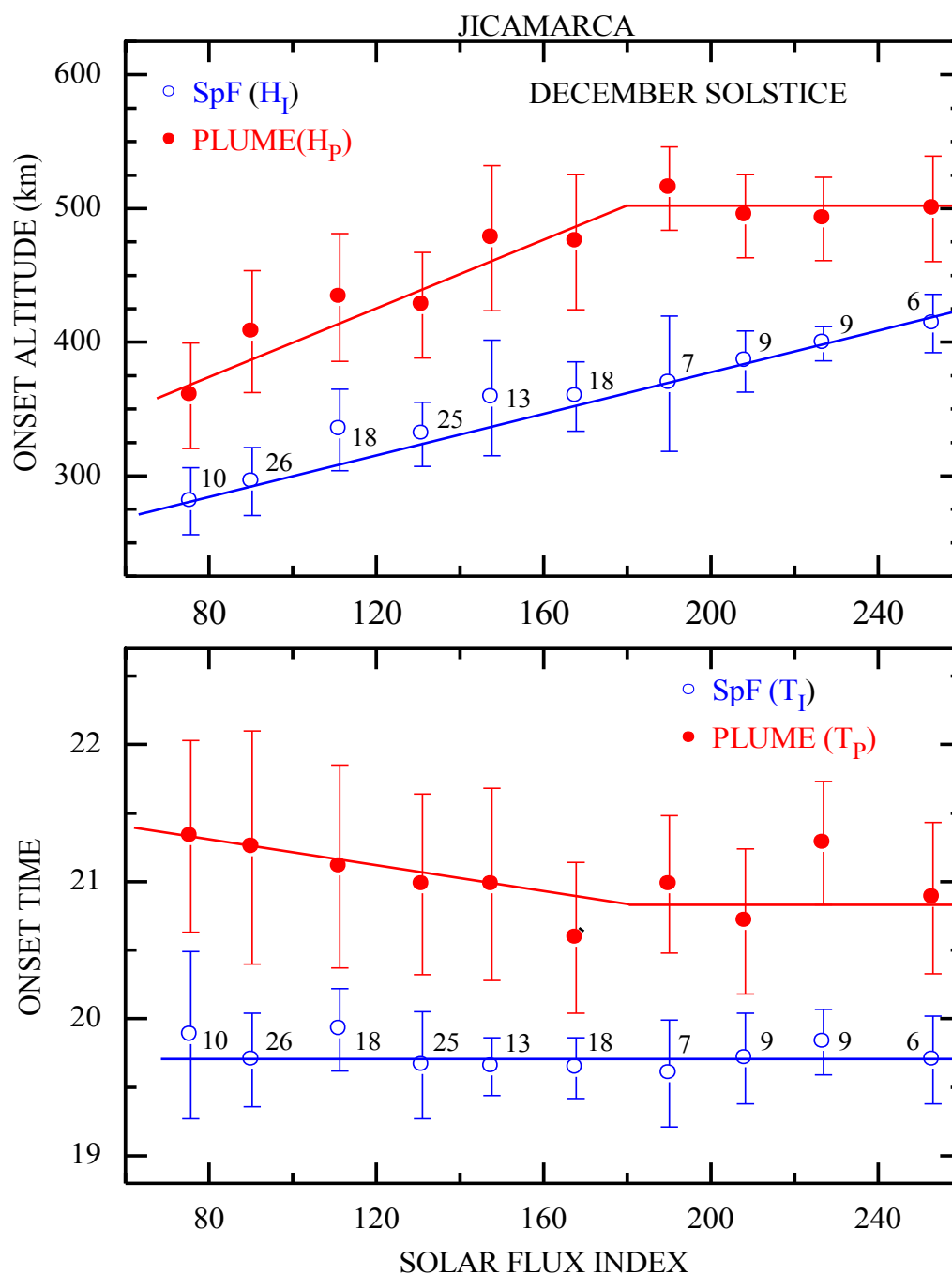
Figure 7.5. The variations of onset altitudes and times of equatorial spread *F* and radar plumes with solar flux during the December solstice. The solid lines denote fits to the data.

7.3.2. Plume Peak Heights

Figure 7.6 shows the scatter plots of the onset and peak heights of the spread *F* plumes over Jicamarca as a function of the solar flux. In this case, the database during moderate and high solar flux conditions is much smaller than used in Figures 7.4 and 7.5. The onset height, Hp, can be interpreted as corresponding to the altitude the plume breaks through the top of the F layer. Peak height data were not available during January-February at high solar flux conditions because the peak altitudes cross their full altitude profiles in the RTI plots. Therefore, the December solstice data shown in Figure 7.6 are mainly from November and December.

Figure 7.6 illustrates the peak heights are highly variable, but increase significantly from solar minimum to solar maximum. The average plume onset heights increase from about 310 to 500 km as the solar flux index increases from 70 to 200. The peak heights have much larger scatter than the spread *F* onset heights (see Appendix, Figure A.3). The equations for the average peak heights are $H_{PK}(km) = 472+4.3\Phi$ for the equinox, $H_{PK}(km) = 604 +2.6\Phi$ for the December solstice, and $H_{PK}(km) = 443 +3.8\Phi$ for the June solstice. The peak values are about 700 and 1400 km during solar minimum and maximum, respectively. The maximum plume altitude recorded at Jicamarca was about 1800 km during the equinox. The percentages of plumes above 900 km during equinox and December solstice are about 15%, 60%, and 75% for low, moderate, and high solar activity, respectively (see Appendix, Figure A.4). During the June solstice, this percentage is about 25% for both low and high solar flux conditions.
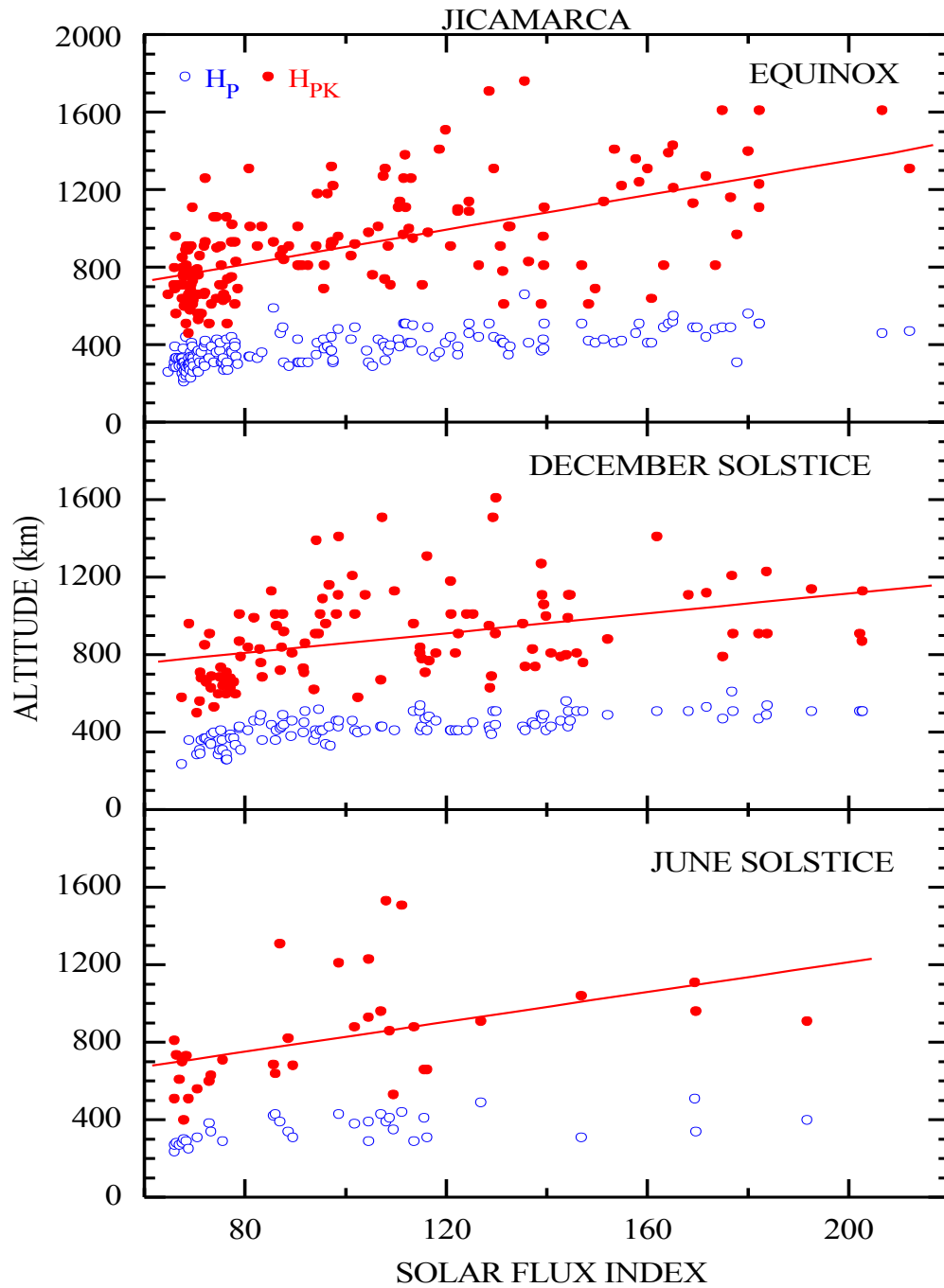
Figure 7.6. Scatter plots of radar plume onset (H_P) and peak (H_{PK}) heights as a function of solar flux. The straight lines indicate least squares fits to the peak altitude data.

7.3.3. Relationships to the Vertical Drift Velocity

Figure 7.7 illustrates the solar flux dependence of the times of evening drift peak and drift reversal, and spread *F* and plume onset times. As shown in the earlier studies [e.g., *Fejer,* 1991; *Scherliess and Fejer,* 1999], the evening vertical drift peaks and drift reversals occur later in the December solstice than during the equinox, and are latest in January. Since spread *F* onset does not change with solar flux, but the times of drift peak and reversal occur earlier at solar minimum than at solar maximum, the onset times change from near the reversal times to closer to the drift peak times with increasing solar flux. Figure 7.7 shows plume onsets over Jicamarca occur about 2 h after the drift reversal during solar minimum, and after about 30 min near solar maximum. Figure 7.8 shows the seasonal and solar cycle dependence of the prereversal vertical drift peaks and of the drift velocities preceding the onset of weak spread *F,* and also of spread *F* with subsequent development of radar plumes. The drift velocities were obtained using incoherent scatter radar measurements within ±5 min of spread *F* onset and at the onset height. We should point out these onset velocities are not necessarily directly related to the observed spread *F* events, since these irregularities could have been generated outside the radar beam. Figure 7.8 illustrates the large variability of these velocities, particularly during the equinox. Early night downward drifts do not lead to the development of radar plumes during the equinox and inhibit the development of spread *F* during the December solstice. Weak spread *F* can occur even when the local drift velocities near dusk are downward provided the prereversal peak velocities are positive, which is in good agreement with the results of *Fejer et al*. [1999].
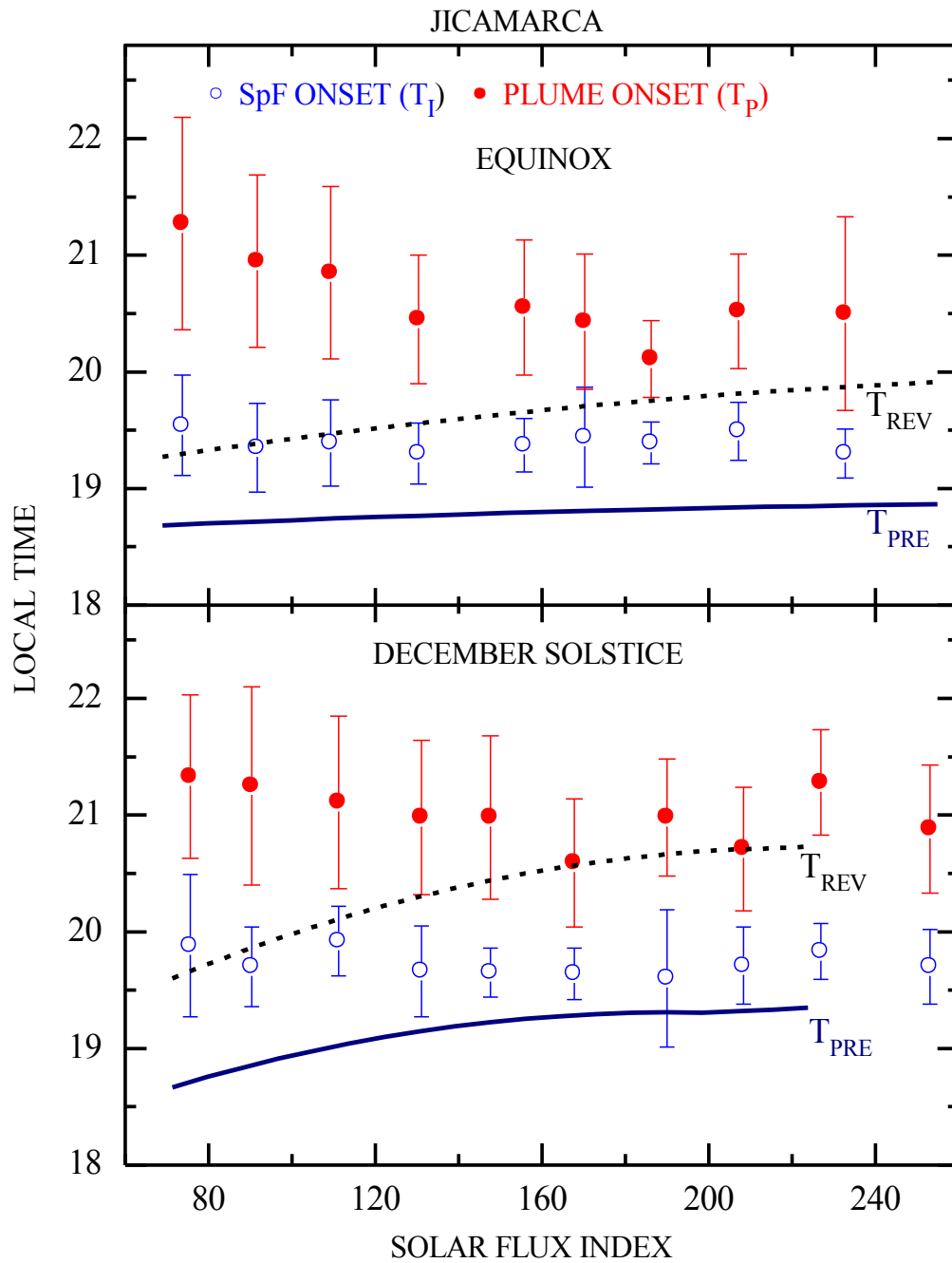
Figure 7.7. Times of average vertical prereversal drift peaks (solid lines), drift reversals (dashed lines), and spread F (T_I) and corresponding radar plume onset times (T_P) as a function of solar flux index.
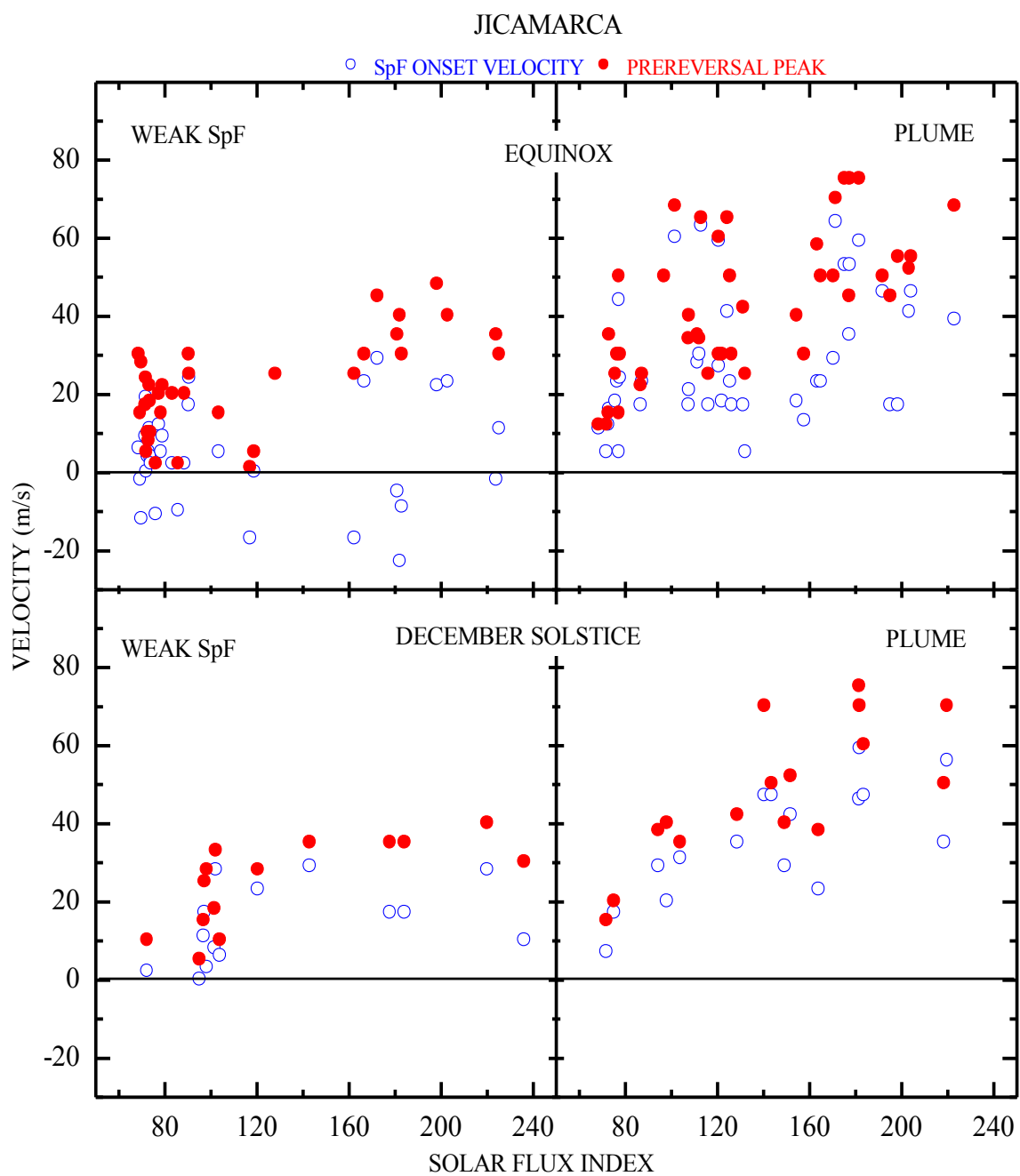
Figure 7.8. Scatter plots of weak spread *F* and plume onset velocities and corresponding prereversal drift peaks as a function of solar flux index.

The onset drifts and the corresponding prereversal velocity peaks are generally higher on nights of spread *F* plumes. The variability of the onset drifts and prereversal velocity peaks generally decrease with increasing solar activity. We do not present the results for the June solstice when strong spread *F* echoes are rarely seen; only very few of them have been observed with incoherent scatter radar measurements.

7.4. Discussion

The main results of our observations are:

1. The spread *F* average onset heights over Jicamarca strongly increase from solar minimum to solar maximum, but their onset times are essentially solar flux independent.

2. Strong spread *F* events have generally higher onset heights than weak spread *F* for all seasons.

3. The onset heights of the radar plumes increase with solar flux, but the onset times become earlier from low to moderate solar flux conditions, and remain nearly constant for higher flux values.

4. The average peak heights of radar plumes increase from about 700 to 1400 km from solar minimum to solar maximum.

5. Over Jicamarca, spread *F* onsets occur close to the evening drift reversal times during the equinox for all solar flux values. During the December solstice, they occur near drift reversal time near solar minimum, and, for higher solar flux conditions, closer to the time of the prereversal velocity peak.

6. The spread *F* onset velocities and the prereversal drift peaks are highly variable; these velocities generally determine the equatorial spread *F* signature and echo strength.

The effects of the PRE on the height of the F layer and spread *F* onset have been discussed by several authors [e.g., *Farley et al.,* 1970; *Abdu et al.,* 1983; *Sultan,* 1996; *Fejer et al.,* 1999]. *Hysell and Burcham* [2002] used JULIA radar data to show the height of bottomtype layers typically increase from about 200 to 400 km for an increase in solar flux index from 70 to 200. *Jyoti et al.* [2004] used ground-based ionospheric data from Trivandrum (8.5ºN, 76.5ºE) and Sriharikota (13.7ºN, 80.2ºE), India, to show the average base heights of the bottomside of the F region (h'F) at the time of triggering equatorial spread *F* during the equinox increase from about 225 to 350 km with the increase in the solar flux index from about 70 to 120.

Kudeki and Bhattacharyya [1999] have shown that bottomside spread *F* commences near the post-sunset velocity vortex, which is characterized by upward and downward flows to the west and to the east and eastward and westward flows on the top and the bottom, respectively. They also reported near solar minimum, this vortex is centered at an altitude of about 250 km. The evening upward drift velocities increase with solar flux moving the base of the equatorial F layer and the velocity vortex to higher altitudes. Our spread *F* onset height data suggest the altitude of the evening vortex reaches up to about 400 km near solar maximum.

We have seen as solar flux increases, the onset heights of spread *F* and plumes occur at higher altitudes, and radar plumes penetrate to higher topside altitudes. *Valladares et al.* [2004] showed a radar plume detected by JULIA extending to a peak height of about 1600 km, and that the corresponding larger-scale scintillations extended up to magnetic latitudes of about 22°. *Tsunoda and Ecklund* [2007] examined the post-

sunset rise of the equatorial F layer and the development of equatorial spread *F* using 50 MHz back-scatter radar observations from Pohnpei, Micronesia (7°N, 158.2°E). They reported radar plumes rising to an altitude of about 1400 km. These earlier results are in good agreement with our climatological heights.

Apex height mapping of airglow depletions have shown altitudes above 2000 km can be reached [e.g.*, Kelley et al.,* 2002; *Otsuka et al.,* 2002; *Mendillo et al.,* 2005; *Martinis and Mendillo,* 2007; *Makela and Miller,* 2008]. Recently, *Huba et al.* [2008] reported 3D simulations showing the bubbles rise from about 400 to 1000 km altitude in roughly one hour, and then to about 1600 km in the next half hour during moderate solar conditions. Our results indicate the characteristic heights of the 50 MHz scattering layers over Jicamarca are consistent with those from larger-scale spread *F* plasma structures.

We have pointed out that spread *F* onset heights do not change much with geomagnetic activity and the onset drifts and prereversal velocity enhancements are generally higher on nights of radar plumes. These results further suggest the major role of geomagnetic activity on equatorial spread *F* results from its effect on the vertical drift velocity, which is consistent with the results of *Fejer et al.* [1999].

7.5.   Summary

This Chapter presents a climatological study of post-sunset equatorial spread *F* over Jicamarca using an extensive data set of coherent and incoherent radar observations. We showed the onset heights of equatorial spread *F* related to the evening velocity vortex over Jicamarca strongly increase from solar minimum to solar maximum, but the onset times remain nearly unchanged. The onset heights prior to strong spread *F* are generally

larger than those of weak spread *F* during moderate and maximum solar conditions. Radar plumes onset shift to earlier local times from solar minimum to solar moderate conditions and remain constant for high flux values. Plume onset heights increase with solar flux. The peak heights of the radar plumes inside the Jicamarca radar beam are highly variable, but on average, they increase by about 500 km from solar minimum to solar maximum.

The spread *F* onsets during the equinox generally occur close to the reversal times of the vertical drift velocity, when the F layer reaches its highest altitude. During the December solstice, these radar echoes first occur near the drift reversal time near solar minimum and closer to the time of the prereversal drift peak velocity for high solar flux values. The prereversal vertical drift peaks and spread *F* onset drifts are highly variable, and the characteristics of the scattering layer and echo strength are strongly dependent on the values of these velocities.

CHAPTER 8

SUMMARY AND FUTURE RESEARCH

8.1.   Result Overview

We have used ground-based optical measurements and radar observations to investigate the development and dynamics of equatorial spread *F*. Campaign optical observations have been made at equatorial regions from different longitudinal sectors from Christmas Island in the Central Pacific Ocean and Ascension Island in South Atlantic Ocean with long term observations from Brasilia and Cariri in Brazil. Using these airglow image measurements under nearly similar solar conditions from these three regions, we have analyzed the evolution, development and dynamics of equatorial plasma bubbles. Moreover, the long-term radar observations have been used to study the climatology of the post-sunset equatorial spread *F* parameters including the onset times and heights of initial spread *F* and radar plumes, and the relationships between spread *F* onset velocities and prereversal drift peak velocities.

8.1.1. Onset, Evolution, and Structures
of EPBs

OI (630.0 nm) airglow images measurements from Christmas Island, Brasilia, and Cariri from Brazil reveal the airglow depletion structures associated with ionospheric plasma bubbles were observed on every clear sky night in pre-midnight period during the campaigns. The depletion structures from all stations exhibited similar features as previously reported in the literature, i.e., generation after sunset followed by poleward expansion corresponding to the upward instability growth over the equator. However, the

optical signatures obtained from different longitudinal sectors clearly illustrate strong variability in the bubble structures and their development. Marked fossilized bubble structures were also seen during the post-midnight period on several nights from Christmas Island, which were significantly weaker from Brasilia and Cariri. The structures were aligned along the magnetic field lines throughout the nights. However, the bubble propagation on April 4-5, from Ascension Island displayed an unusual counterclockwise rotation resulting in non-field aligned structures. Furthermore, the bubbles from Ascension Island were often bifurcated, similar to a previous study from Ascension Island reported by *Mendillo and Baumgardner* [1982], but during high solar flux condition.

Most of the nights the ESF onset occurred shortly after the local sunset outside the western edge of the camera's field of view and then they drifted eastward. However, on several nights EPBs onset was clearly observed inside the FOV of the camera in the early evening hours around 19:30-20:30 LST from Christmas Island and Ascension Island. Similar trends of onset times were also seen from both Brasilia and Cariri. These results are consistent with the climatological results obtained from radar observations of ESF from Jicamarca, Peru. The Christmas Island result also illustrates the number of plasma bubbles occurrences during each night is well correlated with initial onset times of EPBs and their persistence period during each night.

The bubbles often revealed smooth elongated magnetic field aligned structures exhibiting a range of zonal separations that differed during the course of night and also from night-to-night. Measurements of the separations between individual bubble

structures (from all stations) revealed similar scale-sizes predominantly ranging from 100-250 km [*Pautet et al.,* 2009; *Chapagain et al.,* 2011].

To study local variability of the EPBs evolution, structures and propagation, data from two sites in Brasilia and Cariri were used, each with approximately the same magnetic latitude and separated by ~1500 km with overlapping FOV's. These measurements have revealed surprising day-to-day and longitudinal variations in the onset of EPBs and their spatial characteristics. The exact cause of longitudinal differences in the evolution and development of plasma bubbles is difficult to explain [*Pautet et al.,* 2009]. Nevertheless, the data are consistent with a more localized origin for the seeding/growth of the plasma bubbles, possibly associated with tropospheric convection [e.g., *McClure et al.,* 1998; *Vadas et al.,* 2009]. Furthermore, a correlation between tropospheric convective activities, gravity waves propagating through the MLT layer, and the generation of plasma bubbles in the ionosphere has recently been reported by several authors in associated studies using these data from the SpreadFEx campaign [*Fritts et al.,* 2008; *Pautet et al.,* 2009; *Takahashi et al.,* 2009; *Vadas and Fritts,* 2009].

8.1.2. EPB Zonal Velocity

The plasma bubble zonal velocities from all three regions show similar trend during the pre-midnight period with eastward propagation. The average velocities peaked around ~90-100 m/s for Christmas Island, ~90-110 m/s for Ascension Island, ~100-125 m/s for Brasilia and Cariri at a couple of hours after sunset (~21:00-22:30 LST) and then they decreased around midnight and the post-midnight periods. This downward trend of the velocities with local time is mainly due to the decreasing vertical component of the

ambient electric field. These results are in good quantitative agreement with previous measurements from the same longitudinal sector under similar geomagnetic and solar conditions [e.g*., Taylor et al.,* 1997; *Sobral et al*., 2002; *Martinis et al.,* 2003; *Yao and Makela,* 2007].

The velocities exhibited significant day-to-day variabilities in their magnitudes from all sites with more pronounced variability at Christmas Island. The average pre-midnight velocities from Christmas Island were consistent with the results from other sites, but the post-midnight period remained nearly constant at an unusually higher value, ~80 m/s, significantly deviating from results of other optical measurements near the dip equator from different longitudinal sectors. This result demonstrates that there can be significant longitudinal variability in the electrodynamics conditions. We have examined the plasma drift model calculated from the simple electric field model of Eccles using Horizontal Wind Model (HWM-93 and HWM-07). The modeled post-midnight magnitudes were much smaller than observed. However, when the HWWM-07 model field was modified by a factor ~1.5, a more consistent agreement with the observed EPB velocities was obtained [refer to Chapter 4].

The velocity measurements from Ascension Island although typical on most nights also revealed an unusual shear (up to ~55 m/s) with latitude (or apex altitude) on April 4-5 around local midnight. In contrast, latitudinal shear velocities of the bubble from Brasilia and Cariri were relatively very small. From Ascension Island, the bubble exhibited westward motion at lower latitudes (apex altitudes ~500-800 km) and eastward at higher latitudes (apex altitudes ~800-1400 km). Consequently, the bubbles aligned

significantly off the magnetic meridian and tilted to the east, contrary to the trend for westward tilts commonly referred to in the literature (e.g., *Makela,* 2006, and references therein). The neutral wind motion for this location computed from Horizontal Wind Model (HWM-93) was eastward throughout the night and did not reproduce the observed shear. Westward motion of a bubble structure of ~10 m/s was seen from Cariri after midnight (~02:00 LT) on October 1-2 and also been reported from Alcantara [*Taylor et al.,* 1997]. On these occasions the westward drifts were temporary and probably resulted from a reversal in the night time F-region dynamo or from a large increase in the altitude of the shear in the nighttime F-region plasma drift. A similar mechanism may also have been responsible for the strong westward shear observed from Ascension Island.

8.1.3. Jicamarca Radar Measurements of ESF

We have presented a climatological study of post-sunset equatorial spread *F* over Jicamarca, Peru using an extensive data set of coherent and incoherent scatter radar observations during 1996-2006. We showed the onset heights of ESF related to the evening velocity vortex over Jicamarca strongly increase from solar minimum to solar maximum, but the average onset times remain nearly unchanged. The effect of increasing solar flux is to cause irregularities to occur at higher altitudes on average. This is consistent with increase in both amplitude of the prereversal enhancement and the time of the evening reversal of the zonal electric field associated with increasing solar flux. The onset heights prior to strong spread *F* were generally larger than those of weak spread *F* during moderate and maximum solar conditions. Radar plumes onset shifted to earlier local times from solar minimum to solar moderate conditions and remained constant for

high flux values. Plume onset heights increased with solar flux. The peak heights of the radar plumes inside the Jicamarca radar beam were highly variable, but on average, they increased by about 500 km from solar minimum to solar maximum.

The ESF onsets during the equinox generally occurred close to the reversal times of the vertical drift velocity, when the F layer reached its highest altitude. During the December solstice, these radar echoes first occurred near the drift reversal time near solar minimum and closer to the time of the prereversal drift peak velocity for high solar flux values. The prereversal vertical drift peaks and ESF onset drifts were highly variable, and the characteristics of the scattering layer and echo strength were strongly dependent on the values of these velocities.

8.2. Future Research

Imaging studies of low-latitude ionospheric irregularities have made significant progress over the past three decades. New insights continue to be made into the cause of irregularities when optical instruments are combined with other observing techniques such as radio and satellite data. However, there is still much to be learned about the post-sunset equatorial ionospheric phenomenon. Some of the outstanding issues that need to be studied in the near future are outlined below.

- ***Multi-instruments arranged in closely spaced longitude to study the longitudinal variation of EPB development and to investigate the seeding questions.***

The exact source of the seeding mechanism for the RTI process is still the cause of much debate. Although imaging techniques are used more as a monitoring tool for developing and fully developed bubbles (or plumes), they can provide additional

information on the seeding process. Optical imagers arranged in arrays at closely spaced longitudes (as initially performed during the SpreadFEx-1 campaign) would be very useful to corroborate the longitudinal variations of the plasma depletion development and contribute to detail investigation of the seeding question. Although imaging may not be able to actually observe the seeding mechanism, observations of their development and developed bubbles provide useful information on their occurrence and morphology. For example, by studying the distance between bubble structures, several studies have concluded that gravity waves are responsible for the seeding mechanism of RTI [e.g., *Fagundes et al.,* 1999; *Sinha and Raizada,* 2000; *Makela and Kelley*, 2003; *Takahashi et al.,* 2009]. More detailed studies could investigate gravity waves using new ray tracing techniques to determine their penetration into the thermosphere [*Vadas and Fritts,* 2009].

• *Conjugate studies of magnetic storm-time phenomena.*

Image data also show interesting effects during magnetic storms [e.g., *Taylor et al.,* 1997; *Pimenta et al.,* 2007]. The storms can affect the dynamo fields causing a reversal of the nocturnal zonal drift direction from eastward to westward. This can also cause secondary instabilities to develop on the eastern wall of the depletions [*Makela,* 2006]. Additionally, *Pimenta et al.* [2007] have reported the plasma blobs (localized plasma density enhancements) associated with large-scale plasma density depletions in the OI (630.0 nm) airglow emissions observed at low-latitude F-region during a major geomagnetic disturbance. It would be very important to distinguish which of these effects are local and which of these affect the entire flux-tube geometry. A conjugate study would lead to better understanding of these storm-time phenomena. Furthermore,

simultaneous measurements of plasma bubble drifts and wind motions under magnetically quiet and disturbed conditions will give new information on the conditions leading to the development of unusual shear velocities evident in some depletion structures.

- ***Coordinated ground and space-based tomographic measurements of depletion structures.***

The OI (630.0 nm) airglow structures seen with all-sky cameras is a two-dimensional image of a three-dimensional phenomenon. An even more informative technique for the investigation of the vertical extent of the plasma structures would be to use multiple imagers with overlapping FOV's from ground (and space), to make tomographic measurements of the structures (e.g., 3D characteristics of EPBs) [*Kamalabadi et al.,* 2009]. For example, the continued analysis of data obtained from equatorial Brazil using ground-based instruments in the coordination with the C/NOFS satellite, as a part of equatorial SpreadFEx-2 campaign during 2009/2010, will provide important information for the investigation of bubble dynamics and associated thermospheric conditions.

- ***Comparative study between optical and radar measurements.***

Coincident optical and radar measurements will give important information for the determination of the ESF parameters, such as onset times and heights of initial spread *F* and radar plumes (bubbles). The comparative study of apex heights from optical measurements and peak altitudes from radar observations will provide an important capability for the investigation of the morphology of the depletion structures.

- ***Possible coupling relationships between EPBs and Medium-Scale Traveling Ionospheric Disturbances (MSTIDs).***

Previous studies of coincidence observations of MSTIDs and EPBs argued the MSTIDs may play an important role for the generation of low-latitude irregularities [*e.g.*, *Miller et al.,* 2009]. The study of the EPBs with coincident observations of MSTIDs is important to investigate possible coupling between the low- and mid-latitude ionospheres. Using multi-instrument observations from different locations, we will be able to search for influences of MSTIDs on both the development and decay of EPBs.

REFERENCES

Abalde, J. R., P. R. Fagundes, J. A. Bittencourt, and Y. Sahai (2001), Observations of equatorial F-region plasma bubbles using simultaneous OI 777.4 nm and OI 630.0 nm imaging: new results, *J. Geophys. Res., 106*(A12), 30,331–30,336.

Abalde, J. R., P. R. Fagundes, Y. Sahai, V. G. Pillat, A. A. Pimenta, and J. A. Bittencourt (2004), Altitude-resolved ionospheric drifts at low latitudes from simultaneous OI 777.4 nm and OI 630.0 nm imaging observations, *J. Geophys. Res., 109,* A11308, doi:10.1029/2004JA010560.

Abdu, M. A. (2001), Outstanding problems in the equatorial ionosphere-thermosphere electrodynamics relevant to spread *F*, *J. Atmos. Terr. Phys., 63*, 869-884.

Abdu, M. A., R. T. Medeiros, J. A. Bittencourt, and I. S. Batista (1983), Vertical ionization drift velocities and range type spread F in the evening equatorial ionosphere, *J. Geophys. Res. 88,* 399-402.

Abdu, M. A., J. R. de Souza, I. S. Batista, and J. H. A. Sobral (2003), Equatorial spread F statistics and empirical representation for IRI: a regional model for the Brazilian longitude sector, *Adv. Space Res., 31,* 703-716.

Arruda, D. C. S., J. H. A. Sobral, M. A. Abdu, V. M. Castilho, H. Takahashi, A. F. Medeiros, and R. A. Buriti (2006), Theoretical and experimental zonal drift velocities of the ionospheric plasma bubbles over the Brazilian region, *Adv. Space Res., 38*, 2610-2614.

Baker, D. J., and A. T. Stair (1988), Rocket measurements of altitude distributions of the hydroxyl airglow, *Physica scripta, 37*, 611.

Balsley, B. B., G. Haerendel, and R. A. Greenwald (1972), Equatorial spread F: recent observations and a new interpretation, *J. Geophys. Res., 77,* 5625-5628.

Basu, S., Su. Basu, J. Aarons, J. P. McClure, and M. D. Cousins (1978), On the coexistence of kilometer- and meter-scale irregularities in the nighttime equatorial F-region, *J. Geophys. Res., 83,* 4219-4226.

Basu, S., K. M. Groves, J. M. Quinn, and P. Doherty (1999), A comparison of TEC fluctuation and scintillations at Ascension Island, *J. Atmos. Sol.-Terr. Phys., 61,* 1219-1226.

Batista, I. S., M. A. Abdu, and J. A. Bittencourt (1986), Equatorial F-region vertical plasma drifts: seasonal and longitudinal asymmetries in the American sector, *J. Geophys. Res., 91,* 12055-12064.

Berkner, L. V., and H. W. Wells (1934), F-region ionosphere – Investigation at low latitudes, *Terres. Magn., 39,* 215, 1934.

Bilitza, D. (1990), International Reference Ionosphere 1990, *NSSDC 90-22*, Greenbelt, Maryland.

Bilitza, D., and B. Reinisch (2008), International Reference Ionosphere 2007: Improvements and new parameters, *J. Adv. Space Res., 42* #4, 599-609, doi:10.10166/j.asr2007.07.048.

Booker, H. G., and H. W. Wells (1938), Scattering of radio waves by the F-region of the ionosphere, *J. Geophys. Res., 43*, 249-256.

Coley, W. R., and R. A. Heelis (1989), Low-latitude zonal and vertical ion drifts seen by DE-2, *J. Geophys. Res., 94*, A6, 6751-6761.

de Paula, E. R., and D. L. Hysell (2004), The Sao Luis 30 MHz coherent scatter ionospheric radar: system description and initial results, *Radio Sci., 39,* RS1014, doi:10.1029/2003RS002914.

de Paula, E. R., et al. (2002), Ionospheric irregularity zonal velocities over Cachoeira Paulista, *J. Atmos. Sol.-Terr. Phys., 64*(12), 1511 –1516.

Drob, D. P., et al. (2008), An empirical model of the Earth's horizontal wind fields: HWM07, *J. Geophys. Res., 113*, A12304, doi:10.1029/2008JA013668.

Dungey, J. W. (1956), Convective diffusion in the equatorial F-region, *J. Atmos. Terr. Phys., 9,* 304-310.

Eccles, J. V. (1998), A simple model of low-latitude electric fields, *J. Geophys. Res., 103(*A11), 26699-26708.

Eccles, J. V., N. Maynard, and G. Wilson (1999), Study of the evening plasma drift vortex in the low-latitude ionosphere using San Marco electric field measurements, *J. Geophys. Res., 104*(A12), 28133-28143.

Fagundes, P. R., Y. Sahai, I. S. Batista, M. A. Abdu, J. A. Bittencourt, and H. Takahashi (1999), Observations of day-to-day variability in precursor signatures to equatorial F-region plasma depletions. *Annals of Geophysics 17* (8), 1053–1063.

Farley, D. T., B. B. Basley, R. F. Woodman, and J. P. McClure (1970), Equatorial spread F: Implications of VHF radar observations, *J. Geophys. Res., 75,* 7199-7216.

Farley, D. T., E. Bonelli, B. G. Fejer, and M. F. Larsen (1986), The prereversal enhancement of the zonal electric field in the equatorial ionosphere, *J. Geophys. Res., 91,* 13723.

Fejer, B. G. (1991), Low latitude electrodynamic plasma drifts; a review, *J. Atmos. Terr. Phys., 53*, 677-693.

Fejer, B. G. (1997), The electrodynamics of the low-latitude ionosphere: recent results and future challenges, *J. Atmos Terr. Phys., 13,* 1465-1482.

Fejer, B. G., and M. C. Kelley (1980), Ionospheric irregularities, *Rev. Geophys., 18,* 401-454.

Fejer, B. G., D. T. Farley, C. A. Gonzales, R. F. Woodman, and C. Calderon (1981), F region east-west drifts at Jicamarca, *J. Geophys. Res., 86,* 215.

Fejer, B. G., E. Kudeki, and D. T. Farley (1985), Equatorial F-region plasma drifts, *J. Geophys. Res., 90*, 12249-12255.

Fejer, B. G., E. R. de Paula, S. A. Gonzales, and R. F. Woodman (1991), Average vertical and zonal F region plasma drifts over Jicamarca, *J. Geophys. Res., 96*, 13,901–13,906.

Fejer, B. G., E. R. de Paula, and R. A. Heelis, and W. B. Hanson (1995), Global equatorial ionospheric vertical drifts measured by the AE-E satellite, *J. Geophys. Res., 100*, 5769-5776.

Fejer, B. G., L. Scherliess, and E. R. de Paula (1999), Effect of the vertical plasma drift velocity on the generation and evolution of equatorial spread F, *J. Geophys. Res., 104*(A9), 19,859-19,869.

Fejer, B. G., J. R. Souza, A. S. Santos, and A. E. Costa Pereira (2005), Climatology of F-region zonal plasma drifts over Jicamarca, *J. Geophysics. Res., 110,* A12310, doi:10.1029/2005JA011324.

Fritts, D. C., et al. (2008), Gravity wave and tidal influences on equatorial spread F based on observations during the Spread F Experiment (SpreadFEx), *Ann. Geophys., 26,* 3235–3252.

Fritts, D. C., et al. (2009), Overview and summary of the spread F experiment (SpreadFEx), *Ann. Geophys., 27,* 2141–2155.

Garcia, F. J., M. J. Taylor, and M. C. Kelley (1997), Two-dimensional spectral analysis of mesospheric airglow image data, *Applied Optics, 36*, No. 29.

Gordon, W. E. (1958), Incoherent scattering of radio waves by free electrons with applications to space exploration by radar*, Proc. IRE, 46*, 1824.

Haase, J. S., T. Dautermann, M. J. Taylor, N. P. Chapagain, E. Calais, and P.-D. Pautet (2011), Propagation of plasma bubbles observed in Brazil from GPS and airglow data, *Adv. Space Res.,* doi:10.1016/j.asr.2010.09.025.

Haerendel, G. E. (1973), Theory of equatorial spread F, Report, *Max Planck Institut fur Extraterre. Phys.,* Garching, Germany.

Haerendel, G., J. V. Eccles, and S. Cakir (1992), Theory for modeling the equatorial evening ionosphere and the origin of the shear in the horizontal plasma flow, *J. Geophys. Res. 97,* 1209-1223.

Hammer, P. R., and I. A. Bourne (1976), A high resolution ionosonde, Technique and analysis methods, *J. Atmos. Terr. Phys., 38,* 935-943.

Hanson, W. B., and S. Sanatani (1973), Large Ni gradients below the equatorial F peak, *J. Geophys. Res., 78,* 1167-1172.

Hargreaves, J. K. (1995), The solar-terrestrial environment, Cambridge Atmospheric and Space Science Series*, Cambridge University Press,* New York.

Hedin, A. (1991), Extension of the MSIS thermosphere model into the middle and lower atmosphere, *J. Geophys. Res., 96*(A2), 1159-1172.

Hedin, A., et al. (1991), Revised global model of thermosphere winds using satellite and ground-based observations, *J. Geophys. Res., 96*(A5), 7657-7688.

Hedin, A., et al. (1996), Empirical wind model for the upper, middle and lower atmosphere, *J. Atmos. Terr. Phys. 58,* 1421-1447.

Heelis, R. A., P. C. Kendall, R. J. Moffet, D. W. Windle, and H. Rishbeth (1974), Electrical coupling of the E and F-regions and its effect on the F-region drifts and winds, *Planet. Space Sci., 22,* 743–756.

Henderson, S. B., C. M. Swenson, A. B. Christensen, and L. J. Paxton (2005), Morphology of the equatorial anomaly and equatorial plasma bubbles using image subspace analysis of Global Ultraviolet Imager data, *J. Geophys. Res., 110,* A11306, doi:10.1029/2005JA011080.

Huba, J. D., and G. Joyce (2007), Equatorial spread F modeling: Multiple bifurcation structures, secondary instabilities, large density 'bite-outs', and supersonic flows, *Geophys. Res. Lett., 34,* L07105, dio: 10.1029/2006GL028519.

Huba, J. D., G. Joyce, and J. Krall (2008), Three-dimensional equatorial spread F modeling, *Geophys. Res. Lett., 35*, L10102, doi:10.1029/2008GL033509.

Huba, J. D., S. L. Ossakow, G. Joyce, J. Krall, and S. L. England (2009), Three-dimensional equatorial spread F modeling: zonal neutral wind effects, *J. Geophys. Res., 36,* L19106, doi:10.1029/2009GL040284.

Hysell, D. L. (2000), An overview and synthesis of plasma irregularities in equatorial spread F, *J. Atmos. Sol.-Terr. Phys., 62,* 1037-1056.

Hysell, D. L., and M. C. Kelley (1997), Decaying equatorial F-region plasma depletions, *J. Geophys. Res., 102*(A9), 20,007.

Hysell, D. L., and J. D. Burcham (1998), JULIA radar studies of equatorial spread F, *J. Geophys. Res., 103,* 29,155-29,167.

Hysell, D. L., and J. D. Burcham (2002), Long term studies of equatorial spread F using the JULIA radar at Jicamarca, *J. Atmos. Sol.-Terr. Phys., 64,* 1531-1543.

Hysell, D. L., M. C. Kelley, W. E. Swartz, and R. F. Woodman (1990), Seeding and layering of equatorial spread F by gravity waves, *J. Geophys. Res., 95,* 17,253.

Hysell, D. L., E. Kudeki, and J. L. Chau (2005), Possible ionospheric preconditioning by shear flow leading to equatorial spread F, *Ann. Geophys., 23,* 2647.

Immel, T. J., H. U. Frey, S. B. Mende, and E. Sagawa (2004), Global observations of the zonal drifts speed of equatorial ionospheric plasma bubbles, *Ann. Geophys., 22,* 3099-3107.

Immel, T. J., E. Sagawa, S. L. England, S. B. Henderson, M. E. Hagan, S. B. Mende, H. U. Frey, C. M. Swenson, and L. J. Paxton (2006), The control of equatorial ionospheric morphology by atmospheric tides, *Geophys. Res. Lett., 33,* L15108, doi:10.1029/2006GL026161.

Jayachandran, B., N. Ballan, P. B. Rao, J. H. Sastri, and G. J. Bailey (1993), HF Doppler and ionosonde observations on the onset conditions of equatorial spread F*, J. Geophys. Res., 98,* 13741-13750.

Jensen, J. W., and B. G. Fejer (2007), Longitudinal dependence of middle and low latitude zonal plasma drifts measured by DE-2, *Ann. Geophys.,* 22, 2251-2559.

Johnson, M. H., and E. O. Hulburt (1950), Diffusion in the ionosphere*, Phys. Rev., 79*, 802-807.

Jyoti N., C. V. Devasia, R. Sridharan, D. Tiwari (2004), Threshold height (h′F)c for the meridional wind to play a deterministic role in the bottom side equatorial spread F and its dependence on solar activity, *Geophys. Res. Lett., 31,* L12809, doi:10.1029/2004GL019455.

Kamalabadi, F. , J. M. Comberiate, M. J. Taylor, and D. Pautet (2009), Electron densities in the lower thermosphere from GUVI 135.6nm tomographic inversions in support of SpreadFEx, *Ann. Geophys., 27*, 1–10.

Kelley, M. C. (1989), The Earth's Ionosphere: Plasma physics and electrodynamics, vol. 43, *Academic Press,* San Diego, California.

Kelley, M. C., M. C. Larsen, and C. LaHoz (1981), Gravity wave initiation of equatorial spread F: a case study, *J. Geophys. Res., 86,* 9087-9100.

Kelley, M. C., R. Pfaff, K. D. Baker, J. C. Ulwick, R. Livingston, C. Rino, and R. Tsunoda (1982), Simultaneous rocket probe and radar measurements of equatorial spread F – transitional and short wavelength results, *J. Geophys. Res., 87*, 1575.

Kelley, M. C., J. J. Makela, B. M. Ledvina, and P. M. Kintner (2002), Observations of equatorial spread F from Haleakala, Hawaii, *Geophys. Res. Lett., 29,* doi:10.1029/2002GL015509.

Kelley, M. C., J. J. Makela, L. J. Paxton, F. Kamalabadi, J. M. Comberiate, and H. Kil (2003), The first coordinated ground- and space-based optical observations of equatorial plasma bubbles, *Geophys. Res. Lett., 30*, 1766, doi:10.1029/2003GL017301.

Klostermeyer, J. (1978), Nonlinear investigation of the spatial resonance effect in the night-time equatorial F-region, *J. Geophys. Res., 83*, 3753.

Kudeki, E., and S. Bhattacharyya (1999), Postsunset vortex in equatorial F region plasma drifts and implications for bottomside spread F, *J. Geophys. Res., 104*, 28,163-28,170.

Kudeki, E., B. G. Fejer, D. T. Farley, and H. M. Ierkic (1981), Interferometer studies of equatorial F region irregularities and drifts, *Geophys. Res. Lett., 8*, 377.

Kudeki, E., A. Akgiray, M. Milla, J. L. Chau, D. L. Hysell (2008), Equatorial spread F initiation: Post-sunset vortex, thermospheric winds, gravity waves, *J. Atmos. Sol.-Terr. Phys., 69,* 2416–2427.

Labelle, J., J. -M Jahn, R. F. Pfaff, W. E. Swartz, J. H. A. Sobral, M. A. Abdu, P. Muralikrishna, and E. R. de Paula (1997), The Brazil/Guara equatorial spread F campaign: results of the large-scale measurements. *Geophys. Res. Lett., 24*(13), 1691-1694.

Makela, J. J. (2006), A review of imaging low-latitude ionospheric irregularity processes, *J. Atmos. Sol.-Terr. Phys., 68*(13):1441–1458.

Makela, J. J., and M. C. Kelley (2003), Field-aligned 777.4 nm composite airglow images of equatorial plasma depletions, *Geophys. Res. Lett.,* 30(8).

Makela, J. J., and E. S. Miller (2008), Optical observations of the growth and day-to-day variability of equatorial plasma bubbles, *J. Geophys. Res., 113*, A03307, doi:10.1029/2007JA012661.

Makela, J. J., B. M. Ledvina, M. C. Kelley, and P. M. Kintner (2004), Analysis of the seasonal variations of equatorial plasma bubble occurrence observed from Haleakala, Hawaii, *Ann. Geophys., 22*, 3109-3121.

Makela J. J., M. C. Kelley, and R. T. Tsunoda (2009), Observations of midlatitude ionospheric instabilities generating meter-scale waves at the magnetic equator, *J. Geophys. Res. 114,* A01307, doi:10.1029/2007JA012946.

Martinis, C., and M. Mendillo (2007), Equatorial spread F- related airglow depletions at Arecibo and conjugate observations, *J. Geophys. Res., 112*, A10310, doi:10.1029/2007JA012403.

Martinis, C., J. V. Eccles, J. Baumgardner, J. Manzano, and M. Mendillo (2003), Latitude dependence of zonal plasma drifts obtained from dual site airglow observations, *J. Geophys. Res., 108*(A3), 1129, doi:10.1029/2002JA009462.

Maruyama, T., and N. Matuura (1984), Longitudinal variability of annual changes in activity of equatorial spread F and plasma bubbles, *J. Geophys. Res., 89*(A12), 10903–10912, doi:10.1029/JA089iA12p10903.

Maynard, N. C., T. L. Aggson, F. A. Herrero, M. C. Liebracht, and J. L. Saba (1995), Average equatorial zonal and vertical ion drifts determined from San Macro S electric field measurements, *J. Geophys. Res., 100,* 17465-17479.

McClure, J. P., W. B. Hanson, and J. H. Hoffman (1977), Plasma bubbles and irregularities in the equatorial ionosphere*, J. Geophys. Res., 8*, 2650.

McClure, J. P., S. Singh, D. K. Bamgboye, F. S. Johnson, and H. Kil (1998), Occurrence of equatorial F-region irregularities: evidence for tropospheric seeding, *J. Geophys. Res., 103,* 29,119-29,136.

Mendillo, M., and J. Baumgardner (1982), Airglow characteristics of equatorial plasma depletions, *J. Geophys. Res., 87*, 7641–7652.

Mendillo, M., and A. Tyler (1983), Geometry of depleted plasma regions in the equatorial ionosphere, *J. Geophys. Res., 88,* 5778-5782.

Mendillo, M., E. Zesta, S. Shodham, P. J. Sultan, R. Doe, Y. Sahai, and J. Baumgardner (2005), Observations and modeling of the coupled latitude- altitude patterns of equatorial plasma depletions, *J. Geophys. Res., 110*, A09303, doi:10.1029/2005JA011157.

Meriwether, J. W., M. A. Biondi, and D. N. Anderson (1985), Equatorial airglow depletions induced by thermospheric winds, *Geophys. Res. Lett., 12*, 487–490.

Miller, E. S., J. J. Makela, and M. C. Kelley (2009), Seeding of equatorial plasma depletions by polarization electric fields from middle latitudes: experimental evidence, *Geophys. Res. Lett., 36, L18105,* doi:10.1029/2009GL039695.

Mukherjee, G. K. (2003), Studies of equatorial F-region depletions and dynamics using multiple wavelength nightglow imaging, *J. Atmos. Terr. Phys., 65,* 379-390.

Muralikrishna, P., and M. A. Abdu (2006), Rocket measurements of ionospheric electron density from Brazil in the last two decades, *Adv. Space Res., 37*(5), 1091-1096.

Ossakow, S. L. (1981), Spread F theories – a review, *J. Atmos. Terr. Phys., 43*, 437.

Otsuka, Y., K. Shiokawa, T. Ogawa, and P. Wilkinson (2002), Geomagnetic conjugate of equatorial airglow depletions, *Geophys. Res. Lett., 29(*15), 1753, doi:10.1029/2002GL015347.

Patra, A. K., D. Tiwari, S. Sripathi, P. B. Rao, R. Sridharan, C. V. Devasia, K. S. Viswanathan, K. S. V. Subbarao, R. Sekar, and E. A. Kherani (2005), Simultaneous radar observations of meter-scale F region irregularities at and off the magnetic equator over India, *J. Geophys. Res., 110,* A02307, doi:10.1029/2004JA010565.

Pautet, P.-D., and G. Moreels (2002), Ground-based satellite-type images of the upper atmosphere emissive layer, *Appl. Opt., 41*(5), 823.

Pautet, P.-D., M. J. Taylor, N. P. Chapagain, H. Takahashi, A. F. Medeiros, F. T. Sao Sabbas, and D. C. Fritts (2009), Simultaneous observations of equatorial F-region plasma depletions over Brazil during the spread F Experiment (SpreadFEx), *Ann. Geophys., 27,* 2371–2381.

Pimenta A. A., P. R. Fagundes, J. A. Bittencourt, Y. Sahai, D. Gobbi, A. F. Medeiros, M. J. Taylor, and H. Takahashi (2001), Ionospheric plasma bubble zonal drift: a methodology using OI (630.0 nm) all-sky imaging systems, *Adv. Space Res., 27*, 1219-1224.

Pimenta, A. A., J. A. Bittencourt, , Y. Sahai, R. A. Buriti, H. Takahashi, and M. J. Taylor (2003a), Ionospheric plasma bubble zonal drifts over the tropical region: a study using OI (630.0 nm) emission all-sky images, *J. Atmos. Terr. Phys., 65*, 1117-1126.

Pimenta, A. A., P. R. Fagundès, Y. Sahai, J. A. Bittencourt, and J. R. Abalde (2003b), Equatorial F-region plasma depletion drifts: latitudinal and seasonal variations, *Ann. Geophys., 21,* 2315-2322.

Pimenta, A. A., Y. Sahai, J. A. Bittencourt, and F. J. Rich (2007), Ionospheric plasma blobs observed by OI 630 nm all-sky imaging in the Brazilian tropical sector during the major geomagnetic storm of April 6–7, 2000, *Geophys. Res. Lett.,* 34, L02820, doi:10.1029/2006GL028529.

Rishbeth, H. (1971), Polarization fields produced by winds in the equatorial F-region, *Planet. Space Sci.,* 19, 357–369.

Rohrbaugh, R. P., W. B. Hanson, B. A. Tinsley, B. L. Cragin, and J. P. McClure (1989), Images of trans-equatorial bubbles based on field-aligned airglow observations from Haleakala in 1984-1986*, J. Geophys. Res., 94,* 6763-6770.

Sagawa, E., T. Maruyama, T. J. Immel, H. U. Frey, and S. B. Mende (2003), Global view of the nighttime low-latitude ionosphere by the IMAGE/FUV 135.6 nm observations, *Geophys. Res. Lett., 30*, 1534, doi:101029/2003/GL017140.

Sahai, Y., J. A. Bittencourt, N. R. Teixeira, and H. Takahashi (1981), Plasma irregularities in the tropical F-region detected by OI 777.4 nm and a 630 nm airglow measurements, *J. Geophys. Res., 86*, 3496-3500.

Sahai, Y., J. Aarons, M. Mendillo, J. Baumgardner, J. A. Bittencourt, and H. Takahashi (1994), OI (630.0 nm) imaging observations of equatorial plasma depletions at 16˚S dip latitude, *J. Atmos. Terr. Phys., 56*, 1461-1475.

Santana, D. C., J. H. A. Sobral, H. Takahashi, and M. J. Taylor (2001), Optical studies of the ionospheric irregularities over the Brazilian region by nocturnal images of the OI (630.0 nm) emission, *Adv. Space Res., 27,* 6, 1207-1212(6).

Scherliess, L., and B. G. Fejer (1999), Radar and satellite global equatorial F-region vertical drift model, *J. Geophys. Res. 104*, 6829-6842.

Schunk, R. W., and A. F. Nagy (2000), Ionospheric physics, plasma physics, and chemistry, *Cambridge University Press,* New York.

Singh, S., F. S. Johnson, and R. A. Power (1997), Gravity wave seeding of equatorial plasma bubbles, *J. Geophys. Res., 102*(A4), 7399–7410, doi:10.1029/96JA03998.

Sinha, H. S. S., and S. Raizada (2000), Some new features of ionospheric plasma depletions over the Indian zone using all sky optical imaging. *Earth Planets Space 52* (8), 549–559.

Sobral, J. H. A., M. A. Abdu, and Y. Sahai (1985), Equatorial plasma bubble eastward velocity characteristics from scanning airglow photometer measurements over Cacheoeira Paulista, *J. Atmos. Terr. Phy.*, 47, 895-900.

Sobral, J. H. A., M. A. Abdu, H. Takahashi, H. Sawant, and C. J. Zamlutti (1999), Solar and geomagnetic activity effects on nocturnal zonal velocities of ionospheric plasma depletions, *Adv. Space Res., 24*, 1507-1510.

Sobral, J. H. A., M. A. Abdu, H. Takahashi, M. J. Taylor, E. R. de Paula, C. J. Zamlutti, M.G. de Aquino, and G. L. Borba (2002), Ionospheric plasma bubble climatology over Brazil based on 22 years (1977–1998) of 630 nm airglow observations, *J. Atmos. Terr. Phys., 64,* 1517– 1524.

Sobral, J. H. A., et al. (2009), Ionospheric zonal velocities at conjugate points over Brazil during the COPEX campaign: experimental observations and theoretical validations, *J. Geophys. Res., 114*, A04309, doi:10.1029/2008JA013896.

Sultan, P. J. (1996), Linear theory and modeling of the Rayleigh-Taylor instability leading to the occurrence of equatorial spread F, *J. Geophys. Res., 101*, 26,875-26,891.

Takahashi, H., et al. (2009), Simultaneous observation of ionospheric plasma bubbles and mesospheric gravity waves during the SpreadFEx Campaign, *Ann. Geophys., 27,* 1477–1487.

Taylor, M. J., and M. J. Hill (1991), Near-infrared imaging of hydroxyl wave structure over an ocean site at low latitudes*, J. Geophys. Res.,18,* 1333-1336.

Taylor, M. J., and F. J. Garcia (1995), A two-dimensional spectral analysis of short period gravity waves imaged in the OI (557.7 nm) and near infrared OH nightglow emissions over Arecibo, Puerto Rico, *Geophys. Res. Lett., 22*, 2473.

Taylor, M. J., M. B. Bishop, and V. Taylor (1995), All-sky measurements of short period waves imaged in the OI (557.7 nm), Na (589.2 nm) and near infrared OH and O2 (0,1) nightglow emissions during the ALOHA- 93 campaign, *Geophys. Res. Lett., 22,* 2833.

Taylor, M. J., J. V. Eccles, J. LaBelle, and J. H. A. Sobral (1997), High resolution OI (630 nm) image measurements of F-region depletion drifts during the Guára campaign, *Geophys. Res. Lett., 24* 1699–1702.

Terra, P. M., J. H. A. Sobral, M. A. Abdu, J. R. Souza, and H. Takahashi (2004), Plasma bubble zonal velocity variations with solar activity over the Brazilian region, *Ann. Geophys., 22,* 1-6.

Tinsley, B. A., A. B. Christensen, J. Bittencourt, H. Gouveia, P. D. Angreji, and H. Takahashi (1973), Excitation of oxygen permitted line emissions in the tropical nightglow, *J. Geophys. Res., 78*, 1174–1186.

Tinsley, B. A., R. P. Rohrbaugh, W. B. Hanson, and A. L. Broadfoot (1997), Images of trans-equatorial F-region bubbles in 630 and 777-nm emissions compared with satellite measurements, *J. Geophys. Res., 102*(A2), 2057-2077.

Tsunoda, R. T. (1985), Control of the seasonal and longitudinal occurrence of equatorial scintillations by the longitudinal gradient in integrated E region Pedersen conductivity, *J. Geophys. Res., 90*(A1), 447–456, doi:10.1029/JA090iA01p00447.

Tsunoda, R. T. (2005), On the enigma of day-to-day variability in equatorial spread F, *Geophys. Res. Lett., 32,* L08103, doi:10.1029/2005GL022512.

Tsunoda, R. T. (2008), On blanketing sporadic E and polarization effects near the equatorial electrojet, *J. Geophys. Res., 113,* A09304, doi:10.1029/2008JA013158.

Tsunoda, R. T., and W. L. Ecklund (2007), On the post-sunset rise of the equatorial F layer and superposed upwellings and bubbles, *Geophys. Res. Lett., 34,* L04101, doi:10.1029/2006GL028832.

Tsunoda, R. T., R. C. Livingston, J. P. McClure, and W. B. Hanson (1982), Equatorial plasma bubbles: vertically elongated wedges from bottomside F layer, *J. Geophys. Res., 87,* 9171.

Vadas, S. L., and D. C. Fritts (2009), Reconstruction of the gravity wave field from convective plumes via ray tracing, *Ann. Geophys., 27,* 147–177.

Vadas, S. L., M. J. Taylor, P.-D. Pautet, P. A. Stamus, D. C. Fritts, H.-L. Liu, F. T. So Sabbas, V. T. Rampinelli, P. Batista, and H. Takahashi (2009), Convection: the likely source of the medium-scale gravity waves observed in the OH airglow layer near Brasilia, Brazil, during the SpreadFEx campaign, *Ann. Geophys., 27*, 231–259.

Valladares, C. E., R. Sheehan, S. Basu, H. Kuenzler, and J. Espinoza (1996), The multi instrumented studies of equatorial thermosphere aeronomy scintillation system: climatology of zonal drifts, *J. Geophys. Res., 101,* 953 26839-26850.

Valladares, C. E., J. W. Meriwether, R. Sheehan, and M. A. Biondi (2002), Correlative study of neutral winds and scintillation drifts measured near the magnetic equator, *J. Geophys. Res.,107*(A7), 1112, doi:10.1029:2001JA000042.

Valladares, C. E., R. Sheehan, and J. Villalobos (2004), A latitudinal network of GPS receivers dedicated to studies of equatorial spread F, *Radio Sci., 39,* RS1S23, doi:10.1029/2002RS002853.

Walker, J., J. Koehler, F. Creutzberg, A. McNamara, A. Jones, and B. Whalen (1981), Post substorm convection and auroral arc currents determined from multiple ionospheric, magnetic, and electric field observations, *J. Geophys. Res., 86*(A12), 9975-9988.

Wayne, R. P. (1991), Chemistry of atmospheres: an introduction the chemistry of atmospheres of earth, the planets, and their satellites, *Oxford University Press*, New York.

Weber, E. J., J. Buchau, R. H. Eatther, and S. B. Mende (1978), North-south aligned equatorial airglow depletions, *J. Geophys. Res.,* 83, 712–716.

Whitehead, J. D. (1971), Ionization disturbances caused by gravity waves in the presence of an electric field and background wind. *J. Geophys. Res.,* 76, 238-241.

Woodman, R. F. (1970), Vertical velocities and east-west electric fields at the magnetic equator, *J. Geophys. Res., 75,* 6249.

Woodman, R. F. (1972), East-west ionospheric drifts at the magnetic equator, *Space Res., 81,* 5447–5466.

Woodman, R. F., and C. LaHoz (1976), Radar observations of F-region equatorial irregularities, *J. Geophys. Res., 81*, 5447-5466.

Yao, D., and J. J. Makela (2007), Analysis of equatorial plasma bubble zonal drift velocities in the pacific sector by imaging techniques, *Ann. Geophys., 25*, 701-709.

Yokoyama, T., S. Fuko, and M. Yamamoto (2004), Relationship of the onset of equatorial F region irregularities with the sunset terminator observed with the equatorial atmosphere radar, *Geophys. Res. Lett., 31,* L24804, doi:10.1029/2004GL021529.

Zalesak, S. T., S. L. Ossakow, and P. K. Chaturvedi (1982), Nonlinear equatorial spread F: The effect of neutral winds and background Pedersen conductivity, *J. Geophys. Res., 87,* 151.

APPENDICES

APPENDIX A

PLOTS OF JICAMARCA RADAR MEASUREMENTS OF ESF
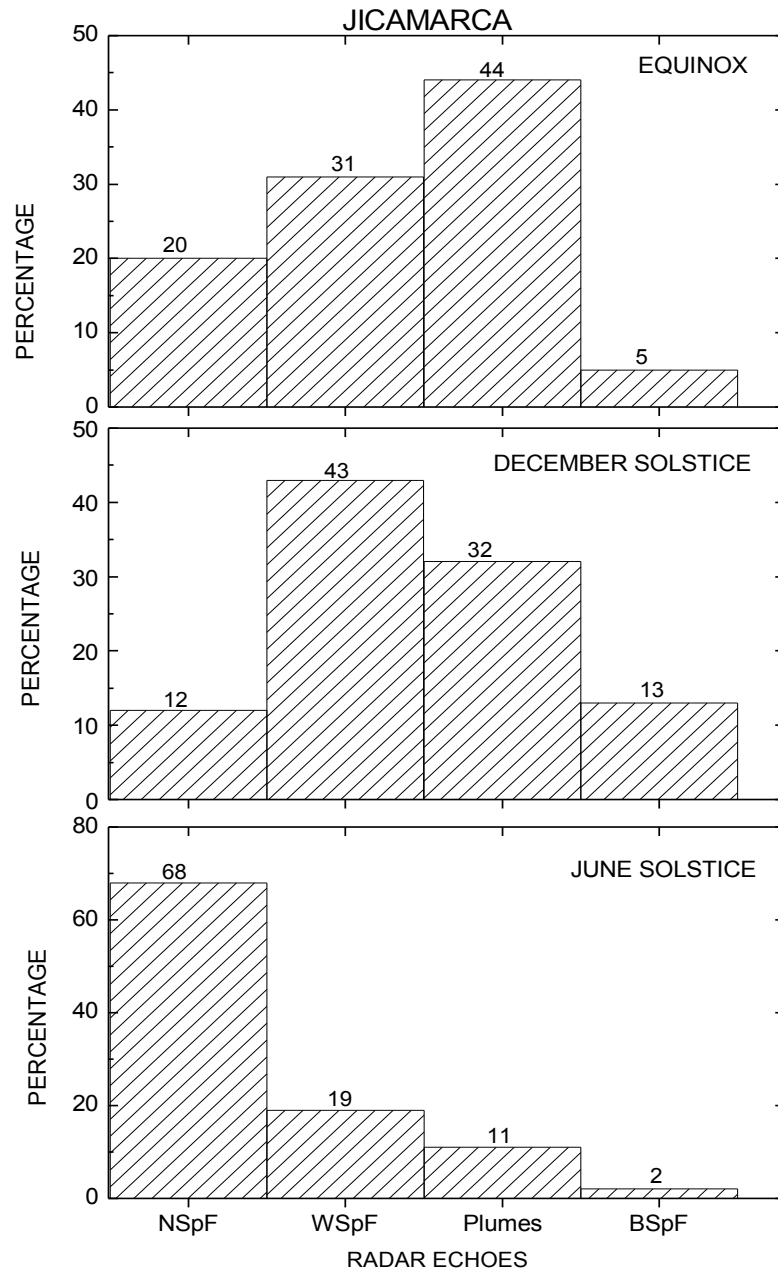
Figure A.1. Percentages of radar echoes occurrences for nonspread *F* (NSpF), weak spread *F* (WSpF), radar plume, and broad spread *F* (BSpF) from Jicamarca radar observations on equinox, December and June solstices during 1996-2006.
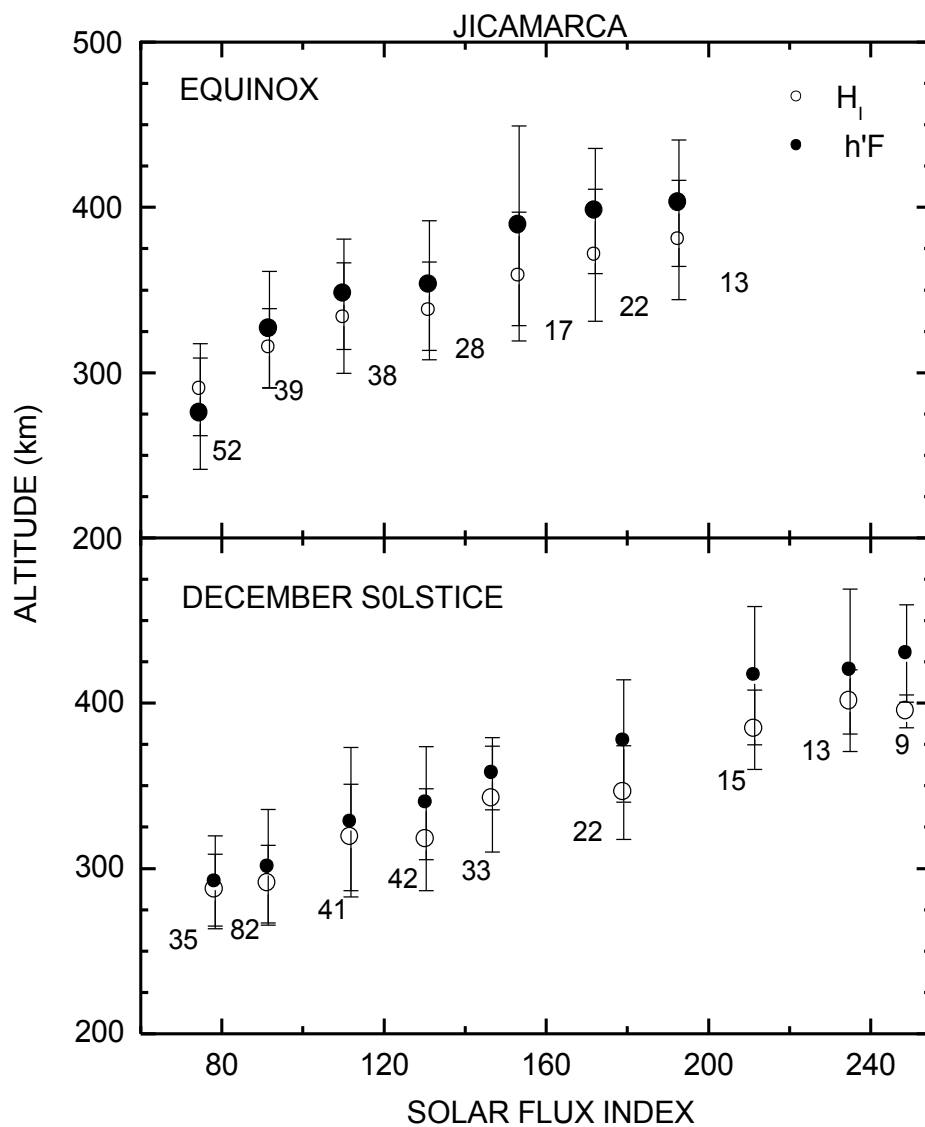
Figure A.2. Onset altitudes of ESF (H_I) and virtual heights of F-peak layer (h'F) from Jicamarca coherent and incoherent scatter radar observations and digisonde data, respectively, during 1996-2006.
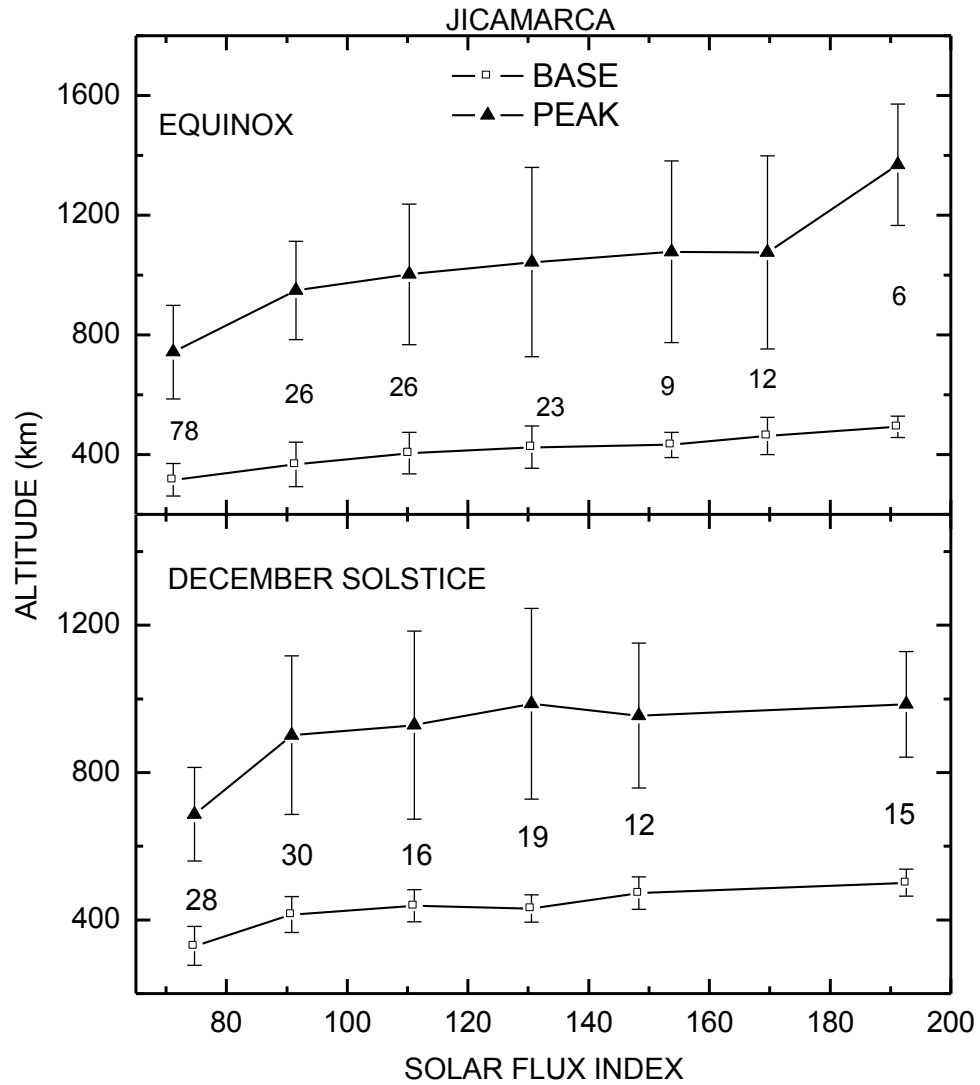
Figure A.3. Average peak and base altitudes of radar plumes as a function of solar flux index from Jicamarca radar observations during equinox and December solstice from 1996 to 2006.
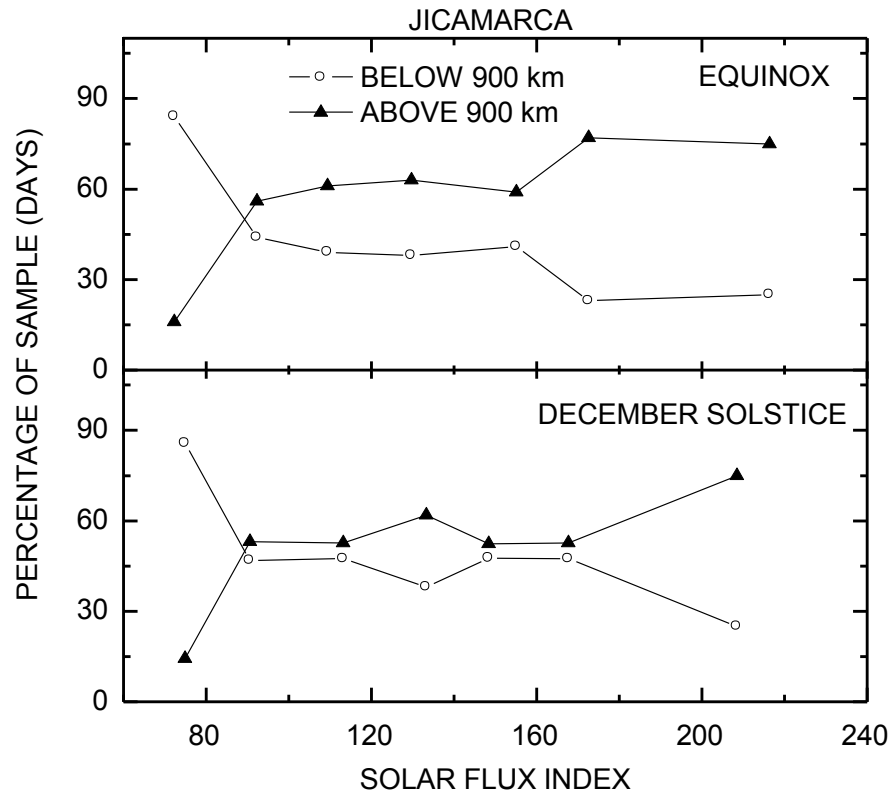
Figure A.4. Percentage of radar plume occurrences with peak altitudes below and above 900 km as a function of solar flux during equinox and December solstice from 1996 to 2006.

APPENDIX B

COPYRIGHT INFORMATION

Appendix B.1. AGU Permissions and Copyright Information

We are pleased to grant permission for the use of the material requested for inclusion in your thesis. The following non-exclusive rights are granted to AGU authors:

- All proprietary rights other than copyright (such as patent rights).
- The right to present the material orally.
- The right to reproduce figures, tables, and extracts, appropriately cited.
- The right to make hard paper copies of all or part of the paper for classroom use.
- The right to deny subsequent commercial use of the paper.

Further reproduction or distribution is not permitted beyond that stipulated. The copyright credit line should appear on the first page of the article or book chapter. The following must also be included,   "Reproduced by permission of American Geophysical Union." To ensure that credit is given to the original source(s) and that authors receive full credit through appropriate citation to their papers,

We recommend that the full bibliographic reference be cited in the reference list. The standard credit line for journal articles is: "Author(s), title of work, publication title, volume number, issue number, citation number (or page number(s) prior to 2002), year. Copyright [year] American Geophysical Union."

 If an article was placed in the public domain, in which case the words "Not subject to U.S. copyright" appear on the bottom of the first page or screen of the article, please substitute "published" for the word "copyright" in the credit line mentioned above.

Copyright information is provided on the inside cover of our journals. For permission for any other use, please contact the AGU Publications Office at AGU, 2000 Florida Ave., N.W., Washington, DC 20009.

Michael Connolly
American Geophysical Union
2000 Florida Avenue, NW
Washington, DC 20009
202-777-7365
mconnolly@agu.org

Appendix B.2. Copyright permission request to the American Geophysical Union

10th February, 2011

Narayan P. Chapagain
CASS, Utah State University
4405 Oldmain Hill
Logan, UT, 84322-4405
(435) 797-3519
n.chapagain@aggiemail.usu.edu

American Geophysical Union
2000 Florida Avenue N. W.
Washington, DC 20009-1277

Dear Permissions Editor,

I am in the process of preparing my Ph.D. dissertation in Department of Physics, Utah State University. I hope to complete by March 2011.

I am requesting your permission to include the manuscripts of my papers in its entirety in my dissertation. I will include acknowledgements and appropriate citations and copyright and reprint rights information in an appendix. The papers published on JGR are following:

1. Chapagain, N. P., B. G. Fejer, and J. L. Chau (2009), Climatology of Post-Sunset Equatorial Spread F Over Jicamarca, *J. Geophys. Res., 114*, A07307 doi:10.1029/2008JA013911.
2.   Chapagain, N. P., M. J. Taylor, and J. V. Eccles (2011), Airglow observations and modeling of F region depletion zonal velocities over Christmas Island, *J. Geophys. Res.*, 116, A02301, doi:10.1029/2010JA015958.

I hope you will reply immediately. If you are not copyright holder, please forward my request to the appropriate person or institution.

Thank you for your cooperation,

Narayan P. Chapagain

Appendix B.3. Permission and copyright information from ELSEVIER

Dear Narayan P. Chapagain,
As an author, you retain rights for a large number of author uses, including use by your employing institute or company. These rights are retained and permitted without the need to obtain specific permission from Elsevier. These include:

- the right to make copies of the article for your own personal use, including for your own classroom teaching use;
- the right to post a pre-print version of the article on Internet web sites including electronic pre-print servers, and to retain indefinitely such version on such servers or sites (see also our information on electronic preprints for a more detailed discussion on these points.);
- the right to present the article at a meeting or conference and to distribute copies of such paper or article to the delegates attending the meeting;
- for the author's employer, if the article is a 'work for hire', made within the scope of the author's employment, the right to use all or part of the information in (any version of) the article for other intra-company use (e.g. training);
- the right to include the **article in full or in part in a thesis or dissertation** (provided that this is not to be published commercially);
  the right to use the article or any part there of in a printed compilation of works of the author, such as collected writings or lecture notes (subsequent to publication of the article in the journal); and the right to prepare other derivative works, to extend the article into book-length form, or to otherwise re-use portions or excerpts in other works, with full acknowledgement of its original publication in the journal.

Other uses by authors should be authorized by Elsevier through the Global Rights Department (for addresses see Obtaining Permissions), and authors are encouraged to let Elsevier know of any particular needs or requirements.

I hope that you find the above information useful. If you feel that further permissions are required apart from the above, please contact our Global Rights Department who will arrange alternative license for you.

My best regards,
Heather

Heather Pitt
Journal Manager | Elsevier Ireland Ltd.

Appendix B.4. Reprint Permission

Narayan P. Chapagain
CASS, Utah State University
4405 Oldmain Hill
Logan
UT 84322-4405
USA

The Edinburgh Building
Shaftesbury Road
Cambridge CB2 8RU, UK

www.cambridge.org

Telephone +44 (0)1223 312393
Fax +44 (0)1223 315052
Email information@cambridge.org

March 8, 2011

Dear Narayan P. Chapagain

Figures 11.29 and 11.30 from Robert W. Schunk and Andrew F. Nagy, Ionospheres, (2000).

Thank you for your recent permission request, to include the above extract/s in:
your forthcoming Ph.D. dissertation, for non-commercial publication.

Non-exclusive permission is granted free of charge for this specific use on the
understanding that you have checked that we do not acknowledge another source for this material.

Please ensure full acknowledgement (author, title, publication date, and
Cambridge University Press).

Yours sincerely

C. Tayl

Claire Taylor
Publishing Assistant
email   ctaylor@cambridge.org

Appendix B.5. Reprint Permission

Radio Observatorio de
JICAMARCA
Radio Observatory

February 18th, 2011

To Whom It May Concern:

I hereby give permission to Narayan P. Chapagain to reprint the following material in his dissertation, as I know that he is in the process of preparing his Ph.D. dissertation in Department of Physics, Utah State University.

As a coauthor of the paper "Climatology of Post-Sunset Equatorial Spread F Over Jicamarca", I have accepted his request to include the material in tis entirety in his dissertation. He will include acknowledgements of my contributions as an author to this manuscript as part of a footnote on the page of that chapter. In addition, a copy of this letter will be printed in an Appendix to his dissertation.

The bibliographical citation will appear at the end of the manuscript as shown:

Chapagain, N. P., B. G. Fejer, and J. L. Chau (2009), Climatology of Post-Sunset Equatorial Spread F Over Jicamarca, J. Geophys. Res., 114, A07307 doi:10.1029/2008JA013911.

Sincerely yours,

Jorge L. Chau, Ph.D.
Radio Observatorio de Jicamarca
Instituto Geofísico del Perú

Appendix B.6. Reprint Permission

24 February 2011

Narayan P. Chapagain
CASS, Utah State University
4405 Oldmain Hill
Logan, UT, 84322-4405
(435) 797-3519
n.chapagain@aggiemail.usu.edu

Dear Dr. Vince Eccles,

I am in the process of preparing my Ph.D. dissertation in Department of Physics, Utah State University. I am planning to submit it by March, 2011.

You were a co-author of my paper "Airglow Observations and Modeling of F-region Depletion Zonal Velocities over Christmas Island, *J. Geophys. Res.*, 116, A02301, doi:10.1029/2010JA015958. I am requesting your permission to include the manuscript in its entirety in my dissertation. I will include acknowledgements of your contributions as an author to this manuscript as part of a footnote on the page of that chapter. In addition, a copy of this letter will be printed in an Appendix to my dissertation.

Please indicate your approval of this request by signing in the endorsement below. I will be happy to answer any question or special request regarding this letter.

Thank you for your time and consideration.

Narayan P. Chapagain

I hereby give my permission to Narayan P. Chapagain to reprint the following manuscript in his dissertation.

Chapagain, N. P., M. J. Taylor, and J. V. Eccles (2011), Airglow observations and modeling of F region depletion zonal velocities over Christmas Island, *J. Geophys. Res.*, 116, A02301, doi:10.1029/2010JA015958.
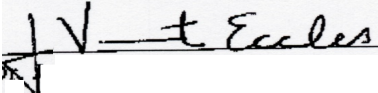
Signed   *J V—t Eccles*   Date : Feb 25, 2011

 Dr. J. Vincent Eccles
Space Environment Corporation
Providence, Utah, USA.

Appendix B.7. Reprint Permission

Narayan P. Chapagain
CASS, Utah State University
4405 Oldmain Hill
Logan, UT, 84322-4405
n.chapagain@aggiemail.usu.edu

Dear Dr. P-Dominique Pautet,

I am in the process of preparing my Ph.D. dissertation in Department of Physics, Utah State University. I am planning to submit it by March, 2011.

I am co-author of papers (1) Simultaneous observations of equatorial F-region plasma depletions over Brazil during the spread F Experiment (SpreadFEx), *Ann. Geophys., 27*, 2371–2381. 2009, and (2) Propagation of Plasma Bubbles Observed in Brazil from GPS and Airglow Data, *Adv. Space Res.*, doi:10.1016/j.asr.2010.09.025. I am requesting your permission to include the materials from these manuscripts in my dissertation. I will include acknowledgements of your contributions as an author to this manuscript as part of a footnote on the pages of the chapters. In addition, a copy of this letter will be printed in an Appendix to my dissertation.

Please indicate your approval of this request by signing in the endorsement below. I will be happy to answer any question or special request regarding this letter.

Thank you for your cooperation,

Narayan P. Chapagain

_____

I hereby give permission to Narayan P. Chapagain to reprint the following material in his dissertation.

Pautet, P.-D., M. J. Taylor, N. P. Chapagain, H. Takahashi, A. F. Medeiros, F. T. Sao Sabbas, and D. C. Fritts,(2009), Simultaneous observations of equatorial F-region plasma depletions over Brazil during the spread F Experiment (SpreadFEx), *Ann. Geophys., 27*, 2371–2381.

Haase, J. S., T. Dautermann, M.J. Taylor, N. P. Chapagain, E. Calais, and P.-D. Pautet (2011), Propagation of Plasma Bubbles Observed in Brazil from GPS and Airglow Data, *Adv. Space Res.*, doi:10.1016/j.asr.2010.09.025.

Signed   *D. Pautet*   Date 24th February, 2011

Dr. P-Dominique Pautet
CASS, Utah State University, Logan, UT.

Appendix B.8. Reprint Permission

February 21st, 2011

Dr. Jennifer Haase   Narayan P. Chapagain
 Purdue University   CASS, Utah State University
Department of Earth and Atmospheric Sciences   4405 Oldmain Hill
West Lafayette, Indiana, USA   Logan, UT, 84322-4405
                                                      n.chapagain@aggiemail.usu.edu

Dear Dr. Jennifer Haase,

I am in the process of preparing my Ph.D. dissertation in Physics Department, Utah State University. I am planning to submit it on March, 2011.

I am co-author of your paper "Propagation of Plasma Bubbles Observed in Brazil from GPS and Airglow Data", *Adv. Space Res.*, doi:10.1016/j.asr.2010.09.025. I am requesting your permission to include the materials (Figure 14 and table 2) in my dissertation. I will include acknowledgements of your contributions as an author to this manuscript as part of a footnote on the page of that chapter. In addition, a copy of this letter will be printed in an Appendix to my dissertation.

Please indicate your approval of this request by signing in the endorsement below. I will be happy to answer any question or special request regarding this letter.

Thank you for your time and consideration.

Narayan P. Chapagain

_____

I hereby give my permission to Narayan P. Chapagain to reprint the following material in his dissertation.
Haase, J. S., T. Dautermann, M.J. Taylor, N. P. Chapagain, E. Calais, and P.-D. Pautet (2011), Propagation of Plasma Bubbles Observed in Brazil from GPS and Airglow Data, *Adv. Space Res.*, doi:10.1016/j.asr.2010.09.025.

Signed …   Date……2/21/2011..

Dr. Jennifer Haase
Purdue University
Department of Earth and Atmospheric Sciences
West Lafayette, Indiana, USA

Appendix B.9. Reprint Permission

22 February 2006

Narayan P. Chapagain
CASS, Utah State University
4405 Oldmain Hill
Logan, UT, 84322-4405
(435) 797-3519
n.chapagain@aggiemail.usu.edu

Dear Dr. E. Calais,

I am in the process of preparing my Ph.D. dissertation in Department of Physics, Utah State University. I am planning to submit it by March, 2011.

You were also the co-author of paper "Propagation of Plasma Bubbles Observed in Brazil from GPS and Airglow Data, Adv. Space Res., doi:10.1016/j.asr.2010.09.025. I am requesting your permission to include the material of the manuscript in my dissertation. I will include acknowledgements of your contributions as an author to this manuscript as part of a footnote on the page of that chapter. In addition, a copy of this letter will be printed in an Appendix to my dissertation.

Please indicate your approval of this request by signing in the endorsement below or by replying by email. I will be happy to answer any question regarding this letter.

Thank you for your cooperation.

Narayan P. Chapagain

I hereby give my permission to Narayan P. Chapagain to reprint the following manuscript in his dissertation.

Haase, J. S., T. Dautermann, M.J. Taylor, N. P. Chapagain, E. Calais, and P.-D. Pautet (2011), Propagation of Plasma Bubbles Observed in Brazil from GPS and Airglow Data, Adv. Space Res., doi:10.1016/j.asr.2010.09.025.
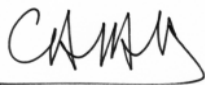
Signed _____   Date : …2/22/2011…….

Dr. E. Calais

Appendix B.10. Reprint Permission

13 February 2011

Narayan P. Chapagain
CASS, Utah State University
4405 Oldmain Hill
Logan, UT, 84322-4405
(435) 797-3519
n.chapagain@aggiemail.usu.edu

Dear Dr. Hisao Takahashi,

I am in the process of preparing my Ph.D. dissertation in Department of Physics, Utah State University. I am planning to submit it by March, 2011.

You were also the co-author of paper "Simultaneous observations of equatorial F-region plasma depletions over Brazil during the spread F Experiment (SpreadFEx), *Ann. Geophys.*, 27, 2371–2381. 2009. I am requesting your permission to include the material of the manuscript in my dissertation. I will include acknowledgements of your contributions as an author to this manuscript as part of a footnote on the page of that chapter. In addition, a copy of this letter will be printed in an Appendix to my dissertation.

Please indicate your approval of this request by signing in the endorsement below or by attaching a letter for permission. I will be happy to answer any question regarding this letter.

Thank you for your cooperation.

Narayan P. Chapagain

I hereby give my permission to Narayan P. Chapagain to reprint the following manuscript in his dissertation.

Pautet, P.-D., M. J. Taylor, N. P. Chapagain, H. Takahashi, A. F. Medeiros, F. T. Sao Sabbas, and D. C. Fritts,(2009), Simultaneous observations of equatorial F-region plasma depletions over Brazil during the spread F Experiment (SpreadFEx), *Ann. Geophys.*, 27, 2371–2381.
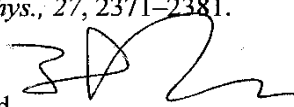
Signed ....   Date March 15, 2011

Dr. Hisao Takahashi

Appendix B.11. Reprint Permission

from: Dave Fritts dave@cora.nwra.com
to: "N.P. Chapagain" npchapagain@gmail.com
date: Wed, Feb 23, 2011 at 6:26 AM
sub: Re. Permission for reprint
mailed-by: cora.nwra.com
signed-by: cora.nwra.com

Hi Narayan,

I hereby give my permission to Narayan P. Chapagain to reprint the following materials in his dissertation. "Pautet, P.-D., M. J. Taylor, N. P. Chapagain, H. Takahashi, A. F. Medeiros, F. T. Sao Sabbas, and D. C. Fritts,(2009), Simultaneous observations of equatorial F-region plasma depletions over Brazil during the spread F Experiment (SpreadFEx)*, Ann. Geophys., 27*, 2371–2381".

Good luck with your defense.

Cheers,
Dave

North West Research Associates
CoRA Division
 Boulder, CO, USA

Appendix B.12. Reprint Permission

from: Amauri afragoso@df.ufcg.edu.br
to: "N.P. Chapagain" npchapagain@gmail.com
date: Wed, Feb 23, 2011 at 9:27 AM
sub: Re. Permission for reprint the manuscript
mailed-by: df.ufcg.edu.br

Dear Narayan,
I hereby give my permission to Narayan P. Chapagain to reprint the following materials
in his dissertation. "Pautet, P.-D., M. J. Taylor, N. P. Chapagain, H. Takahashi, A. F.
Medeiros, F. T. Sao Sabbas, and D. C. Fritts,(2009), Simultaneous observations of
equatorial F-region plasma depletions over Brazil during the spread F Experiment
(SpreadFEx)*, Ann. Geophys., 27*, 2371–2381".

Amauri

Prof. Amauri Fragoso de Medeiros
Unidade Acadêmica de Física - UFCG
Av. Aprígio Veloso, 882 - Bloco CY - Bodocongó
CEP: 58.109-970 Campina Grande -Paraíba
Office : +55 (83) 2101-1196
Home: +55 (83) 3321-4569
Cel. 83-8858-4963, 83-8113-5679
E-mail: afragoso@df.ufcg.edu.br

Appendix B.13. Reprint Permission

from: Thomas.Dautermann@dlr.de
to: "N.P. Chapagain" npchapagain@gmail.com
date: Tue, Feb 22, 2011 at 12:47 AM
sub: Re. Permission for reprint the manuscript
mailed-by: dlr.de

Hello Narayan,

I hereby give my permission to Narayan P. Chapagain to reprint the following materials
in his dissertation. "Haase, J. S., T. Dautermann, M.J. Taylor, N. P. Chapagain, E. Calais,
and P.-D. Pautet (2011), Propagation of Plasma Bubbles Observed in Brazil from GPS
and Airglow Data, *Adv. Space Res.*, doi:10.1016/j.asr.2010.09.025.

Cheers,
Thomas Dauterman

German Aerospace Center (DLR)
Department of Communication and Navigation
Oberpfaffenhofen, 82253
Wessling, Germany

CURRICULUM VITAE

NARAYAN P. CHAPAGAIN

Center for Atmospheric and Space Sciences
Physics Department
Utah State University
Logan, UT 84322
(435) 797-3519
n.chapagain@aggiemail.usu.edu

EDUCATION

Ph.D.   April 2011   Utah State University, Logan, UT, USA
Area of study: Space and Ionospheric Physics
Dissertation: Dynamics of Equatorial Spread F using Ground-based Optical and Radar Measurements

M.Tech.   August 2003   Andhra University, Andhra Pradesh, India
Area of study: Atmospheric and Space Sciences
Thesis: Total Ozone Measurements over Kathmandu Using Brewer Spectrophotometer

M.S.   March 1992   Tribhuvan University, Kathmandu, Nepal
Major: Physics
Thesis: The Study on Preheat in D-D and D-T as a Fusion Fuel in Inertial Confinement Fusion Plasma

B.S.   September 1988   Tribhuvan University, Kathmandu, Nepal
Major: Physics and Mathematics

SCHOLARSHIPS AND AWARDS

- Claude E. ZoBell Scholarship (2009-2010), College of Science, Utah State University (USU), UT, USA.
- 2009 Graduate Student Senate (GSS) Enhancement Award, USU, USA.
- First prize in oral presentation from College of Science, '*2009 Intermountain Graduate Research Symposium*', USU, USA.
- 2008 Howard L. Blood Endowed Scholarship, Physics Department, USU, USA.
- 2007 Laboratory Teaching Assistant of the Year, Physics Department, USU, USA.
- 2006 Gene Adam Award, Outstanding Academic Performance, Physics Department, USU, USA.

- Scholarship for Post Graduate Course in Space and Atmospheric Sciences - Conducted by Centre for Space Science and Technical Education in Asia and the Pacific (CSSTE-AP) affiliated to the United Nations, 1999-2000.

PROFESSIONAL EXPERIENCE
- Graduate Teaching Assistant, 2005-2011, Physics Department, Utah State University, UT, USA.
- Graduate Research Assistant, 2006-2009, Center for Atmospheric and Space Sciences, Utah State University, UT, USA.
- Reviewer, Journal of Geophysical Research (JGR) - Space Physics.
- Lecturer, 1995-2005, Tribhuvan University, Kathmandu, Nepal.
- Assistant Lecturer, 1992-1995, Tribhuvan University, Kathmandu, Nepal.
- Academic Director, 2000-2005, Kathmandu Bernhardt College, Kathmandu, Nepal.
- Head, Department of Physics, 1998-2000, Patan M. Campus, Tribhuvan University, Lalitpur, Nepal.
- Head, Department of Physics, 1997-2000, Kathmandu, Donbosco College, Nepal.

SELECTED MEMBERSHIPS AND SERVICES
- American Geophysical Union (AGU).
- American Physical Society (APS).
- Life Member, Nepal Physical Society (NPS), Nepal.
- University Teacher Association, Tribhuvan University, Nepal (1992-2005).
- Member of Board of Director, Kathmandu Bernhardt College, Nepal (2000-2005).
- Subject Committee Member in Physics, Mahendra Sanskrit University, Kathmandu, Nepal (2002-2004).
- Joint Secretary, Nepal Physical Society (NPS), Nepal (1999–2001).
- Treasurer, University Teacher Association, Patan M. Campus, Nepal (1993-1995).

PUBLICATIONS

Main Publications
Chapagain, N. P., B. G. Fejer, and J. L. Chau (2009), Climatology of post-sunset equatorial spread *F* over Jicamarca, *J. Geophys. Res., 114*, A07307 doi:10.1029/2008JA013911.

Chapagain, N. P., M. J. Taylor, and J. V. Eccles (2011), Airglow observations and modeling of F region depletion zonal velocities over Christmas Island, *J. Geophys. Res.*, 116, A02301, doi:10.1029/2010JA015958.

Chapagain, N. P., and M. J. Taylor, OI (630.0 nm) Airglow depletion zonal velocity measurements over Ascension Island (*Manuscript ready to submit on JGR*).

Pautet, P.-D., M. J. Taylor, N. P. Chapagain, H. Takahashi, A. F. Medeiros, F. T. Sao Sabbas, and D. C. Fritts (2009), Simultaneous observations of equatorial F-region plasma depletions over Brazil during the spread F Experiment (SpreadFEx)*, Ann. Geophys., 27*, 2371–2381.

Haase, J. S., T. Dautermann, M. J. Taylor, N. P. Chapagain, E. Calais, and P.-D. Pautet (2011), Propagation of plasma bubbles observed in brazil from GPS and airglow data, *Adv. Space Res.*, doi:10.1016/j.asr.2010.09.025.

Other Publications

Chapagain, N. P. and L. N. Jha (1996), Preheat in D-D and D-T as a fusion fuel in inertial confinement fusion plasma*, Proceedings paper of 21st International College on Physics and Contemporary Needs*, Nathiagali, Pakistan.

Chapagain, N. P.**,** S. Lal, and S. Gurung (2002), The relation between total ozone and UV irradiation over Ahmedabad and comparison of total ozone over Ahmedabad and Kathmandu, *Proceedings paper of the Nepal Physical Society,* 18th Annual Convention, Kathmandu, Nepal.

Chapagain, N. P. (2003), The diurnal variation of total ozone over Kathmandu measured with Brewer Spectrophotometer, *Proceeding paper of The Nepal Physical Society, 19th Annual Convention,* Kathmandu, Nepal.

Chapagain, N. P. (2003), The variability in atmospheric ozone over Kathmandu measured with a Brewer Spectrophotometer, *Journal of Royal Nepal Academy of Science and Technology (RONAST)*.

Co-author of Books Publications

B. Gautam, S. K. Neupane, and N. P. Chapagain (2001)**,** Textbook of Physics for Proficiency Certificate Level First Year, *Kala Publication*, Nepal.

B. Gautam, S. K. Neupane, and N. P. Chapagain (2001), Textbook of Physics for Proficiency Certificate Level Second Year, *Kala Publication*, Nepal.

B. Gautam, S. K. Neupane, and N. P. Chapagain (2000)**,** Textbook of Physics for Class XI*, Kala Publication*, Nepal.

B. Gautam, S. K. Neupane, and N. P. Chapagain (1999)**,** Textbook of Physics for Class XII*, Kala Publication,* Nepal.

CONFERENCE PRESENTATIONS

Chapagain, N. P. and M. J. Taylor, Dynamics of ionospheric plasma depletion measured by airglow emissions, *American Physical Society Four Corners Fall Meeting*, Weber State University, Ogden, Utah, October 15-16, 2010.

P.-D. Pautet, N. P. Chapagain, M. J. Taylor, A. F. Medeiros, J. J. Makela, H. Takahashi, and D. C. Fritts: Investigating the ionospheric bubble structures

observed from Northeastern Brazil, *AGU Spring Meeting*, Foz do Iguassu, Brazil, August 8-12, 2010.

Chapagain, N. P., and M. J. Taylor, Dynamics of equatorial spread *F* from optical measurements*, 2010 Intermountain Graduate Research Symposium,* Utah State University, Logan, UT, April 2010.

Chapagain, N. P., and M. J. Taylor, Airglow depletion zonal velocities over Ascension Island, poster presentation, *AGU Fall Meeting,* San Francisco, CA, December 2009.

Chapagain, N. P., and M. J. Taylor, Ionospheric OI 630 nm airglow depletion zonal velocities over Ascension Island, poster presentation, *CEDAR-DASI Workshop,* Santa Fe, NM, June 2009.

Chapagain, N. P., M. J. Taylor, and V.J. Eccles, Ionospheric plasma bubble zonal velocities from Christmas Island Using airglow emissions, poster presentation, *Space Weather Workshop*, Boulder, CO, April 2009.

Chapagain, N. P., and M. J. Taylor, Optical measurements of ionospheric plasma bubbles from Christmas Island, *2009 Intermountain Graduate Research Symposium*, Utah State University, Logan, UT, April 2009.

Chapagain, N. P., and M. J. Taylor, Optical measurements of equatorial plasma depletions from Christmas Island, poster presentation, *AGU Fall Meeting*, San Francisco, CA, December 2008.

Chapagain, N. P., M. J. Taylor, and B. G. Fejer*,* Equatorial spread *F* and plasma bubble*,* Physics colloquium, *Utah State University*, UT, September 2008.

Chapagain, N. P., M. J. Taylor, P.-D Pautet, H. Takahashi, and D. C. Fritts, Simultaneous observations of equatorial ionospheric plasma bubbles from two sites during the SpreadFEx campaign*,* poster presentation, *CEDAR-DASI Workshop*, Midway, UT, June 2008.

Chapagain, N. P., M. J. Taylor, T. Dautermann, and J. S. Haase, Properties and propagation of plasma bubbles observed over Brazil during the SpreadFEx campaign, 2005, poster presentation, *Space Weather Workshop,* Boulder, CO, April 2008.

Chapagain, N. P., and M. J. Taylor, Propagation of plasma bubble in Brazil observed with GPS and airglow, Graduate Research Symposium, Utah State University, UT, April 2008.

Chapagain, N. P., and B. G. Fejer, Study of early night equatorial spread *F* over Jicamarca*,* poster presentation, *CEDAR-DASI Workshop*, Santa Fe, NM, June 2007.

Chapagain, N. P., The variability in the atmospheric total ozone over Kathmandu measured with Brewer Spectrophotometer, *20th Annual convention of Nepal Physical Society,* Kathmandu, Nepal, June 2003.

Chapagain, N. P., The variability in the atmospheric total ozone over Kathmandu from TOMS satellite data, *4*^{*th*} *National convention, Royal Nepal Academy of Science and Technology (RONAST)*, April 2002.

Chapagain, N. P., S. Lal, and S. Gurung, The relation between total ozone and UV irradiation over Ahmedabad, India and comparison of total ozone over Ahmedabad and Kathmandu, *18*^{*th*} *Annual convention of Nepal Physical Society*, Kathmandu, Nepal, June 2001.

Chapagain, N. P., and L. N. Jha, Preheat in D-D and D-T as a fusion fuel in inertial confinement fusion plasma, poster presentation, *21*^{*st*} *International Summer College on Physics and Contemporary Needs,* Nathiagali, Pakistan, June-July 1996.

Chapagain, N. P. and L. N. Jha, Self heating in inertial confinement fusion plasma, *RONAST Second National Conference on Science and Technology,* Kathmandu, Nepal, June 1994.

Chapagain, N. P. and L. N. Jha, Self Heating in inertial confinement fusion plasma, *SAHA Centenary Symposium on Plasma Science and Technology*, University of Allahabad, Allahabad, India, October 1993.